System Level Segmented Telescope Design (SLSTD) Final Report

Contract 80NSSC18K0817

Lockheed Martin Corporation

Lockheed Martin Space

Advanced Technology Center

April 1, 2019

CAGE Code: 06887

Lockheed Martin Space, Sunnyvale, CA 94088-3504

Note: This document is APPROVED for public release by Lockheed Martin Space. The material herein is based upon work supported by NASA under award No(s) 80NSSC18K0817. Any opinions, findings, and conclusions or recommendations expressed in this material are those of Lockheed Martin Space and do not necessarily reflect the views of the National Aeronautics and Space Administration.

The System Level Segmented Telescope Design Team

Lockheed Martin Space, Advanced Technology Center

Larry Dewell, Principal Investigator
Alison Nordt, Program Manager
Raymond Bell, Sr. Fellow and Technical Advisor
William Marquardt, Contracts Sr. Staff
Ankur Chopra, Control Systems Engineer Sr. Staff
Kiarash Tajdaran, Control Systems Research Scientist
Michael Jacoby, Structural Dynamics Principal
Torben Andersen, Optical Engineer Sr. Staff
Clem Tillier, Systems Engineering Sr. Staff

Collins Aerospace (United Technologies)

Bari M. Southard, Program Manager and Technical Lead
Brandon Olson, Technical Contributor
Corey Pullen, Technical Contributor

Harris Corporation (Space and Intelligence Systems)

Lynn Allen, Program Manager
Rob Egerman, Chief Systems Engineer
Matthew East, Opto-mechanical Engineer
Hannah Miller, Metrology Engineer

Coherent

Jay Daniel, Program Manager and Technical Lead

Revisions

Rev	Authority	Change Description	Approval Date
–		Initial Release (Public Release Approval Pending)	2019-04-01
A	LM PIRA #SSS201904003	Public Release Approved: watermark removed and Coherent footers with restrictions removed with authorization from Coherent	2019-04-15
B	A. Nordt, L.Dewell, LM PIRA #SSS201904045	Section 8.2 added	2019-04-24

TABLE OF CONTENTS

LIST OF FIGURES

Page

LIST OF TABLES

Page

1. Executive Summary

The top-level goal of the System-Level Segmented Telescope Design (SLSTD) study was to provide NASA with technical insights from an industry perspective on future large space-based telescope architectures under consideration by the 2020 Decadal Committee. Lockheed Martin Space is pleased to provide a report of the results of this study, executed by engineers and scientists at the Advanced Technology Center, as well as our external partners from Collins Aerospace, Harris International and Coherent.

This team has worked closely with the NASA-led Science and Technology Design Teams (STDTs) to understand the baseline large-telescope architectures, develop integrated performance models, predict system performance, assess manufacturability and production processes, and develop technology maturation plans. While these areas of focus are described in detail in this report, the key finding from the study are:

Large Ultraviolet/Optical/InfraRed (LUVOIR) Surveyor dynamic stability: The line-of-sight (LOS) and wavefront error (WFE) dynamic stability requirements for the 15-meter LUVOIR architecture can feasibly be met with a non-contact vibration isolation and precision pointing system (VIPPS). Compliance with the stability requirements is predicted with conservative assumptions on structural dynamics, spacecraft-payload residual coupling and disturbances arising from actuator exported loads and sensor noise. Fast Steering Mirror (FSM) errors dominate the high temporal frequency range of the WFE stability, and Control Moment Gyro (CMG) and VIPPS disturbances dominate at low frequencies. Total root-mean-square (RMS) WFE stability of 5.1 picometers is predicted in the presence of all modeled disturbances.

LUVOIR Fast Steering Mirror (FSM) and LOS dynamic stability performance: Under the disturbances and noise sources considered in this study, and when a non-contact vibration isolation system is employed, a FSM does not appear to be necessary to meet the LUVOIR dynamic stability requirements for LOS and WFE stability. Moreover, there is a range of realistic FSM disturbances and bandwidth parameters consistent with the current state-of-the-art for which LOS stability without a FSM outperforms a system with a FSM. While articulation of the LOS by means of a FSM may be needed to support other instrument operations of the observatory concept of operation in general, this finding underscores the importance of carefully specifying the bandwidth and noise characteristics of the FSM.

LUVOIR transient settling: A key feature of the LUVOIR architecture is its ability to perform science over a hemispherical anti-sun field-of-regard, with articulation of the telescope and payload optical instruments with respect to the sunshade. Transient settling time of the LOS and WFE for the 15-meter LUVOIR architecture, under conservative assumptions on structural dynamics and considering only slew of the entire observatory about the sunline, is estimated to be on the order of 5-10 minutes, depending on the design parameters of the slew and the slew agility.

Habitable Exoplanet (HabEx) Mission stress, strength and lifetime: Fracture durability for large monolithic (4m) mirrors requires extensive knowledge of material properties, testing, initial flaw size and load prediction. The HabEx mirror design appears to be capable of surviving over its lifetime, more test data (particularly for ULE), analysis and glass inspection will be critical. Moreover, glass inspection is required to ensure no flaws are greater than a certain size.

HabEx thermal stability system performance: An integrated thermal model for the baseline 4-meter HabEx architecture, including active thermal control and variation in solar heating over realistic observatory operations, predicts worst-case mirror-local temperature stability of the Primary Mirror of 0.0003°C over a 10-minute window and 0.0012°C over a 56-hour window. These temperature changes are predicted to result in worst-case combined RMS wavefront change of 33 picometers over 56 hours (long-term stability) and 1.1 picometers over 10 minutes. This degree of thermal stability was achieved with an orbital average power consumption of under 600 Watts.

2. Study Scope and Objectives

In the next decade, NASA will begin to develop large space-based observatories to answer for humankind perhaps the most fundamental astronomy question of our age – are we alone in the universe? Three such envisioned missions architectures – the Origins Space Telescope (OST), the Habitable Exoplanet (HabEx) Imaging Mission, and the Large Ultraviolet/Optical/InfraRed (LUVOIR) Surveyor – all require extreme levels of dynamic stability and precision pointing and wavefront error performance over long observation durations. Achieving ultra-stability of segmented optical systems with integrated coronagraphs involves the integration of high-performance subsystems, including isolation, reaction-cancelling fast steering mirrors, wavefront sensing and control and segment relative position control, to name a few. This presents significant systems engineering and integrated design challenges, including requirements flowdown and definition, system-level modeling to quantify the performance and assess compliance, and the development of plans for further technology development.

The eight key technical objectives of this study were the following:

1. Develop a comprehensive integrated model of a segmented optical space telescope, using the LUVOIR 15-meter architecture as a specific example, that includes detailed models of structural dynamics, control systems, segmented telescope optical sensitivities and realistic disturbance sources;
2. Quantify the dynamic errors, using the LUVIOR 15-meter architecture as an example, of a space-based segmented telescope arising from realistic disturbance sources and physical parameters, particularly as those errors relate to the dynamic stability requirements to support coronagraph instruments;
3. Quantify the transient characteristics (such as settling time) of those dynamic errors when a large space telescope undergoes slew maneuvers as part of its retargeting concept of operation, and study the sensitivity of these transient error properties to relevant design degrees of freedom;
4. Design a complete line-of-sight control system architecture for of the LUVOIR observatory that integrates a Fast Steering Mirror (FSM), LOS measurement derived from a payload science instrument , and a noncontact spacecraft-payload vibration isolation interface;
5. Analyze the design of a large monolithic optical telescope, using HabEx as the specific example, in terms of Primary Mirror stress, strength and lifetime structural integrity;
6. Perform integrated Structural Thermal Optical (STOP) modeling of the HabEx observatory, and predict quasi-static Primary Mirror figure error due to variation in the operational thermal environment;
7. Assess the manufacturability and manufacturing processes of the key optical components associated with LUVOIR and HabEx, such as coatings, primary mirror segments, low coefficient of thermal expansion (CTE) materials and surface roughness;
8. Develop a technology plan that will mature the TRL of several key enabling technologies for large space-based precision optical systems, including non-contact vibration isolation, metrology systems and integrated modeling tools.

The scope of the specific analysis and trade studies executed was limited to the LUVOIR and HabEx architectures, specifically, the 15-meter segmented LUVOIR architecture and the HabEx 4-meter monolithic architecture. Details on the architectures considered is described in greater detail in the following section. A study on mirror material alternatives for the Origins Space Telescope (OST) was performed by Coherent and is detailed in their report in Section 7. Although the designs for other large telescopes that are in consideration for the 2020 Decadal Survey (the Origins Space Telescope (OST) and the Lynx X-ray observatory) were not specifically with the scope of this work, many of the trade methodologies and analyses approaches performed as part of this study are likewise applicable.

With respect to modeling and performance prediction of dynamic stability, the scope of the models were generally restricted to be linear: linear structural dynamics, and linear optical sensitivities. The steady-state frequency-domain results of section 6.1 were restricted to considering band-limited stationary white noise sources. Errors from individual sources were assumed to be uncorrelated. In addition, all control loops were modeled in the continuous-time domain, and discrete-time control effects were not modeled.

3. Mission Architectures and Analyses and Trades Considered

This section provides descriptions of the mission architectures for LUVOIR and HabEx that were studied. We had frequent interaction and communication with the STDTs and utilized models provided by these teams. We used the information and models provided for the baseline observatory designs which allowed us to leverage previous work and to ensure that our work was valuable and relevant. We present an overview of the analyses and trades studied for each architecture and present suggestions for further trade studies and model improvements.

3.1 LUVOIR Mission Architectures and Analyses and Trades Considered

3.1.1 LUVOIR Architecture Description

The LUVOIR-A architecture was the baseline for the integrated modeling and dynamics analyses performed for this study. LUVOIR-A is a 15-meter aperture design which incorporates 120 primary mirror segments. The design is documented in the LUVOIR Interim Report [1] while some salient design features relevant to our study are discussed here.

The LUVOIR telescope payload includes the Optical Telescope Element and the Backplane Support Frame which houses the science instruments. [Figure 3.1-1] Pointing of the telescope relative to the sunshield is achieved through an articulated boom and a two-axis gimbal at the telescope end of the boom. The LUVOIR boom maintains the telescope center of gravity in line with the center of solar pressure on the sunshield and spacecraft. [Figure 3.1-2]

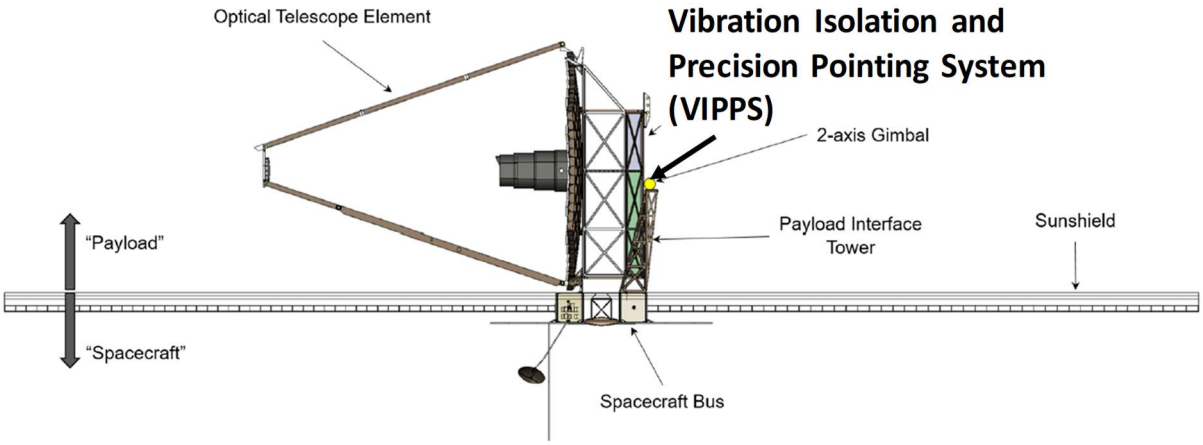

Figure 3.1-1: LUVOIR telescope illustrating the VIPPS location
(Image Credit: LUVOIR Interim Report [1])

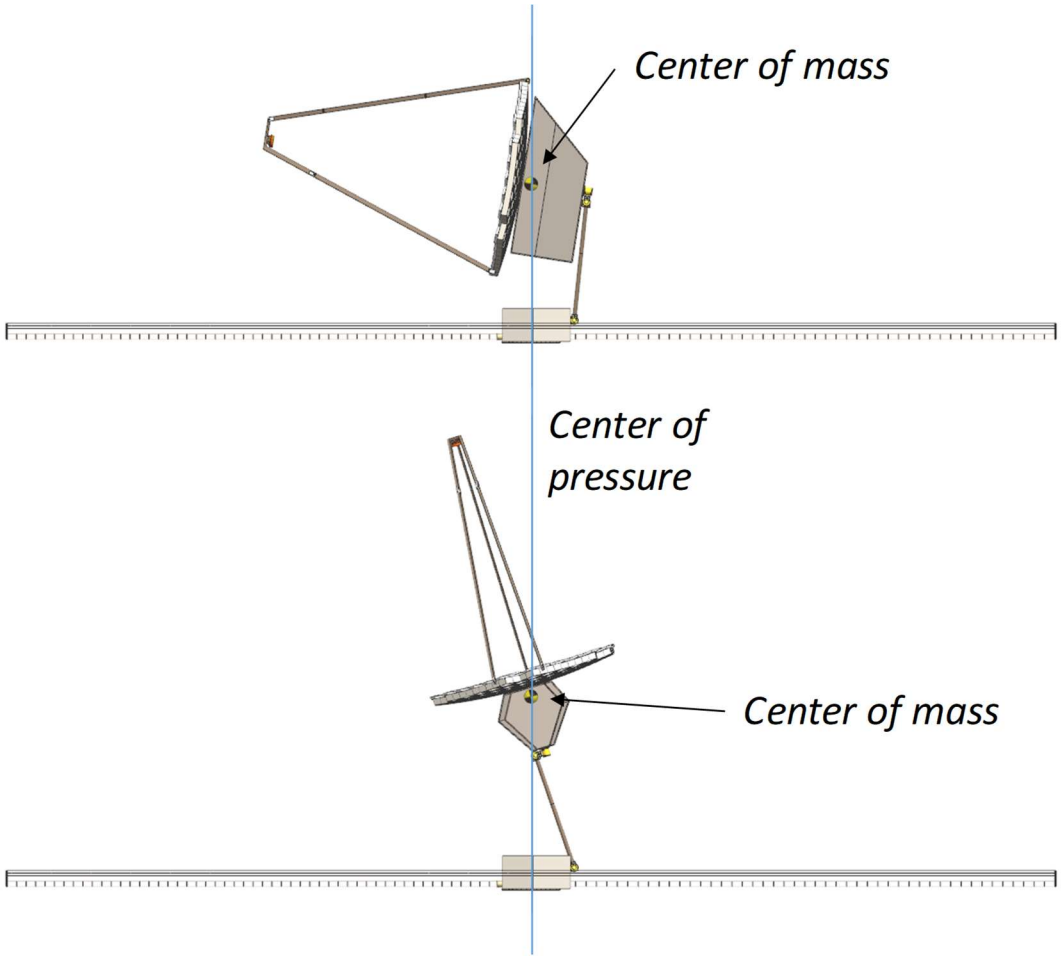

Figure 3.1-2: LUVOIR boom keeps the center of mass in line with the center of pressure (Image Credit: LUVOIR STDT)

The LUVOIR telescope achieves vibration isolation from spacecraft disturbances by physically separating the telescope from the spacecraft and sunshield. The Vibration Isolation and Precision Pointing System (VIPPS) enables the telescope to achieve extreme pointing and image stability while still meeting the line-of-sight agility requirements consistent with its astronomical Surveyor goals. The payload controls overall payload attitude and telescope line-of-sight by pushing against the spacecraft inertia using a set of six non-contact voice coil actuators, while the spacecraft controls its inertial attitude such that interface stroke and gap are maintained. Since the telescope is physically separated, the disturbances and structural excitation of the spacecraft and sunshield do not propagate to the telescope, enabling extreme stability across a broad frequency range. Under such an architecture, individual isolation of spacecraft disturbance sources is not needed, and knowledge of the spacecraft structural dynamics is not needed to achieve the required system dynamic line-of-sight and wave front error stability. The VIPPS interface is located between the gimbal and the backplane of the telescope. [Figure 3.1-1]

The LUVOIR VIPPS is a key element of the design as it relates the integrated modeling and dynamics and control simulations that were the focus of this study. The VIPPS control architecture is depicted in the block diagram shown in Figure 3.1-3. This control architecture was the basis for our dynamics induced optical performance analysis performed in the frequency domain. During steady-state science observations, several control systems are together managing the observatory to meet dynamic stability.

- HDI-FSM LOS control: The High-Definition Imager provides real-time measurement of LOS error, which is corrected by the FSM at ~10 Hz bandwidth.
- VIPPS control: An offload signal from the FSM, together with Payload STA/IMU measurements and interface 6-Degree of Freedom (DOF) pose measurements, are used to derive VCA force commands and a spacecraft CMG torque command.
- Gimbal control: The two-axis gimbal is held at its setpoint associated with observation of the target star.

3.1.2 LUVOIR STDT Interface and Models Received

We conducted weekly telecons with the LUVOIR STDT at GSFC during the study. Through weekly coordination we described our analysis and trade studies and provided timely updates. Frequent communication was valuable as we were able to receive valuable feedback that was immediately useful. We received multiple revisions of several models from the LUVOIR team at GSFC as summarized below:

- Optical Models:
  - Optical prescription of the OTE (not including instruments)
  - Linear Optical Models providing sensitivity of Wave Front Error (WFE) and Line of Sight (LOS) pointing to 6DOF pose of each OTE optical component for both monolithic and segmented primaries. (not including instruments)
- Structural Models:
  - Finite Element Model
  - Mechanical solid model (stp format) in stowed and deployed configurations

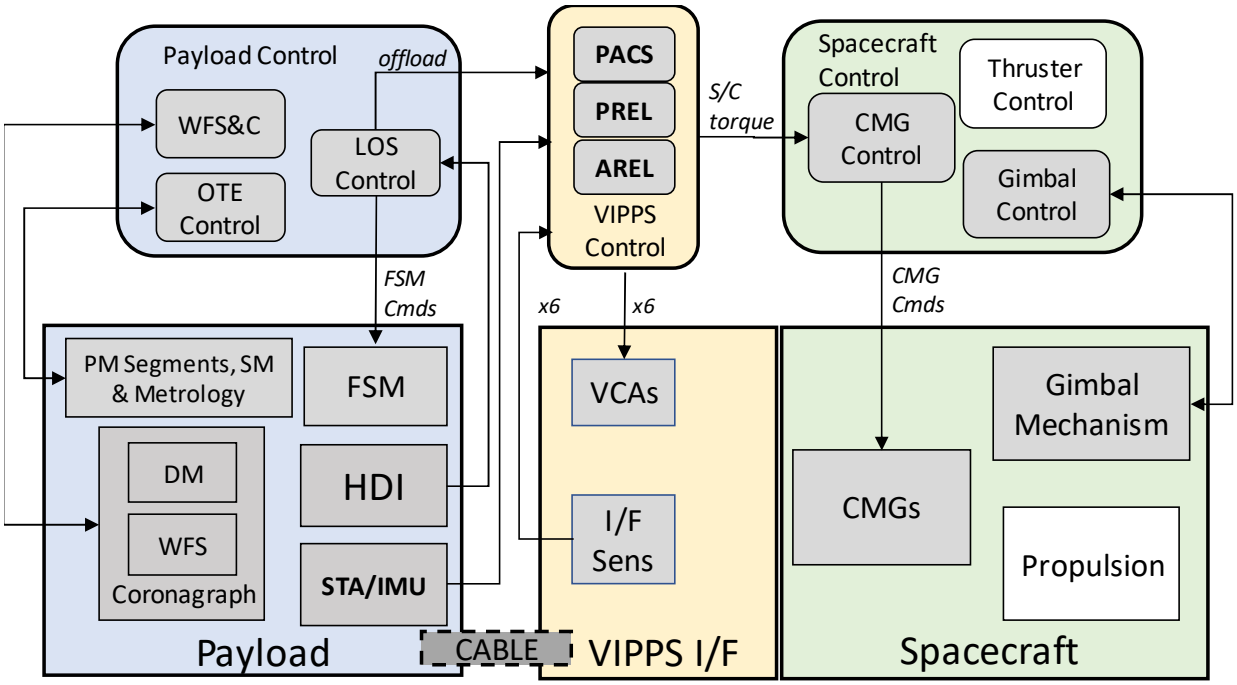

Figure 3.1-3: LUVOIR overall pointing control architecture during steady-state science observation

3.1.3 LUVOIR Trade Studies

A summary of the LUVOIR trade studies is presented in Table 3.1-1. For each trade study on LUVOIR we assessed Wave Front Error (WFE) and Line Of Sight (LOS) performance with different configurations, conditions and disturbances. The details, methods used and results of each trade are described in subsequent sections.

Table 3.1-1: LUVOIR Analyses and Trade Studies Performed

Study Title	Analysis/Trade performed	Next Steps suggested
Fast Steering Mirror	Assessed performance with and without FSM in the control loop; only one FSM bandwidth was considered	Assess effects with different FSM bandwidths and assess the effect of position sensor noise
Slew Performance	Assessed performance after a slew of the telescope rolled around the sun line; several slew profiles studied	Assess slews with pitch angle and a combination of pitch and roll
Control Moment Gyro (CMG) Momentum States	Assessed performance with CMGs having 5 different momentum states	Additional states if necessary
Cable Stiffness models	Assessed performance with two different cable stiffness models (generated through measured data)	Additional cable configurations as necessary
Pitch Angles	Assessed performance when the telescope is pointed at different pitch angles relative to the sunshade	Additional pose states as needed

In addition to the “Next Steps Suggested” that are extensions of the LUVOIR trades performed during this study, we recommend several additional trade studies for future work.

Control Moment Gyro Isolation: Assess WFE and LOS performance as a function of level of isolation of the CMGs. The study will determine if the CMGs should be mounted on an isolated platform.

Instrument Exported Disturbances: Assess OTE sensitivity of optical performance to instrument exported disturbances. This study will help to define the requirements on instruments to ensure that one instrument’s generated disturbance will not adversely affect a different instrument.

VIPPS Interface Location: Currently the VIPPS interface is located at OTE end of the payload interface tower between the OTE and the gimbals. This study will assess performance differences if the VIPPS is located at the Spacecraft end of the payload interface tower.

Momentum dump operations: Assess the contrast loss and optical performance degradation if science operations are conducted during momentum dump operations. This study will help to inform the operations concept and mission plan when determining the frequency and level of momentum dumps.

Several model fidelity enhancements are also recommended for a future study.

Instrument performance: During the current study the instruments were not included in the optical models and their performance was not assessed. Local effects within the instruments, particularly the coronagraph could be included in future work.

Contrast sensitivity: Coronagraphic contrast ratio is a critical parameter for exo-planet discovery. It would be helpful to conduct a study where the figure of merit is contrast ratio instead of WFE or LOS pointing stability. A future study topic is to create a “Contrast LOM” in which sensitivity of contrast to each optic’s 6 DOF pose is determined and then used to assess the affects of each parameter studied here.

Incorporate payload attitude reference: Currently the High Definition Imager (HDI) instrument is used to determine the payload tip and tilt. In a future study the star tracker and Inertial Measurement Unit (IMU) could be used to provide roll determination and help determine model errors.

3.2 HabEx Mission Architectures and Analyses and Trades Considered

3.2.1 HabEx Architecture Description

The HabEx four-meter monolithic primary mirror design was the architecture used for this study. This design is described in the HabEx Interim Report [2] and shown in Figure 3.2-1 with relevant features summarized here. This design incorporates an Optical Telescope Assembly that is connected to the spacecraft through an interface ring. The OTA is housed within a baffle tube and secondary mirror tower. Pointing control is achieved through the use of microthrusters.

3.2.2 HabEx STDT Interface and Models Received

We coordinated with members of the HabEx STDT at JPL and MSFC to understand the architecture and determine what studies might be useful. We received multiple revisions of the following models.

Optical Model: Zmax optical prescription of the OTA
Structural Model: NASTRAN finite element model
Thermal Model: Thermal Desktop model

3.2.3 HabEx Analyses and Trade Studies

The following HabEx analyses and trade studies were initiated. There is still significant work to be done to fully execute some of these trades. The studies are summarized here and are fully described in the subsequent sections.

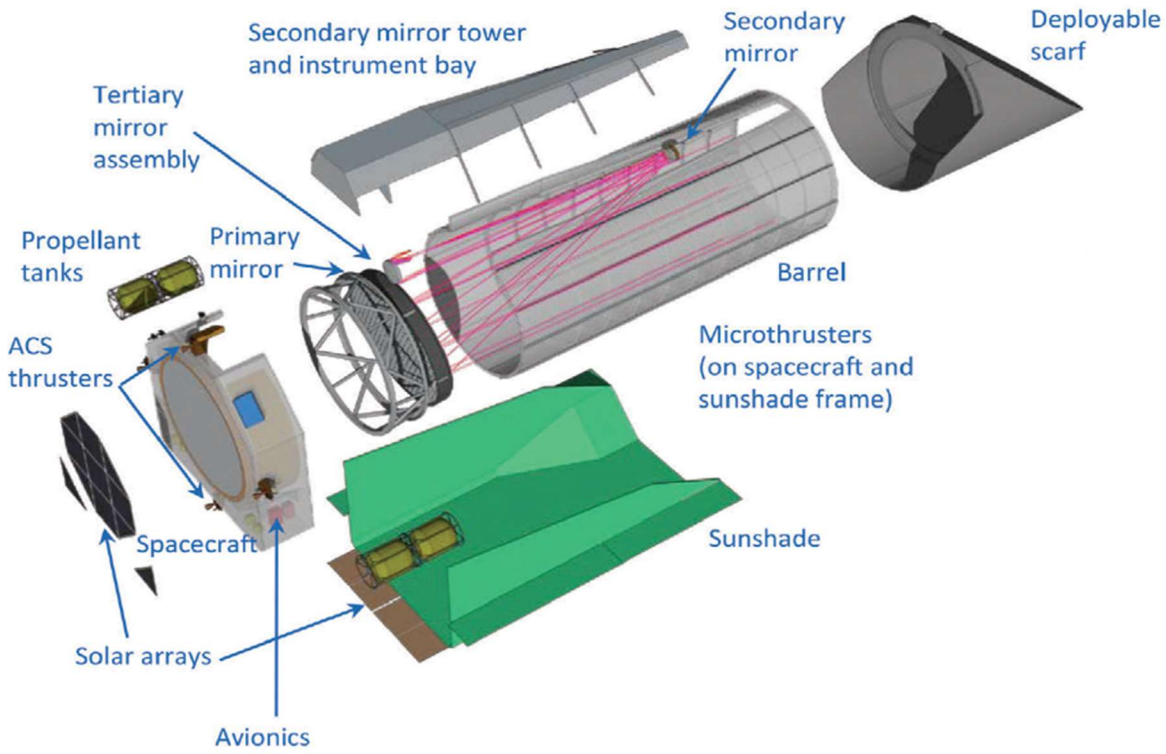

Figure 3.2-1: HabEx Observatory (credit HabEx Interim Report [2])

Table 3.2-1: HabEx Analyses and Trade Studies Performed

Study Title	Analysis/Trade performed	Next Steps suggested
Microthrusters vs Disturbance Free Payload	Initial steps were performed: state space models created for spacecraft and payload	Frequency domain dynamics analysis and performance assessment
Primary mirror stress analysis	Stresses were determined over the course of a hypothetical life time	Refine lifetime assumptions particularly for launch and vibe loads
Primary mirror strength and life analysis	Assessment fracture safety of the 4m monolithic primary and compared ULE and Zerodur	Additional fracture data and life cycle load definition fidelity
Linear Optical Model for LOS	Created linear sensitivities for LOS pointing to each optical component in 6DOF	To be used in the microthrusters vs DFP trade study

In addition to the "Next Steps Suggested" that are extensions of the HabEx studies performed during this period, we recommend the following study for future work.
CTE Non-uniformity: A future study could examine the effects of CTE non-uniformity within the primary mirror. The study would evaluate current state of the art property uniformity in both ULE and Zerodur and analyze the effects on WFE and internal mirror stresses due to expected thermal loading conditions.

3.3 Mirror Manufacturing Trades Considered

Lockheed Martin's partners in the SLSTD study, Collins, Harris and Coherent, have examined the state of the art of many aspects of mirror manufacturing, testing and performance. Each has addressed different aspects of mirror production and performance. A brief summary of trades and testbeds suggested for future studies and work performed by each organization is presented here while Section 7 contains individual reports from each partner which contain more details.

3.3.1 Collins

HabEx Thermal Analysis: The Collins team performed thermal analysis for a HabEx mission with a 4-meter monolithic Zerodur open-back mirror. They determined the thermal mapping for an assumed mission profile then assessed static and transient thermal and optical performance and power consumption for both orbital average and peak power.
Mirror Coating Assessment: The Collins conducted a study of mirror coatings for far UltraViolet wavelength reflectance. They provided and overview of coating techniques ranging from historic methods to the state of the art. Storage and effects on long term life were considered as well.

Collins has suggested numerous additional trade studies, analyses and testbed activities related to thermal modeling and stability and far UV coatings. These are described in the Collins report in Section 7.

3.3.2 Harris

Mirror Manufacturing Process: The Harris team assessed the processes and issues involved in manufacturing the large number (~120) of LUVOIR-scale (~1.2m) mirror segments within the minimum time period possible. They have identified numerous considerations including:

- Order of operations in processing (manufacturing and testing) closed back optics rapidly
- Design of mirror segments
- Temporal and special frequency of segment actuation

- Incorporation of new technologies (e.g. flame polishing, additive manufacturing, in-situ metrology)

Thermal Trade Studies: Harris has identified several considerations for thermal architecture and performance for LUVOIR including heater placement and set points, ULE CTE selection and optimization, mirror edge and support thermal management and passive or active temperature control during slews.
Testbeds proposed: Harris has proposed testbeds involving demonstration of rapid manufacturing and testing processes and development of hybrid Rigid Body Actuators with sub-nanometer precision and long duration stability.

These testbeds and numerous trade studies are described in detail in the Harris report in Section 7.

3.3.3 Coherent

Metal Mirror Manufacturing and Testing: The Coherent team performed an assessment of metal mirror manufacturing. They discussed lessons learned from JWST concerning polishing and testing of the Beryllium mirrors. They also evaluated a trade between Beryllium and Aluminum mirrors for use in the Origins Space Telescope. OST is currently baselining use of Beryllium mirrors yet new advances in Aluminum mirrors may present a longer cost (and admittedly lower performance) option for OST. Coherent has presented this trade and identified future trades and testbeds to support metal mirrors for future missions in detail in the Coherent report in Section 7.

4 Dynamic Stability Requirements Analysis and Design Drivers

The optical system requirements for the large telescope architectures under consideration by the 2020 Decadal Committee are ultimately derived in the aggregate by considering the individual requirements of the instruments comprising the observatories. For those instrument performance requirements that are dependent on a front-end Optical Telescope Element (OTE), the flowdown effectively reduces specifying required quality of the Point Spread Function (PSF) of the OTE, or more specifically the extent to which the PSF deviates from its ideal diffraction limited characteristics. Metrics of PSF quality may, in turn address both the spatial characteristics of the PSF, its temporal characteristic (such as its degree of change over time, or *dynamic stability*) or other metrics. There are certainly other optically-related requirements that address performance of the instrument optics themselves (some of these will be addressed for a coronagraph in Section 4.1, for example). The principal study of our analysis for this phase of the SLSTD effort was focused on addressing the requirements decomposition, and the predicted performance, of the OTE that supports the science for large telescope architectures such as LUVOIR, HabEx and OST. Future follow-on SLSTD phases may address the requirements and performance within the individual science instruments themselves.

There is a substantial body of work in the literature that addresses the overall challenge of requirements flowdown and error budgeting for the observatories under consideration. For example, an error budget structure has been defined for LUVOIR that flows down requirements of Wave Front Error (WFE), thermal stability and image motion stability based on the individual instrument requirements ([3], [4]). This error budget foundation described in the open literature was also applied by the LUVOIR STDT to develop WFE, image motion and line-of-sight stability budgets [5]. For the HabEx telescope, detailed error budgets for WFE and line-of-sight jitter that address its instrument requirements have been developed ([6], [7]).

4.1 Dynamic stability for coronagraph performance

The basic optical system architecture of a coronagraph is illustrated in Figure 4.1-1 [8]. A deformable mirror (DM) compensates for any quasi-static, low-frequency aberrations in the optical

system; for LUVOIR, two DMs are employed per optical channel to independently compensate amplitude and phase of the incoming wavefront. In the Apodized Pupil Lyot Coronagraph (APLC) design depicted in Figure 4.1-1, a set of two masks effectively removes the central core of the stellar PSF. The light from the planet misses this mask system, and its light is focused on a detector. The image seen on the focal plane is of an annular "dark hole" defined by an Inner Working Angle (IWA) and Outer Working Angle (OWA), as shown in Figure 4.1-1. Any residual wavefront error contributes to a "speckle" pattern in the dark hole associated with coherent scatter of light in the coronagraph optics.

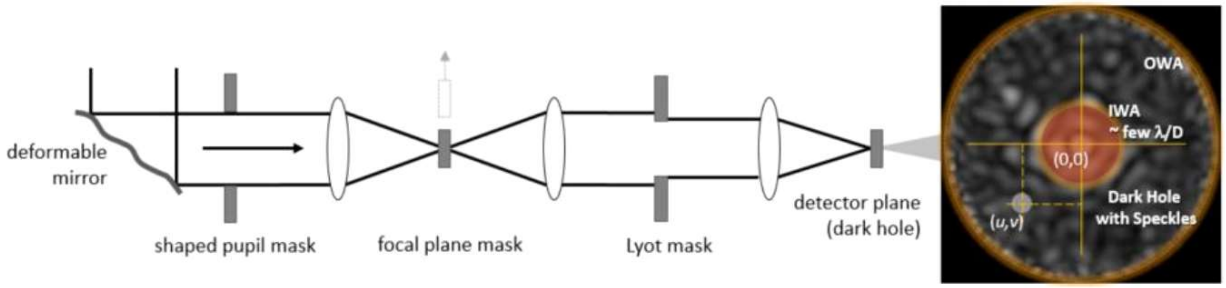

Figure 4.1-1: The elements of a basic coronagraph [8]

Since residual WFE after compensation by the Wavefront Sensing and Control (WFSC) determines contrast in the dark hole, and thereby coronagraph performance, the stability of the residual WFE between wavefront sensing and control steps is critical to system performance as well. Indeed, if a system contrast of 10^{-10} is desired, then contrast stability on the order of 10^{-11} is needed [9]. The LUVOIR yield calculations assume 5-10 magnitude stars, and it is estimated that the wavefront sensing and control update rate for a magnitude 10 star is up to 2 minutes. Thus, a good starting point for a stability window for the wavefront error is 2 minutes [9].

Translating the overall system-level contrast stability requirement into required stability of the WFE is, of course, dependent on the optical system. For LUVOIR, the system WFE stability requirement is 10 picometers RMS over the stability window [5]. For HabEx, the allowable WFE stability is about 1600 picometers RMS [7]. While it is certainly the case that the overall performance of the coronagraph cannot be completely reduced to a single RMS wavefront stability, such top-level metrics provide a good starting point for assessing system design and predicted performance, as it pertains to stability of the wavefront between sensing and control steps.

Segmented Primary Mirrors (such as for LUVOIR) add an additional source of degradation of the optical PSF, and thereby degradation of coronagraph contrast. Recently, some powerful analytical methods have been developed that relate PM segment rigid-body motion to overall coronagraph system contrast [10] [11]. These analytical tools allow for the development of approximate models of the entire coronagraph optical system. While not within the scope of this initial study, combination of these analytical segmented-PM coronagraph models with observatory structural dynamics and control systems would allow for direct computation of system-level contrast degradation due to disturbances, rather than scoring performance against a particular value (or values) for RMS WFE.

However, WFE stability is not the only contributor to the performance of a coronagraph. Dynamic change of the Line-of-Sight (LOS) (sometime call LOS jitter or pointing stability) causes smearing of the PSF and degrades the IWA of the coronagraph. Like the WFE stability metric, the specific requirement on LOS stability depends on the optical design. For LUVOIR, an RMS LOS stability of 0.3 mas in output space is required to meet system-level contrast stability [1]. For HabEx, this requirement is 0.7 mas [2]. LOS error is primarily driven by the large optics in the system, such as the LUVOIR OTE.

In this study, we focus both our requirements decomposition and performance assessment on these two dynamic stability metrics of the LUVOIR coronagraph system performance. In section 7, some quasi-static sources of wavefront error (such as thermally-induced errors) are addressed for HabEx.

4.2 LUVOIR stability requirements decomposition analysis

In this section, we review the key pointing and control requirements for the LUVOIR observatory, particularly as it relates to coronagraph dynamic stability. We also derive error budgets that are focused on the key sensing and actuation errors that were assessed in this study, and put forward an error budgeting methodology that addresses both spatial and temporal frequency dependence of the error metrics.

4.2.1 Review of established requirements and existing budgets

A key performance driver for the LUVOIR OTE is the wavefront error stability necessary to maintain a stable 10^{-10} contrast ratio in the dark hole between wavefront sensing and control steps, whose time interval is several minutes for LUVOIR [4]. This metric is referred to as WFE stability, and for error budgeting purposes, the WFE stability is evaluated over a typical temporal window of 2 minutes. This WFE stability metric was discussed in Section 4.1.

Some additional basic design specifications and requirements for the OTA are summarized in Table 4.2-1. The RMS pointing stability metric of 0.3 mas was previously mentioned in the discussion of coronagraph system performance. Additional requirements related to agility are unique aspects of the LUVOIR surveyor mission. In particular, the OTE must meet the LOS pointing stability metrics while also tracking a moving target at a track rate of 60 mas/sec (compliance against this track requirement was not within the scope of this study phase). The LOS repositioning requirement given in Table 4.2.1-1 is addressed in Section 6.2, in terms of settling time required for LUVOIR to achieve compliance WFE and LOS stability after a repositioning maneuver.

Table 4.2-1: Key performance specification for the LUVOIR Optical Telescope Element (OTE) **[1]**

Specification	Value
Aperture diameter	15 meters
Field-of-View	15 arcmin x 8 arcmin
Static wavefront error	< 38 nm RMS
Pointing stability	+/- 0.3 mas (1σ) per axis over observations
Object tracking	60 mas/sec
Slew rate	Req: repoint anywhere in anti-sun hemisphere in 45 minutes Goal: repoint anywhere in anti-sun hemisphere in 30 minutes

The design for the LUVOIR Architecture A OTE is shown in Figure 4.2-1. The segmented Primary Mirror consists of 120 hexagonal segments, with each segment having a flat-to-flight dimension of 1.223 meters [1]. The OTE includes a Fast Steering Mirror (FSM) in compact space which provides a fine level of LOS pointing beyond that provides by the Vibration Isolation and Precision Pointing System (VIPPS). The LUVOIR OTE field-of-view is shared by four science instruments, as follows:

- LUVOIR Ultraviolet Multi-Object Spectrograph (LUMOS);
- High Definition Imager (HDI);
- Extreme Coronagraph for Living Planetary Systems (ECLIPS)
- POLLUX (a high-resolution UV spectro-polarimeter)

Figure 4.2-2 shows how the LUVOIR OTE field-of-view is shared amongst these instruments, overlayed on the static WFE associated with the OTE optical system [1].

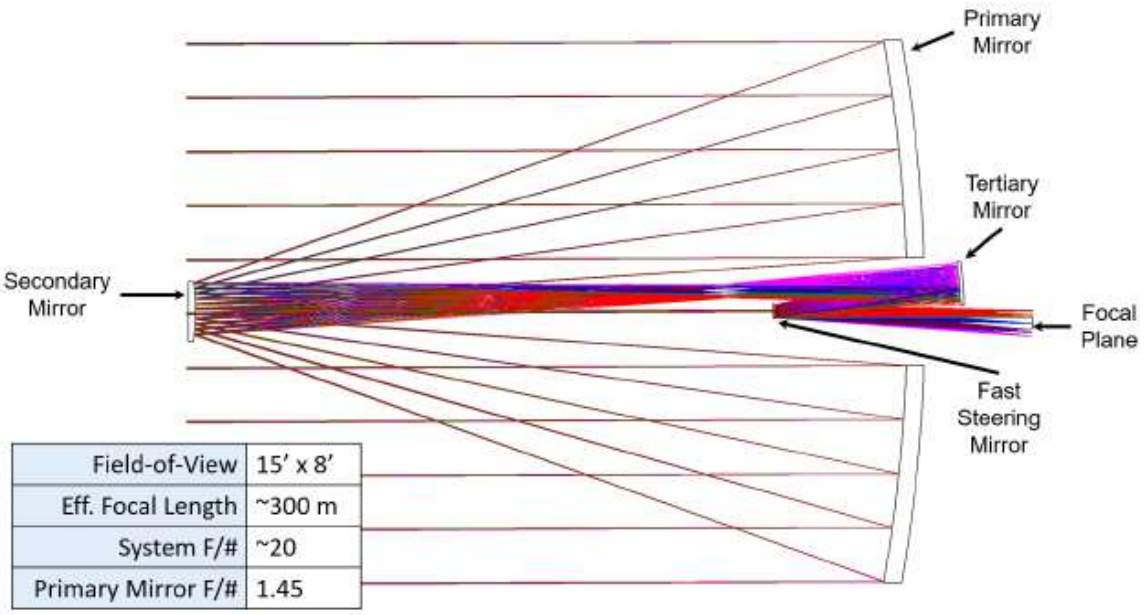

Figure 4.2-1: LUVOIR Architecture A Optical Telescope Element (OTE) optical design [1]

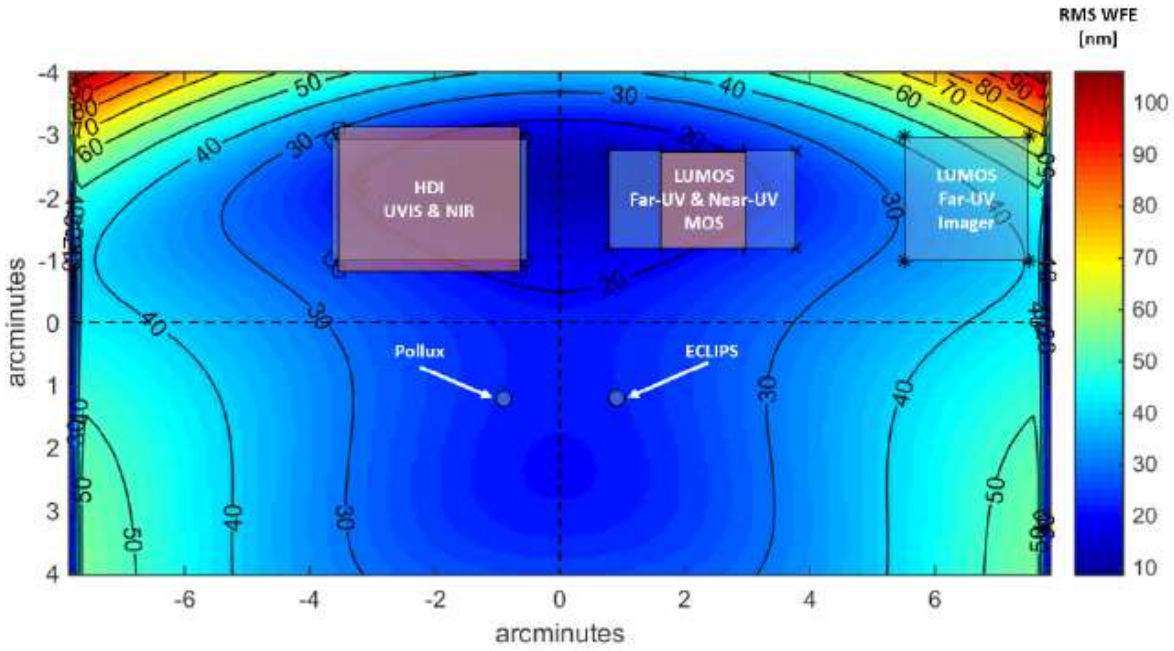

Figure 4.2-2: The LUVOIR Architecture A OTE Field-of-View and its individual instrument Fields of View [1]

Very detailed error budgets have been developed by the LUVOIR STDT to flow down system-level WFE and LOS stability into its constituent elements, both the individual elements of the optical system as well as disturbance sources [4]. It was not the objective of this study to reproduce an alternative to these comprehensive error budgets. In this study, we instead focused on the role that actuator mechanical disturbances and sensor noise plays on the dynamic stability of LUVOIR, when the entire integrated system of structural dynamics, optical sensitivities and control system are considered as a whole. This error budget perspective is described in the next section.

4.2.2 Development of Sensor and actuator error budgets for LUVOIR

Mechanical systems such as large telescopes are disturbed by actuator or mechanical elements that are mounted to it, or by the environment itself. If the system commands those actuators using a sampled-data control systems, then error in the sensors that support the control systems transmits noise to actuator commands, which again is a source of disturbance. This feedback structure is shown in the simple block diagram in Figure 4.2-3. In the case of actuators, sometimes their disturbances arise from limitations in their mechanical assembly, such as balancing or alignment tolerances. In other instances, actuator disturbances themselves arise from sensor noise at the actuator level, such as the jitter induced on a Fast Steering Mirror due to an internal sensor that controls the mechanism. In this way, the distinction between sensors and actuators as noise categories is more semantic than substantive, but this organizing principle provides powerful insights to error budget decomposition, particularly with systems where control systems are highly imbedded and integrated.

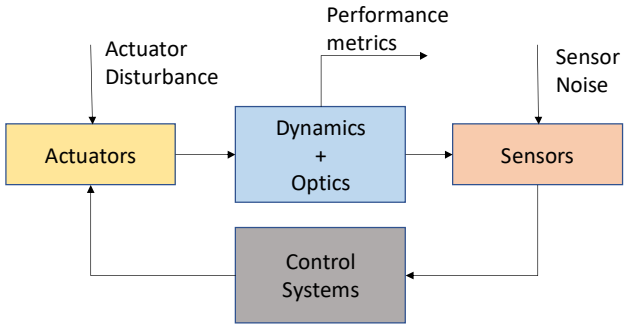

Figure 4.2-3: Sensor and actuator noise in dynamic systems

4.2.2.1 Actuator disturbances

The following actuator disturbances were modeled and included in the error budget for this study phase:

Control Moment Gyro induced vibration: The LUVOIR spacecraft is equipped with a complement of Control Moment Gyros (CMGs), which are spinning rotors whose spin axis can be rotated relative to the spacecraft body. Application of torque to the spin axes imparts a reaction torque on the spacecraft, conserving system angular momentum. Induced vibration is caused by mass and inertia eccentricity in the spinning rotors. This error model is described in detail in Section 5.1.4.1.

Fast Steering Mirror (FSM) exported loads: When FSM is actuated to control LOS, the acceleration imparted on the FSM is reacted against the payload structure. In most precision control application, the FSM is designed to minimize exported loads to the structure, with either passive or active reaction cancelling design features. However, this cancellation is not perfect, and some residual exported forces and torques to the payload structure are present. In this study, realistic FSM exported loads were included in the modeling; a model is described in Section 5.1.4.2. They were not selectively removed when the sensitivities were performance (their effect

is already captured in the other model outputs), and therefore to not have a separate allocation or performance value.
VIPPS non-contact actuator noise: Voice coil actuators to not contain any moving mechanical parts – an axial force is generated between a permanent-magnet field assembly (mounted on the payload side of the VIPPS interface) and a coil-wound bobbin (mounted on the spacecraft side of the VIPPS interface). Electrical noise and quantization effects in the voice coil motor drive electronics (arising primarily from sensor noise of the current used to close a fast current control loop) result in additive current noise, which causes broad band force noise applied at the interface. The model of the VIPPS actuator noise is described in Section 5.1.4.3.
VIPPS electro-magnetic coupling: The voice coil actuators generate eddy currents within the field assembly and bobbin, that is proportional to their relative velocity. These eddy currents dissipate this mechanical energy to some extent. Typically, design features are implemented in the voice coil actuator design to minimize this effect, but it is nonzero. While this effect was induced in the model described in Section 5.1.4.3 below, it was not selectively removed as part of the sensitivity studies, and therefore does not show up as a separate error budget term.

In addition to these modeled actuator error sources, an additional placeholder actuator noise for the 2-axis gimbal that is part of the overall LUVOIR architecture is included in the error budgets appearing in Section 4.2.2.4. An error model was not developed for this actuator in this study phase.

4.2.2.2 Sensor noise

The following sensor noise sources were modeled in this study, and are included in the error budgets appearing in Section 4.2.2.4:
FSM servo control sensor noise: The FSM generally includes a local servo control loop, that realized the commanded tip/tilt of the FSM relative to the optical bench by means of tip/tilt sensors and internal actuators. Additive noise in these tip/tilt sensor is the primary source of FSM jitter. The transmission of this sensor noise to FSM mechanical jitter is dependent primarily on the FSM servo control system bandwidth. This sensor noise model is described in Section 5.1.4.2.
HDI LOS sensor noise: The HDI measures the error in the overall observatory LOS during science observations. This measurement is available to the LOS control system at a relatively high rate (up to 500 Hz is assumed for this study). Error in the centroiding process on the HDI focal plane arising from focal plane quantization, dark current and other effects leads to measurement noise. A simplified sensor noise model is summarized in Section 5.1.4.5.
VIPPS non-contact sensor noise: Non-contact sensors at the VIPPS interface provide a real-time measurement of the interface relative translation and rotation; this measurement is used in the VIPPS control system to maintain stroke and gap at the interface. A simplified error model used in this study is describe in Section 5.1.4.4.

In addition to the noise sources described above, a placeholder for payload attitude reference sensor noise appears in the error budgets of Section 4.2.2.3. A model for this measurement was not developed for this study and predicted performance values are not populated in the error budgets.

4.2.2.3 Other dynamics parameter dependencies

The noise sources described above are the disturbances sources that lead to time-varying wavefront and LOS error. There are other aspects of the dynamic system whose parameters affect to the resulting performance. Some of these parameters include the following:

- Structural dynamics: structural dynamics lead to local resonances, which heavily affect system output relative to a rigid-body assumption. All physical structures possess inherent structural dynamics.
- Modal damping: the structural dynamics have dissipative parameters that describe the dissipation of vibrational energy. The assumption of damping ratio can significantly

affect the predicted performance of a structural dynamic system. In this study, a conservative uniform damping ratio of 0.25% was assumed; this is described in greater detail in 5.1.1.

- VIPPS cable stiffness and damping: the presence of power and/or data cables that bridge the interface introduces low-frequency structural dynamics in the system. This is an inherent aspect of the mechanical design, and so is not included as a separate error budget term. A full mechanical stiffness and damping model for the cables, anchored to test data, was included in the baseline structural dynamic model of this study; this model is described in Section 5.1.4.6. If in a future study the trade study of a wireless power and data transmission option is entertained, this term may be elevated to an error source.

4.2.2.4 Dynamic stability error budgets

A detailed discussion of a frequency-domain analysis that was conducted for the LUVOIR Architecture A dynamic system is provided in Section 6.1. The error budgets in Tables 4.2-2 and 4.2-3 summarize the numerical values that resulted from the analysis. In the WFE error budget, two bins of spatial frequency are defined: less than about 1 cycle/segment and greater than about 1 cycle/segment. The spatial filtering was realized by applying a 2-D Finite Impulse Response (FIR) spatial filter to the Optical Path Difference (OPD) data, with a cutoff frequency of 0.1875 cycles/aperture; this break frequency corresponds to 1.125 cycles/segment, or 11.25 cycles/aperture for LUVOIR. Within each spatial frequency bin, the total temporal frequency range available to the models was divided into three bins: < 1 Hz, 1-10 Hz and > 10 Hz. This same temporal binning was also observed in the LOS error budget, but of course no spatial groupings were applicable in the case of LOS error. In both budgets, an allocation is made for each error source, and for each bin. Roll-ups of both allocation and prediction are made for the overall categories of sensor and actuator noise. At the bottom of each table, the total requirement, total RMS performance, and both performance margin and allocation margin are shown. A nonzero allocation margin indicates allocation reserve to accommodate future error sources or further maturation of the budget.

ECLIPS Wavefront error stability budget: Table 4.2-2 indicates that we are carrying a 49% total margin against the 10 picometer RSM WFE stability requirement. We also show a 19% allocation margin, indicating room for growth of the budget to accommodate additional error sources. The most significant WFE contributors were CMG induced vibration in the mid and high frequency bins, VIPPS non-contact actuator noise in the same bands, and both FSM and HDI sensor noise in the mid-frequency bin. A separate trade study is described in Section 6.1 whereby the FSM is removed from the system; in that case, the overall WFE stability performance was not altered significantly.

Table 4.2-2: LUVOIR Wavefront stability sensor and actuator error budget

Spatial frequency bins	Low Spatial (< 1 cycle/segment)						High Spatial (> 1 cycle/segment)					
Temporal frequency bins (Hz)	< 1		1 - 10		> 10		< 1		1 - 10		> 10	
	Alloc	Perf	Alloc	Perf	Alloc	Perf	Alloc	Perf	Alloc	Perf	Alloc	Perf
Actuator Effects	**2.9**	**0.2**	**4.5**	**4.1**	**1.1**	**0.2**	**1.4**	**0.1**	**5.2**	**2.9**	**1.1**	**0.2**
CMG induced vibration	1.00	0.00	4.00	3.80	1.00	0.15	1.00	0.00	5.00	2.68	1.00	0.11
Fast Steering Mirror exported loads	N/A	Modeled	N/A	Modeled	N/A	Modeled	N/A	Modeled	N/A	Modeled	N/A	Modeled
VIPPS non-contact actuator noise	2.50	0.19	2.00	1.57	0.50	0.17	1.00	0.07	1.50	1.14	0.40	0.13
VIPPS electromagnetic coupling	N/A	Modeled	N/A	Modeled	N/A	Modeled	N/A	Modeled	N/A	Modeled	N/A	Modeled
Gimbal mechanism actuator noise	1	TBD	0.2	TBD	0.1	TBD	0.2	TBD	0.2	TBD	0.2	TBD
Sensor Effects	**0.5**	**0.1**	**1.0**	**0.3**	**1.4**	**0.8**	**0.5**	**0.0**	**0.3**	**0.1**	**1.0**	**0.2**
Fast Steering Mirror servo control sensing error	0.05	0.00	0.20	0.11	1.00	0.73	0.05	0.00	0.30	0.02	1.00	0.15
HDI LOS sensing noise	0.05	0.10	1.00	0.30	1.00	0.27	0.05	0.02	0.10	0.06	0.10	0.05
Payload attitude reference sensing noise	0.5	TBD	0.1	TBD	0.05	TBD	0.5	TBD	0.1	TBD	0.05	TBD
VIPPS non-contact sensing noise	0.1	0	0.1	0	0.1	0	0.1	0	0.1	0	0.1	0
TOTAL (by column)	**2.9**	**0.2**	**4.6**	**4.1**	**1.8**	**0.8**	**1.5**	**0.1**	**5.2**	**2.9**	**1.5**	**0.2**
TOTAL (Performance)	**5.13**											
REQUIREMENT	**10**											
TOTAL MARGIN (Performance)	**49%**											
TOTAL MARGIN (Allocation)	**19%**											

LOS Stability error budget: Table 4.2-3 indicates that with the baseline LUVOIR Architecture A system, and with assumed models for sensor and actuator noise, we are currently carrying a *negative* margin 19% against the 0.3 mas LOS error requirement. As the error budget indicates, the principal error sources were CMG induced vibration and FSM measurement noise. It is interesting to note that when the FSM is removed from the system architecture, the LOS error becomes compliant to the 0.3 requirement, with an overall predicted performance of 0.19 masec; the details of this performance trade study are given in Section 6.1. It should be noted that the observation does not necessarily mean that the FSM should be removed the system; rather, it points to the importance of trading off FSM bandwidth with improved system LOS performance: a higher-bandwidth FSM may provide potentially higher disturbance rejection, but also comes at the penalty of increased sensor noise transmission.

Table 4.2-3: LOS stability sensor and actuator error budget

ECLIPS LOS Stability (milli-arcsec, RMS)						
Temporal frequency bins (Hz)	< 1		1 - 10		> 10	
	Alloc	Perf	Alloc	Perf	Alloc	Perf
Actuator Effects	**0.15**	**0.23**	**0.15**	**0.15**	**0.02**	**0.00**
CMG induced vibration	0.02	0.00	0.15	0.15	0.01	0.00
Fast Steering Mirror exported loads	N/A	Modeled	N/A	Modeled	N/A	Modeled
VIPPS non-contact actuator noise	0.15	0.23	0.02	0.01	0.01	0.00
VIPPS electromagnetic coupling	N/A	Modeled	N/A	Modeled	N/A	Modeled
Gimbal mechanism actuator noise	0.02	TBD	0.02	TBD	0.02	TBD
Sensor Effects	**0.05**	**0.03**	**0.11**	**0.09**	**0.17**	**0.21**
Fast Steering Mirror servo control sensing error	0.01	0.00	0.03	0.03	0.15	0.20
HDI LOS ssensing noise	0.05	0.03	0.10	0.08	0.07	0.07
Payload attitude reference sensing noise	0.01	TBD	0.04	TBD	0.02	TBD
VIPPS non-contact sensing noise	0.01	0	0.01	0	0.01	0
TOTAL (by column)	**0.2**	**0.2**	**0.2**	**0.2**	**0.2**	**0.2**
TOTAL (Performance)	**0.36**					
REQUIREMENT	**0.3**					
TOTAL MARGIN (Performance)	**-19%**					
MARGIN (Allocation)	**0%**					

4.3 HabEx stability requirements decomposition analysis

A detailed analysis and flowdown of HabEx dynamic stability has recently been performed by Stahl [7]; selected stability requirements are summarized in Table 4.3.x. In this analysis, a total contrast instability allocation of 40 parts per trillion over the coronagraph instrument integration time (typically on the order of 24 hours [6]) was flowed down to telescope wavefront error dynamic stability. Here, WFE due to relative motion of rigid optics (called “LOS WFE Stability” in [7]) and WFE due to PM structural dynamics (called “Inertial WFE Stability”) are separately allocated in Table 4.3-1 and [7].

The baseline HabEx architecture mitigates the mechanical disturbance sources that degrade WFE stability in a fundamentally different manner than LUVOIR. For HabEx, source observatory LOS pointing is achieved during coronagraphic imaging by means of microthrusters, which produce a continuous thrust that is proportional to applied current. Initial modeling efforts to lay the foundation for assessing an alternative HabEx architecture that involves a non-contact vibration isolation system with spacecraft-mounted momentum exchange devices is summarized in Section 5.

Table 4.3-1: Selected HabEx optical system stability requirements (**[6]**, **[7]**)

Specification	Value
Jitter (per-axis	< 10 Hz: < 1 mas > 10 Hz: < 0.5 mas (for coronography)
Contrast instability	<40 parts per trillion (ppt) of contrast leakage
Wavefront Error Stability	LOS: < 892 pm (rigid optics) Inertial: < 892 pm (PM flexibility)

5 Large Telescope Integrated Modeling

5.1 LUVOIR Integrated Models

5.1.1 Structural Dynamics

Integrated modeling of the LUVOIR observatory with VIIPS starts with the observatory finite element model (FEM) received from the LUVOIR Science Technology Definition Team (STDT). The FEM is shown in Figure 5.1-1.

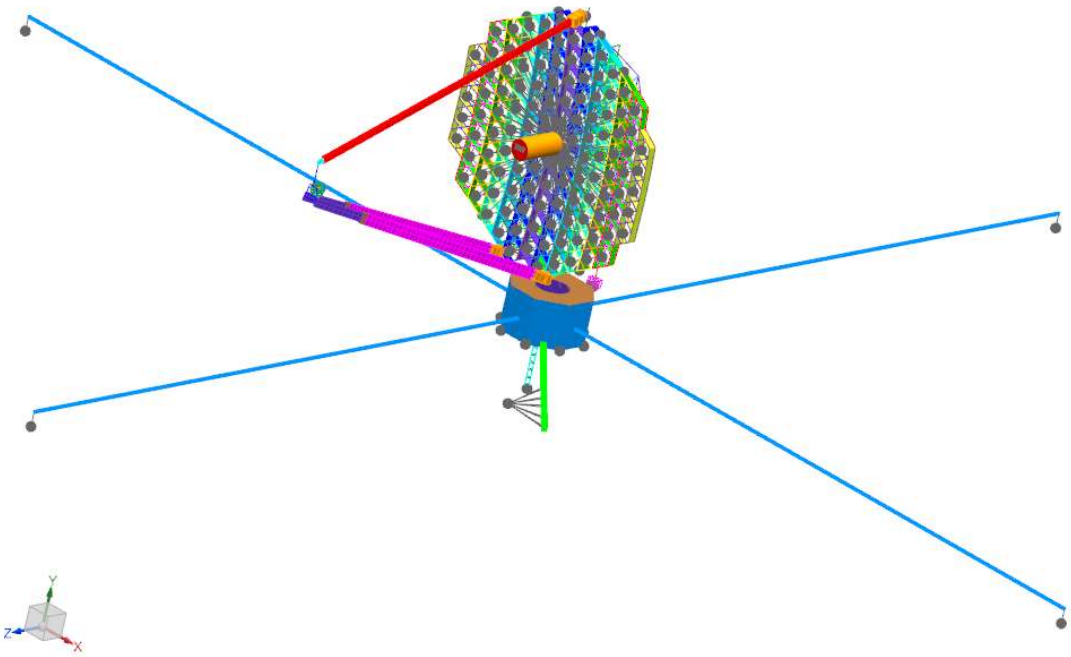

Figure 5.1-1: LUVOIR Finite Element Model

The FEM is high quality and passes all standard model quality checks. A survey of the assumed material and physical properties was performed and found to be reasonable. The FEM is comprised of 51266 grid points and 61768 elements of various types. A constraint element is used to "collect" primary mirror segment motions into average motion of the overall primary mirror. These motions are used when evaluating the primary mirror as a monolith. The mass of the telescope and instrument portion of the FEM is approximately 23128 Kg, while the mass of the spacecraft, including VIIPS, is 11490 Kg.

The FEM has been used to calculate all free-free vibration models of the system, up to a frequency of 450 Hz. This was done for several variants of the observatory FEM, corresponding to different elevation angles of the telescope. These are shown in Figure 5.1-2 through 5.1-6.

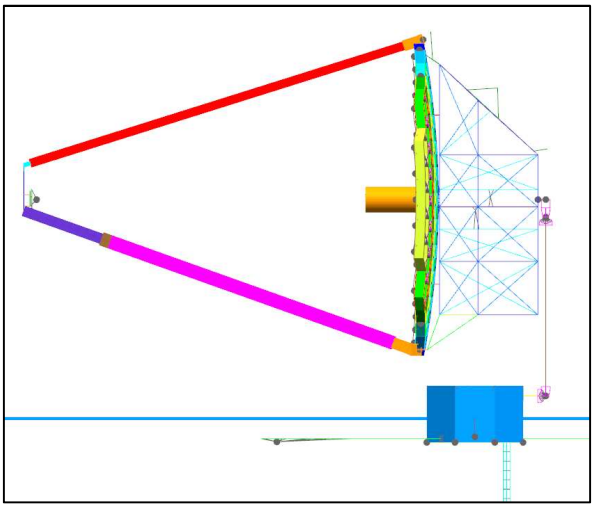

Figure 5.1-2: Observatory configured for a 0-degree elevation angle

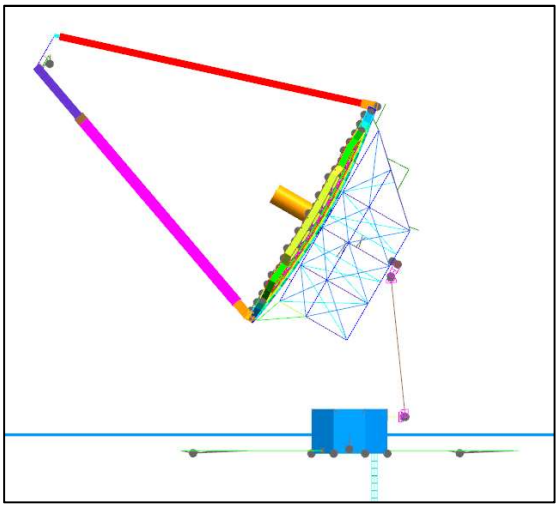

Figure 5.1-3: Observatory configured for a 30-degree elevation angle

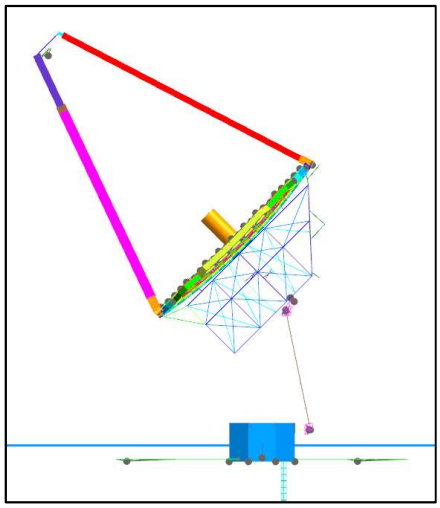

Figure 5.1-4: Observatory configured for a 45-degree elevation angle

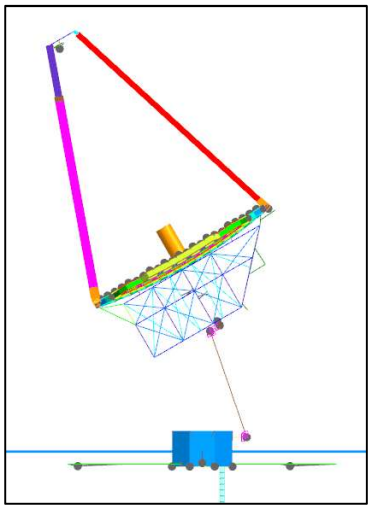

Figure 5.1-5: Observatory configured for a 60-degree elevation angle

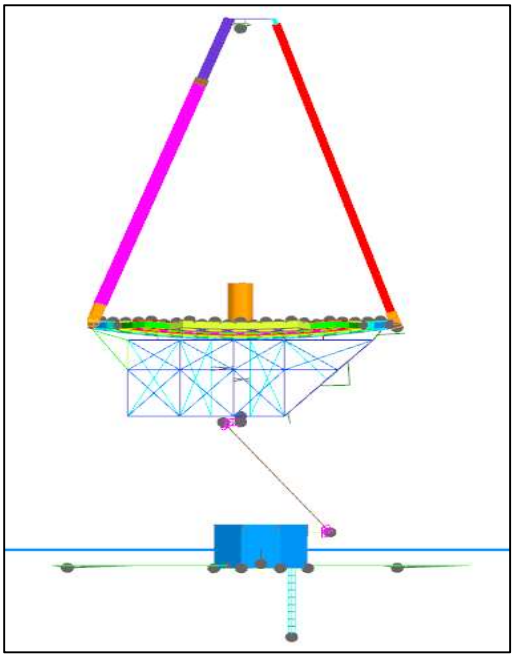

Figure 5.1-6: Observatory configured for a 90-degree elevation angle

In the variants the VIIPS boom geometry was modified in such a way that the lateral position of the telescope center-of-gravity remains constant. This constraint requires both ends of the boom be articulated as illustrated in the figures. The vertical distance between the observatory and spacecraft centers-of-gravity do change because the VIIPS boom is of fixed length.

Depending on the elevation angle, there are in excess of 17260 vibration modes of the system below 450 Hz, including the 12 rigid body models (6 each for the telescope and spacecraft). The vibration frequencies, and the corresponding mass-normalized modal amplitudes at each of the primary mirror segments, the “average” motion of the primary mirror, each subsequent optic (secondary mirror, tertiary mirror, fast steering mirror, internal image, etc.), reaction wheel/CMG locations, VIIPS interfaces, and boom gimbal interfaces were reported out, and used to construct plant state space models for DFP controls simulation and analysis.

Figures 5.1-7 through 5.1-11 illustrate several interesting or significant vibration modes of the system. Figures 5.1-7 through 5.1-9 show modes giving rise to significant motion across the VIIPS interface. Figures 5.1-10 and 5.1-11 illustrate the lowest vibration modes of the telescope portion of the observatory, corresponding the bending of the secondary mirror support truss.

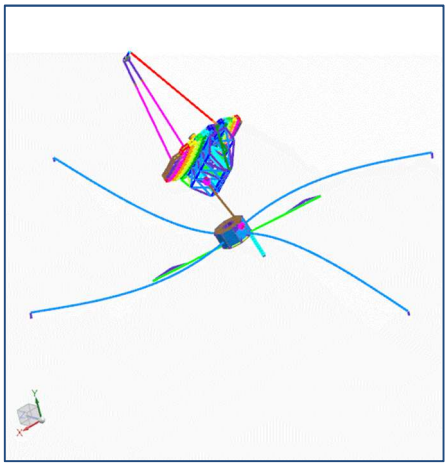

Figure 5.1-7: System vibration mode (mode 18) at 0.099 Hz

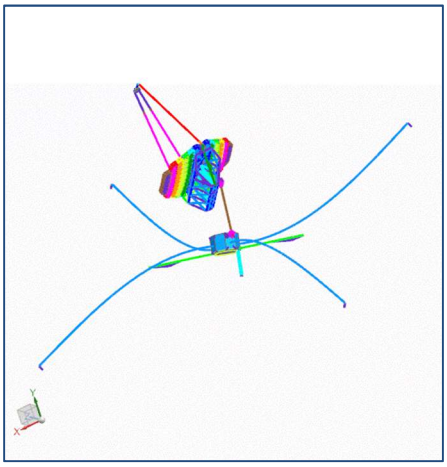

Figure 5.1-8: System vibration mode (mode 19) at 0.117 Hz

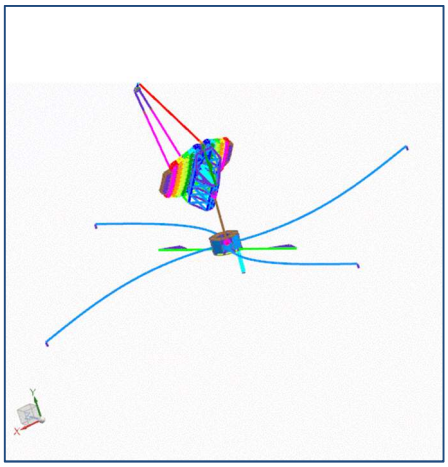

Figure 5.1-9: System vibration mode (mode 20) at 0.15 Hz

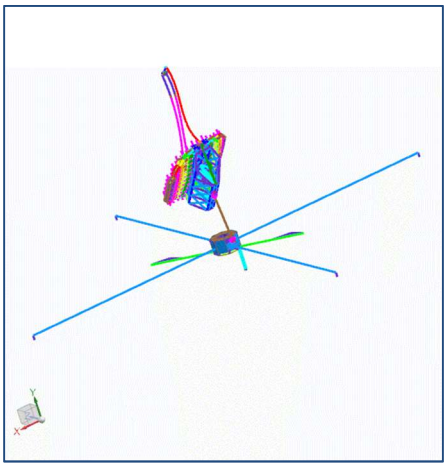

Figure 5.1-10: System vibration mode (mode 29) at 0.736 Hz

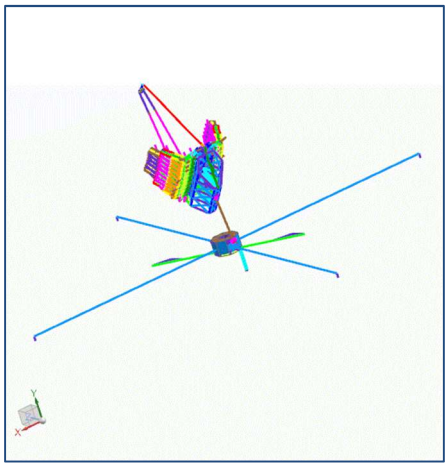

Figure 5.1-11: System vibration mode (mode 31) at 0.9 Hz

5.1.2 Pointing Control and Isolation

The baseline integrated Spacecraft and Payload pointing control system was introduced in the LUVOIR STDT interim report [1]. The current study focuses on the principle control system configuration used during science observations, which is illustrated in Figure 5.1-12. The actuators and sensors for this configuration are described in Tables 5.1-1 and 5.1-2 respectively, where each component is categorized by objective, location, and modeling fidelity for this study phase.

Table 5.1-1: Principle actuation elements of the baseline LUVOIR control system

Actuator	Location	Function	Modeling Notes
Fast Steering Mirror (FSM) *This study explored a flexure-mounted mirror with passive-reaction-cancelation, 4 voice coil actuators (VCA), and 2-differential position sensors*	FSM is part of the Optical Telescope Element (OTE)	• Actuation for fastest, highest-bandwidth pointing and tracking control loop • Offload to VIPPS • A key trade study addressed in this study phase was an alternative pointing control system that does **not** involve a FSM	FSM exported disturbance and mechanism Tip/Tilt measurement noise models are described in Section 5.1.4.2
Vibration Isolation and **Precision Pointing System (VIPPS)** *Stewart platform consisting of six independent (translational) voice-coil non-contact actuators (NCA) with parallel inductive sensors*	Mechanical interface between Spacecraft and Payload bodies, located between gimbal and backplane support frame	• Actuation and sensing for 6-DOF control of Spacecraft-Payload relative displacements (i.e. isolation of SC disturbances) • Actuation for 3-DOF Control of Inertial Payload attitude • Offload from FSM, in-turn offloads to CMG (central component of the pointing system)	Noise models of VIPPS voice coil actuators and non-contact sensors are described in Sections 5.1.4.3 and 5.1.4.4
4 x single-axis Control Moment Gyroscope (CMG)	Spacecraft-body	• Actuation for coarse space-vehicle attitude control	Induced vibration disturbance model

Table 5.1-1: Principle actuation elements of the baseline LUVOIR control system

Actuator	Location	Function	Modeling Notes
		• Large-angle slewing within operational pointing zone • Receives offload from VIPPS	described in Section 5.1.4.1

Table 5.1-2: Principle sensing elements of the baseline LUVOIR control system

Sensor	Location	Function	Modeling Notes
Attitude reference system *Hardware and processing for fusing measurements from at least two optimally oriented star-tracker (STA) optical heads and a bias-stable inertial measurement unit (IMU), as needed*	Sensor hardware mounted on the Payload-body Note: Per [1], the electronics and processing for this function are considered part of the Spacecraft	• Sensing for Inertial Payload attitude control • Used independently and in concert with fine-guidance measurements from HDI instrument	In this study phase, errors associated with payload attitude were not modeled. Future trade studies are recommended to assess architecture options, such as gyro-less operations, optimal sensor orientation, and LOS noise transmission
Fine Guidance Sensor, High Definition Imager (HDI) instrument *Includes camera for imaging bright foreground stars in UVIS or NIR, plus related image processing, centroiding algorithms*	HDI is an instrument within the Payload	• Sensing of LOS error provided to FSM and/or VIPPS • Sample rate ≤ 500Hz, concurrent with science operations	A simplified additive noise model of HDI sensed pointing error is described in Section 5.1.4.5

Reference [1] also discusses LUVOIR control system modes that support large-angle slewing, target acquisition, and routine maintenance operations. Hardware components related to these modes were not explicitly modeled in this study phase; Table 5.1-3 describes these additional elements, and the degree to which they were accounted for.

Table 5.1-3: LUVOIR control system elements not explicitly modeled in this study

Hardware	Location	Function	Modeling Notes
2-axis pitch gimbal, drives, and **corresponding control electronics**	Mechanical linkage between Spacecraft and Payload bodies, connects to backplane support frame via VIPPS	Actuation for limited coarse repositioning of the OTE in roll or pitch, while maintaining optimal sun-shield attitude and separation between the center-of-solar pressure and center of mass	Structural dynamics model includes basic representations of the gimbal booms. Gimbals were locked in 6 discrete orientations spanning the expected range of operation (see Section 5.1.1)
Propulsion and thruster control system	Spacecraft-body	Actuation for orbit injection, trim burns, station-keeping, momentum desaturation, safe-hold control	Not modeled in either control architecture or as a disturbance source

The actuators and sensors from Tables 5.1-1 and 5.1-2 are used to close three cascaded pointing loops, as shown in Figure 5.1-12. In this block diagram, control system inputs and outputs are identified as green and red oval boxes, respectively. Elements of the control law are also distinguished from the physical plant model, as indicated by the legend in the figure.

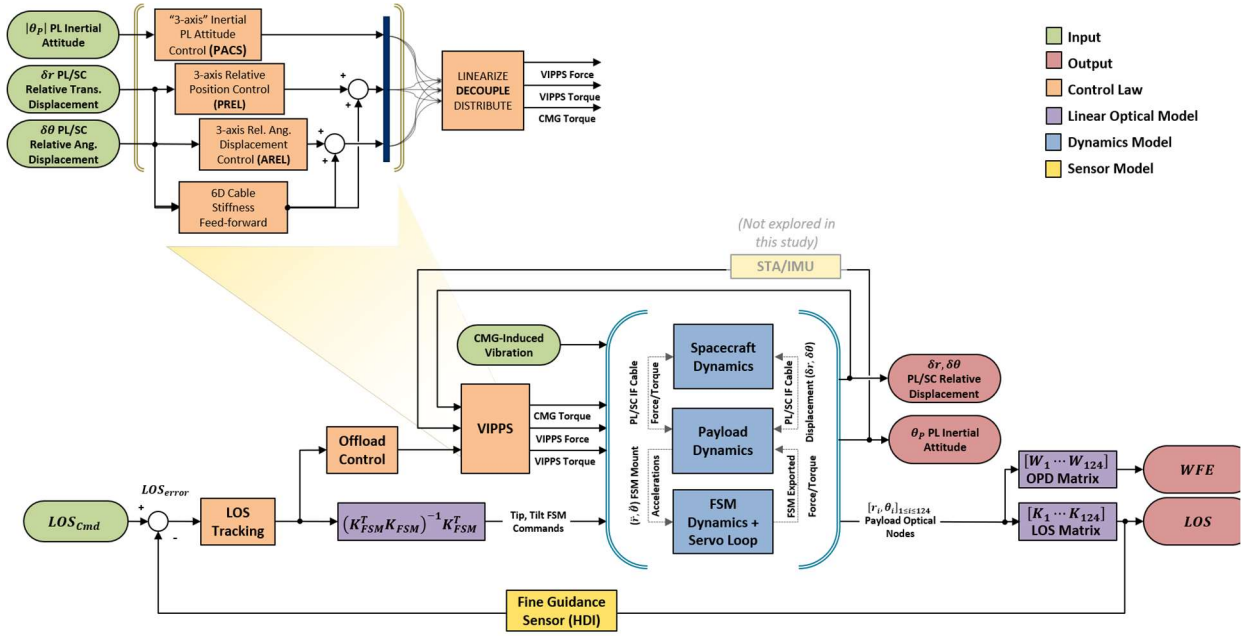

Figure 5.1-12: Overall LUVOIR control system architecture analyzed

The baseline control system utilizes three types of actuators: FSM, VIPPS, and CMG. Each actuator imposes stroke and bandwidth limitations on the pointing system, as shown in Table 5.1-4 below.

Table 5.1-4: Control system actuators, range of motion and bandwidth

Actuator	Effective Stroke (Object Space)	-3dB Bandwidth Limitations
FSM	~ ±10 arcsec	~ 100Hz Tip/Tilt control servo-loop bandwidth
VIPPS	~ ±1 deg	• << 1Hz inertial attitude & relative displacement control loops • > 100Hz voice coil current loops for feed-forward
CMG	Unlimited range of motion within system momentum storage capacity and agility constraints	~4Hz torque control servo-loop bandwidth

The FSM enables high-bandwidth, low-noise tracking of focal-plane feedback produced by the HDI instrument's primary Fine Guidance Sensor (FGS) function, as shown in the Figure 5.1-12 block diagram. Given the relatively tight stroke limitation, the FSM commands are continually offloaded to the VIPPS Payload Attitude Control system (PACS), which utilizes non-contact voice coil actuators with larger range of travel and higher torque output. Feedback for PACS is provided by an attitude reference system with Payload-mounted hardware, presumably two or more optimally oriented star-tracker optical heads and a bias-stable rate sensor package. As was noted in Table 5.1.2-2, the payload attitude reference system was not modeled in this study; that is,

transmitted sensor noise and control bandwidth limitations were not considered. The attitude reference feedback is also used in an alternate configuration, referred to as "FSM-less LOS Control", which is described at the end of this section.

The VIPPS also non-contact isolation of spacecraft-exported disturbances is maintained via the relative position (PREL) and relative attitude (AREL) control elements. Per Table 5.1-1, the interface includes inductive sensors for measuring 6DOF Spacecraft-Payload relative displacements, i.e. the feedback signals used by the PREL and AREL controllers. The VIPPS Stewart platform also provides full 6DOF actuation for PREL and PACS, but with the limited NCA stroke and a very high Payload-to-Spacecraft mass ratio of nearly 2.0[1], another high-torque actuator with unlimited stroke is needed to effectively control inertial pointing via relative angular displacement. This is of course the perfect role for the CMGs, which are located on the Spacecraft body, isolated from the jitter-sensitive Payload by means of the non-contact interface[2].

Since there is a high degree of cross-coupling between the nine-by-nine PACS, PREL, and AREL system, a decoupling step has been added in the distribution law, per the block diagram shown on Figure 5.1-13.

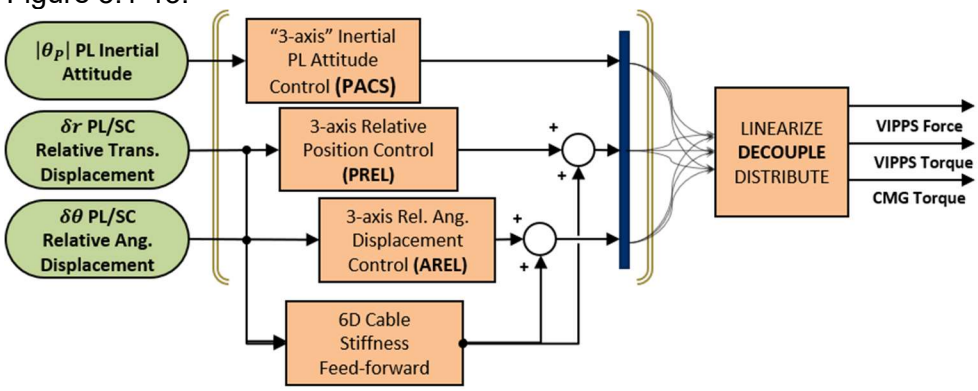

Figure 5.1-13: Block diagram detail of the VIPPS control system

The approach of decoupling the VIPPS control loops was chosen merely to simplify control system synthesis and tuning; the down-side of this convenience is that noise from all sensors is transmitted to actuators on both sides of the VIPPS interface, though it is expected to be small and heavily low-pass filtered through the closed loops. Once more mature structural dynamics models become available, this system can be refactored for full-state feedback, making it compatible with more advanced multi-input, multi-output control synthesis methods such as Linear Quadratic optimal control.

The following equations describe how the distribution and decoupling is accomplished:

$$\mathbf{R}_{\mathrm{SC}} = \left[\begin{bmatrix} \mathrm{I}^{3x3} & 0 \\ [r_{SC}^{1} - cm_{SC}]^{\mathrm{x}} & \mathrm{I}^{3x3} \end{bmatrix} \cdots \begin{bmatrix} \mathrm{I}^{3x3} & 0 \\ [r_{SC}^{i} - cm_{SC}]^{\mathrm{x}} & \mathrm{I}^{3x3} \end{bmatrix}\right] \tag{1}$$

$$\mathbf{R}_{\mathrm{PL}} = \left[\begin{bmatrix} \mathrm{I}^{3x3} & 0 \\ [r_{PL}^{1} - cm_{PL}]^{\mathrm{x}} & \mathrm{I}^{3x3} \end{bmatrix} \cdots \begin{bmatrix} \mathrm{I}^{3x3} & 0 \\ [r_{PL}^{j} - cm_{PL}]^{\mathrm{x}} & \mathrm{I}^{3x3} \end{bmatrix}\right] \tag{2}$$

$$\mathbf{R}_{\mathrm{VIPPS}} = \begin{bmatrix} \mathbf{R}_{\mathrm{PL}} & 0 \\ 0 & \mathbf{R}_{\mathrm{SC}} \end{bmatrix} \tag{3}$$

[1] A very small Payload-to-Spacecraft mass ratio, $m_{PL}/m_{SC} << 1.0$, would effectively enable inertial attitude control of the Payload body via relative-angular-displacement control over the full range of motion of the interface, at least for cases where absolute drift and disturbances are small.

[2] CMG disturbances are discussed in Section 5.1.4.1.

$$\mathbf{J}_{\mathrm{VIPPS}} = \begin{bmatrix} \mathbf{m}_{\mathrm{PL}} & 0 & & \\ 0 & \mathbf{I}_{\mathrm{PL}} & & 0 \\ & & \mathbf{m}_{\mathrm{SC}} & 0 \\ & 0 & 0 & \mathbf{I}_{\mathrm{SC}} \end{bmatrix} \quad (4)$$

$$\mathbf{G}_{\mathrm{VIPPS}} = \mathbf{V}_y * \mathbf{R}_{\mathrm{VIPPS}}{}^{T} * \mathbf{J}_{\mathrm{VIPPS}}{}^{-1} * \mathbf{R}_{\mathrm{VIPPS}} * \mathbf{V}_u \quad (5)$$

$$\mathbf{D}_{\mathrm{VIPPS}} = \mathbf{G}_{\mathrm{VIPPS}}{}^{-1} \quad (6)$$

Where $\mathbf{D}_{\mathrm{VIPPS}}$ is the linear decoupling and distribution matrix; $\mathbf{G}_{\mathrm{VIPPS}}$ is the linearized rigid body solution for the two detached bodies, $\mathbf{J}_{\mathrm{VIPPS}}$ defines their mass properties; $\mathbf{V}_u$ and $\mathbf{V}_y$ are used for mapping inputs and outputs to and from the system rigid body vector, $\mathbf{R}_{\mathrm{VIPPS}}$; which is a diagonal concatenation of the rigid body vectors, $\mathbf{R}_{\mathrm{SC}}$, corresponding to i relevant nodes on the Spacecraft body; and $\mathbf{R}_{\mathrm{PL}}$ corresponding to j nodes on the Payload body. In all equations above, $[a]^{\mathrm{x}}$ denotes the cross-product matrix according to the convention, $a \times b$, and b is the post-multiplied factor.

Together, the FSM and VIPPS actuators provide the disturbance suppression and isolation needed to meet the exceptionally fine pointing and wavefront stability required for this mission. The following is a discussion of the interactions between the various control loops of the integrated LUVOIR pointing system, in terms of bandwidth.

Figure 5.1-14 shows relevant low-to-high frequency cascaded control loop interactions, indicated by red arrows; as well as high-to-low frequency offload interactions, indicated by green arrows. This strategy and supporting terminology are explained in the paragraphs below.

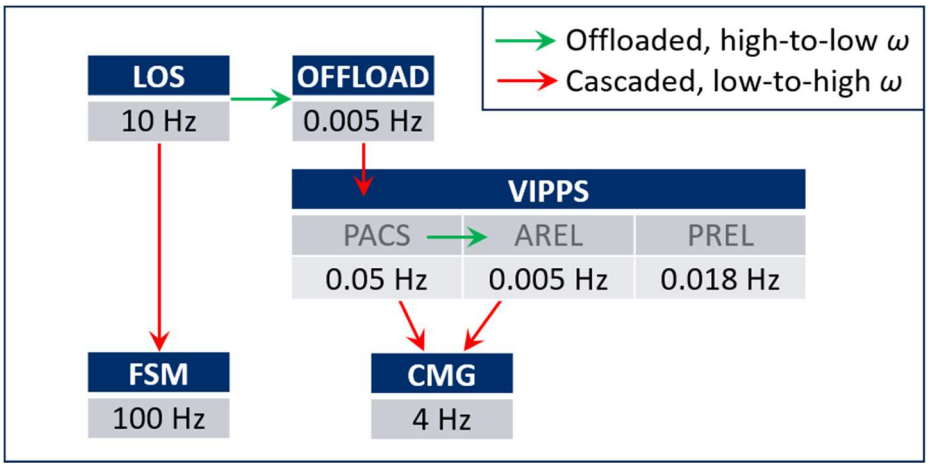

Figure 5.1-14: Flowdown of bandwidth for LUVIOR pointing control

Since LOS control uses the FSM as its primary actuator, LOS and the FSM-internal servo-control are considered *cascaded* control loops; that is, the output of one controller is the input of the other. In such interactions, the actuator loop typically runs at much higher bandwidth than the outer loop in order to limit phase-lag, which supports robustness and performance.

Alternatively, since the FSM can only travel over a small angular range, LOS Control also shares its command with the lower bandwidth Offload and VIPPS-PACS components. This strategy results in complimentary low-pass filtered and high-pass filtered commands to the VIPPS-PACS and FSM, respectively; the net result is that any high-amplitude, low-frequency content in the command or control error (from science target tracking or drift) is offloaded to the VIPPS-PACS, allowing the FSM to remain close to its null position.

The above discussion focuses on the baseline control system configuration proposed for science operations, as described in the LUVOIR STDT Interim Report [1]. This study also

explored an alternate configuration, referred to here as “FSM-less LOS control”. Modifications for this configuration are illustrated in the Figure 5.1-15 block diagram.

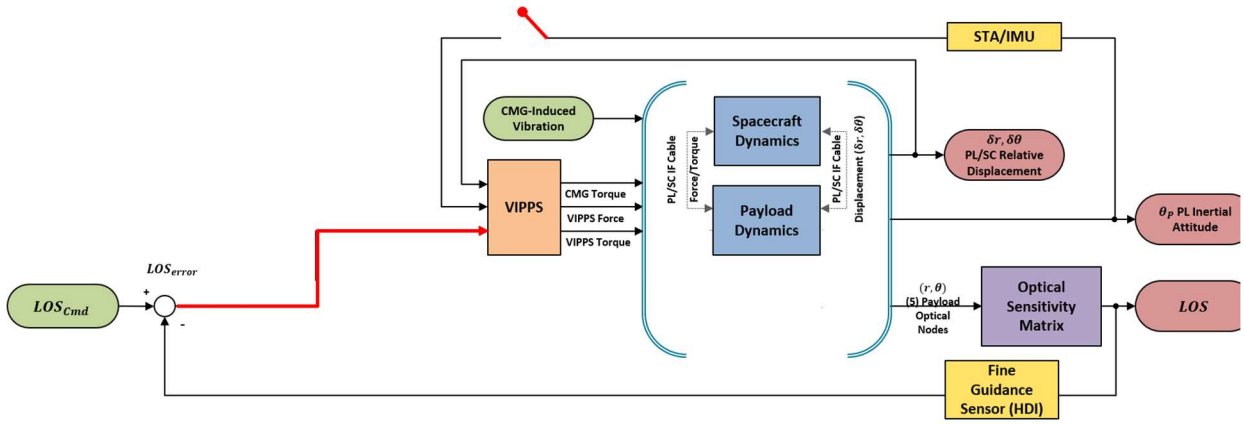

Figure 5.1-15: Alternative FSM-less LOS control architecture

In this configuration, cross-boresight measurements from the HDI-FGS are combined with single-axis measurements from the traditional payload attitude reference system, essentially a twist angle about the boresight, to complete the feedback signal for the VIPPS-PACS controller. The advantage of this approach is that it eliminates the FSM, reducing complexity, cost, and sources of noise and vibration. The disadvantage is a reduction in jitter rejection capability, as explored in the disturbance sensitivity discussion below.

Figure 5.1-16 illustrates the disturbance rejection strategy for the LUVOIR LOS pointing control system. The figure shows transmissibility of external disturbances on the Spacecraft-side of the VIPPS interface, to line-of-sight. This metric is shown in a layered or cumulative sense, as the elements of the LUVOIR pointing control system are built-up, according the following sequence:

1. The Spacecraft and Payload bodies are connected only by the interface cable, all control loops open (shown as the blue line)
2. VIPPS-PREL relative position control loop is closed (shown in green)
3. VIPPS-AREL relative angular displacement control loop is closed (red)
4. VIPPS-PACS inertial payload attitude control loop is closed (cyan)
    - “FSM-less LOS Control” configuration is built up at this point
5. FSM is mechanically integrated (magenta)
6. LOS control loop is closed (yellow)
7. Offload connection to VIPPS-PACS is made (black)
    - This is the Baseline LOS Control configuration

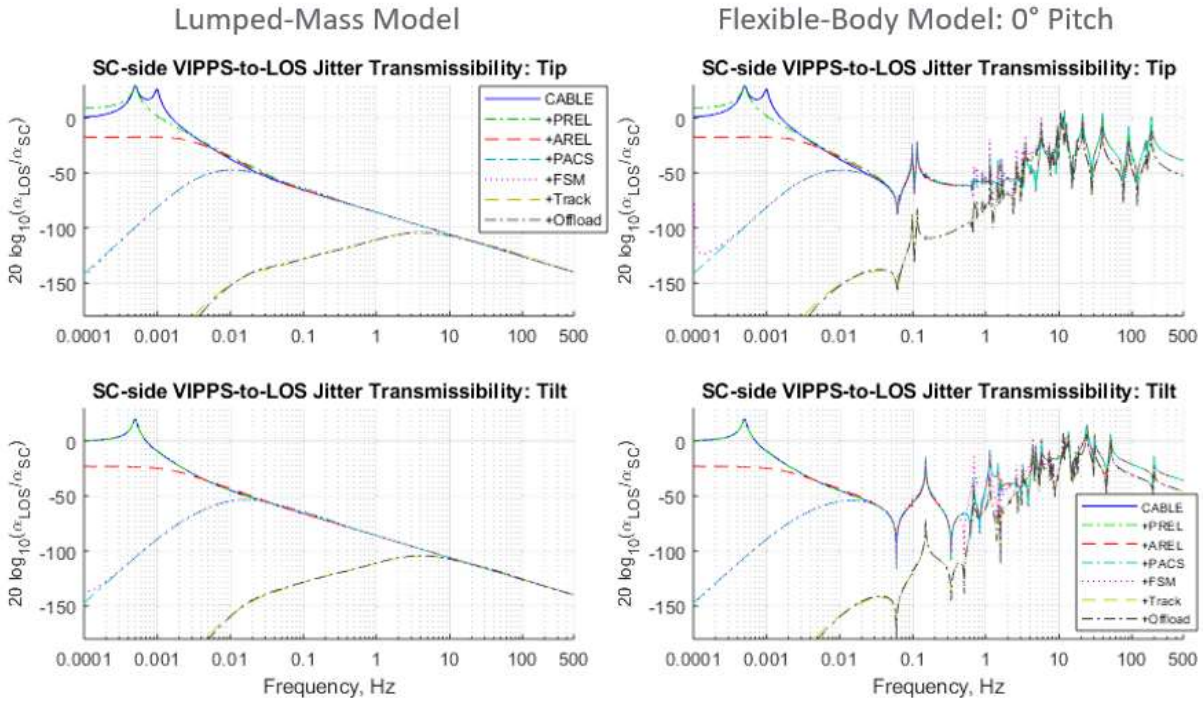

Figure 5.1-16: Rigid-body and flexible-body spacecraft disturbance transmissibility

In the left-hand column of plots in Figure 5.1-16, the Spacecraft and Payload bodies are represented as lumped-masses; the overall disturbance rejection strategy is shown most clearly in this configuration. With just the structure and interface cable, the system starts with 0 dB (or 1-to-1) transmissibility of disturbances at frequencies below the fundamental SC-PL interface modes. Tracing the blue line from low-frequency to high-frequency, there is resonance at the fundamental SC-PL interface mode frequencies (due to cable stiffness), followed by -40dB per decade roll-off. The green line shows that relative position control does not significantly affect disturbance rejection about angular degrees of freedom, which is an expected result. Performance is not significantly altered until the first *inertial* control system is added, i.e. VIPPS-PACS, which provides infinite disturbance rejection at steady-state, as depicted by the cyan line and magenta lines. This point of control system integration represents the "FSM-less" configuration, which yields a disturbance suppression bandwidth of 0.01Hz, as measured and indicated at the point where the cyan and magenta curves rise up and meet the rest of the curves. Similarly, Figure 5.1-16 shows that the Baseline configuration achieves a disturbance suppression bandwidth of 10Hz. So the FSM boosts disturbance rejection bandwidth by roughly three orders of magnitude, as tuned for this study. The outcome of the Baseline vs. FSM-less LOS control trade discussed in Section 6.1.

Focusing next on the right-hand column of plots in Figure 5.1-16, the disturbance sensitivity profiles outlined above are now shown for the case where the Payload and Spacecraft both include flexible-body dynamics. While low frequency trends are identical between the left and right hand column plots, the flexible-body dynamics clearly eliminate the -40dB per decade structural roll-off that the lumped-mass model exhibited. This is due to structural amplification and an effect called mass-shedding. Also, the right-hand column plots in 5.1-16 clearly highlight the risk that disturbances which lie beyond the bandwidth of the control system will pass through to the LOS, heavily amplified by the structural modes of the telescope.

Another notable trend is persistence of the blue curve, which shows up in all plots at high frequency. Recall that the blue curve corresponds to the fully-open-loop system, with only the two bodies connected across the interface cable. Per Figure 5.1-16, an increase in cable stiffness

would shift low frequency resonances to the right, thereby shifting *up* the entire family of curves at high frequency. The net result in an increase in disturbance sensitivity, hence the inclusion of the cable stiffness modeling and characterization efforts in this study phase.

5.1.3 Linear Optical Model (LOM)

The line-of-sight and wavefront stability results documented in this report rely on a validated linear optical model (LOM), which is used to map or project optical node displacements onto an image plane. As implemented, the LOM consists of a matrix of sensitivities for modeling the primary feedback in the LOS pointing control process, [$\mathbf{K}_i$… $\mathbf{K}_n$]; as well as a matrix of sensitivities for estimating dynamic wavefront error (WFE), [$\mathbf{W}_i$… $\mathbf{W}_n$], which was the focus of this study. Throughout this report, the terms LOM and 'optical sensitivity' are used interchangeably.

The following 124 optical elements were modeled both in the FEM and LOM:

- 120 Primary mirror segments (PMSEG001… PMSEG120)
- Secondary mirror (SM)
- Tertiary mirror (TM)
- Fast steering mirror (FSM)
- Image plane (IMG)

In addition to the primary mirror segments, optical sensitivities for a purely monolithic primary mirror were generated, and the FEM included a corresponding single response point for consolidating motion of the120 PM segments in a least-squares sense.

Though the FEM included a fair amount of detail for certain optics, motion of each was reduced to 6DOF for this study, at least in terms of the FEM-LOM interface. Care was taken to ensure that the 6DOF FEM response-point displacements were aligned with the 6DOF LOM input perturbations, in terms of coordinate frames, pivot-point locations, and DOF ordering[3].

The LOM was validated and integrated with the FEM using a process subsequently referred to as the "rigid-body check". This is useful check whenever perturbations are applied in local coordinates, or in the general case like LUVOIR, where they are globally coordinatized but applied locally at each optic instead of at the global origin. As this description suggests, the check involves converting local perturbations into global perturbations using the rigid body transformation matrix. The transformed sensitivities for each optic are then summed and compared with the expected result. The rigid body check is discussed in more detail below.

The optical analysis which covered the 120 individual PM segments was independent from the analysis which dealt with the monolithic PM, SM, TM, and back-end optics. Outputs of these efforts are referred to as the "Monolithic LOM" and "Segmented LOM", and they are covered in sections 5.1.3.1 and 5.1.3.2, respectively. Note that line-of-sight was assumed to be fairly insensitive to motion of the individual PM segments; as such, LOS sensitivities were only generated for the monolithic PM case, and the sections below focus on WFE sensitivities.

5.1.3.1 Monolithic PM LOM Analysis

Earlier in the program, a monolith PM LOM was provided by the LUVOIR design team at NASA GSFC. In this monolithic model the PM is modelled as a rigid body, and includes 5 optical elements: Monolithic PM, SM, TM, FSM, and IMG. While this monolithic model is significantly simplified compared to the segmented optical model, it is a valuable tool in verification of the end-to-end telescope integrated modeling and allows for easy evaluation of a preliminary dynamic WFE result.

To verify and integrate the LOM with the FEM, the rigid-body check was performed on the model to produce global WFE sensitivities. The global WFE sensitivities were produced by perturbing each optical element (5 optical elements in the monolithic model) via rigid-body translation and

[3] Several coordinate frame, pivot point location, and DOF-ordering mismatches between the FEM and LOM were encountered and rectified during the model integration process.

rotation about the global origin, summing the sensitivities for all optical elements, and removing the 2-D best fit plane to remove tip, tilt, and piston. This check shed light on the quality of the LOM and its ability to estimate picometer level dynamic WFE.

Figure 5.xx1 shows the global WFE sensitivities for the monolithic PM LOM. In all such plots presented herein, the top row of three surface plots represent sensitivity to pure translation about global TX, TY, and TZ; and the bottom row of three plots show sensitivity to rotation about global RX, RY, and RZ, or Rϕ, Rθ, and Rψ. Piston corresponds to TZ, tip and tilt correspond to Rϕ and Rθ, and clocking is Rψ. Here WFE is used synonymously with optical path difference (OPD), the metric that is plotted and analyzed throughout this report. Here WFE is used synonymously with optical path difference (OPD), the metric that is plotted and analyzed throughout this report. According to Figure 5.1-17, pure translational motion and clocking motion of the entire telescope about the global origin has insignificant effect on the WFE, which is an expected result. On the other hand, tip and tilt motion of the entire observatory about the global origin will results in non-zero WFE sensitivity; this is because by changing the pointing of the telescope a different optical path is traveling through the system, and thus a different wavefront.

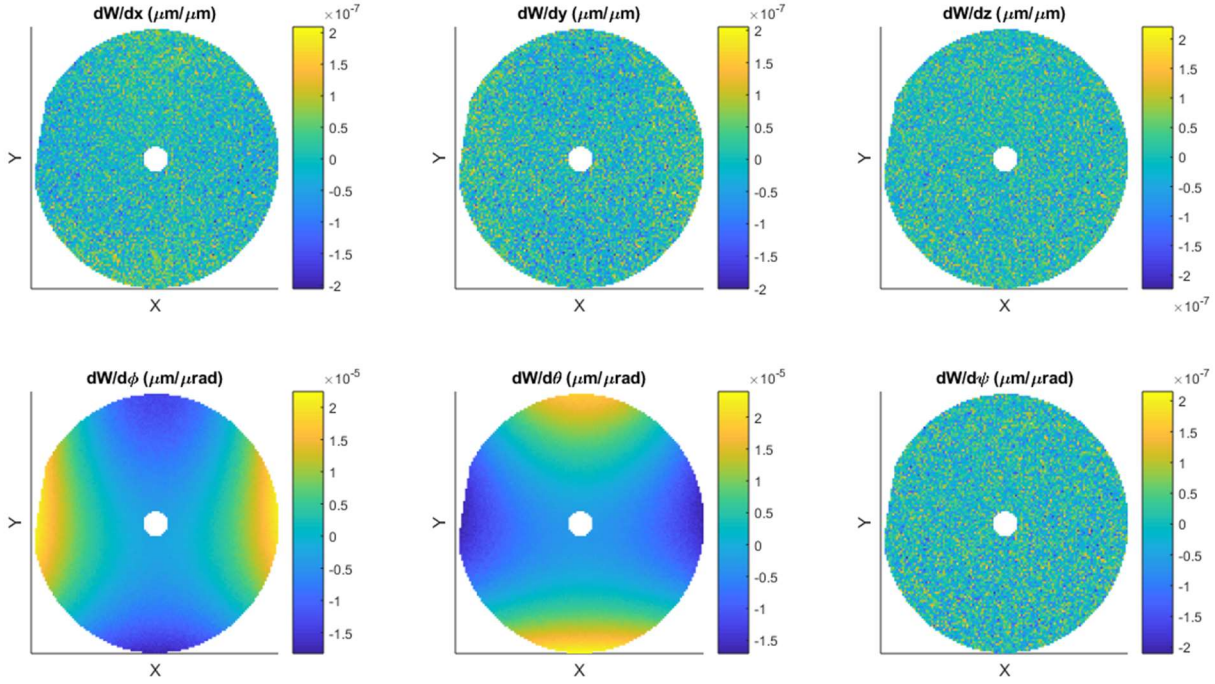

Figure 5.1-17: Global WFE sensitivities for the monolithic PM LOM

Figure 5.1-18 shows the WFE sensitivities for the monolithic PM. In the next section, this figure will be used to compare the accuracy of the segmented PM LOM with the monolithic PM LOM. Note that the WFE sensitivities in this figure are computed under the assumption that all the other optical elements are fixed and only the PM is perturbed in the translational and rotational DOFs. Therefore, in the translational DOFs, the results would be that a linear WFE is developed because the center of curvature of the PM is no longer aligned with the optical prescription. In the rotational DOFs, we also expect to see tip and tilt terms in dW/dϕ and dW/dθ as the observatory is rotated about the x and y axes. Lastly, dW/dψ is near zero as WFE is insensitive to clocking.

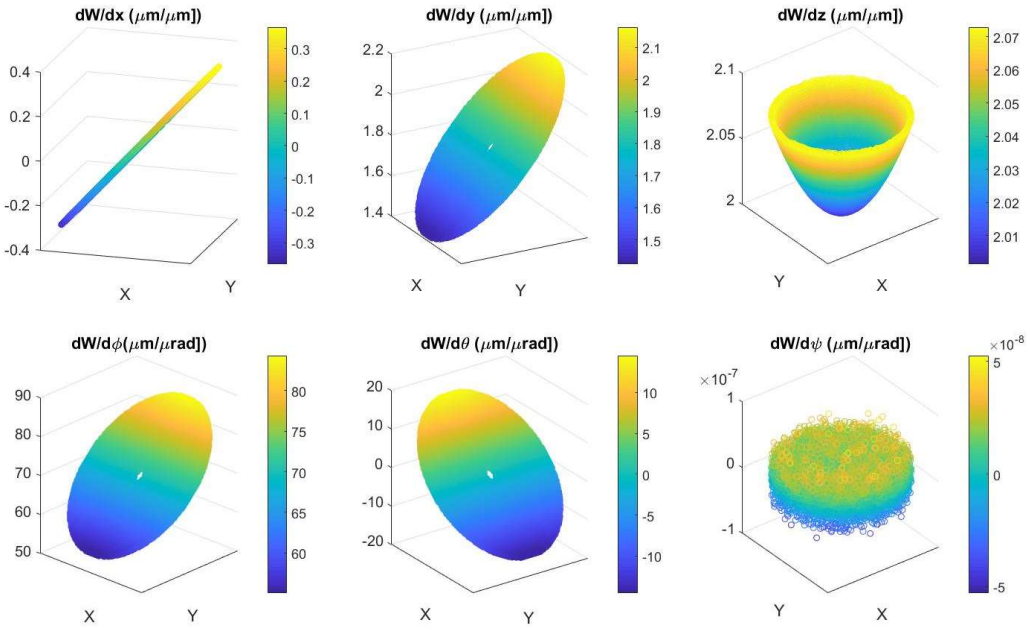

Figure 5.1-18: Global WFE sensitivities for the monolithic PM LOM

5.1.3.2 Segmented PM LOM Analysis

5.1.3.2.1 Efforts Towards First-Principles Modeling of the Segmented Optical System

For the integrated modeling and performance analysis of this study, an existing Segmented Linear Optical Model (LOM) provided to the SLSTD team by the LUVOIR Design Team was leveraged; the details of how the provided Segmented-PM LOM was leveraged are described in detail in the next subsection. In this subsection, we describe efforts to compute the segmented-PM sensitivities via an independent model of the complete segmented LUVOIR OTE, with the specific task to determine sensitivities in wavefront error (WFE) due to 6-DOF perturbations in the primary mirror segments of the LUVOIR telescope. The progress-to-date is summarized here; it provides a solid foundation for detailed analysis of LUVOIR segmented system sensitivities in future study phases.

The LUVOIR telescope is based on the three-mirror anastigmat (TMA) configuration with a primary mirror (PM) with aperture diameter D = 15000 mm and a total system focal length of f = 296705 mm. The f-number for the telescope is $F\# = f/D$ = 19.78. The PM is segmented consisting of 120 hexagonal segments each within a circumscribed circle of radius R_s = 709.27 mm. The layout of the telescope with the segmented primary is seen in Figure 5.1-19.

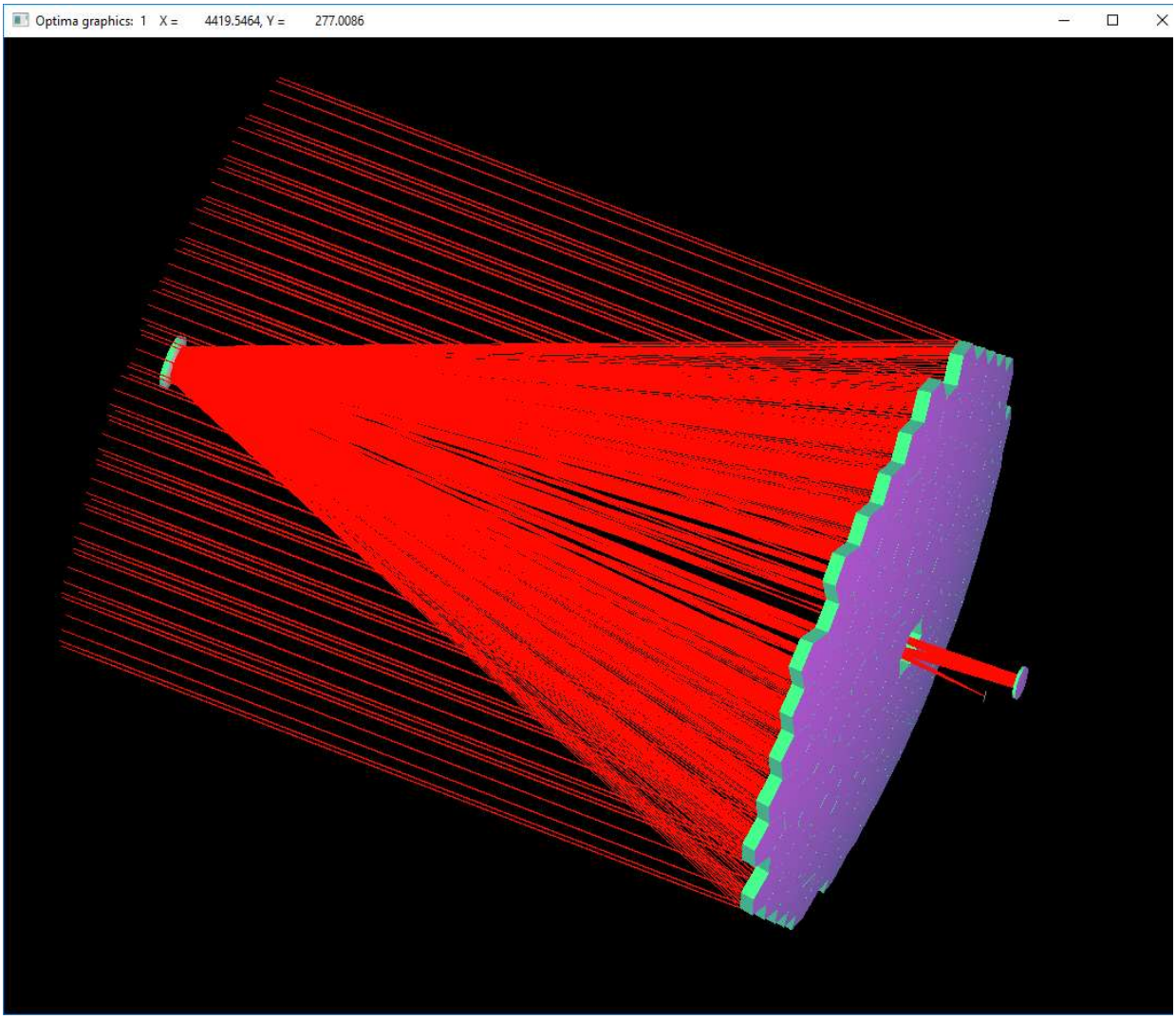

Figure 5.1-19: Layout of LUVOIR telescope

The layout of the segments is seen in Figure 5.1-20.

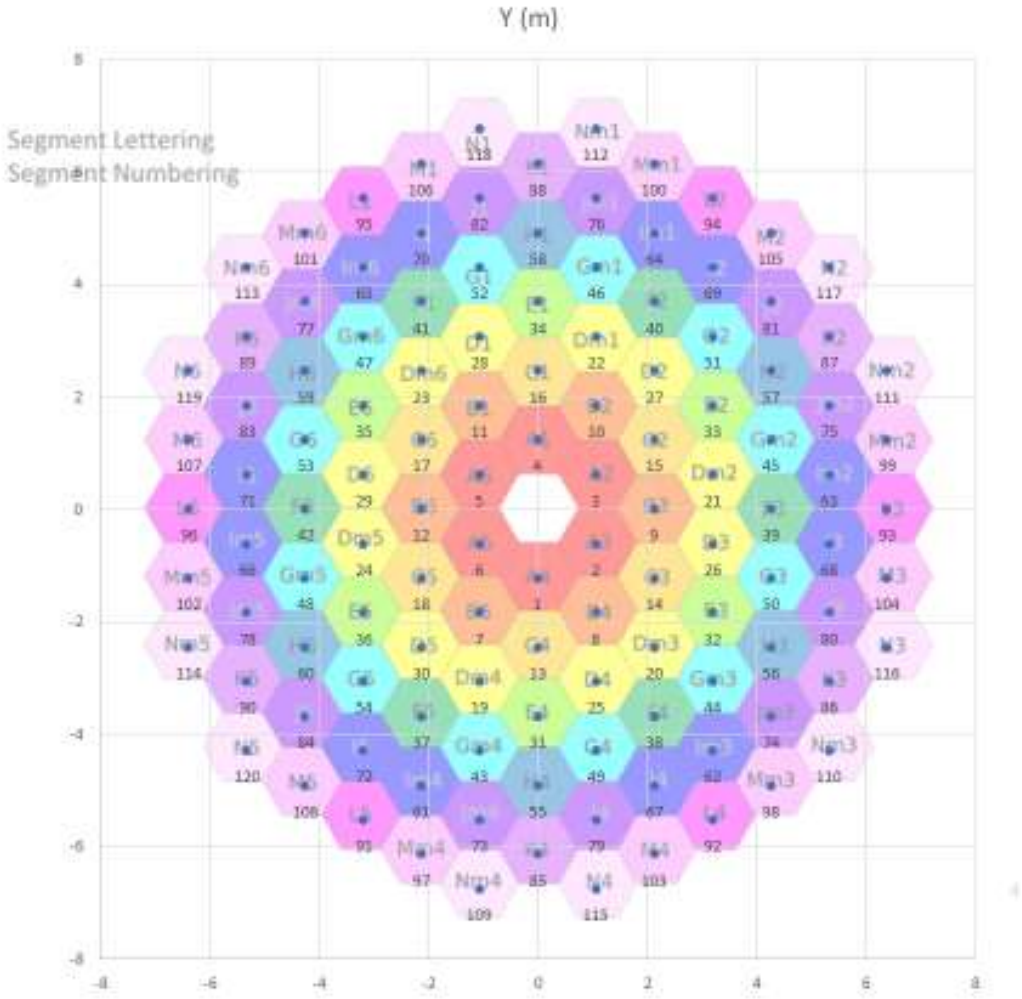

Figure 5.1-20: Layout of Primary Mirror segments projected to the PM vertex tangential plane.

Results of sensitivity analyses for imaging with segmented spaces telescope have been presented by [12], [10]. Due to the hexagonal shape of the segments, analysis using the Zernike circle polynomials must be converted to similar analysis for sets of polynomials that are orthogonal on the hexagonal aperture shape as has been demonstrated by Janin-Potiron et al. [13].

In this analysis we performed the optical modeling with Lockheed Martin's in-house software Optima for optical design and analysis [14] [15] equipped with Zernike circle polynomial fitting using very fast and accurate algorithms [16].

Because the f-number the wavefront impinging on one segment is about $(F\#)_s = \frac{f}{D_s} = 209.2$, the wavefront associated with one segment can be fitted very accurately with Zernike circle polynomials through a low radial order of 4, corresponding to $5 \cdot \frac{6}{2} = 15$ Zernike polynomials in the Noll standard notation.

For each segment s we calculated sensitivities in the segment Zernike circular coefficients A_{sj} corresponding to each Zernike circle polynomial Z_j due to the 6 degrees of freedom p_{ks} . Using Table 2 in the paper by Mahajan and Dai [17] it is straightforward to convert the Zernike circular coefficients and their sensitivities to equivalent coefficients B_{sj} corresponding to the hexagonal

polynomials H_j that are orthogonal and normalized over the hexagonal aperture. Since the segments do not overlap and the coefficients B_{sj} and their sensitivities correspond to orthonormal polynomials, we can obtain the total variance corresponding to perturbations $\{\Delta p_{sk}\}$ by RSS-ing the corresponding changes

$$(dWFE)^2 = \sum_s \sum_j \left(\sum_k \frac{\partial B_{sj}}{\partial p_{sk}} \Delta p_{sk} \right)^2$$

5.1.3.2.2 Deriving a Segmented LOM Model from LUVOIR STDT Optical Models

Recall that in the context of this study, the optical path for LUVOIR consists of the image plane, FSM, TM, SM, and PM; and where the PM is rendered as a single element, the integrated optical model is referred to as the "Monolithic LOM"; whereas if the PM is rendered as 120 discrete elements, the integrated optical model is referred to as the "Segmented LOM".

The LUVOIR design team directed two separate optical analyses that accompanied this control system study: one that produced the full integrated Monolithic LOM; and the other focused only on the individual PM segments. WFE sensitivities from the two efforts were unified in terms of parameterization, units, and coordinates; they were then combined to create a first-cut integrated Segmented LOM.

Here we will describe an assessment by the SLSTD team of this *Initial Segmented LOM, or ISLOM*. We also describe here the development of an alternate segmented-PM LOM that was derived from the Monolithic LOM, referred to subsequently as the *Hybrid-Segmented LOM, or HSLOM*. The development of this alternate model was motivated by mismatch between the Segmented LOM and its Monolithic counterpart, when perturbed with rigid-body telescope motion (the Segmented and Monolithic LOMs should agree under this condition). The mismatch is described further below, within this section.

While these two LOMs (the ISLOM and HSLOM) are fundamentally different, the resulting frequency-domain performance predictions using the two different models, included at the end of this section, were not significantly different. As such, the quantitative performance metrics summarized in Section 6.1 of this report are computed using the ISLOM. The weak dependence of the metrics on these two LOMs was primarily due to the fact that the PM segments were not significantly perturbed by transmitted noise and vibration from the LOS control system. This explored further at the end of this section.

Note that in the subsequent discussion, the term 'global WFE sensitivities' refers to the sum of the sensitivities for the full optical path, perturbed about the global origin, with the 2D best-fit plane, i.e. tip, tilt, and piston, removed. These global WFE sensitivities are a gauge of the overall quality of the LOM, shedding light on ability to estimate pico-meter-level dynamic WFE.

Figure 5.1-21 shows the WFE sensitivities for just the primary mirror in the Monolithic LOM, compared against the sum of the 120 PM-elements in the ISLOM, which were globally perturbed. In all such figures in this section, the top row of three surface plots represent sensitivity to pure translation about global X, Y, and Z, denoted as *dx*, *dy*, and *dz*; and the bottom row of three plots show sensitivity to rotation about global X, Y, and Z, denoted as *dϕ*, *dθ*, and *dψ*. Piston corresponds to *dz*, tip and tilt are *dϕ* and *dθ*, and clocking is *dψ*[4]. In the expression *dW/dx*, *W* refers to WFE, or more specifically optical path difference (OPD), which is the metric that is plotted and analyzed throughout this report.

[4] While Euler-angle notation has been used, these refer to small-angle perturbations. Linear optical modeling makes use of small perturbations and small-angle assumptions. This eliminates kinematic cross-coupling and related dependence on sequence of rotation that would normally be relevant with large angle motion.

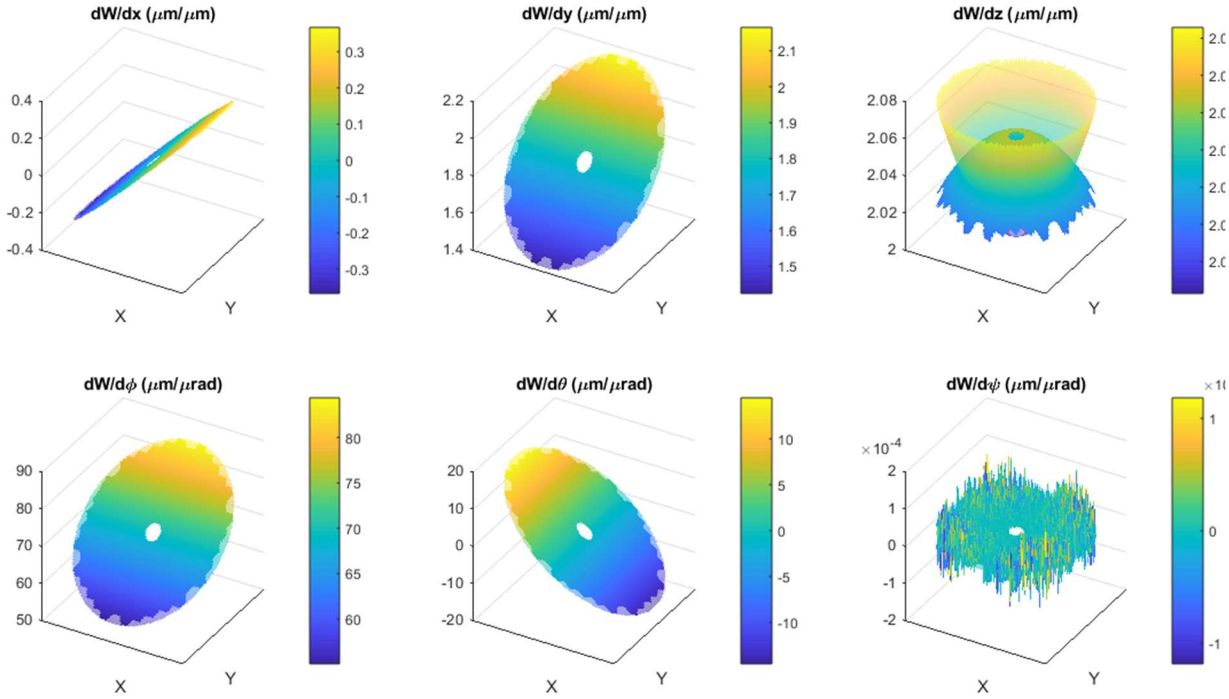

Figure 5.1-21: Comparison of ISLOM segment sensitivities against the monolithic mirror

In the Figure 5.1-21, the faint translucent surfaces with the circular edges correspond to the monolithic PM; and the darker meshed surfaces with the jagged edges obviously correspond to the PM segments. The Figures 5.1-22 through 5.1-25 shows the difference between those two sets of surfaces.

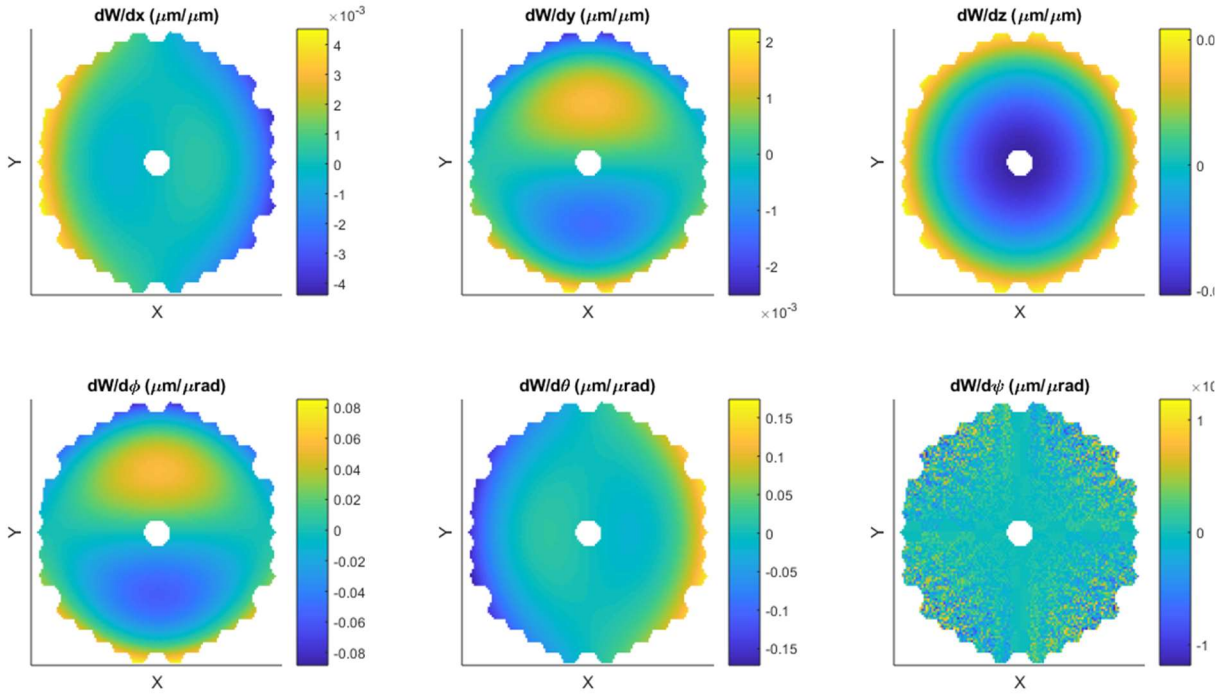

Figure 5.1-22: Difference between monolithic PM and ISLOM segment sensitivities.

As expected, the differences between the Monolithic and Segmented PM sensitivities, directly carry over as error in the global WFE sensitivities, which are shown in the Figure 5.1-23.

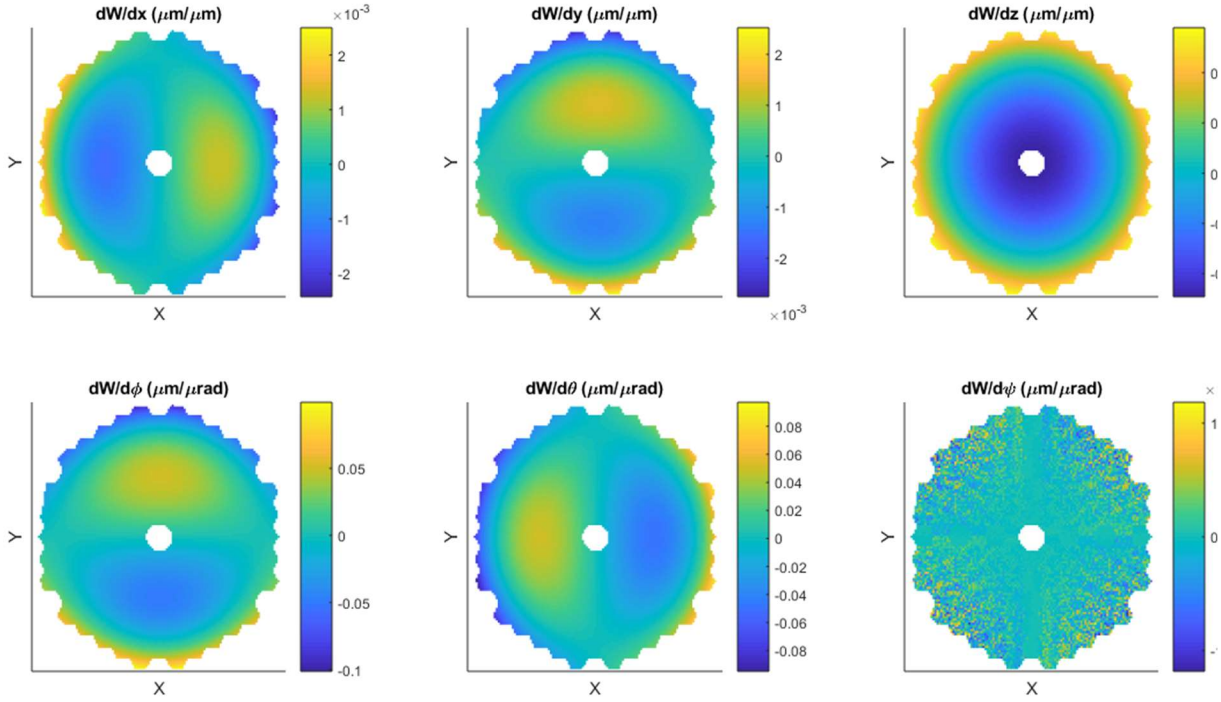

Figure 5.1-23: Global WFE sensitivities for the ISLOM

While significant differences in piston, tip, and tilt were observed between the monolithic and segmented PM models, through communication with the LUVOIR Design Team, the following path-forward was developed.

Noting that the rigid body check which produced the above comparisons could essentially be inverted (starting from the desired monolithic mirror sensitivities), ideal segmented sensitivities were derived, and segment-specific masks were created from the ISLOM. This is precisely the methodology that was used to derive a new segmented LOM, called the Hybrid Segmented LOM (HSLOM). The result is shown below and compared against the Monolithic LOM in the subsequent figure, revealing expected agreement between the two.

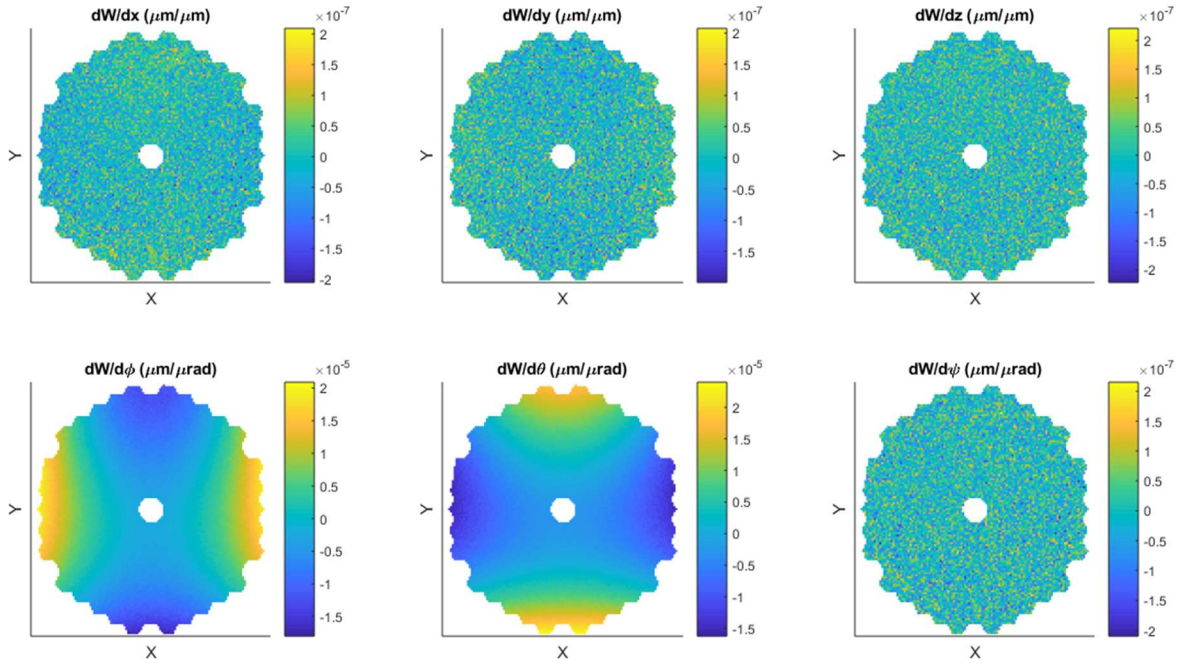

Figure 5.1-24: Global WFE Sensitivities for the HSLOM

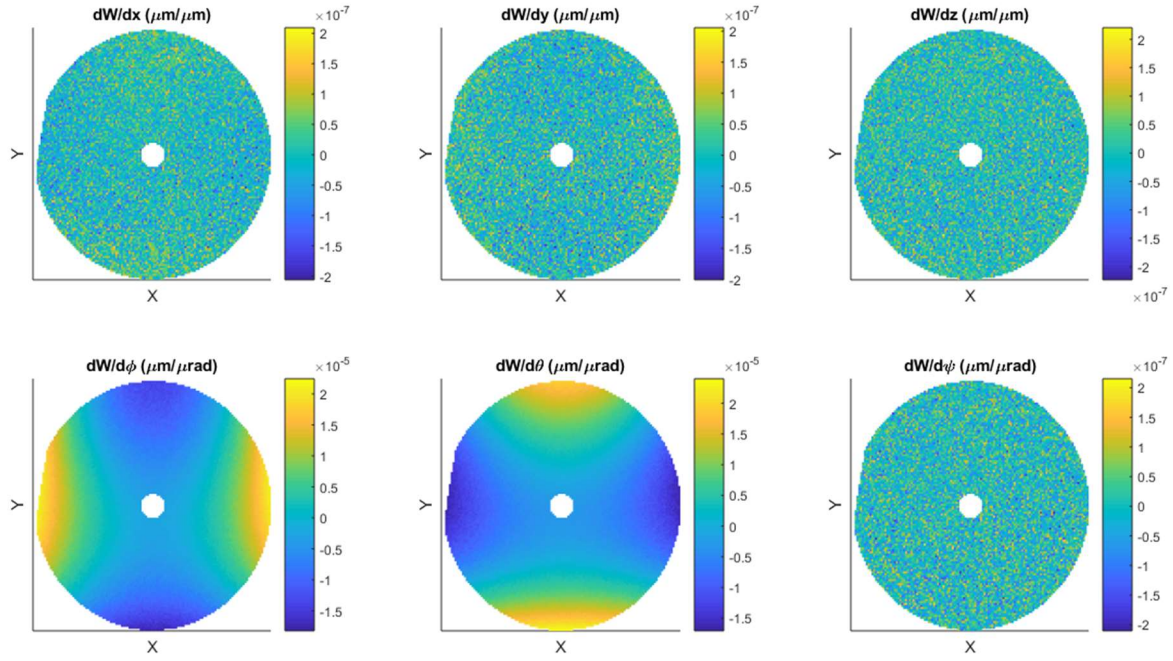

Figure 5.1-25: Global WFE sensitivities for the Monolithic LOM

A family of models was generated to systematically assess the difference in performance between the ISLOM and the HSLOM. In particular, weights of 100%, 10%, 1%, 0.1%, 0.01%

were applied to the ISLOM segment sensitivities, and they were summed with the segment sensitivities of the HSLOM, correspondingly weighted. The segment sensitivities for the 10%-ISLOM version is compared against the monolithic primary mirror in Figure 5.1-26. The figure shows a high degree of similarity between the WFE sensitivities of the monolithic mirror and the summed segment sensitivities of the 10%-ISLOM; this is a vast improvement over the results noted in Figure 5.1-21.

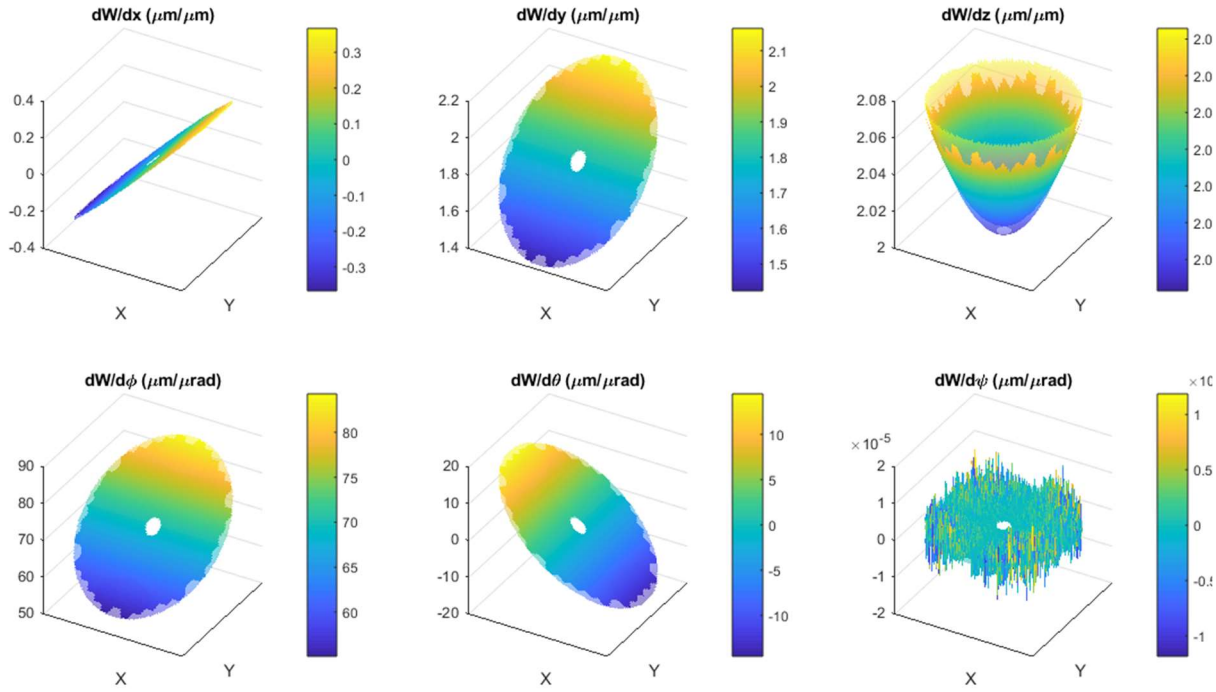

Figure 5.1-26: Comparison of 10%-ISLOM segment sensitivities against the monolithic mirror

After generating the series of hybrid PM segment WFE sensitivities described above; integrating them into the dynamics and control system analysis environment; and playing steady-state disturbances through them, it was discovered that estimated dynamic WFE did not improve or significantly change when the 0% ISLOM was used, as opposed to the 100% ISLOM. This is likely a result of low disturbance transmissibility to the individual PM segments. The full family of 5 weighted-average LOMs were compared for the CMG induced vibration disturbance example, in Figure 5.1-27. In this comparison, CMG vibration was run through all 5 hybrid LOMs over 12 underlying structural model configurations[5], and total dynamics WFE was measured and plotted for each case. The details of the WFE calculation are outlined in the next section and in Section 6.1. This figure highlights agreement between the 5 LOMs to within 0.03 pico-meters; and note that the CMG disturbance was chosen for the illustration since it exhibited the *highest* overall sensitivity to the LOM, compared to the VIPPS, FSM, and HDI-FGS disturbances[5].

[5] The 12 structural model configurations and details of the dynamics WFE analysis are further described in Section 6.1

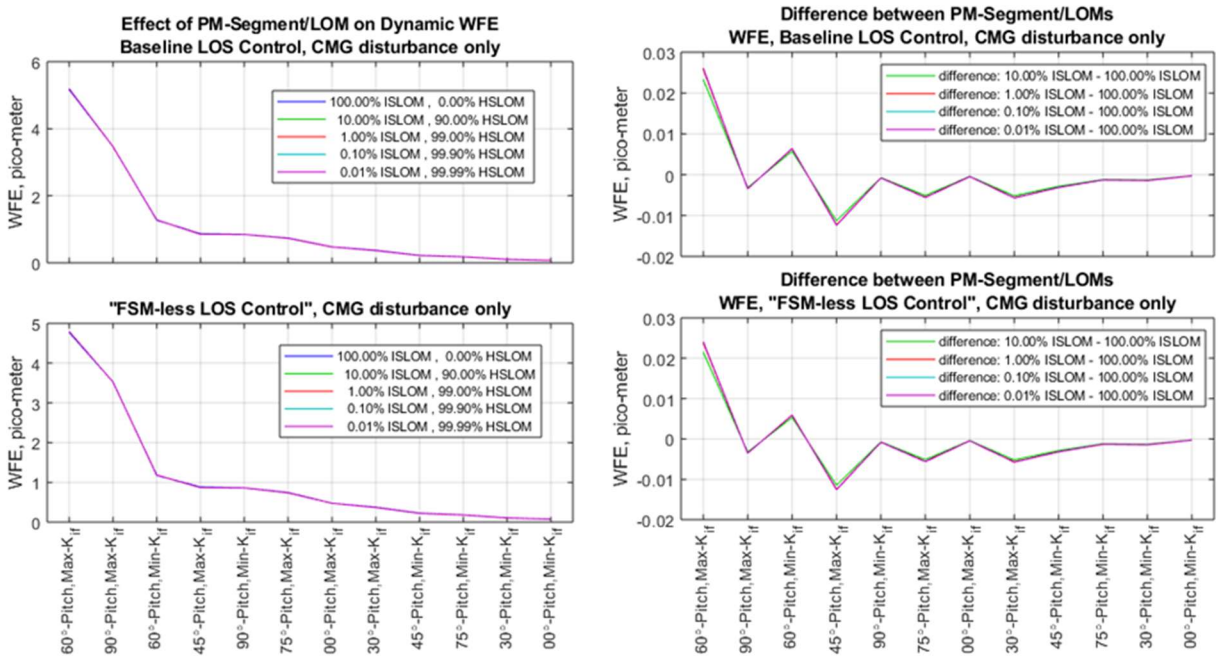

Figure 5.1-27: Effect of PM-segment optical sensitivities on dynamics WFE

Although time did not permit a full investigation of the root cause of this apparent lack of sensitivity to LOM, a local disturbance at a PM segment or backplane support frame (such as for example disturbances arising from a segment actuator) may reveal a difference between the LOMs that was not apparent for the disturbances considered in this study. Following the above findings, all dynamic WFE results presented in Section 6.1 were generated using the ISLOM.

5.1.3.2.3 Implementation in Integrated Modeling

The OPD sensitivities described above essentially create a 128x128 two-dimensional image representing the propagated wavefront. As such, simple image processing techniques such as spatial-frequency filtering are used, and then wavefront error is the spatial-RMS of the resulting images. The cut-off frequency for spatial-frequency filtering was chosen to be on the order of 1 cycle per segment, or roughly 11 cycles per aperture, in order to isolate segment-level dynamic WFE performance. The product of the filtering process is shown for sample time-domain simulation results in the Figure 5.1-28.

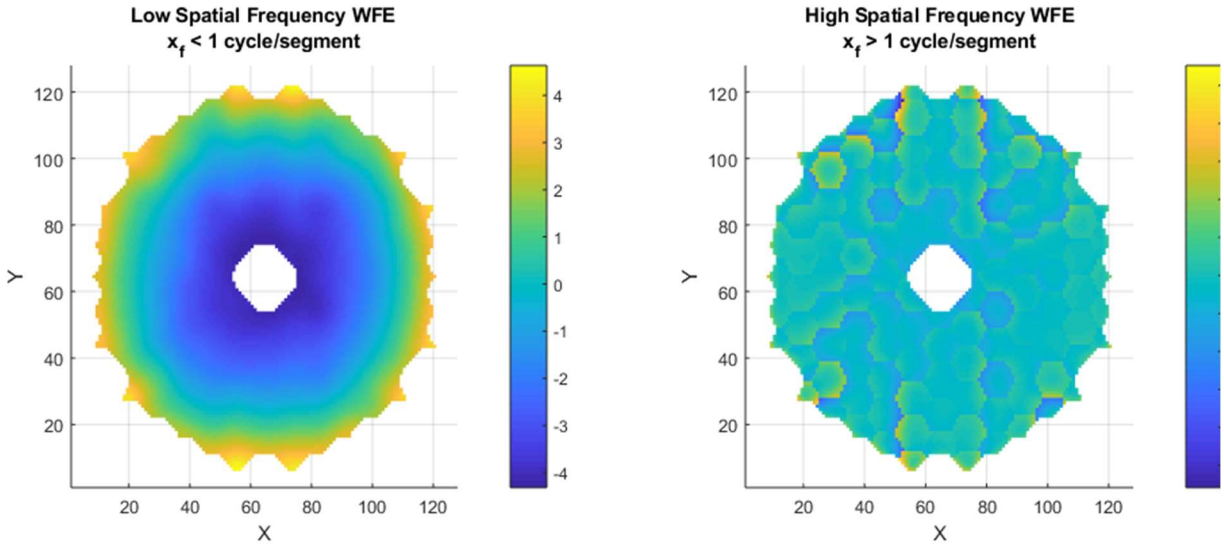

Figure 5.1-28: Illustration of the cut-off for OPD spatial-frequency filtering

The OPD image processing and WFE calculations were shown to be valid and equivalent for both time-domain and temporal frequency-domain inputs. For temporal frequency domain analysis, the OPD maps have PSD units of (pico-meters)^2/Hz instead of pico-meters; a spatial RMS is computed over the surface of these PSD's, and then the total dynamic WFE metric is computed by integrating the resulting spectrum in temporal-frequency domain. Since the spatial frequency content was separated or binned per above, a similar approach was used to characterize WFE RMS in terms of temporal frequency. This process is explained further in Section 6.1.

5.1.4 Disturbance and Component Models

5.1.4.1 Control Moment Gyroscope (CMG)

The space-vehicle model used in this study included a set of four direct-drive CMGs, each having 217 N-m-sec nominal wheel momentum and a maximum gimbal rate capability of 0.4 rad/sec, which were selected based on the notional slew-time requirements for LUVOIR6. A CMG wheel-induced vibration (IV) model was derived from historical test data from similar CMG hardware. The data that was leveraged for this effort was an average of multiple sources; it came in the form of 6DOF exported force and torque (EFT) amplitude spectra, and it was adapted for use in this study according to the following procedure.

For all 6DOF, the RMS of the spectrum was calculated within the following frequency-bins: <25Hz, 25-75Hz, 75-125Hz, 125-175Hz, and >175Hz. The resulting frequency-binned RMS profile was then used to make a new spectrum with an equivalent frequency-binned RMS profile, assuming a flat profile within each bin. This procedure was used in lieu of a frequency-dependent model-uncertainty factor (FDMUF), which is sometimes assumed or required in order to make up for test measurement error; lack of maturity in the structural-dynamics models; inconsistencies in environment and boundary conditions between the test-stand and flight; changes in wheel and gimbal operating-point between test and flight; and generally, to add conservatism.

Figure 5.1-29 shows the conservative CMG-IV disturbance model was used to evaluate steady-state LOS and wavefront stability for LUVOIR. Identical external load spectra were applied to each of four CMG nodes in the integrated system model in a randomized (but seeded) orientation.

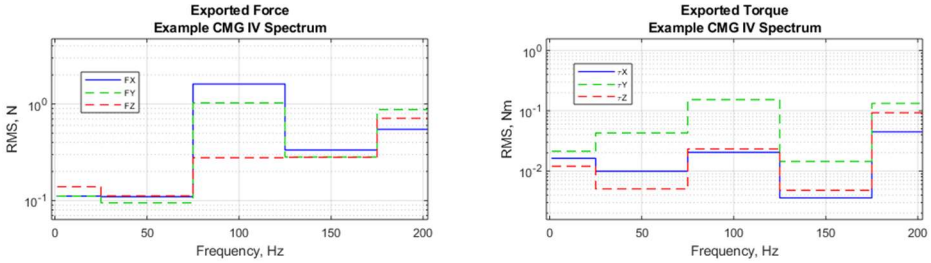

Figure 5.1-29: Simplified CMG wheel induced vibration spectrum.

5.1.4.2 Fast Steering Mirror (FSM)

The FSM model considered in this study included two disturbance sources arising from the mechanism: (a) exported loads to the payload structure due to actuation of the mirror relative to the optical bench; (b) tip/tilt jitter of the mirror surface due to continuous closed-loop servo control. Each of these disturbance sources are briefly described here.

The FSM mechanical model was derived from a recent flight development program, whose clear aperture was approximately 18 cm. This is approximately the correct size for what is needed for LUVOIR Architecture A (with a Primary Mirror aperture of 15 meter and a telescope magnification of 100, this translates to a pupil diameter in compact space of 15 centimeters). FSMs for precision optical systems typically employ a reaction mass to perform momentum-compensation of the moving mirror mass, much as the design for the WFIRST FSM [18]. In momentum-compensated FSMs, the mirror actuates against a reaction mass of nearly identical mass properties. The residual exported loads from the FSM are a function of the mismatch in these mass properties, and in particular on the center-of-mass offset between either the mirror or

[6] Per the LUVOIR Interim Report [1], the space-vehicle is required to reorient itself anywhere within the anti-Sun hemisphere in 30 minutes or less. Optimization of CMG mounting geometry was not considered to be a goal in this study phase and was not required to meet this relaxed agility requirement.

the reaction mass relative to its flexure center-of-rotation. The model included in this study assumed the c.g. offsets for both mirror and reaction mass were 2 mils (51 microns), in a worst-case offset configuration.

Second, the jitter associated with servo control of the FSM was assumed to be entirely due to noise arising from the local tip/tilt angle sensor of the FSM with respect to the base mount. The RMS measurement noise of a sensor can be related to its range through an Effective Resolution (ER), stated simply as:

$$\sigma_S = \frac{r}{2^{ER}} \quad (1)$$

where r is the range of the sensor. For LUVOIR, the FSM range was assumed to +/- 10 arcsec in output space, or +/- 0.14 deg mechanical stroke in local FSM space. An effective resolution of 17 bits is considered to be near the current state-of-the-art in sensor resolution; with this assumption, the RMS sensor noise from equation (1) is 37 nrad in FSM mechanical space. This was modeled as additive white Gaussian noise, inside the FSM servo control feedback path as measurement noise. The FSM closed-loop bandwidth was assumed to be 100 Hz.

5.1.4.3 VIPPS Interface Actuators

The current in the voice coil actuators that actuate on both the payload and spacecraft side of the VIPPS interface in an action-reaction sense are assumed to be controlled by motor drive electronics and includes a high bandwidth current control system. The RMS current noise was conservatively assumed to be 50 micro-Amps per actuator, derived from a zero-to-peak required current range of 5.4 Amps (derived from the force required per-actuator to support the LUVOIR pointing agility requirement). Given an assumed voice coil actuator motor constant of about 5.5 N/Amp, this translates to an RMS force level of 0.27 milli-Newtons RMS per-actuator.

Given these per-actuator RMS force noise levels, size voice coil actuators were assumed to be arranged in a Stewart platform configuration with a 1-meter mounting radius with respect to the center of the VIPPS interface. Three sets of VCA brackets mounted 120 degrees from its neighbors were assumed, with each bracket holding two voice coil actuators canted at 45 degrees with respect to the axial direction. Using this geometry, a full set of RMS disturbance force and torque noise levels, in units of Newtons and Newton-meters, expressed in the payload reference frame, were computed.

5.1.4.4 VIPPS Interface Sensor Noise

Similar to the method used for deriving a FSM RMS sensor noise level described in Section 5.1.4.2, we derived an RMS noise level for each non-contact actuator at the VIPPS interface. Each non-contact sensor at the VIPPS interface was assumed to have a range of +/- 10 mm, consistent with the sizing assumption of the VIPPS non-contact actuators. Assuming an effective resolution of 19 bits, we arrive at a per-sensor RMS measurement error of 19 nm. By assuming that the non-contact sensors are mounted with the same geometry as the VIPPS actuators described in 5.1.4.3, we similarly arrive at a full set of RMS relative position and relative attitude measurement errors, in units of meter and radians, respectively.

5.1.4.5 High Definition Imager (HDI) Centroid Noise

The study included a simplified additive-noise model for the measurement error associated with LOS error from the HDI. The HDI has a pixel Instantaneous Field of View (IFOV) of 2.75 mas/pixel [1]. Measurement of the LOS will involve centroiding on the regions associated with the target star (or stars). Error in this centroid process arises from focal plane random errors, such as dark current and readout error, as well as systematic error associated with pixel nonuniformity. Here, we assume that the error is additive white Gaussian noise. A typical rule-of-thumb is that the centroiding process is accurate to within 1/10 of a pixel – this is generally a conservative assumption, and better centroiding performance can be achieved by customizing the centroiding

algorithm to the focal plane hardware. Under this assumption, however, we assume that the RMS HDI additive measurement noise is 0.275 mas.

5.1.4.6 VIPPS Interface Cable Coupling

In this study, cable stiffness was modeled based on empirical data that was provided under the Cable Stiffness Testbed IRAD in 2018. The testbed was designed to quantify transmissibility of 6-DOF measurement of forces and torques across two sides of the VIPPS interface where the only mechanical connection between the two sides is the cable assembly. This study focused on a specific type of cable harness as specified by partners at NASA with knowledge of the likely makeup of LUVOIR cable harnesses. The testbed also allowed for measuring transmissibility for a variety of cable configurations up to 10 Hz. Analyzing transmissibility for all cable configurations suggested a constant stiffness matrix across the tested frequencies would be an accurate representation of the cable stiffness model. The magnitude of the cable stiffness in 6-DOF proved to be dependent on the cable configuration, as expected. An analysis was done to choose the maximum and minimum stiffness matrices over different cable configurations. In this analysis, the test case that produced the highest SVD values was chosen as the maximum stiffness matrix, and the test case that produced the lowest SVD values was chosen as the minimum stiffness matrix. The stiffness values in all 6-DOFs are tabulated in Table 5.1-5. Lastly, based on the maximum and minimum stiffness matrices, a proportional damping matrix was chosen such that the minimum modal damping for the 6 fundamental modes across the VIPPS interface is not lower than 0.005 (0.5%).

Table 5.1-5: Max and Min VIPPS Interface Stiffness Matrices

Maximum Stiffness Matrix	Minimum Stiffness Matrix
$\begin{bmatrix} \begin{bmatrix} 14.10 & 0.34 & 3.28 \\ 0.15 & 1.99 & 0.09 \\ 4.52 & 0.10 & 3.31 \end{bmatrix}_{[N/m]} & \begin{bmatrix} 0.07 & 2.94 & 0.08 \\ 0.44 & 0.02 & 0.45 \\ 0.01 & 1.52 & 0.06 \end{bmatrix}_{[N/rad]} \\ \begin{bmatrix} 0.13 & 2.08 & 0.08 \\ 13.76 & 0.27 & 3.93 \\ 0.24 & 1.31 & 0.03 \end{bmatrix}_{[Nm/m]} & \begin{bmatrix} 0.56 & 0.04 & 0.44 \\ 0.05 & 3.71 & 0.09 \\ 0.25 & 0.03 & 0.56 \end{bmatrix}_{[Nm/rad]} \end{bmatrix}$	$\begin{bmatrix} \begin{bmatrix} 1.69 & 0.02 & 0.35 \\ 0.03 & 0.17 & 0.01 \\ 0.45 & 0.01 & 0.42 \end{bmatrix}_{[N/m]} & \begin{bmatrix} 0.01 & 0.51 & 0.01 \\ 0.05 & 0.02 & 0.05 \\ 0.01 & 0.30 & 0.01 \end{bmatrix}_{[N/rad]} \\ \begin{bmatrix} 0.01 & 0.22 & 0.02 \\ 1.98 & 0.02 & 0.63 \\ 0.05 & 0.21 & 0.02 \end{bmatrix}_{[Nm/m]} & \begin{bmatrix} 0.11 & 0.02 & 0.07 \\ 0.01 & 0.75 & 0.01 \\ 0.06 & 0.02 & 0.16 \end{bmatrix}_{[Nm/rad]} \end{bmatrix}$

5.2 HabEx Integrated Modeling and Analysis

5.2.1 Structural Dynamics Modal Analysis for Non-Contact Isolation

The current HabEx baseline mission architecture calls for the use of micro-thrusters for pointing control. This section describes preparatory work to examine another possible control architecture, known as Disturbance-Free Payload (DFP) [19]. DFP enables the telescope and instruments to achieve extreme pointing and image stability by physically separating the telescope and instruments from the spacecraft. The payload controls the line-of-sight by pushing against the spacecraft inertia using a set of six non-contact voice coil actuators while the spacecraft controls its inertial attitude such that interface stroke and gap are maintained. Since the telescope is physically separated from the spacecraft, the disturbances and structural excitation of the spacecraft and sunshield do not propagate to the telescope, enabling extreme stability across a board frequency range.

The HabEx analysis starts with the observatory finite element model (FEM) and optical model received from the mission Science Technology Definition Team (STDT). The observatory FEM is shown in Figure 5.2-1, and the optical prescription is shown in Figure 5.2-2.

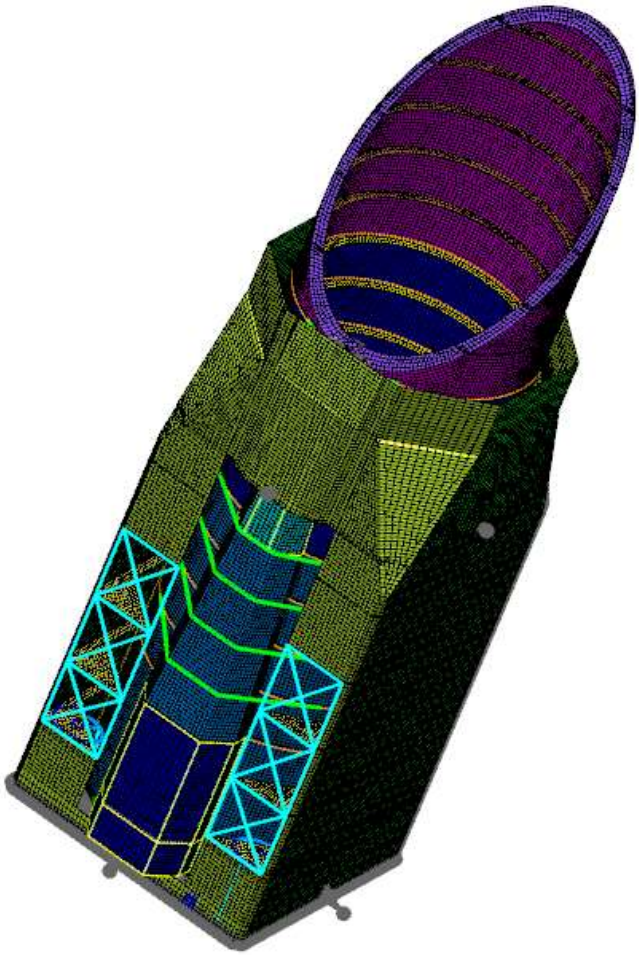

Figure 5.2-1: HabEx Observatory FEM

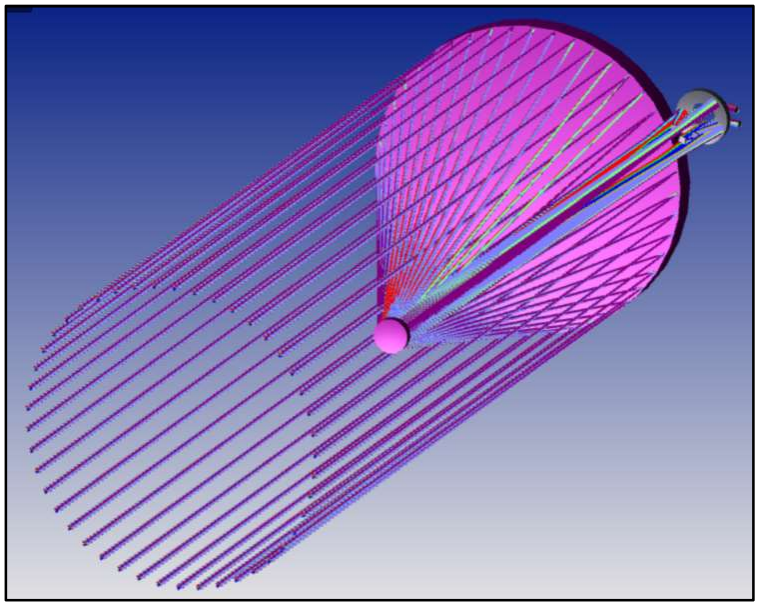

Figure 5.2-2: HabEx Optical Model

The FEM is comprised of 125239 grid points, 105168 elements of various types with 68 physical properties and 12 material properties defined. Model quality and property reasonableness checks were performed; it should be noted that the bipods used to support the primary mirror have the same coefficient-of-thermal-expansion (CTE) as the mirror which may be overly optimistic for thermoelastic analysis. The rationale for its use would be that these bipods are primarily constructed from directional graphite composites, where the axial CTE of the bipods can be tailored by changing the fiber direction of the individual layers in the laminate. For stress analysis described later, this material property was not modified, although the rigid elements used to simulate the fittings connecting the mirror bipods to the mirror were replaced with stiff bars with an assigned CTE. The delivered optical model contained paths to the observatory Fine Guidance Sensor (FGS). None of the aft optics or instrument optical paths were included in the Zemax optical model.

The FEM received from the HabEx STDT (shown in Figure 5.2-1) was modified to accommodate the needed DFP elements. The spacecraft and telescope were separated at the mounting interface ring between the two. Constraint elements were added to central nodes where DFP forces can be applied and DFP motions sensed in the subsequent integrated controls simulation. In addition, the baselined micro-thruster fuel tanks have been replaced by nodes, lumped masses, and constraints for the control momentum gyroscopes (CMGs) necessary for a DFP-controlled observatory.

HabEx, configured for DFP control, is a modally-rich system with 6687 modes (including the 12 rigid body modes, 6 each for spacecraft and telescope) predicted below 450 Hz. The first flexible body vibration mode for the observatory, shown in Figure 5.2-3, occurs at a frequency of 10.8 Hz, and is associated with the spacecraft. Figure 5.2-4 illustrates the 1st telescope flexible body vibration mode at 26.1 Hz. In the figures, the phantom outline in grey shows the “undeformed” shape of the structure.

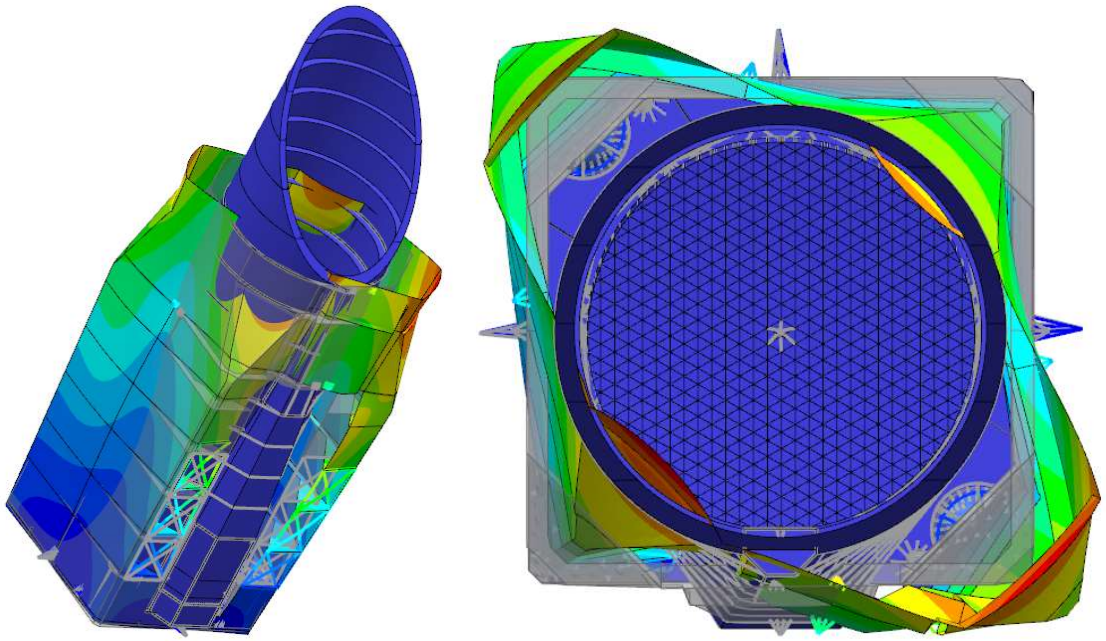

Figure 5.2-3: HabEx Configured for DFP Control, 1st Spacecraft Flexible Body Vibration Mode.

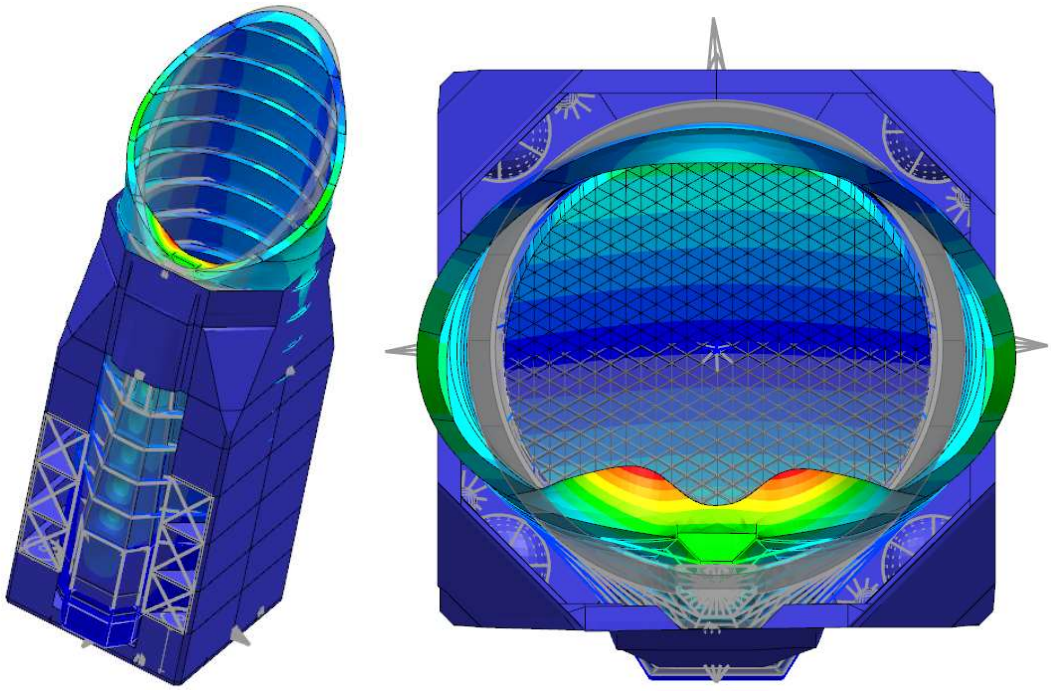

Figure 5.2-4: HabEx Configured for DFP Control, 1st Telescope Flexible Body Vibration Mode

The optical model was used to develop both image and object space line-of-sight perturbation coefficients back to the FGS, for inclusion into the integrated model. The development of these perturbation coefficients is discussed further in Section 5.2.5

To further illustrate the modal characteristics of the HabEx observatory, Figure 5.2-5 presents open-loop transfer functions between the image space FGS line-of-sight and selected components of the net DFP force acting on the telescope at its interface. Note that the *object space* LOS is usually expressed as an angle and is related to the *image space* LOS by the effective focal length of the optical system. The top graph in the figure shows the image space line-of-sight due to a force acting in the X direction acting at the DFP interface, while the bottom graph shows the image space line-of-sight due to a moment acting about the Y direction at the DFP interface. The frequency response was calculated between 1 and 500 Hz, sampled at 0.5 Hz. The calculation assumed 0.25% uniform damping.

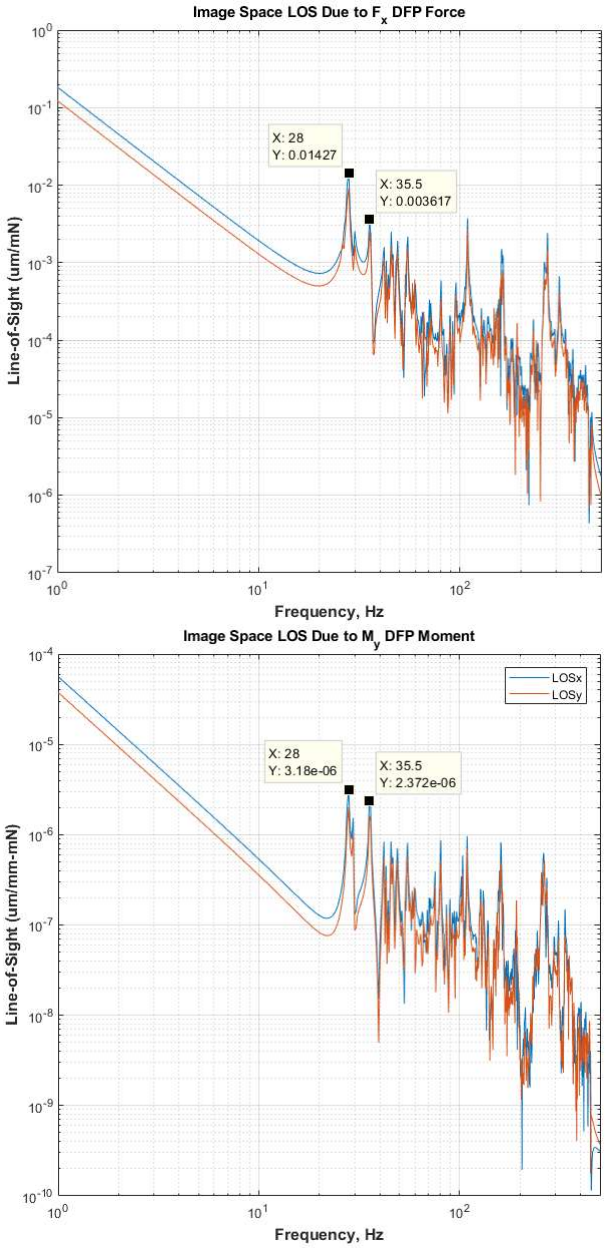

Figure 5.2-5: Telescope Line-of-Sight Transfer Functions
Top: LOS Due to DFP Force, Bottom: LOS Due to DFP Moment

It is evident that the line-of-sight is sensitive to vibration modes of the observatory at approximately 28 (mode 21) and 35.5 (mode 32) Hz. These vibration modes are illustrated in Figure 5.2-6.

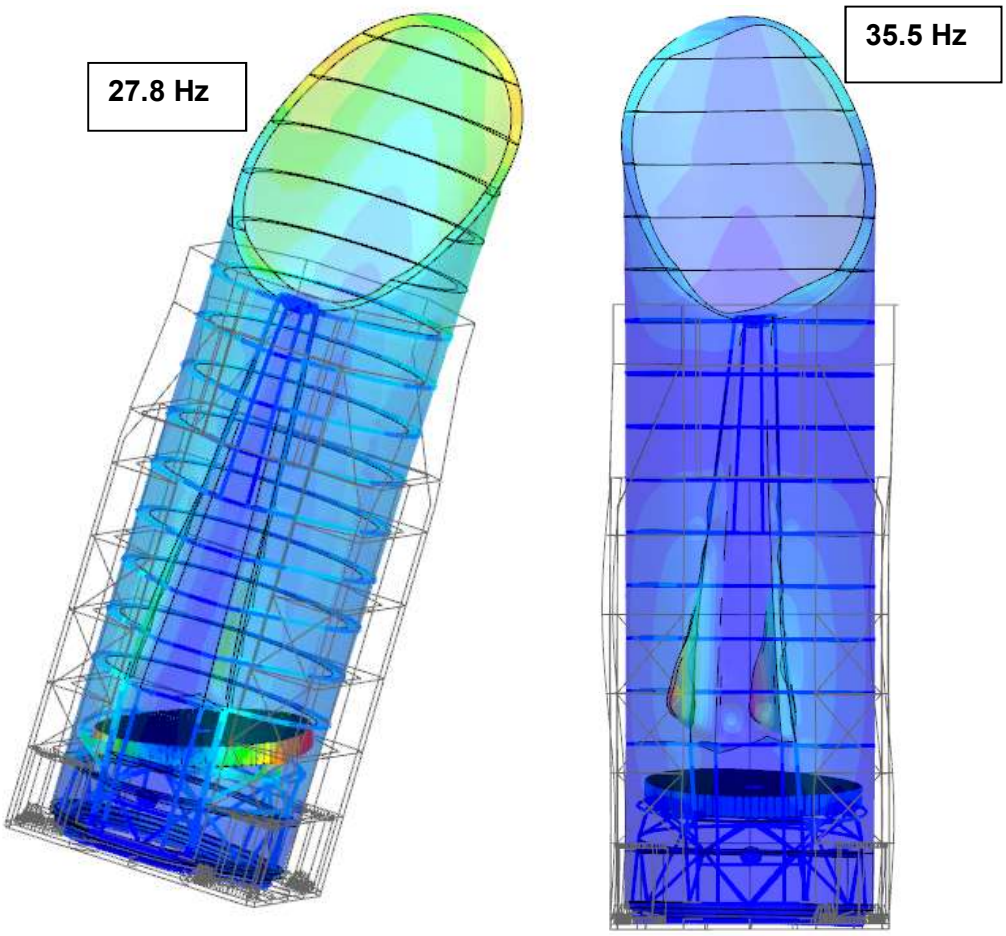

Figure 5.2-6: Vibration Modes Significant to Telescope Line-of-Sight

The modal analysis needed for construction of plant state space models for the HabEx Observatory using DFP control has been completed. In follow-on work, the vibration modes and state space models can be incorporated into the overall DFP control simulations, along with candidate DFP control architecture component models for such as CMG and/or FSM disturbances, sensor noise, etc., for evaluation of control system performance. The value of such integrated modeling can be bolstered if the optical model is updated with aft optics and instrument paths.

5.2.2 Primary Mirror Stress Analysis

In this and the subsequent section, we take a broad view of the integrity of the HabEx 4m primary mirror over its service life. Basic stress analysis and fracture mechanics are used to highlight potential material characterization needed to bolster confidence in the primary mirror design. Two candidate mirror materials are examined: Schott's Zerodur glass-ceramic, and Corning's Ultra-Low Expansion (ULE) glass. Both materials have exceptionally low coefficients-of-thermal expansion (CTE) making them ideal candidates for the HabEx primary mirror.

A subset of the FEM shown in Figure 1 was used to evaluate primary mirror deformations and stresses to certain quasi-static load cases. This breakout model is illustrated in Figure 5.2-7. In the model, the base ring was given cylindrically-oriented boundary conditions, where all degrees-of-freedom are fixed, save the radial translation, which remains free to allow for a free thermal

expansion boundary condition. The breakout model was analyzed for unit (1G) accelerations acting on the assembly in each of the directions illustrated by the coordinate triad in the figure, and a bulk soak temperature of -50C corresponding to the coldest expected operating temperature of the observatory. It is assumed the “stress free” temperature of the assembly is 300K. The mirror stresses generated by these loads were used to evaluate the long-term primary mirror integrity. Table 5.2-1 lists some of the salient mechanical and thermal properties for both candidate materials and have been excerpted from [20] and [21].

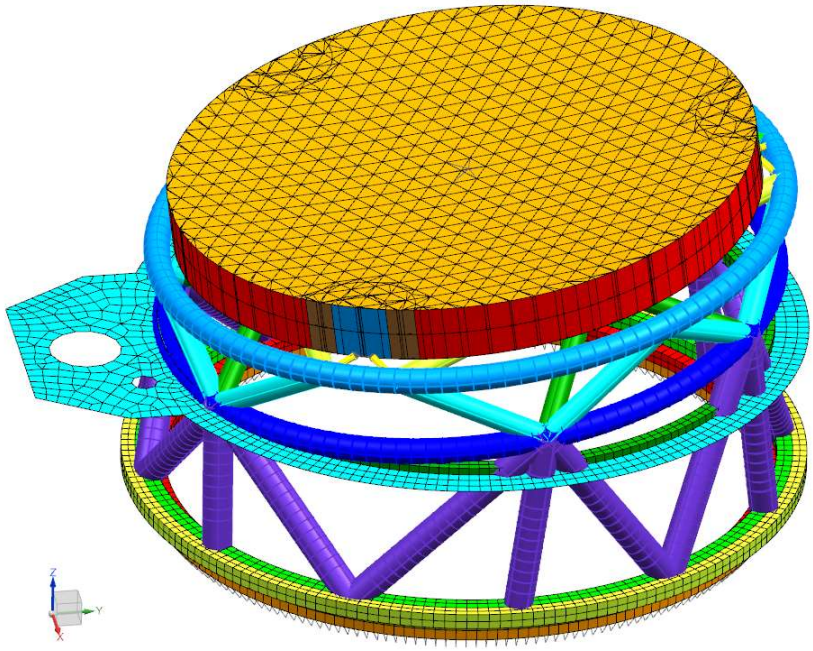

Figure 5.2-7: HabEx Primary Mirror Breakout Model.

Table 5.2-1. Properties of ULE & Zerodur Glasses

Quantity	Units	ULE	Zerodur
Elastic Modulus	Gpa	67	90.3
Poison's Ratio	n/a	0.17	0.24
CTE @ 25C	ppb/K	0 ± 30	0 ± 50
Density	g/cm^3	2.20	2.53
Knoop Hardness	Kg/mm^2	460	620
Fracture Toughness	Mpa $\sqrt{m}$	0.7	0.9
Specific Heat	J/kg-K	766	800
Thermal Diffusivity	10^{-4} m^2/s	0.008	0.0072
Thermal Conductivity	W/m-K	1.31	1.46

Figure 5.2-8 shows a close-up view of one of the primary mirror attachments, as represented in the FEM. The different colors represent different physical properties, and it should be noted that the primary mirror rib structure contains ribs with increased thickness around the load transfer regions of the mirror. The fidelity of the model is likely insufficient to capture what are expected to be highly localized stress gradients around these load transfer points. With this caveat, the FEM is useful for capturing first-order estimates of mirror stresses for broad view assessments of integrity.

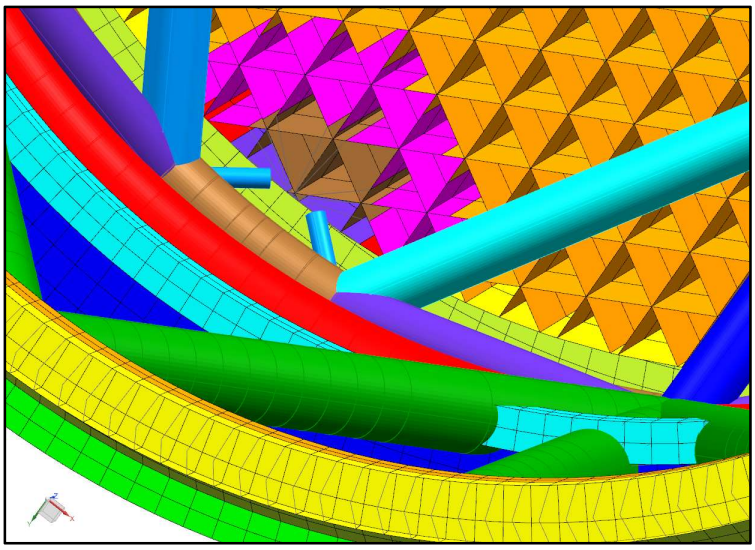

Figure 5.2.8: FEM Close-up View of Primary Mirror Attachment

Figure 5.2-9 illustrates the Zerodur primary mirror principal stress distributions for each of the load cases analyzed, and Figure 5.2-10 illustrates the ULE primary mirror principal stress distributions. In all cases, the peak mirror principal stresses occur at the interfaces to the underlying tubular truss structure as expected. Table 5.2-2 tabulates the maximum principal stresses for each load case and mirror material.

Table 5.2-2. Mirror Maximum Principal Stresses

Load Case	Maximum Principal Stress (Mpa)	
	Zerodur	ULE
1G, X-direction	1.759	1.524
1G, Y-direction	1.498	1.298
1G, Z-direction	1.743	1.510

Table 5.2-2. Mirror Maximum Principal Stresses

Load Case	Maximum Principal Stress (Mpa)	
	Zerodur	ULE
-50G bulk soak temperature	0.933	0.714

As noted earlier, in the delivered FEM the bipods used to attach the mirror to the underlying mirror truss were assigned the same CTE as the mirror, and fittings used to interconnect these bipods to the mirror were modeled as rigid bodies. The bipod CTE was not changed for the calculation of the stresses shown in Table 5.2-2. However, the rigid bodies used to model the fittings were replaced by stiff bars with an assigned CTE. In the -50C bulk soak temperature results summarized in Table 5.2-2 (and the distributions shown in the figures), the fittings have been assigned a CTE equal to the composite truss members. The local mirror stresses are sensitive to this assumption. For the zerodur mirror case, for example, assuming fittings constructed of titanium Ti-6Al-4V results in principal stresses between -22.5 and 10.16 Mpa. For fittings constructed from Invar 36 (a low expansion, low strength nickel-iron alloy often used in optical systems), the principal stresses in the mirror vary between -3.25 and 1.47 Mpa.

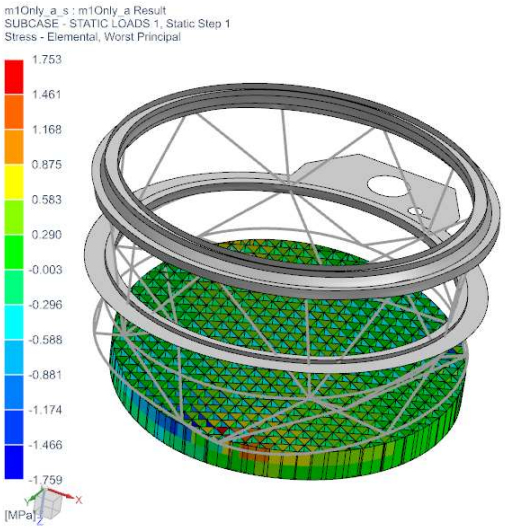

1G, X-Direction

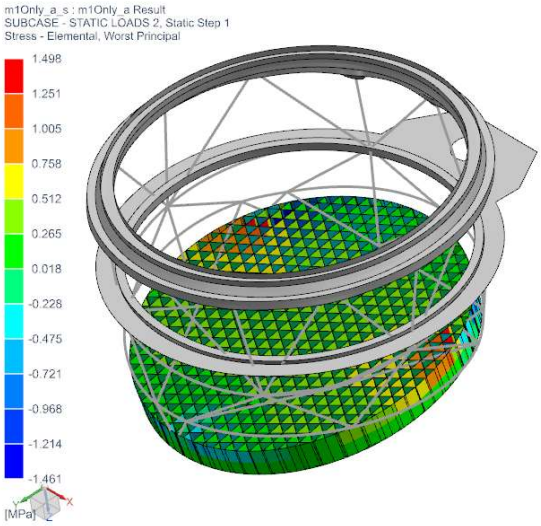

1G, Y-Direction

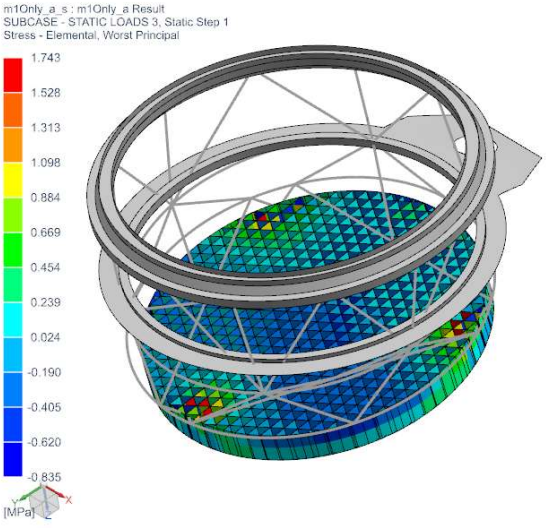

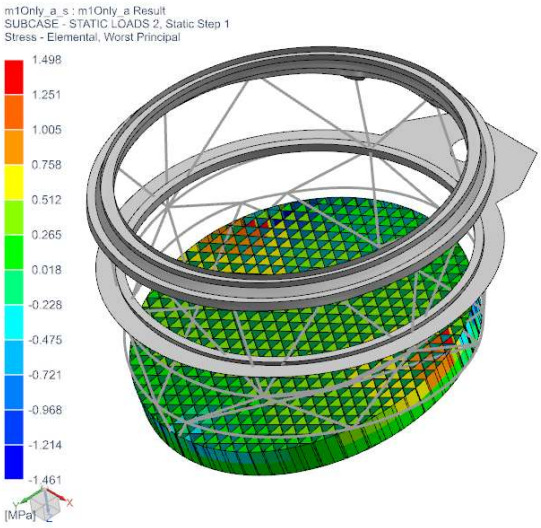

1G, Z-Direction **-50C Bulk Soak Temperature**

Figure 5.2-9: Zerodur Primary Mirror Principal Stress Distributions.

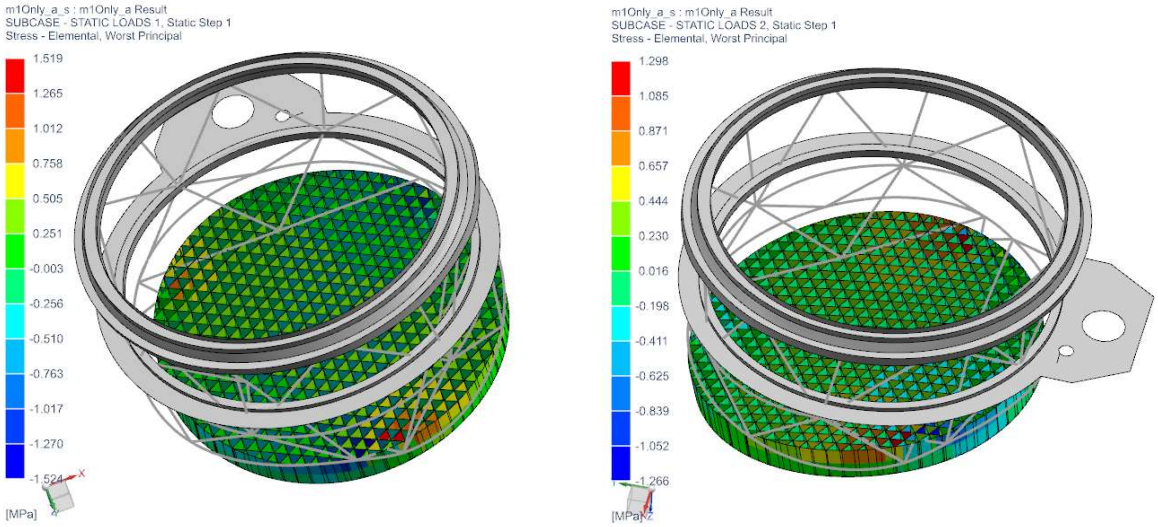

1G, X-Direction **1G, Y-Direction**

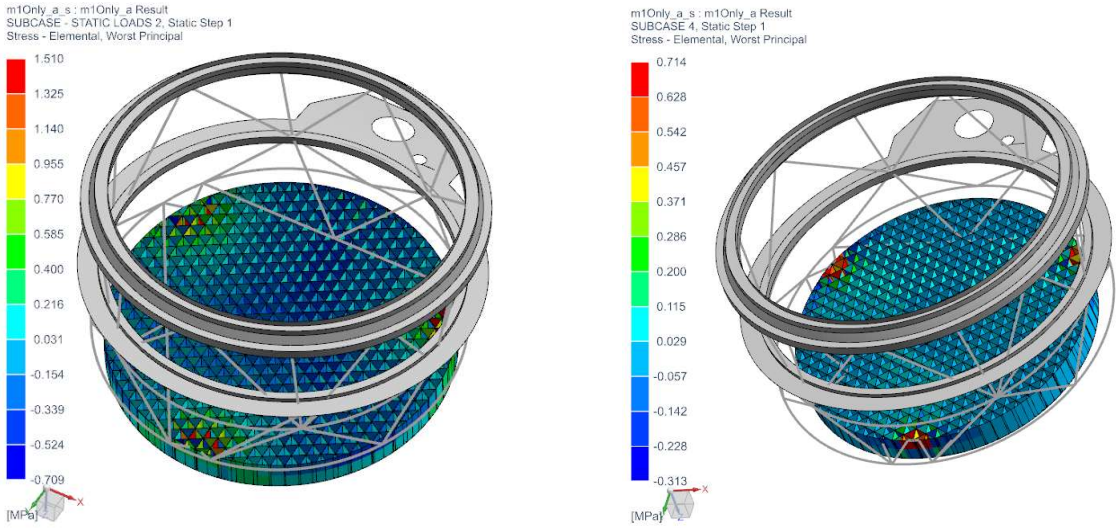

1G, Z-Direction **-50C Bulk Soak Temperature**

Figure 5.2-10: ULE Primary Mirror Principal Stress Distributions.

5.2.3 Primary Mirror Strength and Life Analysis

The stress analysis results shown in Figures 5.2-9 and 5.2-10 and tabulated in Table 5.2-2 can be used to construct a simplified stress lifetime history for the primary mirror, shown in Figure 5.2-11. The history assumes a 10-year life on the ground to account for assembly, integration, and test activities for the observatory. Included in the ground activities is vibration testing. Three sets of vibration tests have been assumed, where each set is comprised of 60 second exposures to test vibration environments in each of three principal axes. For stresses due to vibration, the stresses due to quasi-static limit loads have been multiplied by 1.5 to account for overall resonant behavior and potential force-limiting during the vibration test. A quasi-static limit load of 6Gs has

been assumed for launch and ascent, based on a limited and rough survey of recommended limit loads for large launch vehicles currently in use. Finally, a 10-year mission life once on orbit has been used. For this portion of its life, the primary mirror is assumed to be exposed to a -50C bulk soak temperature. The constructed stress-lifetime history is intended for a rough assessment of the integrity of candidate mirror materials given the current design maturity of the telescope and observatory; more granularity can be added as the mission concept and design evolve. For both candidate mirror materials, the most striking feature of the stress-life history are the elevated stress levels associated with vibration testing and launch.

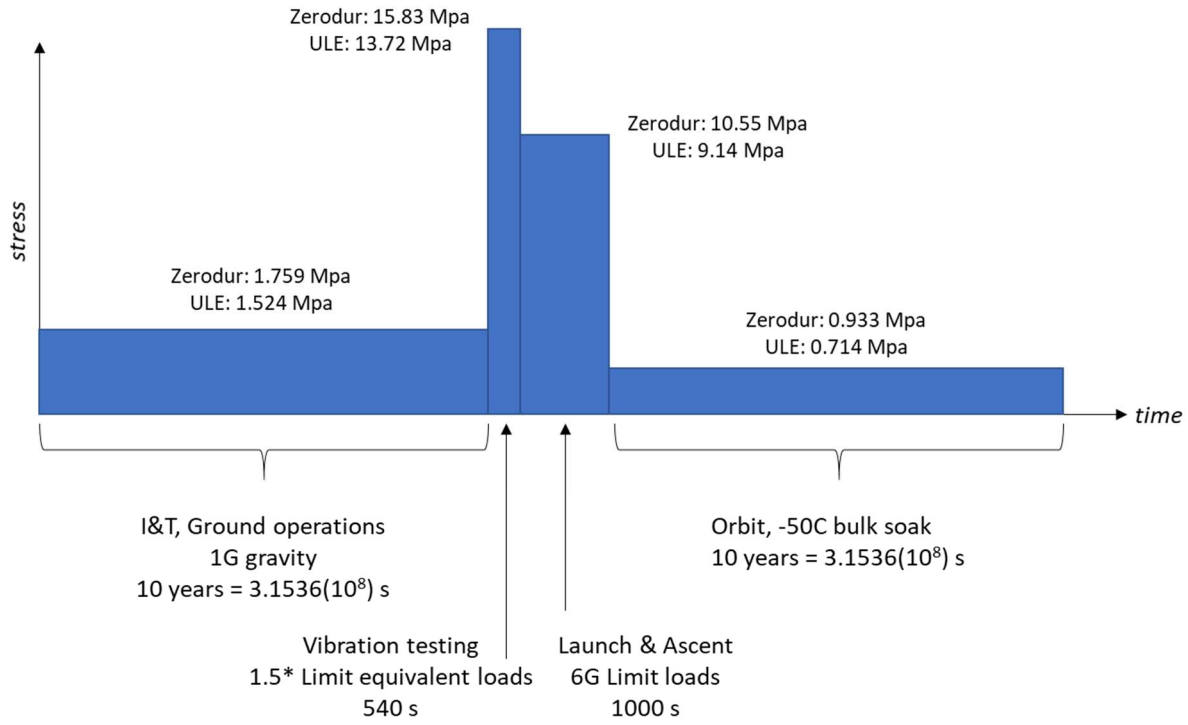

Figure 5.2-11: Simplified Stress-Lifetime History for HabEx Primary Mirror (Not to Scale)

The common approach to assess integrity for the vast majority of flight hardware is to calculate relevant stress metrics (such as Von Mises stress in the case of ductile isotropic metals) due to environmental exposures and compare these with well-defined and controlled allowable stresses. In the case of brittle ceramics and glasses, such an approach is not appropriate, as the de-facto integrity of such materials is a direct function of the surface and internal flaw structure of the manufactured component which are often difficult or impossible to characterize. These materials tend to fail by brittle fracture. A widely used approach in this case is to develop allowable stresses based on Weibull failure models. Weibull failure models characterize the probability-of-failure at different stress levels. The Weibull failure models which appear in wide use are the so-called two- and three-parameter models [21] [22]. The two-parameter Weibull cumulative failure distribution is given by

$$\boldsymbol{F(\sigma) = 1 - e^{-\left(\frac{\sigma}{\sigma_c}\right)^m}}$$

Where

$\boldsymbol{F(\sigma)}$ = Probability-of-failure at stress σ
$\boldsymbol{\sigma_c}$ = Characteristic stress

m = Weibull modulus

The characteristic stress is usually defined as the stress at which the probability-of-failure is ~63%. This characteristic stress and the Weibull modulus are both determined experimentally. Allowable stresses determined by a two-parameter Weibull model need further adjustment to account for differences in the desired probability-of-failure, and the stressed volume or surface area of the test specimens vs. the actual component or part. The failure model does not account for long-term, subcritical crack growth (sometimes called fatigue), which will be discussed later. The three-parameter Weibull model is a generalization of the two-parameter model, and the cumulative failure probability is given by

$$F(\sigma) = 1 - e^{-\left(\frac{\sigma-\gamma}{\mu}\right)^{\beta}}$$

Where μ, γ, and β are experimentally-determined constants. The significant modification for the three-parameter characterization is the parameter γ, which can be thought of as a threshold stress below which the probability-of-failure is zero. No additional areal or volume adjustments are necessary for the strength derived from a three-parameter Weibull distribution.

The differences between the two failure models are illustrated in Figure 5.2-12, where both two-parameter and three-parameter Weibull models have been fit to experimental data [22]. At high probabilities-of-failure, both distributions describe failure well. However, it would be desirable for the HabEx primary mirror to have a vanishingly-small probability-of-failure over its life. In this context, at low probabilities-of-failure (say, < 1%), use of a two parameter Weibull failure model may be overly conservative and lead to unnecessarily heavy design(s). Note that the likely cause for the change in slope (Weibull modulus) seen in Figure 5.2-12 is often attributed to the excitation of two underlying flaw distributions: surface and volumetric flaws, both of which can be present in test specimens. Schott has done extensive characterization of their glass products for both two- and three-parameter Weibull descriptions [22] [23] [24].

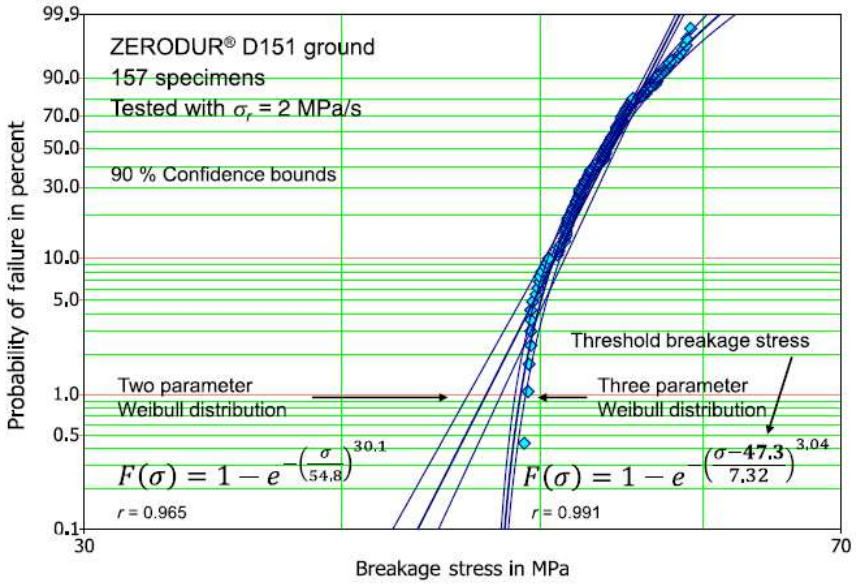

Figure 5.2-12: 2- and 3-parameter Weibull Fits for Zerodur Ground With D151 Diamond Compound [22]

Various test techniques have been used to characterize these Weibull failure models: 3-point and 4-point bending tests, ring-on-ring biaxial tests, and crack indentation [21] [22] [25] [26]. The ring-on-ring test [6] has gained considerable popularity for the characterization of brittle materials. In addition, data reduction standards exist to develop the two-parameter Weibull models [27].

Test sample preparation is critical to the development of appropriate failure models. In particular, the specimens should be made from glass manufactured using the exact process used for the in-situ part (mirror), preferably from the same pour or boule, and have the same surface preparation process; grinding steps, etching depths, and polishing schedules and compounds should all be replicated in the test specimens.

Returning now the HabEx primary mirror, in the case of Zerodur it would appear that the peak stress of 15.83 Mpa (~2.3 Ksi) shown in Figure 9 is well below the threshold stress of 47.3 Mpa (~6.9 Ksi), which is the threshold stress from the three-parameter Weibull model shown in Figure 5.2-12. Using the two-parameter model, the failure probability at 15.83 Mpa is essentially zero (of order 10^{-17}) as well. Indeed, using NASA standard factors-of-safety for glass (= 3), the deterministic margin is essentially zero. It is likely that the actual strength of a HabEx Zerodur mirror will be higher; the surface of such a mirror will be finished to much higher standards than implied by a ground D151 surface. The D151 designation refers to the largest particle size used in the diamond grinding compound; in the case of D151, the largest particle size is 150 μm. For a ULE HabEx primary mirror, three-parameter Weibull models appear to be less-readily available in the open literature. Reference 2 lists a Modulus-of-Rupture (failure stress) of 53.3 Mpa (7.74 Ksi), with a Weibull modulus of 6.1 for a 220-240 grit-finished surface, using ring-on-ring biaxial tests. Reference 4 lists a failure stress of 56.2 Mpa (8.15 Ksi) with a Weibull modulus of 6.95 for polished ULE specimens tested in an inert environment (dry nitrogen) using 3-point bend tests. Using the Reference 2 values without adjustment, the probability-of-failure for a ULE mirror subject to 13.72 Mpa (~2 Ksi) is also essentially zero (of order 10^{-4}). Note that additional measures can be taken to reduce the mirror stresses if desired. For example, [7] points out the primary mirror truss structure is designed to accommodate a launch restraint system which would reduce the mirror stresses during vibration exposures and launch and ascent.

The foregoing paragraph is hopeful for both materials but does not account for long-term stress corrosion effects (sometimes called fatigue). It has been shown that glass can be susceptible to subcritical crack growth when exposed to an aqueous environment, such as partially humid air [21] [28]. It is expected that the HabEx primary mirror will spend an appreciable portion of its life on the ground subject to a 1G load as shown in Figure 8 in air with a relative humidity of ~50%. As such, any cracks present in the stressed regions of the mirror will likely undergo stable growth. When subject to the high stresses from vibration testing and launch, the crack growth rate will increase, and any cracks present will possibly undergo unstable growth leading to subsequent failure.

A well-known crack growth model for brittle materials is the Paris Law, where the crack growth rate is related to the stress intensity at the crack tip. The Paris Law is

$$\frac{da}{dt} = AK_I^n$$

Where

a = characteristic crack dimension
K_I = stress intensity
A = crack growth coefficient, experimentally determined
n = crack growth exponent, experimentally determined (also called the *stress corrosion constant*)

The stress intensity is often expressed as a function of the ambient stress field, and for a crack in an infinite plate (a so-called Griffith crack) is given by

$$K_I = \sigma\sqrt{\pi a}$$

Where σ is the ambient stress. The stress intensity can be compared with a material's fracture toughness, and failure occurs when the stress intensity exceeds the material's fracture toughness.

A common technique for measuring the fracture toughness of a material is the Vicker's indent test, where a diamond-shaped indenter is driven into a specimen with a known force, which leads to a crack system with two orthogonal half-penny cracks. The fracture toughness is then calculated from the length of these cracks. There are subtleties to this measurement of fracture toughness; post-indent slow crack growth due to residual stress relaxation around the indentation site can become significant and correction of as-measured dynamic fatigue data using indentation methods may be required as a result [26].

There have been various techniques used to estimate the Paris Law parameters. A common approach is to use dynamic fatigue measurements which are an adjunct to the strength testing associated with the development of a Weibull failure model. The tests are dynamic in the sense that the test load is applied at a known and controlled rate, and the strength at failure is measured. By using different loading rates, the Paris Law parameters can be estimated. A linear relationship results when the logarithm of the failure stress is plotted against the logarithm of the load rate. The Paris Law parameters are related to the slope and intercept of this linear fit. A more detailed description of the underlying theory and data reduction can be found in the references to this section. Static fatigue is also sometimes used, where constant load is applied, and the time-to-failure is measured. These strength-based measurements can be performed with 3- and 4-point bend testing, or ring-on-ring biaxial testing. A variant uses fracture toughness indentation testing. One critical facet of these tests is to determine the so-called inert strength, which should be measured in an inert environment and at a relatively fast rate, so the failure is not a strong function of the test environment. All methods to estimate the crack growth parameters from basic failure tests can show large amounts of scatter (high variance). When these variations in the underlying failure data are flowed to the crack growth parameters and subsequent life estimation, large variations in predicted life can result.

Ideally, to make a quantitative comparison between ULE and Zerodur material candidates for the HabEx primary mirror, Paris Law parameters and material fracture toughness derived from identical test and data reduction methods (preferably from the same testing laboratory), surface finishes, and ambient environments would be available. Unfortunately, such consistent data is difficult or impossible to find in the open literature. Figure 5.2-13 illustrates the dilemma and is excerpted from Reference 3. Within a given environment (dry, normal, etc.), a wide range of Paris Law exponents (also known as *stress corrosion constants*) have been measured, depending on test method (for example).

Humidity	Method: Ground samples ring-on-ring setup load rate variation	Ground samples ring-on-ring setup load rate variation	Double cleavage drilled compression DCDC	Single crack propagation observation	Crack indention
Dry	79.1 (Dry N_2)	–	50 ± 3 (3%)	–	–
Normal	31.1 (50%)	29.3 +3.6/–2.9 (50%)	31 ± 3 (37%)	51.7 (50%)	59.3 (50%)
Humid	–	–	–	–	30.7 (100%)
Year	2014	2010	2008	1989	1990

Table 4: Stress corrosion constant n of the glass ceramic ZERODUR®. Relative humidity is given in parentheses.

Figure 5.2-13: Zerodur Stress Corrosion Constants (unitless) from Different Sources [22]

Given the lack of consistent comparative data, rather than make a quantitative comparison of ULE and Zerodur a qualitative analysis was performed to illustrate the effects of stress corrosion on the potential life of a HabEx primary mirror. Table 5.2-3 lists the salient parameters chosen for the study. The data for ULE is derived from specimens with a "commercial polish" and is based on 3-point bend tests at three different load rates (0.12, 1.23, and 12.3 Mpa/s), while the Zerodur specimens have a surface ground to D151 and is based on ring-on-ring biaxial bend tests at 0.004, 0.40, and 39.9 Mpa/s rates.

Table 5.2-3. Crack Growth Parameters

Quantity	Description	Units	ULE	Zerodur
n	Paris Exponent	n/a	27.9 [25]	31.1 [29]
B	Dynamic Fatigue Parameter	Mpa^2*s	31.17 [25]	68.34 [29]
K_{1c}	Fracture Toughness	Mpa √m	0.7 [25]	0.9 [26]
A	Paris Coefficient	$M^{(2-N)/2}/(Mpa*s)$	7.34	0.006
Test Environment			90% RH	50% RH

In the table, the Paris Coefficient (A) is derived from the dynamic fatigue parameter (B) by

$$A = \frac{1}{B}\frac{2}{\pi(n-2)K_{1c}^{n-2}}$$

The factor of π reflects the crack geometry, in this case a Griffith crack. The crack growth law can now be integrated over the stress-lifetime history shown in Figure 5.2-11, for a presumed initial flaw. An initial flaw with a characteristic length of ~450 μm was chosen and is based on three times the maximum particle size in a D151 grinding compound. It is expected that the critical surfaces of the HabEx mirror will have much smaller flaws, particularly for those surfaces which are ground and etched and possibly polished.

Figure 5.2-14 illustrates some of the results and shows the stress intensity as a function of time over the life of the mirror. In the figure, the Zerodur initial flaw was 450 μm, while the ULE initial flaw was 447 μm. The figure illustrates crack instability for the ULE mirror developing during vibration testing. The crack growth is arrested when the load is removed, and the crack remains stable thereafter to the end of the mirror's service life. A slightly larger flaw or longer vibration test duration would lead to failure, in this case.

While not strictly predictive, this analysis is intended to illustrate the potential importance of subcritical crack growth over the life of the HabEx mirror. The ULE data is based on an extreme environment to which the primary mirror will never be exposed (>90% relative humidity). The Zerodur data is based on an unrepresentative surface finish. The analysis highlights the need during primary mirror development for crack growth testing and data that reflects all the relevant environments, representative surface conditions and internal flaw distributions, and identical test methods, should the development be open to both mirror materials once all other considerations have been accounted for.

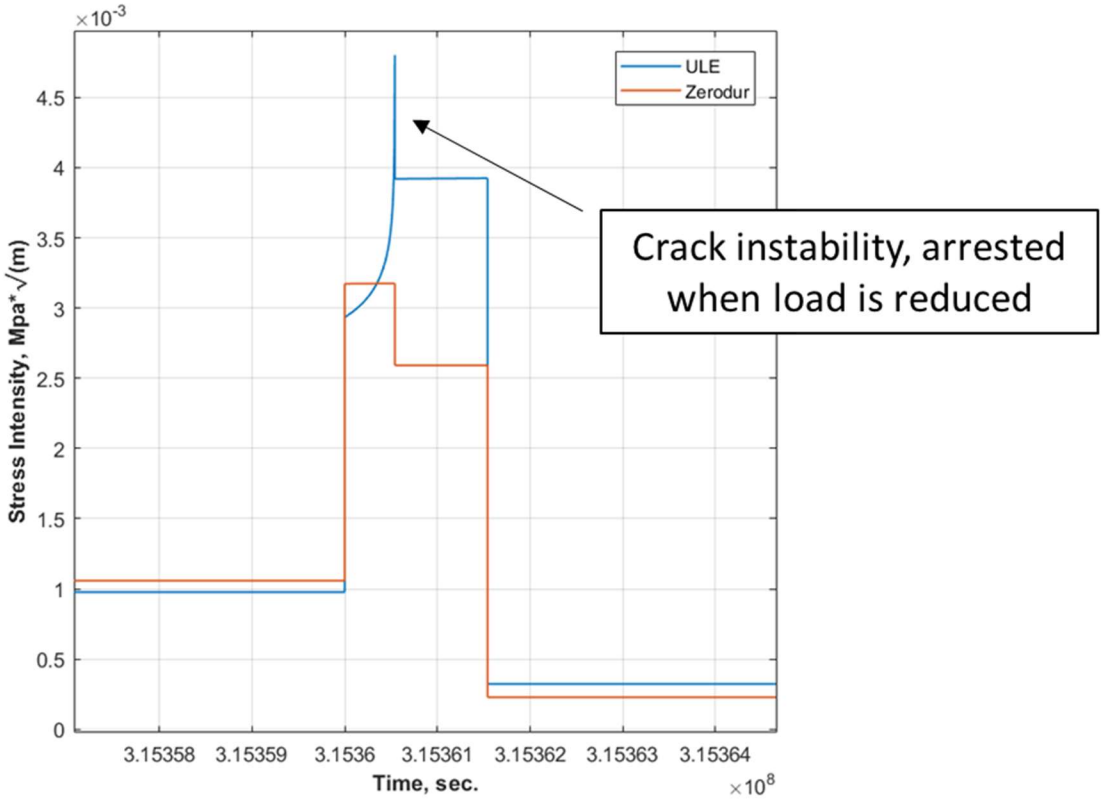

Figure 5.2-14: Crack Growth Scenarios

Finally, large glass ceramic mirrors have flown in space before, and can be viewed as the "existence proof" that the HabEx 4m monolithic glass primary mirror is possible. Acquiring the aforementioned fatigue and crack growth properties will further bolster confidence and potentially lead to weight and cost savings by allowing less conservative design choices to be made.

5.2.4 Primary Mirror Surface Figure Error (SFE) Analysis

Finally, Surface Figure Error (SFE) analysis of the primary mirror is discussed along with potential difficulties which should be overcome to experimentally verify on-orbit performance and anchor orbit performance models.

Primary mirror surface deformations for the load cases described earlier (1G quasi-static accelerations in each of three principal axes, and a -50C bulk soak temperature from 300K) have been analyzed. The deformations from the finite element model were first fit with Noll-ordered Zernike polynomials using 6 radial orders, and the rms and PV surface figures reported after piston, tip, and tilt removal. No masking was performed to account for differences in mechanical and clear apertures. The results for the ULE mirror are shown in Figure 5.2-15 and summarized

in Table 5.2-4. Figure 5.2-16 and Table 5.2-5 illustrate and summarize the results for a Zerodur primary mirror. For reference, the Z axis is along the light path into the primary mirror.
Note that the Collins Report in Section 7 contains a more detailed look at the thermal stability of the primary mirror during and after an on-orbit slew maneuver and the resulting change in SFE with time.

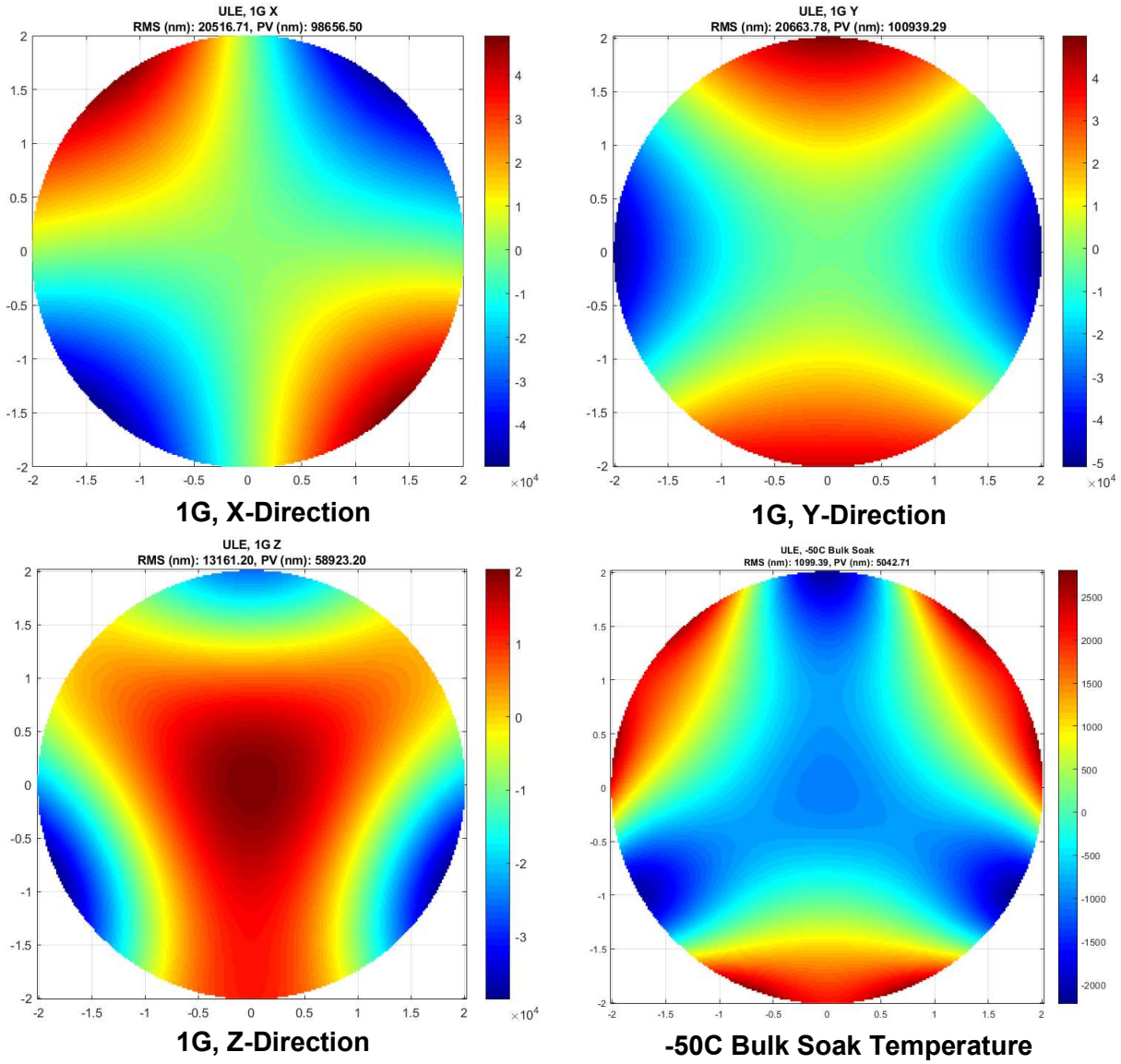

Figure 5.2-15: Surface Figure Error Maps, ULE Primary Mirror.

Table 5.2-4. ULE Mirror SFE Analysis Summary

Load Case	RMS	PV	Dominant Contributor	Contribution
	(nm)			
1G, X Direction	20517	98657	Primary Astigmatism	20457
1G, Y Direction	20663	100939	Primary Astigmatism	20560
1G, Z Direction	13161	58923	Coma	9744
-50C Bulk Soak	1099	5042	Trefoil	896

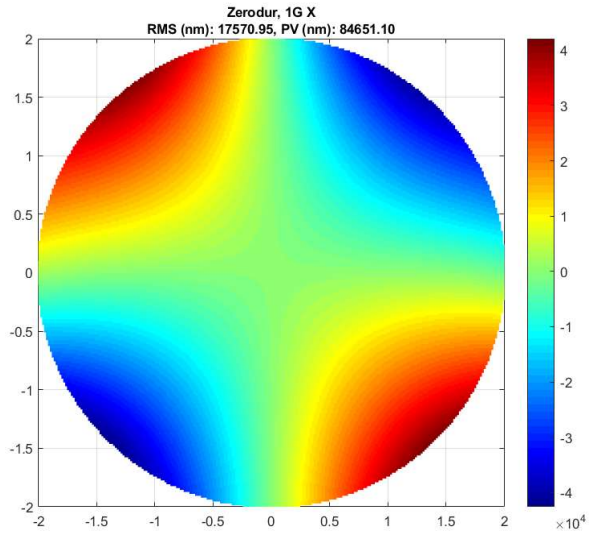

1G, X-Direction

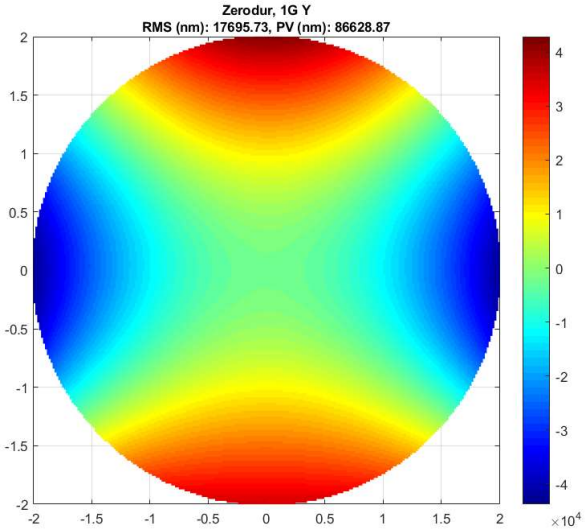

1G, Y-Direction

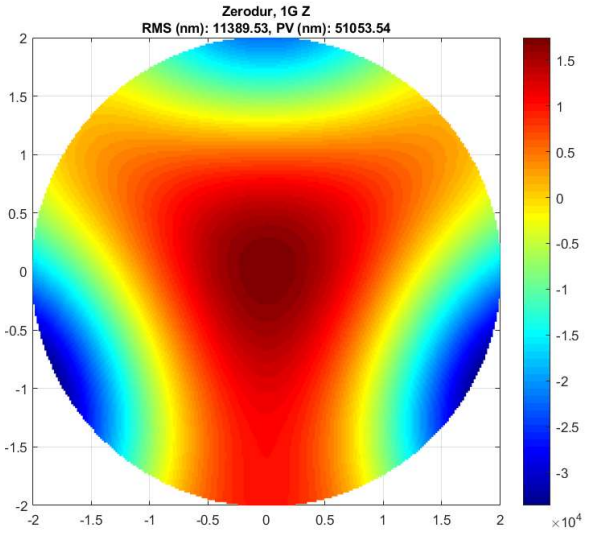

1G, Z-Direction

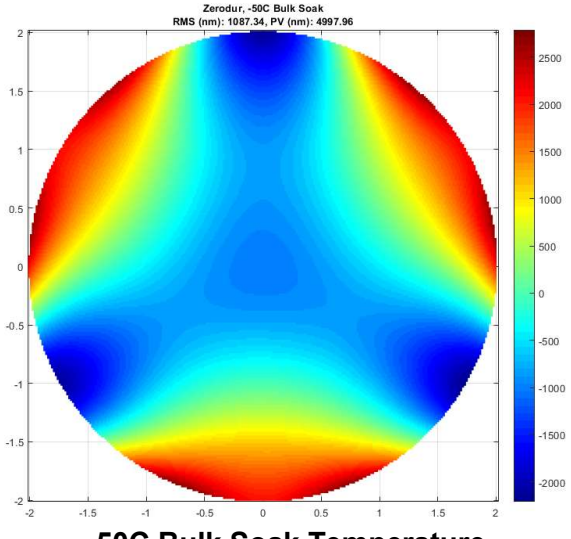

-50C Bulk Soak Temperature

Figure 5.2-16: Surface Figure Error Maps, Zerodur Primary Mirror

Table 5.2-5. Zerodur Mirror SFE Analysis Summary

Load Case	RMS	PV	Dominant Contributor	Contribution
	(nm)			

1G, X Direction	17571	84651	Primary Astigmatism	17520
1G, Y Direction	17696	86629	Primary Astigmatism	17606
1G, Z Direction	11390	51053	Coma	8371
-50C Bulk Soak	1087	4998	Trefoil	885

The SFE results listed in the tables are in substantial agreement with those listed in Reference 14. For ground testing, the results reported in this section assume the mirror is mounted in its support truss.

With that caveat, the results show that direct verification of the on-orbit performance of the mirror and system will be difficult during ground testing: the thermal “signal” will be lost in the gravity “signal”. For direct verification, the gravity contribution must first be well and precisely characterized, and subsequently subtracted from a thermal vacuum measurement. Further, [7] calls for an uncertainty in this measurement of < ~2 nm (rms). Assuming the SFE values listed in Tables 4 and 5 and allocating all of the uncertainty to the 1G room temperature measurement in a “cup up” configuration (gravity roughly normal the mirror reflective surface) calls for determining the SFE to better than 2 parts in 10000.

A separate, formal system engineering study will likely be required to determine the cost and feasibility of doing a detailed experimental verification of the expected on-orbit performance of the primary mirror. Such a study would allocate the required measurement uncertainty to the resolution of the metrology technique (holograms and interferometry) and repeatability (for rotary or flip testing) for mechanical, structural, thermal, and environmental aspects of this measurement. Extremely stringent limits on the stiffness, deformations, and temperatures of fixturing and ground support equipment that must be designed will likely result. Such testing, though likely expensive and delicate, will be valuable also to anchor on-orbit performance models.

5.2.5 Linear Optical Models

The HabEx FGS system consists of a Three-Mirror Anastigmatic (TMA) telescope with aperture D = 4000mm and a system magnification of 84.0 operating in afocal mode, followed by sectored mirrors that take out 4 separate parts of the field and use identical Cassegrain telescopes with focal length 649 mm to image these sectors on 4 separate sensors. The Primary Mirror is very nearly an off-axis parabola, the Secondary Mirror is a hyperboloid, whereas the Tertiary Mirror is strongly ellipsoidal, see [30].

A layout is shown of the system is shown in Fig 5.2-17.

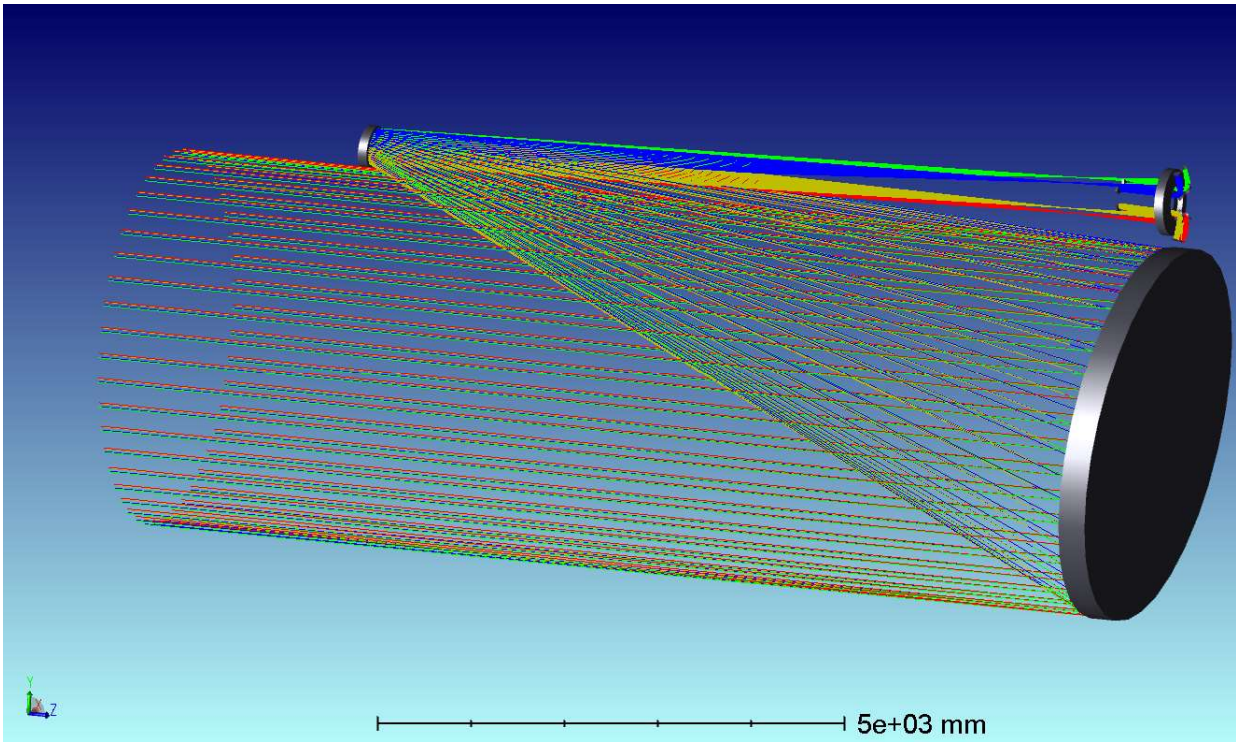

Figure 5.2-17: Layout of HabEx optical system showing the Primary Mirror, Secondary Mirror, and Tertiary Mirror with the four field sectors and associated sensors..

A close-up of the sensor channels is shown in Figure 5.2-18.

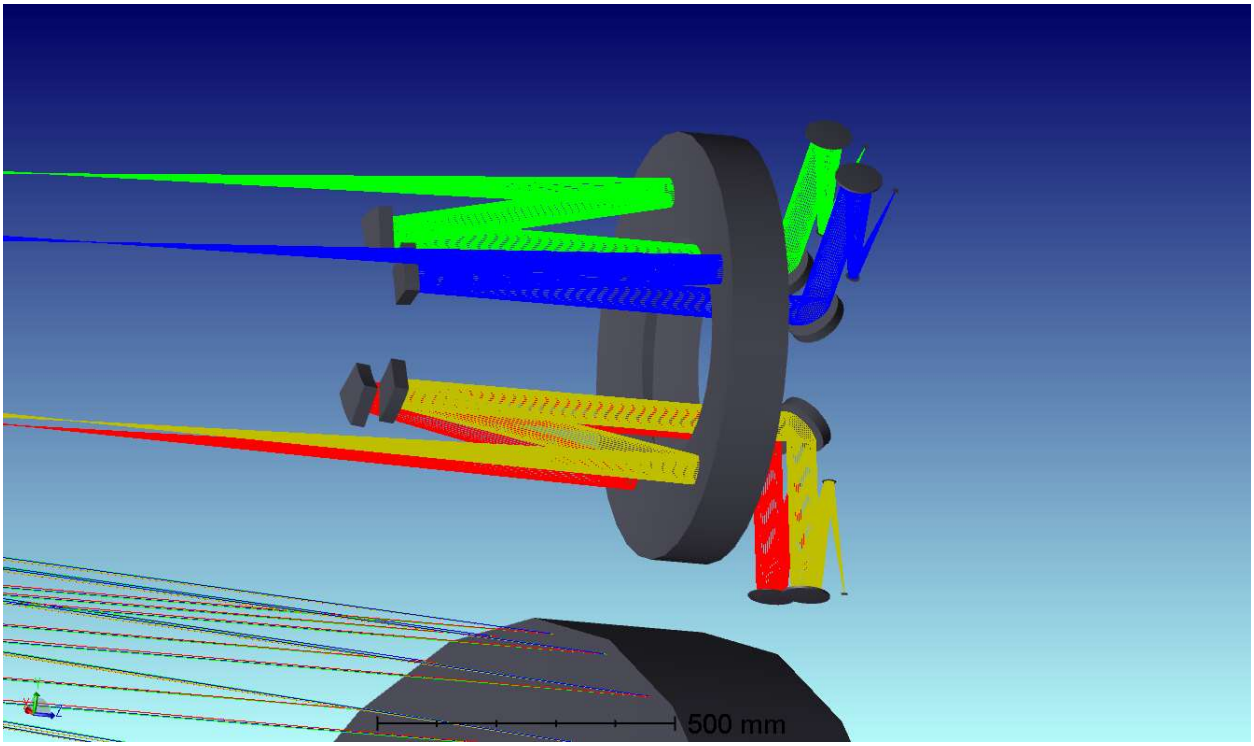

Figure 5.2-18: The four HabEx FGS channels capturing collimated beams reflected off the TM.

Linear sensitivities in the Line-of-sight (LOS) for each optical element in 6 degrees of freedom (DOF) were calculated using dedicated macros written originally for Lockheed Martin's in-house software Optima for optical design and analysis [14] [15] and subsequently transported to OpticStudio (Zemax) [31]. Each optical subsystem was perturbed in 6 DOF (3 in position, and 3 in orientation) described in a common global coordinate system targeted at the mechanical center of each optical subsystem. Changes were recorded in both image space at the FPAs as well as in object space. The results in the form of linear sensitivities (changes in LOS parameters divided by changes in the perturbed DOF) are shown in Table 5.2-6. The Table provides sensitivities in positions X, Y, and angles Xang, Yang in image space at the FPA for each module, as well as in angles Xang, Yang in object space with respect to the DOF (dX, dY, dZ) in position and (dA, dB, dC) in orientation for each optical subsystem. Sensitivities are given for the module from the TM through to the FPAs as well as for each component in this module.

Table 5.2-6: Line-of-sight sensitivities for HabEx FGS optical system.

Lens file: HABEX_1.FGS_FGS1.zmx

Line-Of-Sight Sensitivities
At primary wavelength No. 1, 400.000 nm
At field angles (0.0000, 0.0000)

Elt. srfs.	5	5 M1		FGS1					FGS2						FGS3						FGS4					
			X	Y	Xang	Yang	Xang	Yang	X	Y	Xang	Yang	Xang	Yang	X	Y	Xang	Yang	Xang	Yang	X	Y	Xang	Yang	Xang	Yang
1	1	dX	-4.752	-3.185	9.761	8.665	-0.099	0.000	-4.353	-2.760	10.933	5.244	-0.099	0.000	-4.349	2.761	10.966	-5.349	-0.099	0.000	-4.748	3.183	9.860	-8.625	-0.099	0.000
1	2	dY	3.237	-4.378	-6.646	11.675	0.000	-0.096	3.265	-4.077	-8.453	8.463	0.000	-0.096	-3.254	-4.049	8.474	8.327	0.000	-0.096	-3.197	-4.373	6.423	11.738	0.000	-0.096
1	3	dZ	0.830	-1.124	-1.704	2.996	0.000	-0.025	0.838	-1.046	-2.169	2.170	0.000	-0.025	-0.835	-1.039	2.175	2.138	0.000	-0.024	-0.820	-1.122	1.649	3.012	0.000	-0.025
1	4	dA	67.958	-91.701	-141.963	245.596	0.000	-2.015	68.281	-85.729	-178.124	181.241	0.000	-2.015	-68.083	-84.259	175.784	169.989	0.000	-2.015	-66.577	-91.377	131.316	243.862	0.000	-2.015
1	5	dB	95.088	63.537	-198.900	-173.230	1.984	0.000	86.404	54.588	-216.316	-101.532	1.984	0.000	86.331	-54.615	-216.992	103.680	1.985	0.000	94.965	-63.496	-200.788	172.438	1.985	0.000
1	6	dC	11.885	7.962	-24.474	-21.672	0.249	0.000	10.874	6.893	-27.302	-13.057	0.248	0.000	10.865	-6.894	-27.385	13.320	0.249	0.000	11.873	-7.956	-24.719	21.569	0.249	0.000

Elt. srfs.	6	6 M2		FGS1					FGS2						FGS3						FGS4					
			X	Y	Xang	Yang	Xang	Yang	X	Y	Xang	Yang	Xang	Yang	X	Y	Xang	Yang	Xang	Yang	X	Y	Xang	Yang	Xang	Yang
2	1	dX	4.226	2.833	-8.679	-7.707	0.088	0.000	3.871	2.454	-9.721	-4.656	0.088	0.000	3.868	-2.455	-9.750	4.750	0.088	0.000	4.222	-2.831	-8.766	7.671	0.088	0.000
2	2	dY	-2.867	3.879	5.879	-10.338	0.000	0.085	-2.892	3.610	7.483	-7.484	0.000	0.085	2.882	3.587	-7.505	-7.372	0.000	0.085	2.831	3.874	-5.687	-10.397	0.000	0.085
2	3	dZ	-0.841	1.137	1.725	-3.032	0.000	0.025	-0.848	1.059	2.195	-2.196	0.000	0.026	0.845	1.052	-2.201	-2.164	0.000	0.025	0.830	1.136	-1.670	-3.049	0.000	0.025
2	4	dA	-5.950	8.052	12.186	-21.456	0.000	0.177	-6.005	7.493	15.530	-15.513	0.000	0.176	5.984	7.450	-15.591	-15.336	0.000	0.178	5.881	8.045	-11.830	-21.597	0.000	0.178
2	5	dB	-8.332	-5.585	17.079	15.192	-0.174	0.000	-7.638	-4.844	19.184	9.209	-0.174	0.000	-7.631	4.845	19.240	-9.393	-0.175	0.000	-8.323	5.582	17.248	-15.123	-0.175	0.000
2	6	dC	-0.930	-0.623	1.908	1.696	-0.019	0.000	-0.852	-0.540	2.139	1.025	-0.019	0.000	-0.851	0.540	2.145	-1.046	-0.019	0.000	-0.929	0.623	1.928	-1.687	-0.019	0.000

Elt. srfs.	7	19 M3 Image		FGS1					FGS2						FGS3						FGS4					
			X	Y	Xang	Yang	Xang	Yang	X	Y	Xang	Yang	Xang	Yang	X	Y	Xang	Yang	Xang	Yang	X	Y	Xang	Yang	Xang	Yang
3	1	dX	0.526	0.352	-1.088	-0.959	0.011	0.000	0.481	0.305	-1.210	-0.585	0.011	0.000	0.481	-0.306	-1.214	0.596	0.011	0.000	0.526	-0.352	-1.099	0.955	0.011	0.000
3	2	dY	-0.370	0.500	0.765	-1.335	0.000	0.011	-0.373	0.466	0.968	-0.975	0.000	0.011	0.371	0.463	-0.970	-0.960	0.000	0.011	0.366	0.499	-0.740	-1.343	0.000	0.011
3	3	dZ	0.010	-0.014	-0.020	0.036	0.000	0.000	0.010	-0.013	-0.026	0.026	0.000	-0.001	-0.010	-0.013	0.027	0.026	0.000	0.000	-0.010	-0.014	0.020	0.037	0.000	0.000
3	4	dA	-0.496	0.661	1.073	-1.793	0.000	0.015	-0.495	0.622	1.311	-1.375	0.000	0.015	0.493	0.618	-1.315	-1.356	0.000	0.015	0.490	0.661	-1.040	-1.803	0.000	0.015
3	5	dB	-0.704	-0.465	1.515	1.278	-0.015	0.000	-0.635	-0.407	1.614	0.818	-0.015	0.000	-0.635	0.407	1.619	-0.834	-0.015	0.000	-0.703	0.465	1.529	-1.273	-0.015	0.000
3	6	dC	-0.002	-0.001	0.003	0.000	-0.002	-0.002	-0.002	-0.001	0.001	0.001	-0.002	0.001	-0.002	0.001	0.004	-0.002	0.002	0.001	-0.002	0.001	0.003	-0.003	0.002	-0.002

Elt. srfs.	7	7 M3		FGS1					FGS2						FGS3						FGS4					
			X	Y	Xang	Yang	Xang	Yang	X	Y	Xang	Yang	Xang	Yang	X	Y	Xang	Yang	Xang	Yang	X	Y	Xang	Yang	Xang	Yang
4	1	dX	0.526	0.352	-1.088	-0.959	0.011	0.000	0.481	0.305	-1.210	-0.585	0.011	0.000	0.481	-0.306	-1.214	0.596	0.011	0.000	0.526	-0.352	-1.099	0.955	0.011	0.000
4	2	dY	-0.370	0.500	0.765	-1.335	0.000	0.011	-0.373	0.466	0.968	-0.975	0.000	0.011	0.371	0.463	-0.970	-0.960	0.000	0.011	0.366	0.499	-0.740	-1.343	0.000	0.011
4	3	dZ	0.010	-0.014	-0.020	0.036	0.000	0.000	0.010	-0.013	-0.026	0.026	0.000	-0.001	-0.010	-0.013	0.027	0.026	0.000	0.000	-0.010	-0.014	0.020	0.037	0.000	0.000
4	4	dA	-0.810	1.087	1.720	-2.939	0.000	0.024	-0.812	1.019	2.143	-2.210	0.000	0.024	0.809	1.012	-2.139	-2.187	0.000	0.024	0.803	1.085	-1.687	-2.942	0.000	0.024
4	5	dB	-1.153	-0.764	2.455	2.092	-0.024	0.000	-1.044	-0.667	2.647	1.327	-0.024	0.000	-1.043	0.666	2.648	-1.338	-0.024	0.000	-1.150	0.764	2.462	-2.087	-0.024	0.000
4	6	dC	0.016	0.011	-0.034	-0.030	0.000	0.000	0.015	0.010	-0.038	-0.018	0.000	0.000	0.015	-0.010	-0.038	0.019	0.000	0.000	0.016	-0.011	-0.034	0.030	0.000	0.000

Elt. srfs.	9	9 Sector		FGS1					FGS2						FGS3						FGS4					
			X	Y	Xang	Yang	Xang	Yang	X	Y	Xang	Yang	Xang	Yang	X	Y	Xang	Yang	Xang	Yang	X	Y	Xang	Yang	Xang	Yang
5	1	dX	0.000	0.000	0.000	0.000	0.000	0.000	0.000	0.000	0.000	0.000	0.000	0.000	0.000	0.000	0.000	0.000	0.000	0.000	0.000	0.000	0.000	0.000	0.000	0.000
5	2	dY	0.000	0.000	0.000	0.000	0.000	0.000	0.000	0.000	0.000	0.000	0.000	0.000	0.000	0.000	0.000	0.000	0.000	0.000	0.000	0.000	0.000	0.000	0.000	0.000
5	3	dZ	0.000	0.000	0.000	0.000	0.000	0.000	0.000	0.000	0.000	0.000	0.000	0.000	0.000	0.000	0.000	0.000	0.000	0.000	0.000	0.000	0.000	0.000	0.000	0.000
5	4	dA	0.803	-1.073	-1.657	2.886	0.000	-0.024	0.803	-1.013	-2.102	2.130	0.000	-0.024	-0.800	-1.007	2.087	2.113	0.000	-0.024	-0.798	-1.071	1.644	2.874	0.000	-0.024
5	5	dB	1.145	0.753	-2.393	-2.051	0.024	0.000	1.030	0.662	-2.600	-1.290	0.024	0.000	1.029	-0.660	-2.594	1.286	0.024	0.000	1.140	-0.753	-2.384	2.051	0.024	0.000
5	6	dC	-0.013	-0.143	0.029	0.386	-0.002	-0.002	-0.139	-0.019	0.355	0.030	-0.002	0.001	0.139	-0.019	-0.354	0.030	0.002	0.001	0.013	-0.143	-0.030	0.385	0.002	-0.002

Elt. srfs.	13	13 Selector		FGS1					FGS2						FGS3						FGS4					
			X	Y	Xang	Yang	Xang	Yang	X	Y	Xang	Yang	Xang	Yang	X	Y	Xang	Yang	Xang	Yang	X	Y	Xang	Yang	Xang	Yang
6	1	dX	0.142	-0.029	-1.187	0.465	0.000	0.000	0.056	-0.067	-0.935	0.700	0.000	0.000	0.055	0.066	-0.933	-0.699	0.000	0.000	0.141	0.028	-1.187	-0.464	0.000	0.000
6	2	dY	-0.247	0.050	2.057	-0.806	0.000	0.000	-0.097	0.116	1.620	-1.212	0.000	0.000	0.095	0.114	-1.616	-1.210	0.000	0.000	0.244	0.049	-2.056	-0.803	0.000	0.000
6	3	dZ	0.285	-0.058	-2.375	0.931	0.000	0.000	0.112	-0.134	-1.870	1.399	0.000	0.000	0.110	0.131	-1.866	-1.397	0.000	0.000	0.282	0.057	-2.374	-0.927	0.000	0.000
6	4	dA	-0.958	0.696	1.986	-1.863	-0.005	0.021	-0.987	0.735	2.562	-1.575	-0.005	0.021	0.983	0.729	-2.527	-1.545	0.005	0.021	0.951	0.694	-1.954	-1.849	0.005	0.021
6	5	dB	-0.878	-0.111	1.828	0.309	-0.015	0.005	-0.687	-0.177	1.745	0.315	-0.015	0.005	-0.685	0.178	1.733	-0.326	-0.015	-0.005	-0.872	0.112	1.810	-0.320	-0.015	-0.005
6	6	dC	-0.281	-0.444	0.590	1.200	-0.010	-0.006	-0.101	-0.521	0.230	1.061	-0.011	-0.006	0.102	-0.518	-0.237	1.055	0.011	-0.006	0.280	-0.444	-0.591	1.201	0.010	-0.006

Elt. srfs.	16	16 FGS Primary		FGS1					FGS2						FGS3						FGS4					
			X	Y	Xang	Yang	Xang	Yang	X	Y	Xang	Yang	Xang	Yang	X	Y	Xang	Yang	Xang	Yang	X	Y	Xang	Yang	Xang	Yang
7	1	dX	1.211	1.843	-2.991	-6.386	0.035	0.015	0.873	1.707	-2.648	-5.000	0.035	0.016	0.871	-1.703	-2.644	4.992	0.035	-0.016	1.199	-1.846	-2.970	6.391	0.035	-0.015
7	2	dY	0.136	1.061	-0.920	-3.627	0.011	0.015	-0.055	0.968	-0.178	-2.461	0.011	0.015	0.046	0.947	0.204	-2.414	-0.011	0.015	-0.148	1.054	0.950	-3.606	-0.011	0.015
7	3	dZ	-2.447	0.999	6.641	-3.433	-0.020	0.035	-2.179	1.022	7.173	-3.028	-0.020	0.035	-2.173	-1.012	7.149	3.002	-0.020	-0.035	-2.433	-0.994	6.615	3.413	-0.020	-0.035
7	4	dA	1.242	-0.573	-3.339	1.967	0.010	-0.019	1.132	-0.577	-3.706	1.689	0.010	-0.019	-1.130	-0.584	3.692	1.705	-0.010	-0.019	-1.234	-0.579	3.318	1.987	-0.010	-0.019
7	5	dB	0.715	-0.155	-1.924	0.530	0.007	-0.009	0.632	-0.172	-2.068	0.515	0.007	-0.009	0.641	0.150	-2.095	-0.449	0.008	0.008	0.722	0.138	-1.942	-0.470	0.008	0.008
7	6	dC	0.654	1.221	-1.770	-4.218	0.021	0.012	0.453	1.158	-1.468	-3.291	0.021	0.012	-0.454	1.153	1.474	-3.281	-0.021	0.012	-0.652	1.222	1.769	-4.218	-0.021	0.012

Elt. srfs.	17	17 FGS Secondary		FGS1					FGS2						FGS3						FGS4					
			X	Y	Xang	Yang	Xang	Yang	X	Y	Xang	Yang	Xang	Yang	X	Y	Xang	Yang	Xang	Yang	X	Y	Xang	Yang	Xang	Yang
8	1	dX	-1.050	-0.960	2.494	4.823	-0.021	-0.007	-0.604	-0.608	2.151	3.168	-0.021	-0.007	-0.601	0.609	2.146	-3.161	-0.021	0.007	-1.036	0.964	2.473	-4.830	-0.021	0.007
8	2	dY	0.620	-0.596	0.099	2.781	-0.002	-0.011	0.440	-0.791	-0.234	1.930	-0.002	-0.011	-0.430	-0.766	0.208	1.883	0.002	-0.011	-0.602	-0.588	-0.130	2.761	0.002	-0.011
8	3	dZ	1.312	-0.523	-4.729	2.552	0.011	-0.019	1.173	-0.503	-5.411	2.085	0.011	-0.019	1.168	0.495	-5.390	-2.060	0.011	0.019	1.301	0.519	-4.704	-2.534	0.011	0.019
8	4	dA	-0.465	0.175	1.650	-0.853	-0.003	0.006	-0.383	0.202	1.735	-0.819	-0.003	0.006	0.388	0.210	-1.738	-0.839	0.003	0.006	0.468	0.179	-1.648	-0.874	0.003	0.006
8	5	dB	-0.268	0.072	0.951	-0.351	-0.002	0.003	-0.215	0.094	0.983	-0.383	-0.002	0.003	-0.222	-0.086	1.008	0.344	-0.002	-0.003	-0.276	-0.064	0.973	0.309	-0.002	-0.003
8	6	dC	-0.237	-0.386	0.854	1.905	-0.006	-0.004	-0.124	-0.438	0.686	1.804	-0.006	-0.004	0.125	-0.437	-0.690	1.806	0.006	-0.004	0.236	-0.387	-0.854	1.908	0.006	-0.004

Elt. srfs.	19	19 Image		FGS1					FGS2						FGS3						FGS4					
			X	Y	Xang	Yang	Xang	Yang	X	Y	Xang	Yang	Xang	Yang	X	Y	Xang	Yang	Xang	Yang	X	Y	Xang	Yang	Xang	Yang
9	1	dX	-0.106	-0.802	0.000	0.000	-0.013	-0.009	-0.273	-0.964	0.000	0.000	-0.013	-0.009	-0.274	0.961	0.000	0.000	-0.013	0.009	-0.109	0.801	0.000	0.000	-0.013	0.009
9	2	dY	-0.660	-0.423	0.000	0.000	-0.009	-0.004	-0.373	-0.141	0.000	0.000	-0.009	-0.004	0.372	-0.146	0.000	0.000	0.009	-0.004	0.656	-0.425	0.000	0.000	0.009	-0.004
9	3	dZ	0.905	-0.423	0.000	0.000	0.009	-0.016	0.906	-0.422	0.000	0.000	0.009	-0.016	0.906	0.422	0.000	0.000	0.009	0.016	0.905	0.423	0.000	0.000	0.009	0.016
9	4	dA	0.070	0.071	-0.804	0.121	0.000	0.000	0.082	-0.012	-0.983	0.330	0.000	0.000	-0.085	-0.010	0.980	0.330	0.000	0.000	-0.074	0.074	0.803	0.122	0.000	0.000
9	5	dB	0.026	-0.133	-0.432	0.669	0.000	0.000	-0.110	-0.039	-0.166	0.382	0.000	0.000	-0.113	0.050	-0.170	-0.380	0.000	0.000	0.024	0.139	-0.433	-0.664	0.000	0.000
9	6	dC	0.027	-0.002	-0.410	-0.899	0.000	0.000	-0.021	0.041	-0.364	-0.881	0.000	0.000	0.021	0.039	0.365	-0.882	0.000	0.000	-0.027	-0.002	0.410	-0.899	0.000	0.000

Units for the output sensitivities:
Sensitivity in boresight
X, Y (img.spc.) Xang, Yang (img. + obj.spc.)
w.r.t
pos (X,Y,Z) LU/LU = um/um uRad/um

ang (A,B,C) um/uRad uRad/uRad

6 Telescope LOS and Wavefront Error Dynamic Stability Analysis

6.1 LUVOIR Steady-State Frequency-Domain Performance

Steady-state LOS and WFE stability was estimated for both the Baseline and FSM-less LOS control loops, applied to the twelve structural-dynamics model configurations that are enumerated below, resulting in 24 total integrated models.

1. 0° Payload Pitch, maximum SC-PL interface cable stiffness
2. 0° Payload Pitch, minimum SC-PL interface cable stiffness

3. 30° Payload Pitch, maximum SC-PL interface cable stiffness
4. 30° Payload Pitch, minimum SC-PL interface cable stiffness
5. 45° Payload Pitch, maximum SC-PL interface cable stiffness
6. 45° Payload Pitch, minimum SC-PL interface cable stiffness
7. 60° Payload Pitch, maximum SC-PL interface cable stiffness
8. 60° Payload Pitch, minimum SC-PL interface cable stiffness
9. 75° Payload Pitch, maximum SC-PL interface cable stiffness
10. 75° Payload Pitch, minimum SC-PL interface cable stiffness
11. 90° Payload Pitch, maximum SC-PL interface cable stiffness
12. 90° Payload Pitch, minimum SC-PL interface cable stiffness

The telescope pitch cases above refer to the fixed-orientation of the two-axis gimbal in the structural dynamics model, which is described in Section 5.1. Bounding parameters and rationale for SC-PL interface cable stiffness are provided in section 5.1.4.6. Dynamic WFE and LOS stability results presented in this section were computed over a frequency range of 0.1-200Hz (corresponding to a 400Hz sample rate), which was chosen to balance processing time with model fidelity; disturbances are modeled as being “steady-state”, or at least fixed over the 10-minute wavefront control period for which stability is required and assessed.

The following disturbance spectra from Section 5.1.4 were played through each of the 24 model configurations described above: CMG-induced vibration; VIPPS NCA actuator and inductive sensor noise; HDI-FGS centroid noise; and FSM pointing jitter due to sensor noise. With all relevant control loops active, the resulting 6DOF response spectra of the 124 optical nodes were captured and run through the ISLOM, described in Section 5.1.3. Recall that all steady-state performance results were generated using the ISLOM that was provided by the LUVOIR STDT, as indicated in Section 5.1.3. OPD Images were then collected, 1 cycle/segment spatial-frequency filtering was applied, and a spatial RMS was computed for each image. This process produced a temporal frequency-domain PSD of the spatial-RMS of wavefront error, which is this the core metric that is subsequently plotted, trended, and analyzed below.

Since the PSD is the derivative a signal’s[7] variance with respect to frequency, the area under the PSD curve is the equal to the total variance of that signal, and the square root of total variance is the total RMS. In evaluating the area under the PSD, it is often convenient to plot and analyze the cumulative sum from low frequency to high frequency, or vice-versa. This metric is referred to as a forward or reverse cumulative-RMS, depending on direction, and it sheds light on both the frequency profile and total power of a signal, at the same time. For LUVOIR, much of the disturbance content and structural amplification occurs at frequencies below 10-20Hz, as will be shown in subsequent plots. As such, the cumulative-RMS in the *reverse* direction is plotted and discussed below. Similarly, this analysis makes use of the frequency-binned RMS metric, another illustrative representation of the wavefront error spectrum. In this application, frequency-binned RMS was computed by integrating the spatial-RMS PSD within seven discrete bins in temporal frequency domain, with fixed edges at: 0.1, 29, 57, 86, 114, 143, 171, and 200Hz.

This section has only dealt with details of the wavefront stability calculation, up to this point. The process for extracting line-of-sight stability was similar, though much simpler. Note that in addition to the 124 sets of 6-DOF response spectra for the optical nodes, the 2-DOF line-of-sight error spectra were also collected for the disturbance sources and configurations enumerated above. These were already parameterized as PSDs of line-of-sight error as a natural consequence of the mechanization of this frequency-domain analysis. The magnitude of the 2-DOF LOS error was computed by summing the PSDs of the two axes, and then total, reverse cumulative, and frequency-binned RMS metrics were computed per the methods outlined above.

[7] This assumes a stationary signal, which is consistent with the modeling assumptions discussed in section 5.1.4 above.

Steady-state line-of-sight performance of the baseline primary-mission LOS control system is estimated to be on the order of 0.3-0.35 milli-arcsec total RMS; with a dynamic WFE of 5.1 picometers total RMS. These errors are broken down by source, temporal frequency, and spatial frequency content in the figures below. In all subsequent plots, 0.3 milli-arcsec and 10 pico-meters were used as example requirements for LOS and wavefront stability, respectively. These thresholds were included in order to assess overall closure of the pointing and isolation design; the exact requirements for LUVOIR generally include more than just these two top-level performance metrics (see Section 4).

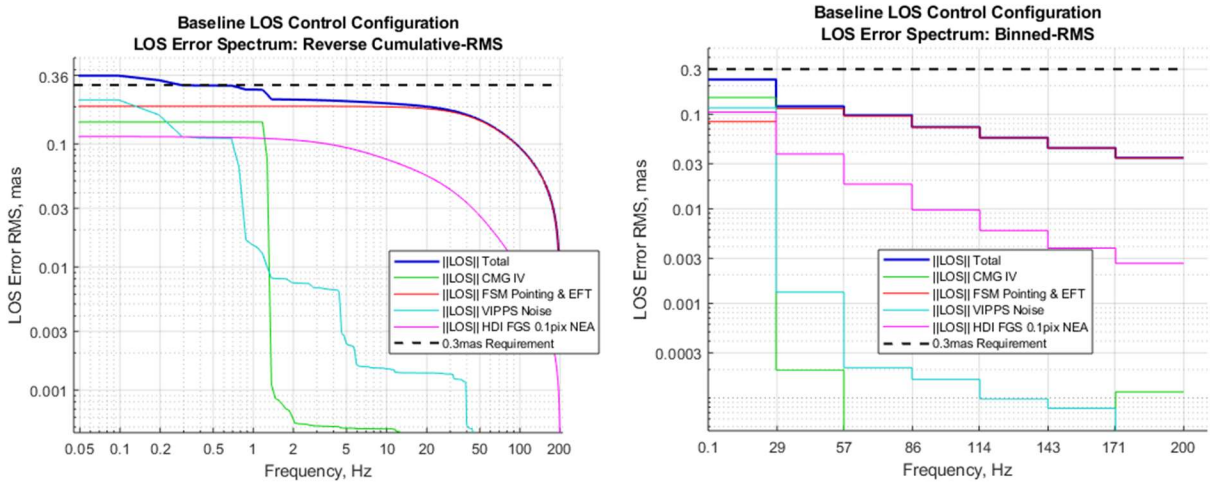

Figure 6.1-1: LOS error spectrum for baseline control system.

In Figure 6.1-2, the wavefront error is broken down by high and low spatial frequency (using 1 cycle per segment as the cut-off), and an additional "FSM-contribution" metric has been introduced. This is explained in the paragraph below.

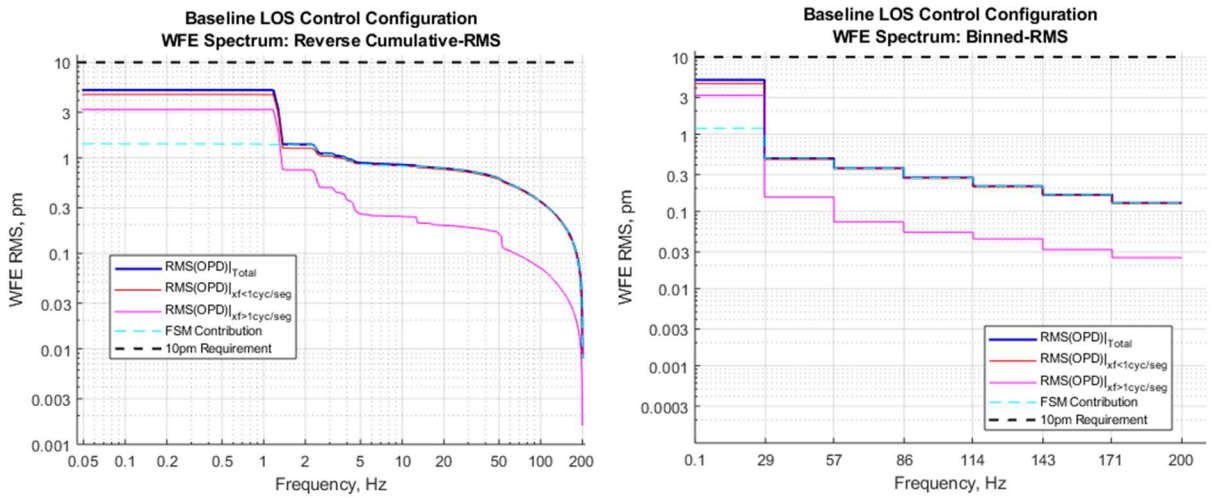

Figure 6.1-2: Wavefront error spectrum for baseline control system, spatial-frequency detail

An extra branch was added to the error processing logic defined at the beginning of this section, where wavefront error was also computed without accounting for the articulating FSM, i.e. 6-DOF response spectra of the FSM-mount was substituted in for the response of the servo-controlled mirror, in order to isolate the contribution of the FSM to overall wavefront error. In

particular, this FSM-contribution was computed by subtracting the original wavefront error spectrum the spectrum corresponding to the FSM-mount, then the result was processed in a similar manner as was described above. This side-study on the FSM's contribution to overall wavefront error produced the finding that the mirror is the dominant source of error above 5Hz, which is also supported by the disturbance-wise breakdown shown in Figure 6.1-3.

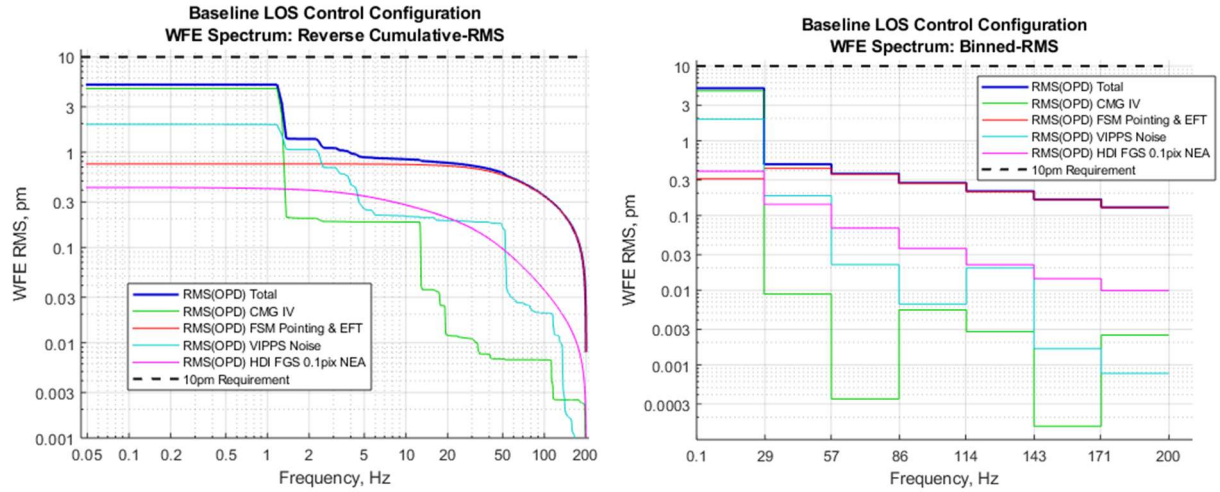

Figure 6.1-3: Wavefront error spectrum for baseline control system, error-source detail

Steady-state line-of-sight performance of the alternate "FSM-less" LOS control system was slightly better than the baseline configuration, at 0.2 milli-arcsec total RMS; and dynamic WFE was essentially unchanged from the baseline configuration, again 5.1 picometers total RMS. These errors were characterized by source, temporal frequency, and spatial frequency in the figures below.

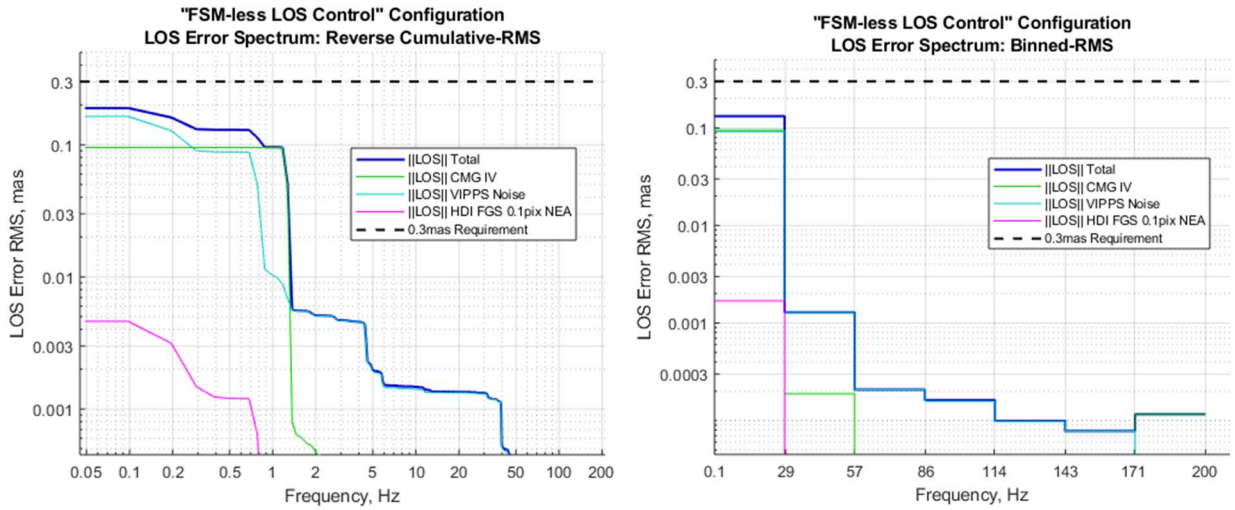

Figure 6.1-4: LOS error spectrum for baseline control system.

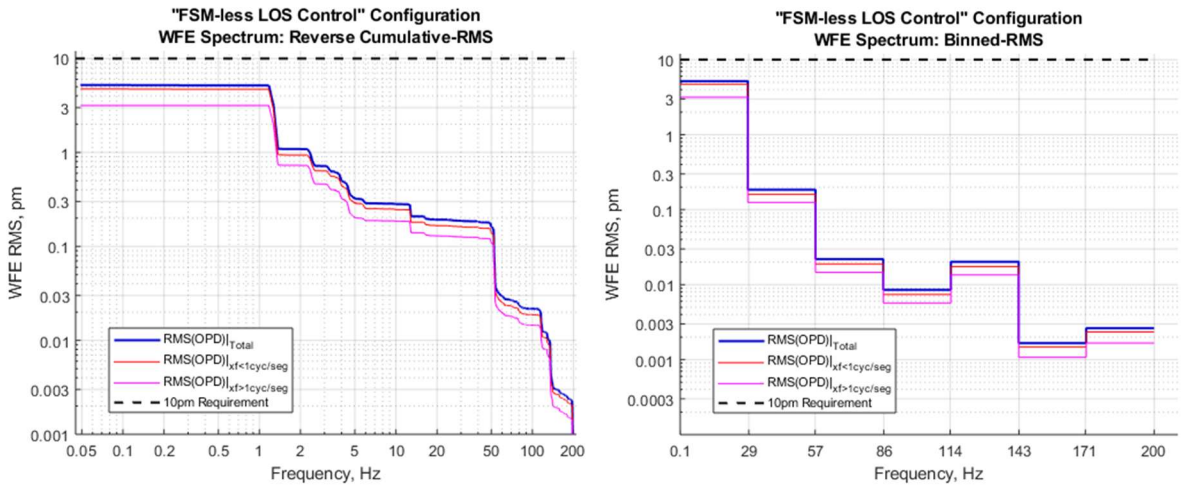

Figure 6.1-5: Wavefront error spectrum for FSM-less control, spatial-frequency detail

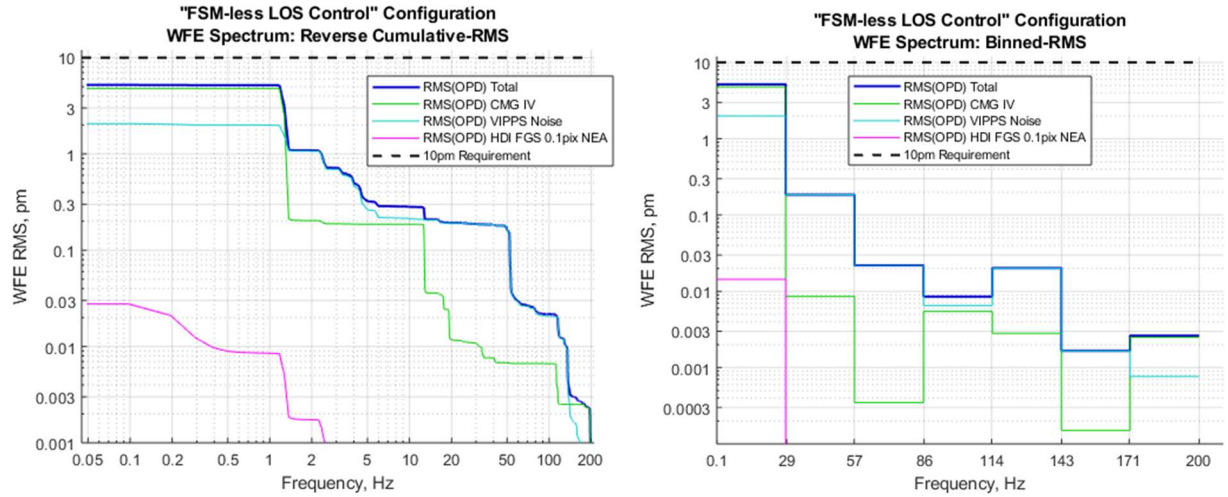

Figure 6.1-6: Wavefront error spectrum for FSM-less control, error-source detail.

The structural dynamics configuration that produced the highest WFE and LOS error was the 60-degree pitch case with maximum Spacecraft-Payload interface cable stiffness, largely due to increased transmissibility of CMG disturbances, seen in all above figures at a frequency just above 1Hz. This was the worst case for transmission of CMG IV and VIPPS noise to wavefront, under either control system configuration. The 45-degree, maximum stiffness model ended up being the worst case for VIPPS noise transmission to LOS. As expected, all minimum cable stiffness configurations tended to transmit less disturbance, yielding smaller wavefront and LOS errors.

While FSM errors dominate the high (temporal) frequency portion of the wavefront error spectrum for the baseline control system, the CMG and VIPPS disturbances dominate at low frequency. Also, more of the HDI-FGS centroid errors were transmitted through to the LOS and wavefront in the baseline configuration, since the FSM enables higher-bandwidth LOS control[8]. HDI-FGS centroid errors were essentially negligible in the alternate FSM-less configuration.

To recap, this study included a key trade involving two control system architectures: the Baseline LOS control, which includes a FSM; and an alternate “FSM-less LOS control” mode

[8] Hence, higher noise transmission

which uses the VIPPS as its primary actuator. The following conclusion was drawn from the findings in the above paragraph: removing the FSM not only simplifies LUVOIR LOS control architecture; it also improves pointing and wavefront stability by eliminating a significant disturbance source.

6.2 LUVOIR Transient Time-Domain Performance

A time-domain integrated model was developed to analyze transient performance of the observatory; specifically, to determine how long it takes for the observatory to settle to acceptable LOS pointing and dynamic WFE performance levels after a repositioning slew maneuver, under disturbances that are modeled in the time domain. The WFE settling time is the time when the WFE reaches and stays below the 10 pm dynamic WFE requirement. For LOS, the settling time is defined as the time when the RSS of LOS in x and y direction reaches and stays below 0.3 mas, which is a conservative definition.

6.2.1 Repositioning Slew Profile

In this study, settling time after a 5 degree roll of the entire observatory about the sun pointing axis (the perpendicular axis to the sunshield) is measured and analyzed. The 5 degree slew angle was chosen since the time-domain integrated model is based on a linearized structural dynamics model, and a small slew angle was required to avoid violating the linear assumption. Additionally, it was assumed that the telescope pitch angle was fixed during repositioning slew. Each slew profile is characterized by 3 parameters: maximum angular rate, acceleration, and jerk. The bounding conditions on the maximum angular rate and acceleration is determined by the momentum envelope of the CMG, non-contact actuator's peak force and peak gap/stroke, as well as LUVOIR's line-of-sight agility requirement (repoint anywhere in anti-sun hemisphere in 45 minutes).

By using a non-linear multi-rigid body tool which was developed under the 2017 Cooperative Agreement Notice between NASA and LM [32] and LM IRAD, and a LM in-house CMG sizing tool, bounding conditions on the maximum angular rate and acceleration were computed such that LUVOIR's line-of-sight agility requirement is met. This analysis showed that, given the current mass properties of LUVOIR-A, the maximum angular rate during slew must stay within [0.36, 0.091] deg/sec, and the maximum acceleration during slew must stay within [3.18×10^{-3},1.06×10^{-4}] deg/sec^2. A sensitivity study is done on the effects of changing the maximum angular acceleration and rate in sections 6.2.4.2 and 6.2.4.1, respectively.

While jerk is not limited by hardware performance, jerk-bounded slew profiles have proven to be important in industrial robotics applications in improving slew tracking [33]. In this study, the roll angle slew profile is defined by a fifth-order polynomial (quintic) which provides a quadratic jerk profile. With quintic slew profiles it is also possible to specify not only endpoint positions, but also endpoint speeds and acceleration which would be useful in designing slew trajectories for tracking a body in the Solar System for future studies. In section 6.2.4.3, observatory settling time is compared between a quintic and a quadratic slew profile with infinite jerk.

6.2.2 Model Fidelity

6.2.2.1 LUVOIR-A Structural Dynamics Model Truncation

All dynamic WFE and LOS transient performance results presented in this section were computed with a structural dynamics model that was truncated at a maximum modal frequency of 45 Hz. This truncation in number of modes was necessary to have a reasonable running time and avoid any memory issues. The cut-off frequency of 45 Hz was determined based on a comparison of the transient performance between a 45 Hz and a 450 Hz plant model. In this comparison slew case, the maximum angular rate, acceleration and jerk were set to the maximum allowable values, the observatory was slewed about the sun pointing axis by 5 degrees, and the

telescope pitch angle was fixed at zero degree. Figure 6.2-1 shows the single-sided amplitude spectrum for the RSS of the LOS in x and y directions, using the 450 Hz plant model, over a window of 10 seconds after the completion of observatory slew and the beginning of settling period. This figure shows that the dominant frequency during settling is 1.3 Hz, which indicates that low frequency modes, as expected, are going to dictate the settling time.

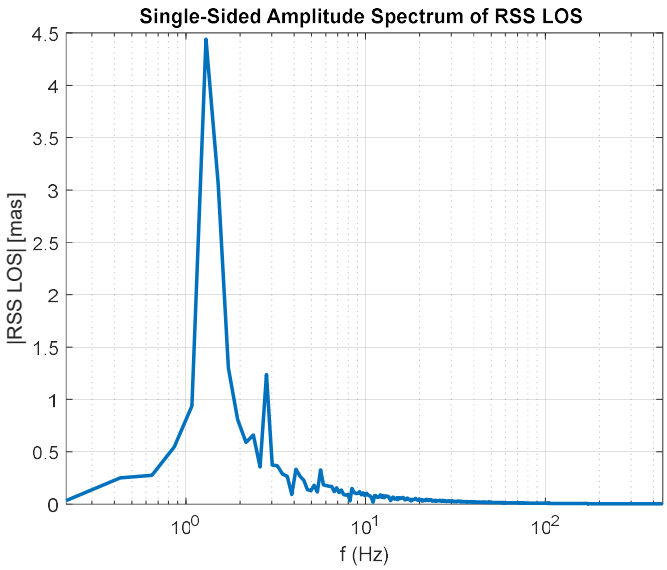

Figure 6.2-1: Single-Sides Amplitude Spectrum for RSS LOS (450 Hz plant model).

To compare the settling performance between the two plant models, the difference between the LOS results, over the same 10 seconds after slew, was computed for the 450 Hz model and the 45 Hz model. Figure 6.2-2 shows the amplitude spectrum for the RSS of the LOS error between the 45 Hz model and the 450 Hz model. Based on this figure, the amplitude difference across all frequencies, especially for frequencies higher than 10 Hz, is relatively insignificant. Additionally, the RMS of the error between the two models, over the first 10 seconds of settling, was computed and is equal to 3.2×10^{-9} masec which further indicates that the errors between the two models are insignificant.

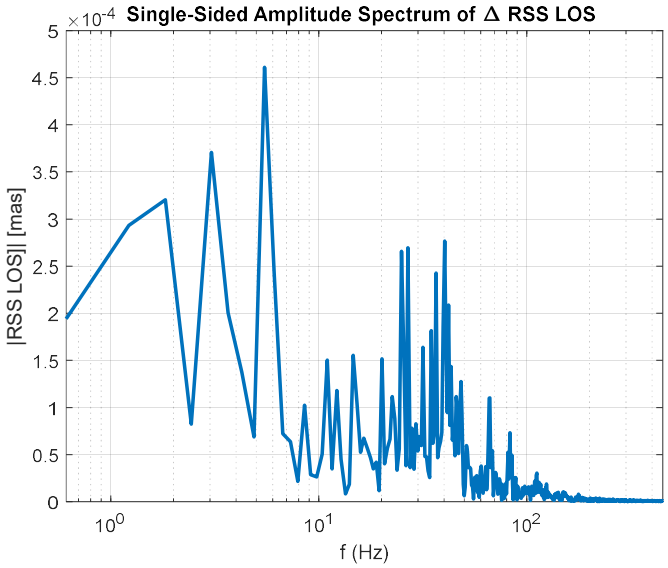

Figure 6.2-2: Single-Sides Amplitude Spectrum for RSS LOS Error between 450 Hz model and 45 Hz model

6.2.2.2 Time-Domain Control Moment Gyro (CMG) Disturbance Model

A conservative model for a CMG is included in the time-domain integrated model. For a given set of torque commands computed by the control law, this CMG model outputs spacecraft disturbance torques that are cause by motor ripple effects, tach ripple effects, and bearing drag. Figure 6.2-3 shows an example of a typical torque step command during a roll axis slew and the CMG output torque in the spacecraft frame. The magnified portion of the plot shows the disturbance torques that are produced by CMG model compared to the torque command.

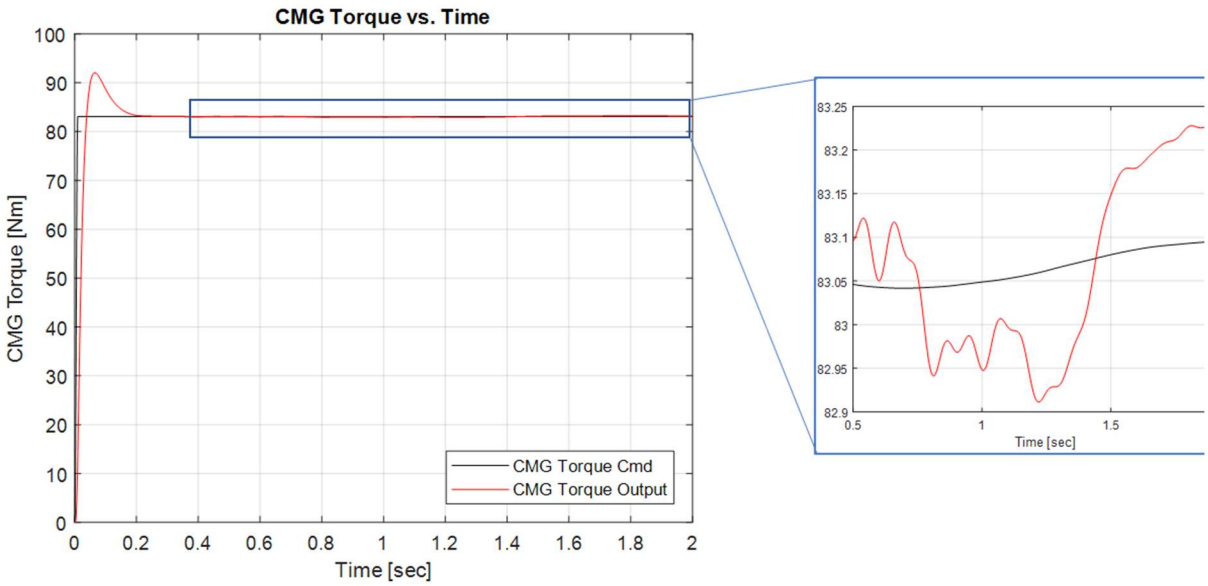

Figure 6.2-3: Time-domain CMG Disturbance Model Torque Output

6.2.3 Control Architecture: Steady-Stade Observation vs Repositioning/Slew

LUVOIR's control system architecture takes maximum advantage of the non-contact VIPPS interface between the optical payload and spacecraft, when the system is both performing a steady-state observation and executing a repositioning/slew maneuver. The steady-state pointing control architecture was previously described in detail in section 5.1.2.

Figure 6.2-4, shows LUVOIR's repositioning slew control architecture that was used in this study. During repositioning slew, the control system cannot have access to the science instruments to derive the payload LOS, therefore, the control system is entirely based on payload star trackers to determined payload inertial attitude. A time-varying attitude slew profile combined with a payload attitude estimate provides inertial payload attitude error which is used as input to the payload attitude control, which then uses the VIPPS non-contact actuators to apply an interface torque. Similar to the steady-state pointing control architecture, the non-contact VIPPS sensors are used as inputs to the relative motion control loops that apply force via VIPPS non-contact actuators and torque via CMGs to ensure that stroke and gap at the interface are maintained. Note that, in Figure 6.2-4, the gimbal servo control loop is not modeled in the slew control law as the telescope pitch angle is assumed to be constant during slew. In section 6.2.4.6, a sensitivity study is done on the impact of the telescope pitch angle on settling time.

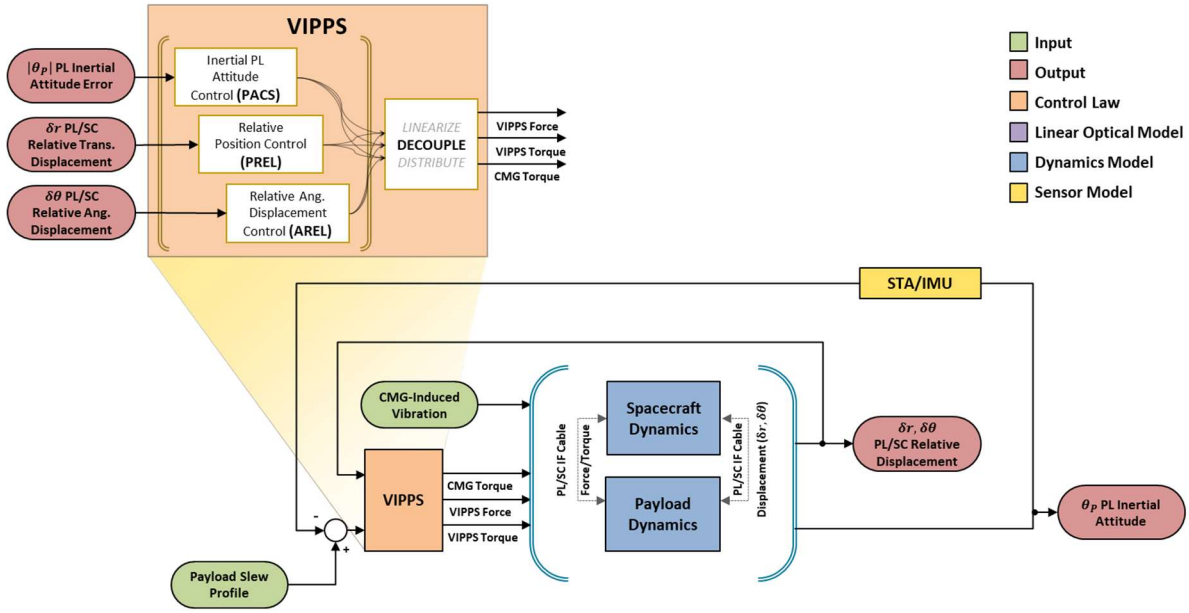

Figure 6.2-4: LUVOIR Repointing and Slewing Control Architecture

Lastly, a "FSM-less LOS control" was introduced in section 5.1 as an alternative to the baseline steady-state pointing control. In section 6.2.4.5, a sensitivity study is done on the effects of the FSM-less control law on the settling time of the observatory. The idea is to determine if a high band-width FSM, once activated after slew, would excite any flexible-body structural dynamics modes that might results in a longer settling compared to the FSM-less control law.

6.2.4 LUVOIR Settling Time Sensitivity Study

In this section, the observatory settling time is studies under the variation of the following parameters: slew profile's maximum angular acceleration, rate, jerk, structural damping, steady-sate pointing control law (FSM vs FSM-less), telescope pitch angle.

6.2.4.1 Impact of Maximum Slew Rate on Settling Time

Figure 6.2-5 shows slew acceleration, rate, and roll-axis angle for the 3 slew cases that were considered in this sensitivity study. In all cases, a quintic slew generator was used with the maximum angular acceleration set to 3.18×10^{-3} deg/sec^2, which is the highest allowable slew acceleration deliverable by the CMGs and VCAs. The maximum angular rate was varied from the highest allowable limit (0.3623 deg/sec - before VCA peak force limit is exceeded) to the lowest allowable limit (0.0906 deg/sec - before LUVOIR's agility requirement is violated).

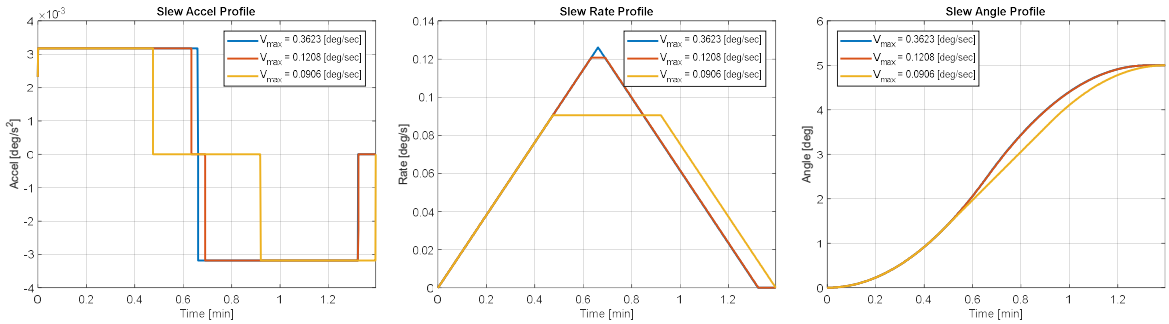

Figure 6.2-5: Slew Profiles for Max Slew Rate Sensitivity Study

Figure 6.2-6 shows the settling of RMS WFE and RSS LOS once the slew is completed. Note that in these plots time zero refers to the time when the repositioning slew is completed and the steady-state pointing control law is activated. The vertical black dashed lines indicate the instance of time when settling below requirement levels occurs. Table 6.2-1, summarizes the settling times for different slew cases. The sensitivity results show that higher angular rate magnitude during slew will results in a higher settling time, although the effect of that seems to be in order of a minute and not very significant.

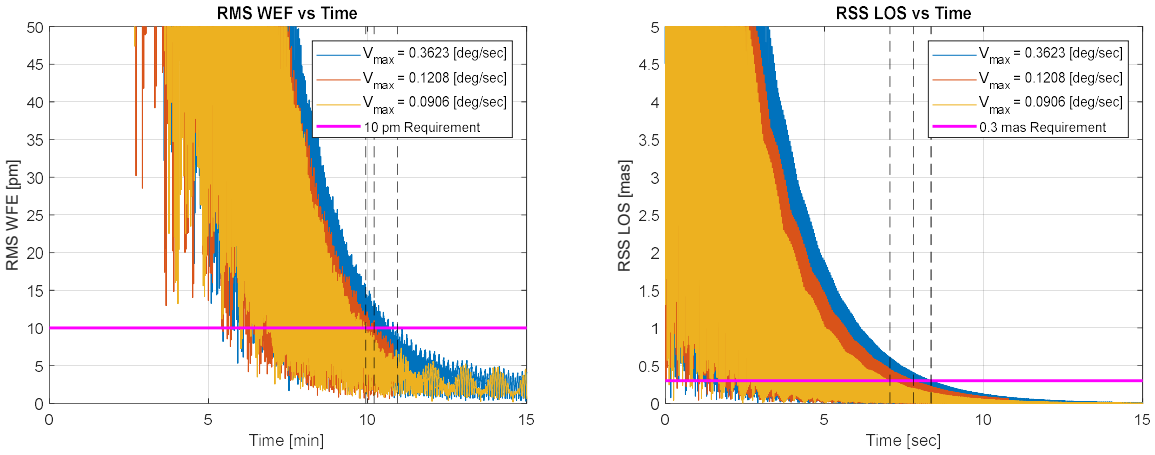

Figure 6.2-6: RMS WFE and RSS LOS Settling for Max Slew Rate Sensitivity Study.

Table 6.2-1: RMS WFE and RSS LOS Settling Times for Max Slew Rate Sensitivity Study

V_{max} [deg/sec]	0.3623	0.1208	0.0906
$T_{s\ (RMS\ WFE)}$ [minute]	10.94	10.21	9.95
$T_{s\ (RSS\ LOS)}$ [minute]	8.35	7.79	7.06

6.2.4.2 Impact of Maximum Slew Acceleration on Settling Time

Figure 6.2-7 shows slew acceleration, rate, and roll-axis angle for the three slew cases that were considered in this sensitivity study. In all cases, a quintic slew generator was used with the maximum angular rate set to 0.3623 deg/sec, which is the highest allowable slew rate deliverable by the CMGs and VCAs. The maximum angular acceleration was changed from the highest allowable limit (3.2x10-3 deg/sec2 - before VCA peak force limit is exceeded), to the lowest allowable limit (1.06x10-4 deg/sec2 - before LUVOIR's agility requirement is violated).

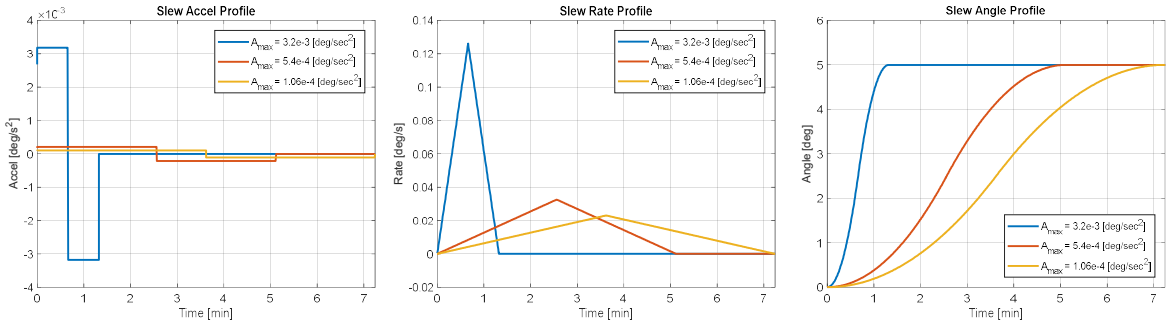

Figure 6.2-7: Slew Profiles for Max Slew Acceleration Sensitivity Study

Figure 6.2-8 shows the settling of RMS WFE and RSS LOS once the slew is completed. Table 6.2-2, summarizes the settling times for different slew cases. Sensitivity results show that lowering acceleration magnitude during slew has a very significant effect on reducing the settling time and should be considered as an important design factors when a designing a slew a profile.

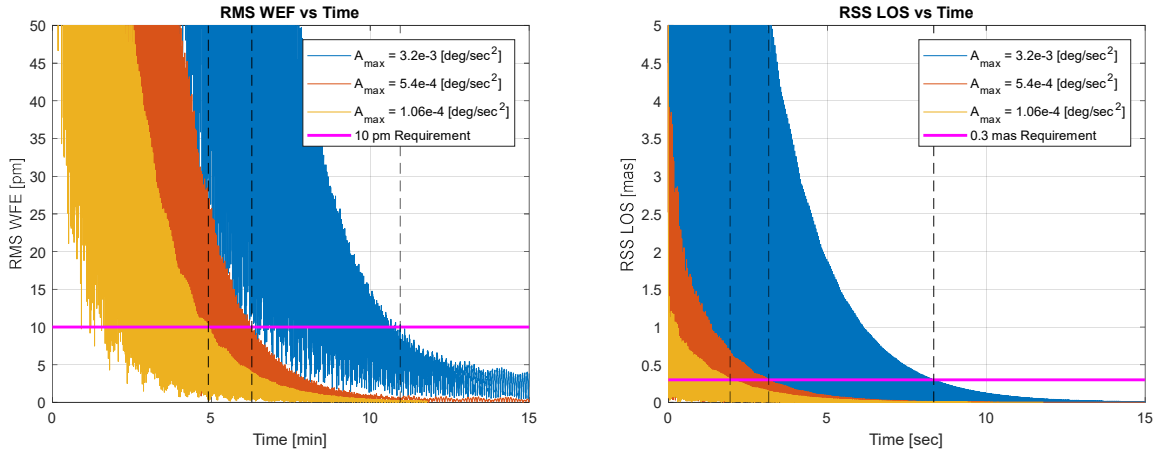

Figure 6.2-8: RMS WFE and RSS LOS Settling for Max Slew Acceleration Sensitivity Study

Table 6.2-2: RMS WFE and RSS LOS Settling Times for Max Slew Acceleration Sensitivity Study

A_{max} [deg/sec^2]	3.2x10^{-3}	5.4x10^{-4}	1.06x10^{-4}
$T_{s\ (RMS\ WFE)}$ [minute]	10.94	6.28	4.91
$T_{s\ (RSS\ LOS)}$ [minute]	8.35	3.16	1.94

6.2.4.3 Impact of Maximum Slew Jerk on Settling Time

In this section, two slew profiles were created: one using a quintic slew generator with max jerk set to 0.1 deg/sec^3, and another one generated by a quadratic slew generator with infinite max jerk. In both cases, max slew acceleration and rate are set to 3.2x10^{-3} deg/sec^2 and 0.3623 deg/sec. Settling time results in Figure 6.2-9 and Table 6.2-3 show insignificant difference between the settling times of the two cases, which suggests that a jerk-bounded slew profile may not improve settling time.

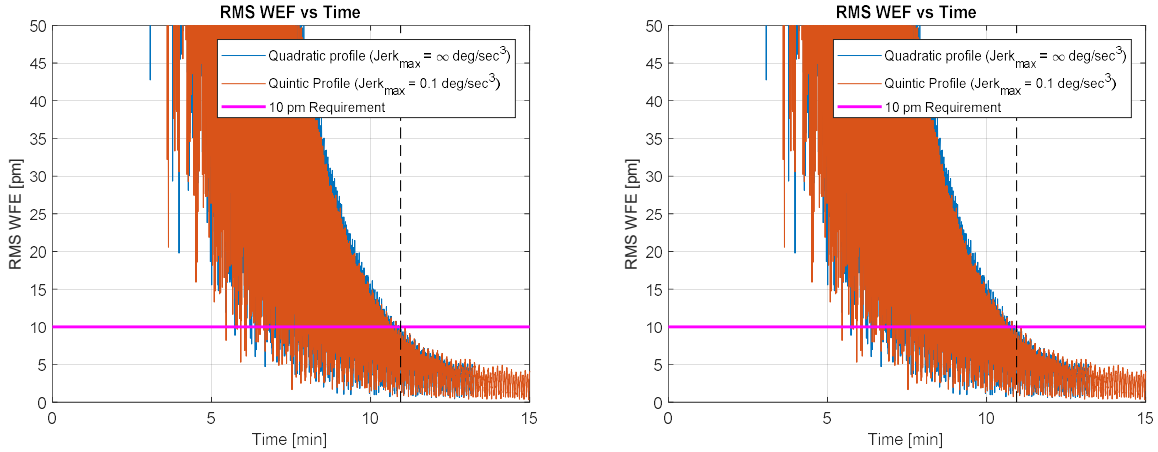

Figure 6.2-9: RMS WFE and RSS LOS Settling for Max Slew Jerk Sensitivity Study.

Table 6.2-3: RMS WFE and RSS LOS Settling Times for Max Slew Acceleration Sensitivity Study

J_{max} [deg/sec^3]	∞	0.1
$T_{s\ (RMS\ WFE)}$ [minute]	10.945	10.943
$T_{s\ (RSS\ LOS)}$ [minute]	8.46	8.35

6.2.4.4 Impact of Structural Damping on Settling Time

In this section, settling time is computed for two cases where the structural damping set to 0.5% and 0.25%. In both cases, a quintic slew generator is used with max slew acceleration and rate set to 3.2×10^{-3} deg/sec^2 and 0.3623 deg/sec, respectively. Settling time results summarized in Figure 6.2-10 and Table 6.2-4 show that, as expected, settling time improves by almost a factor of two when the structural damping is increased from 0.25% to 0.5%.

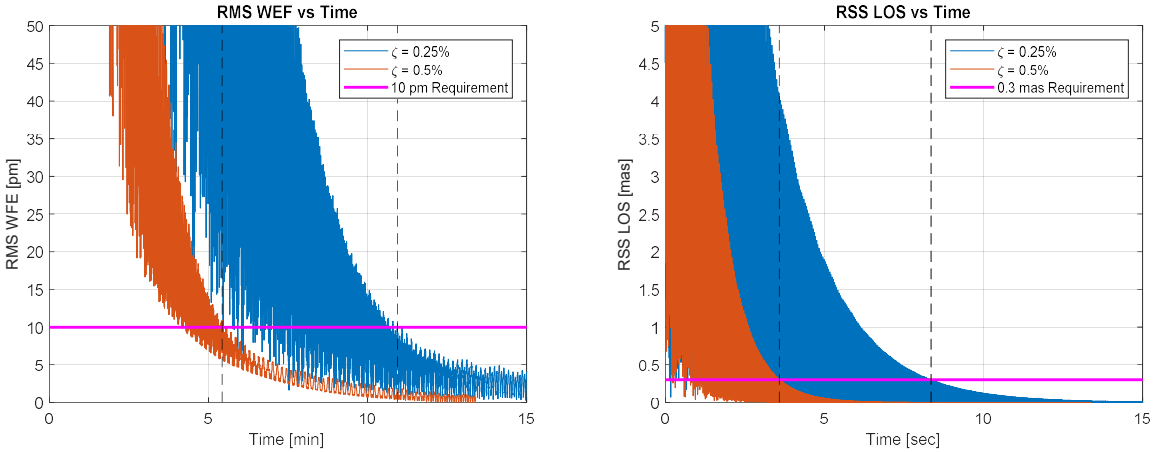

Figure 6.2-10: RMS WFE and RSS LOS Settling for Structural Damping Sensitivity Study.

Table 6.2-4: RMS WFE and RSS LOS Settling Times for Structural Damping Sensitivity Study

ζ	0.5%	0.25%
$T_{s\ (RMS\ WFE)}$ [minute]	5.431	10.94
$T_{s\ (RSS\ LOS)}$ [minute]	3.58	8.35

6.2.4.5 Impact of FSM on Settling Time

The goal of this section is to determine the effects of a FSM on RSS WFE and LOS settling time. Two cases are considered: one uses the baseline steady-sate pointing control law that includes FSM LOS control, and another case where a FSM-less LOS control law is used during stead-state. In both cases, a quintic slew generator is used with max slew acceleration and rate set to 3.2×10^{-3} deg/sec^2 and 0.3623 deg/sec, respectively. Settling time results in Figure 6.2-11 and Table 6.2-5 , suggest that a FSM does not have a significant effect on settling of WFE, but it does help with a faster settling time for LOS.

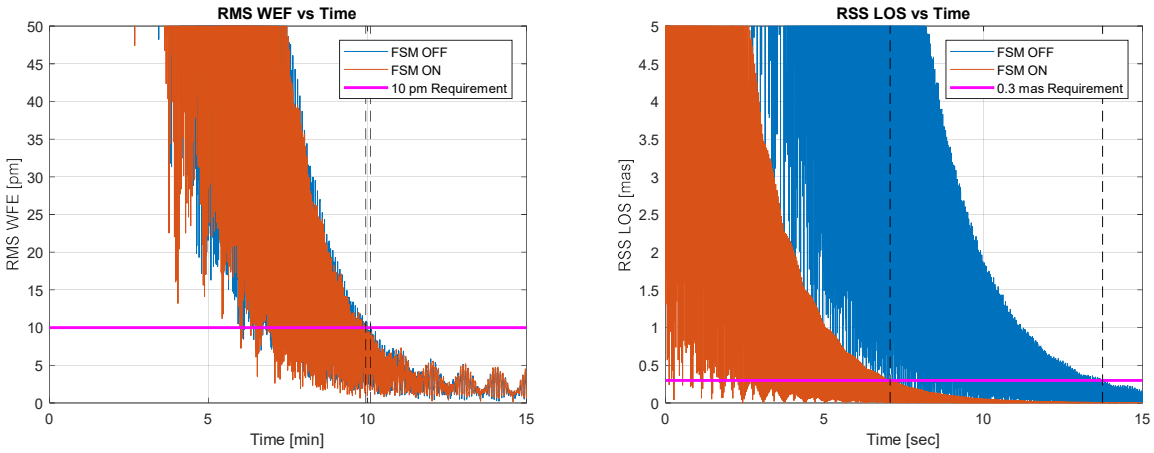

Figure 6.2-11: RMS WFE and RSS LOS Settling for FSM vs No FSM Study

Table 6.2-5: RMS WFE and RSS LOS Settling Times for FSM vs No FSM Study

	FSM ON	FSM OFF
$T_{s\ (RMS\ WFE)}$ [minute]	10.94	10.1
$T_{s\ (RSS\ LOS)}$ [minute]	13.75	7.06

6.2.4.6 Impact of Telescope Pitch Angle on Settling Time

In this section, settling time are computed for four different cases where the telescope pitch angle is raised from 0 degree to 90 degrees. In all cases, a quintic slew generator is used with max slew acceleration and rate set to 3.2×10^{-3} deg/sec^2 and 0.0906 deg/sec, respectively. Settling time results summarized in Figure 6.2-12 and Table 6.2-6 show that by increasing the pitch angle of the telescope from 0 to 90 degrees, the settling time is significantly reduced from about 10 minutes to only 3.9 minutes. In the 0 degree pitch angle case, the tilt axis of the LOS is parallel to the slew axis; therefore it will participate in the structural dynamics modal excitation caused by the slew. As the pitch angle increases to 90 degrees, both LOS axes will become perpendicular to the slew axis, experience less modal excitation, and settle out faster.

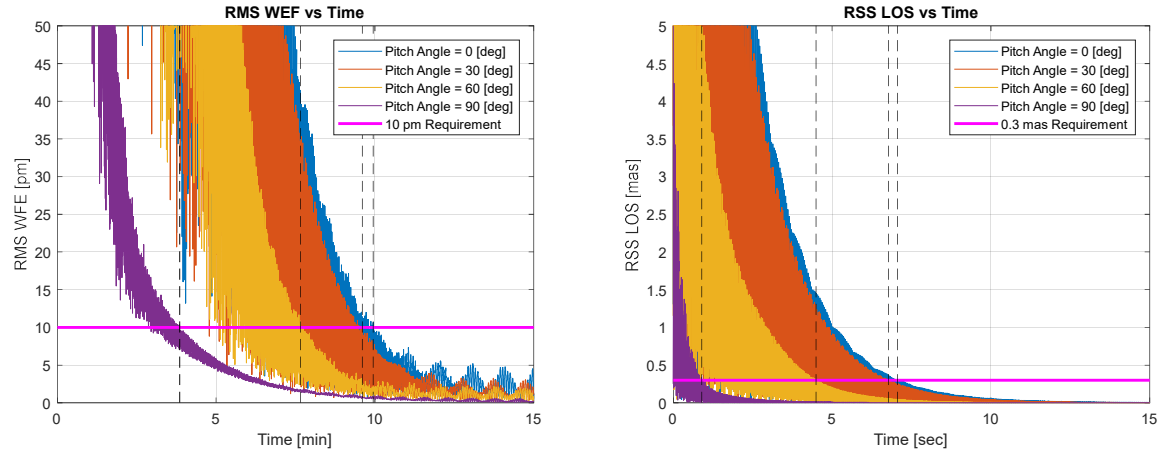

Figure 6.2-12: RMS WFE and RSS LOS Settling for Telescope Pitch Angle Study

Table 6.2-6: RMS WFE and RSS LOS Settling Times for Telescope Pitch Angle Study

Pitch Angle [deg]	0	30	60	90
$\mathbf{T_{s\ (RMS\ WFE)}}$ **[minute]**	9.95	9.61	7.65	3.85
$\mathbf{T_{s\ (RSS\ LOS)}}$ **[minute]**	7.06	6.77	4.49	0.90

7 Large and Segmented Optic Design and Manufacturing

7.1 Collins Report

Document No.: PR-ADP-1065
Release Date: 03-22-2019
CLS10623924

ROSES Segmented Telescope Design Study

This document contains no proprietary information.

U.S. Export Classification: NSR

Collins Aerospace
A United Technologies Company
ISR Systems
100 Wooster Heights Road
Danbury, CT 06810-7509
Telephone (203) 797-5000
CAGE No. 8F963

Table of Contents

1. Task Overview

1.1 Task 1: Thermal Analysis

CTE magnitude, homogeneity and isotropy of mirror substrate materials are a key consideration when modeling the stability of a mirror. To define CTE related requirements for a mirror substrate, the temperature stability of the substrate must also be defined. Hence, the thermal control approach is intimately related to mirror substrate CTE requirements. More generally, temperature stability has significant impact on stability of telescope metering path(s) and the accuracy of the metrology systems that monitor them. Hence, the thermal control approach is related to optical bench structure and metrology system performance/design. Good temperature stability can enable lower cost, less complex designs. Collins has recently developed and demonstrated a new thermal control approach that achieves exceptional temperature stability.

Temperature results for a representative 4-meter HabEx primary mirror concept are predicted utilizing a new thermal control approach developed by Collins for exceptional temperature stability. A thermal model is created incorporating a simplified bus and Outer Barrel Assembly (OBA) suitable for ROM analyses. Representative load cases are utilized to iterate the control approach. This analysis provides the needed time phased temperature maps for defining CTE requirements consistent with HabEx wave-front stability requirements.

Temperatures are mapped onto an existing 4-meter primary mirror detailed structural model suitable for thermal distortion analyses. Thermal distortion analysis is utilized to characterize performance with representative CTE magnitude and uniformity providing a basis for definition of CTE requirements.

Developmental analysis and testing tasks to further define the thermal control architecture and characterize thermal/hygral stability of mirrors and metering path structures are defined.

1.2 Task 2: Coatings

Exposure to ambient environments (oxygen) present challenges for UV reflectance, particularly down to 90nm. This task defines potential coating process flows and their associated technical risks and trades. Legacy processes and hybrid process flows in which the mirror is metalized and a protective coating is applied without exposure to a reflectance degrading environment is reviewed, and companies and universities, e.g. ALD NanoSolutions, MLD Technologies and partnering universities are engaged to support definition of potential process flows. The product of this effort is identification of promising process flows that result in a robust, cleanable, highly reflective coating. An associated test program targeted at providing information for a rational down selection to the most promising process flow is defined.

2. Task 1: Thermal Modeling

2.1 Introduction

The HabEx mission has extraordinarily tight requirements on optical performance both in terms of static diffraction limited performance as well as temporal stability. Both features are critical for providing the high signal-to-noise measurements that are key to the mission. Of specific interest is the ability to hold ~10pm WFE performance over approximately 10-minute periods of time. In terms of thermal control, this represents a significant performance challenge that is well beyond the ability of traditional thermal control methods.

Recent innovative work at Collins has focused on design and testing a super-stable thermal control architecture for next generation space optical systems. Rather than forcing development of new prohibitively expensive materials or technologies, the Collins architecture uses traditional elements (thin film heaters, PID controllers etc.) in a new way to provide temperature stability that is well above typical performance. This approach enables the use of existing low CTE materials such as Zerodur and ULE, and has been proven in both test and flight environments.

In the present application, Collins has adapted this thermal architecture to the general HabEx design as presented in the August 2018 interim report. The thermal control results presented hereafter focus principally on the 4m primary mirror because this is one of the most sensitive and difficult-to-control components. The approaches used to thermally stabilize this mirror are readily extensible to other elements of the telescope metering structure.

Although, the geometries and orbital cases used to assess performance are representative, the design approaches used are quite flexible and can be readily optimized to more specific conditions and environments. The following results show that the proposed thermal architecture is capable of maintaining PM WFE performance that supports the 10pm system level goal.

2.2 Model Description

The computational models modified or developed for this Collins analysis effort are intended to provide a general indication of optical performance. Obviously, the design of the HabEx system is ongoing, hence reasonable assumptions about the design and orbital constraints have been made to allow performance estimates to be made. These assumptions will be specifically identified in each of the appropriate sections. Effort has been invested into making the analysis assumptions meaningfully broad enough to capture a wide range of actual design and operational scenarios.

The following subsections detail the structural model of the primary mirror, the thermal model used to estimate primary mirror temperatures, and the general environmental conditions used in the models. Both models were used cooperatively to estimate optical performance.

2.2.1 Structural Model

The structural finite element model used for this evaluation was a 4m open-back Zerodur design developed by Collins under a previous developmental effort with NASA Marshall, Schott, and JPL. This model was selected because it has design heritage to the HabEx program, and its thermal / CTE performance is representative of many similar designs in this class of mirror. The model was constructed in FEMAP (with MSC Nastran solver) and consists of approximately 2,300,000 nodes. This level of fidelity is somewhat excessive for the present application, but re-meshing and qualifying the model were beyond the scope of the present effort, hence it was used as-is. **Figure 1** illustrates the structural PM model and mesh density. The material properties used in the model are consistent with Class zero Zerodur with a CTE range of +0.02ppm to -0.02ppm (model uses 0.02ppm). Variability in CTE is an important consideration with this size of mirror; however, this is believed to be a second order effect and is beyond the scope of the present effort to assess.

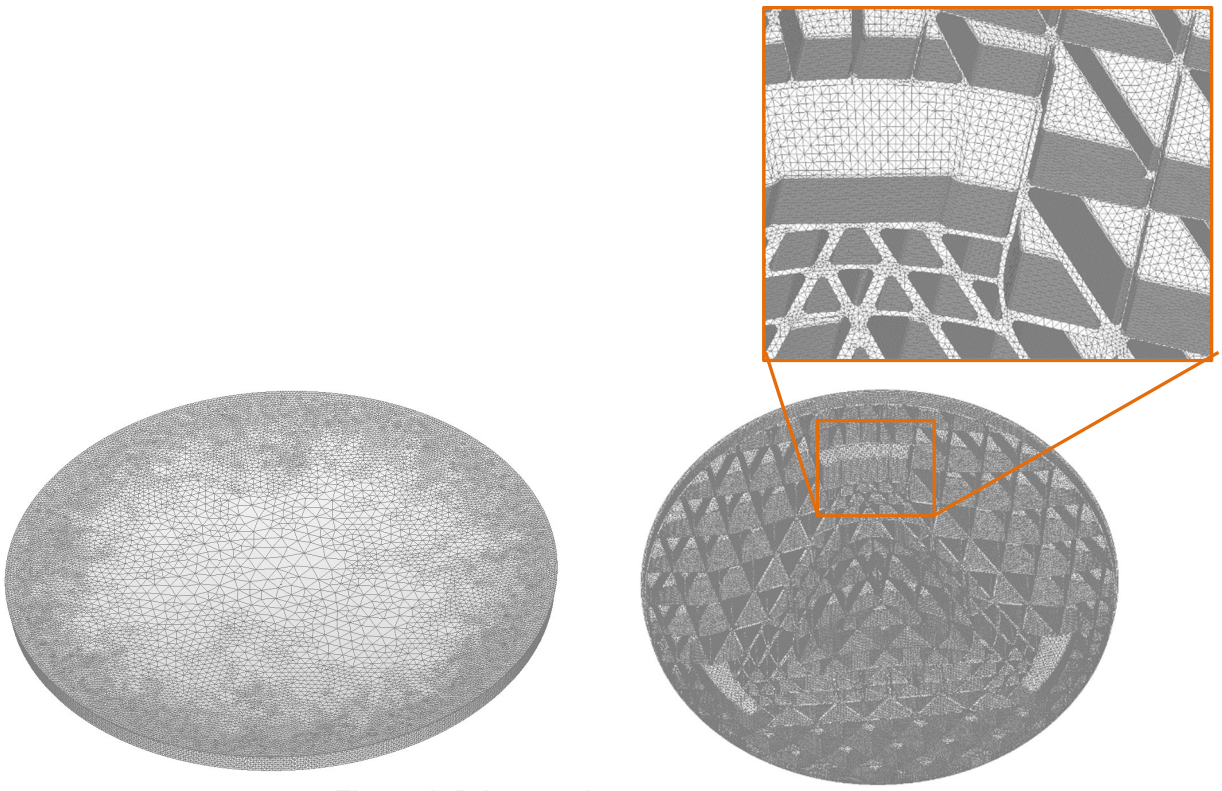

Figure 1: Primary mirror structural model

2.2.2 Thermal Model

The Primary Mirror (PM) thermal model was constructed using plate and solid elements following the geometry of the previously described structural model. Rib thicknesses and geometry, and surface finishes were all modeled to accurately capture both radiative and conductive transfer in the mirror itself and the surrounding telescope structure. Figure 2 illustrates the primary mirror thermal model mesh upper and lower surfaces.

The thermal model uses Schott Zerodur properties (k = 1.46 W/m/C, ρ = 2.53 gm/cm3, Cp = 800 J/kg/C). The reflective finish on the mirror surface was considered to be the standard Collins enhanced silver coating (other reflective coatings are expected to have little impact on thermal analysis results).

The PM is principally heated and controlled via radiative coupling to surrounding surfaces (no direct heat application). Key pieces of the surrounding structure are heated and carefully controlled using an innovative technique developed by Collins specifically for thermally sensitive optical systems. This thermal control architecture has been extensively modeled and tested in representative environments on flight hardware. The present design uses Proportional Integral (PI) controllers consistent with a standard Collins flight design. In addition to the typical PI logic implementation, the controller also features wind-up limiting, visibility to sensor telemetry, and commandable set-point and control parameters.

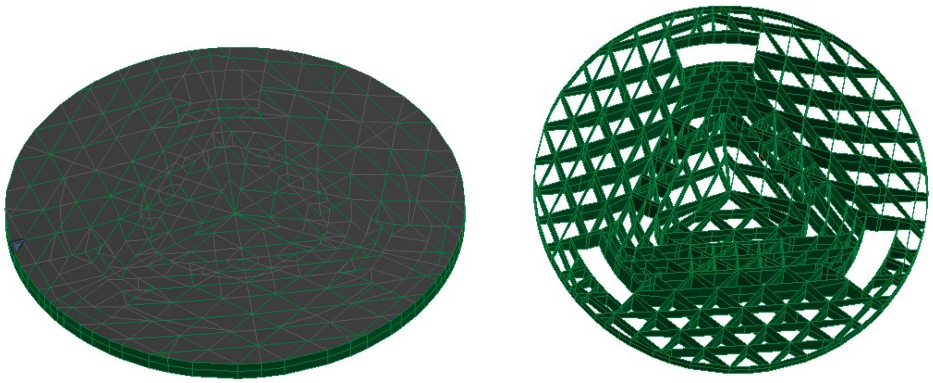

Figure 2: Primary mirror thermal model face (left) and light-weight core (right)

The temperature stability of the Primary Mirror is determined by the thermally controlled surfaces, baffling, insulation and other features that surround it. In the present model, the geometry of the surrounding telescope elements (barrel, scarf, and bus etc.) have been modeled based on the August 2018 HabEx Interim Report. Figure 3 illustrates the comparison between the report images and the present thermal model.

The choice of heater locations, insulation placement, and other features of the thermal control architecture are specific to the individual thermal design. Hence, these features have been chosen to be consistent with standard space telescope design and the Collins thermal architecture described previously. Exterior surfaces are generally Optical Solar Reflector (OSR) blanketing, solar arrays (where appropriate) or black insulation. Surface finishes in the barrel are generally black to assist in stray light control. Surface finishes aft of the PM are either black (for radiative coupling) or reflective for isolation (depending on location).

The Collins thermal architecture uses the forward barrel to assist in maintaining stable mirror and structure temperatures. The barrel is insulated to mitigate heat loss and also temperature controlled to keep the surrounding surfaces thermally stable. The barrel is controlled to a constant temperature of -60°C. This temperature level mitigates heat loss while still providing positive control authority on the heaters. It is possible to heat the barrel to warmer temperatures and reduce the static temperature gradient in the PM, but preliminary analysis has shown that the majority of the optical impact of this gradient can be removed by on-orbit recalibration. Hence, it is presently believed that heating the barrel to a warmer temperature is not necessary.

The present scarf design has it being deployed after launch. Given the difficulties associated with bridging this interface with large numbers of wires, the Collins design only uses passive thermal control elements on the scarf (no heaters). The aft region of the barrel around the primary mirror itself is sectioned into a number of heater zones that allow the PM and supporting structure to remain stable at ~20°C. **Figure 4** illustrates the overall thermal control architecture. The current design uses approximately 75 heater zones.

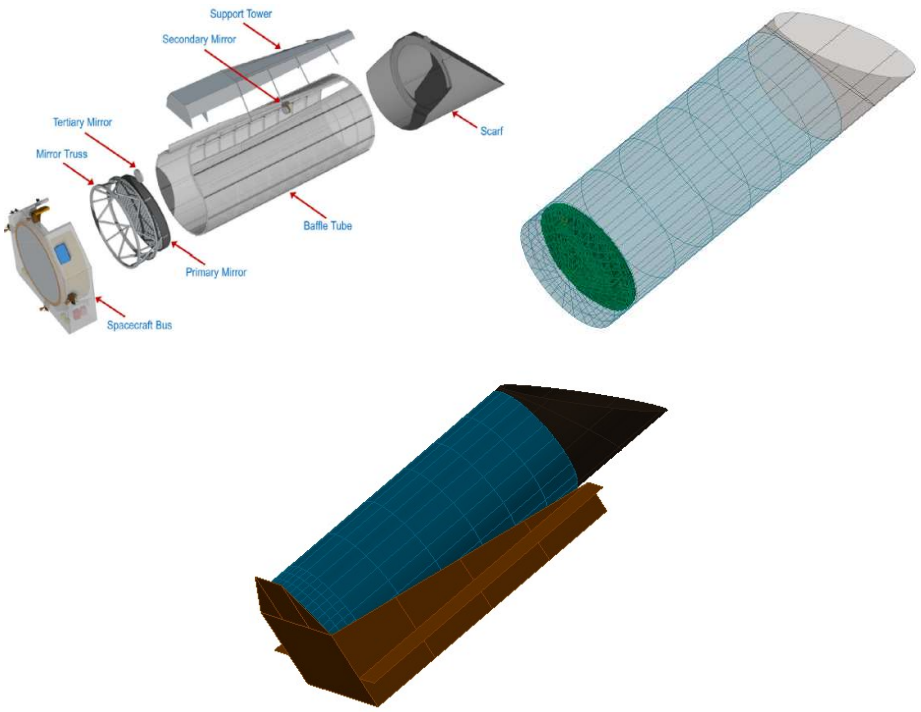

Figure 3: Telescope geometry: HabEx report image (left), thermal model PM & barrel (center) and thermal model barrel, bus, and secondary structure (right)

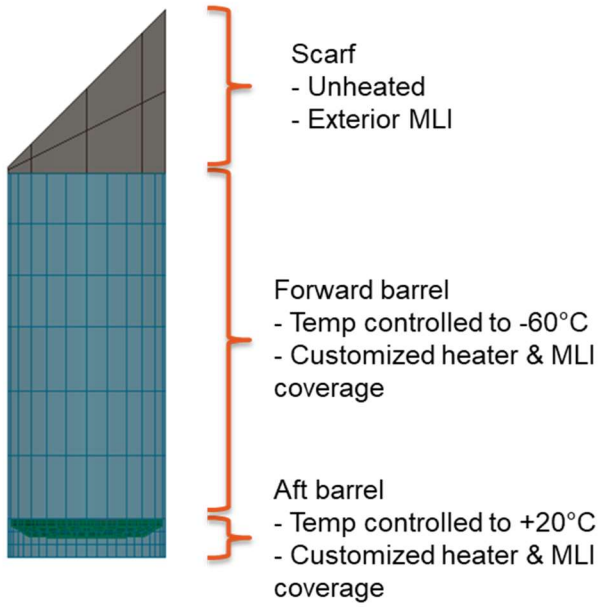

Figure 4: Telescope thermal control detail

2.2.3 Model Environments

Placement of the HabEx telescope in an L2 Halo orbit implicitly implies that the principle disturbance will be the sun. The present orbital model does include the influence of reflected sunlight and radiative emission from the earth, but these are of minimal overall effect. Because the sun is the dominant environmental factor, the presentation angle of the telescope to the sun (and the associated CONOPS) are of key importance. No baseline pointing information was available as part of this study, hence an artificially stressing orbital case was developed using the following guidelines:

- Sunlight is not permitted to fall directly inside the barrel (i.e. no shallow pointing angles)
- Changes in visible scene thermal conditions caused by the moon or other celestial objects (planets etc.) are ignored for this study
- Thermal conditions that are adverse for the primary mirror and structure are most likely to be caused by changes in sun loading on the side of the vehicle
- Highest thermal loading on the vehicle side is produced at a pointing angle of 0° (with respect to the orbital plane)
- Lowest thermal loading on the vehicle side is produced at a pointing angle of 90° (normal to the orbital plane)
- Given the mass of the Primary Mirror, its bulk thermal response will be largest over long periods of time (i.e. many hours)

Given the above assumptions, an artificially stressing orbital case was created to mimic a section of the L2 halo orbit. The performance assessment period of the orbit begins with a full side presentation of the telescope to the sun. Over the next 46 hours, the vehicle gradually shifts pointing attitude to one that has no side sun exposure. After reaching this point, the vehicle holds this pointing attitude for 10 additional hours, bringing the total assessment period length to 56 hours. This maneuver presents the maximum possible change in environmental conditions while simultaneously allowing the mirror and structure plenty of time to maintain a continuous state of quasi-equilibrium (i.e. conservatively maximum thermal change over the time period). The angle change and longer time durations (allowing the mirror more time to respond) are substantially more conservative than HabEx design reference missions.

Ten minute temperature snapshots of the PM were captured at 6 locations over the duration of the assessment orbit segment. Comparisons were made over both the 10-minute periods as well as the entire orbital span. Hence, the results captured in the following sections assess both short and long term stability of the PM.

There are potentially other orbital timeframes and attitudes that may present uniquely stressing cases that should ultimately be analyzed, but the outlined orbit will provide a good general assessment of thermal control robustness. **Figure 5** illustrates the vehicle attitude, times, and angles defined as part of this assessment orbit.

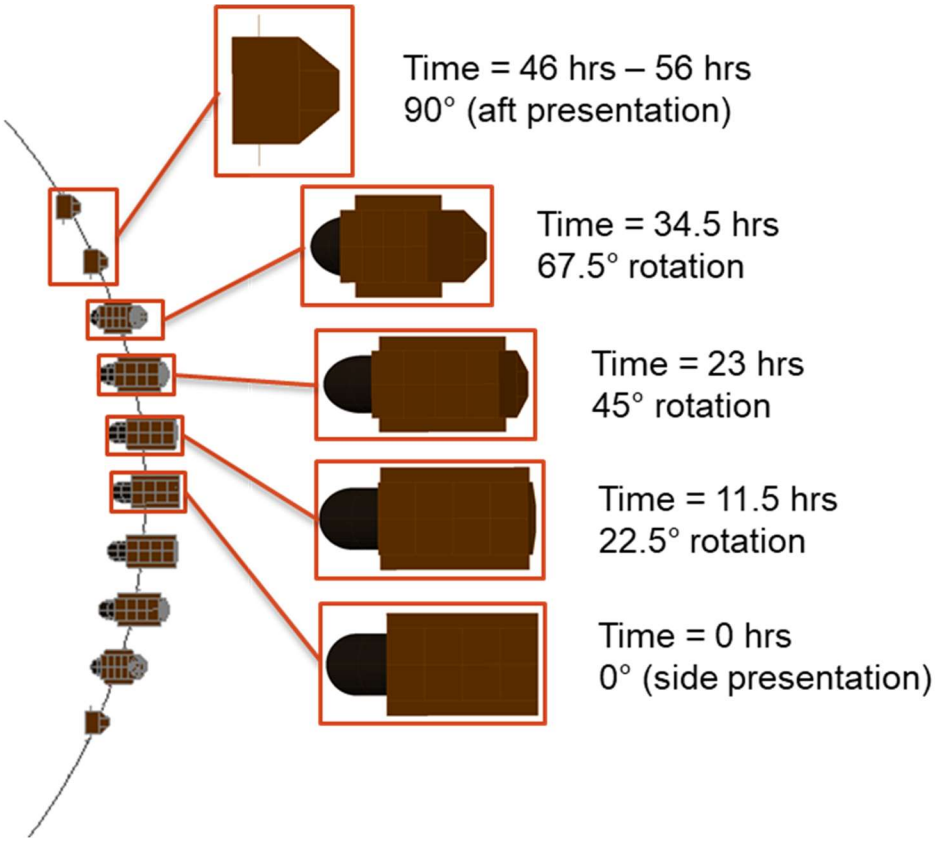

Figure 5: Detail of the stressing thermal assessment orbital case

2.3 Performance Results

Performance of the Collins thermal architecture is divided into three sections:

- Static and transient thermal behavior
- Optical performance
- Power consumption

Each of the subsequent sections will address these topics. The first two sections are obviously closely related, hence the temperature mapping step that connects them will also be addressed.

2.3.1 Thermal Performance

The thermal control architecture has three main objectives for the structure and optics:

1. Minimize the amount of CTE driven optical deformation that occurs between ground calibration and on-orbit usage. This is especially important for optical errors that cannot be easily removed by on-orbit alignment or focus.
2. Minimize the amount of CTE driven optical deformation that occurs due to changes in orbital conditions
3. Protect sensitive components from thermal damage (hot or cold)

Of these three objectives, the second is typically the most difficult and this is especially true with HabEx. The thermal architecture developed by Collins has been specifically tailored to minimize on-orbit thermal variations. Goals 1 and 2 highlight that fact that thermal changes in optically sensitive locations are paramount, hence temperature information by itself is only partially useful. The following results present both thermal performance and the corresponding optical performance for the PM.

The static on-orbit temperature field of the PM is used to estimate the amount of figure error induced by thermal changes from the ground temperature state. Nominally, the average on-orbit temperature should be close to the average ground temperature. The present predictions place the average PM temperature at 20.6°C, which is very near the typical ground test value (this is also adjustable by heater controller setpoint). Generally, it is desirable to minimize thermal gradients in the mirror, however this is less of a concern for deformations that are correctable by the initial (or seasonal) on-orbit calibration. Non-correctable errors are obviously concerning and must be accounted for. **Figure 1** shows the static on-orbit temperature state of the PM. The average temperature and spatial gradients observed are well within typical heritage ranges. A lower set-point of ~ 0.0 °C is expected to reduce spatial gradients. Structural analysis in the subsequent section will show that the ground-to-orbit deformation caused by this temperature distribution is largely correctable (focus), hence the gradients observed here are not particularly concerning.

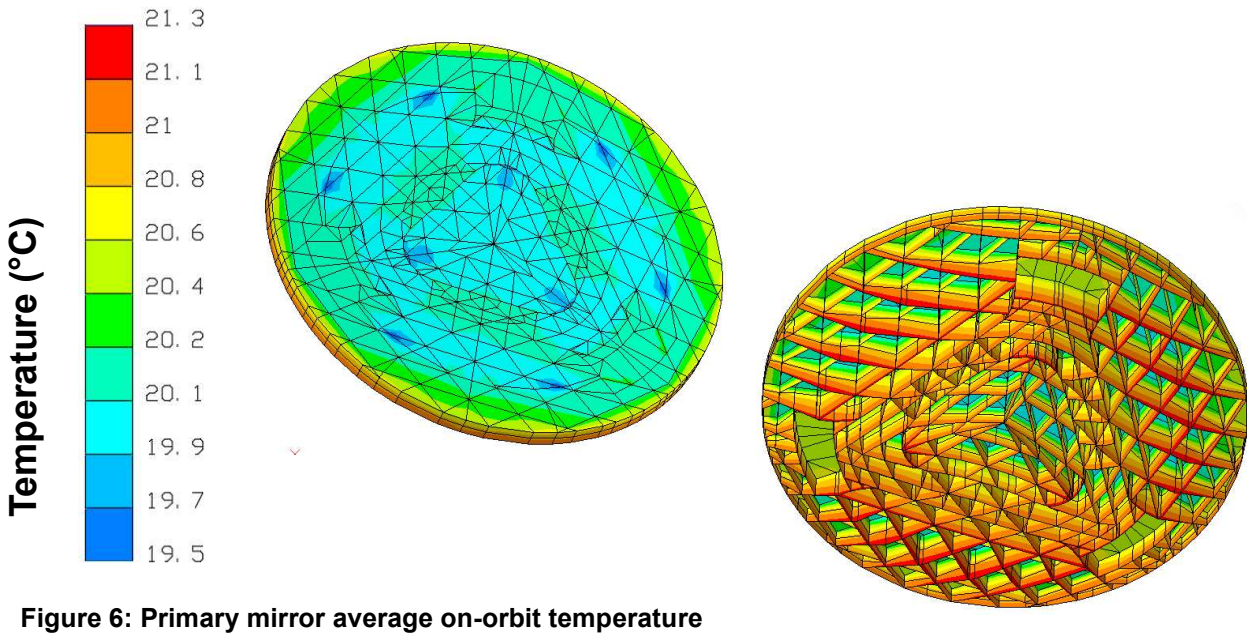

Figure 6: Primary mirror average on-orbit temperature

The principle thermal stability timeframe of interest for the HabEx mission is 10 minutes; however, it is also useful to assess the stability of the telescope over longer periods. This additional comparison provides insight into how long the telescope might be required to dwell before taking imagery, or what types of pointing attitude restrictions might be needed in operation. To that end, the variation of the Primary Mirror temperature was analyzed over the entire 56 hour assessment orbit to identify states where the largest temperature changes could result. Normally, this comparison would be referenced to a likely on-orbit calibration state. In the present assessment orbit, the most likely calibration point would be when the telescope is pointed away from the sun to minimize environmental effects (at 46 hrs). Comparisons indicated, not surprisingly, that the largest thermal deviation from this reference point was when the

telescope is rotated nearly perpendicular to the sun (at time = 11.5 hrs). Even with this fairly dramatic change in pointing attitude, the temperature of the PM remains very stable with a worst-case local temperature change of ~0.006°C over this extended period. **Figure 7** illustrates the orbital locations and the distribution of temperature change.

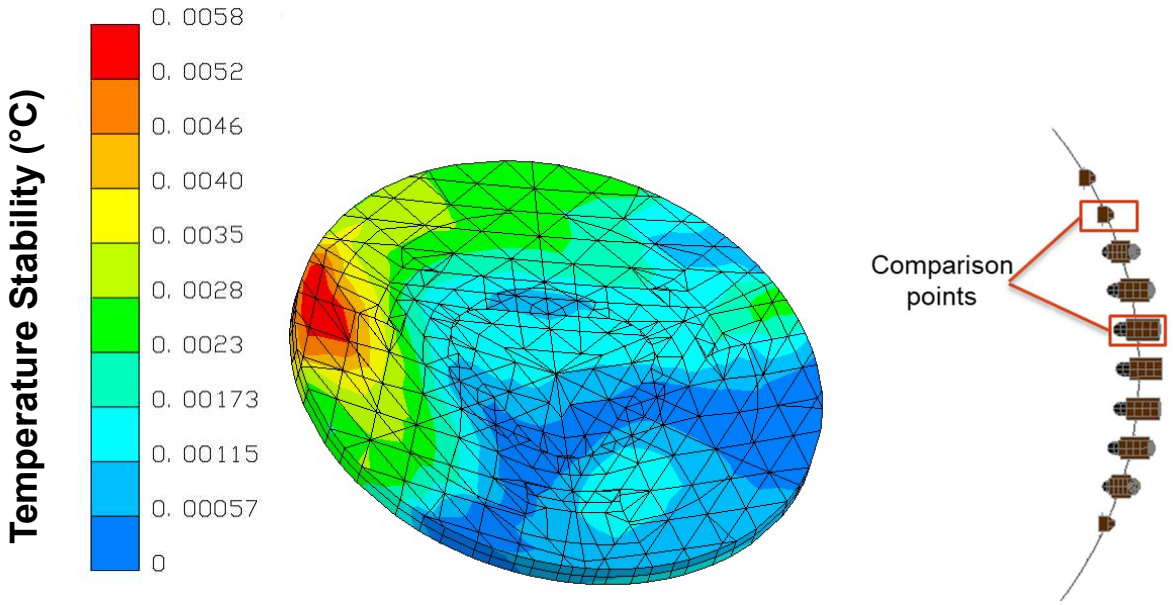

Figure 7: Worst-case on-orbit temperature change (11.5hrs to 46hrs)

The 10-minute temperature stability of the PM was also calculated for 6 locations in the 56 hour orbital segment. These six locations represent a wide range of pointing attitude and rates of angular change. **Figure 8** illustrates the distribution of temperature change across the PM surface for each of these 6 locations. Again, as expected, the final two orbital points show the best stability because their pointing attitude is remaining relatively constant. As with the longer term stability comparison made previously, the highest levels of temperature change occur at hour 11.5. However, even the time locations with elevated levels of thermal change have stability values measured in the µ°C range. Both the long term and 10-minute stability values are summarized in Table 1.

These levels of temperature stability are well beyond the capability of traditional thermal designs and may seem unlikely. In Collin's development of the present thermal architecture, experimental testing showed levels of stability that were in the 0.001 – 0.002°C range. For that test article, additional effort was not expended on improvement because it was not necessary at the time. However, for the HabEx design further attention was paid to optimizing heater zones and insulation, as well as careful tuning of control parameters. These efforts yielded meaningful improvements that are still credibly within the range of model predictability. The Collins approach pays special attention to using installation techniques that are practical.

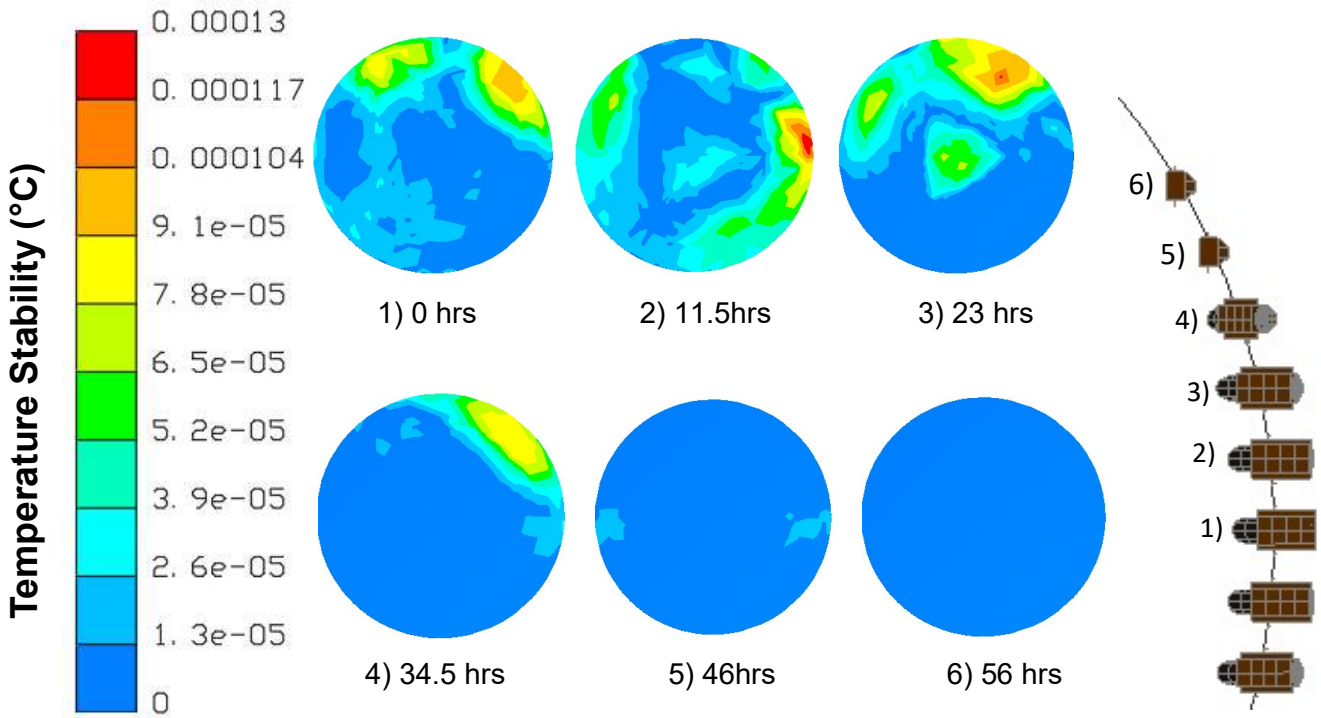

Figure 8: Primary mirror 10-minute temperature stability plots at 6 orbital locations

Table 1: Worst Case Temperature Stability

Performance Metric	Worst-case Temperature Stability (°C)	
	56 hr slew	10-min window
Maximum Local	0.006	.00032
Spatially Averaged	0.0012	0.00003

2.3.2 Temperature Mapping

In order to obtain optical performance estimates, it is necessary to map the thermal model results onto the corresponding structural model nodes. This is done using the temperature mapping utility in Thermal Desktop which interpolates temperatures based on an input file generated by Femap. The mapping algorithm uses a progressively tolerance range technique that identifies the most appropriate nodes for interpolation. At the conclusion of mapping several error checking steps are taken to ensure proper results. One of these steps is to compare temperature renderings from both models for range and distribution accuracy (see example in **Figure 9**).

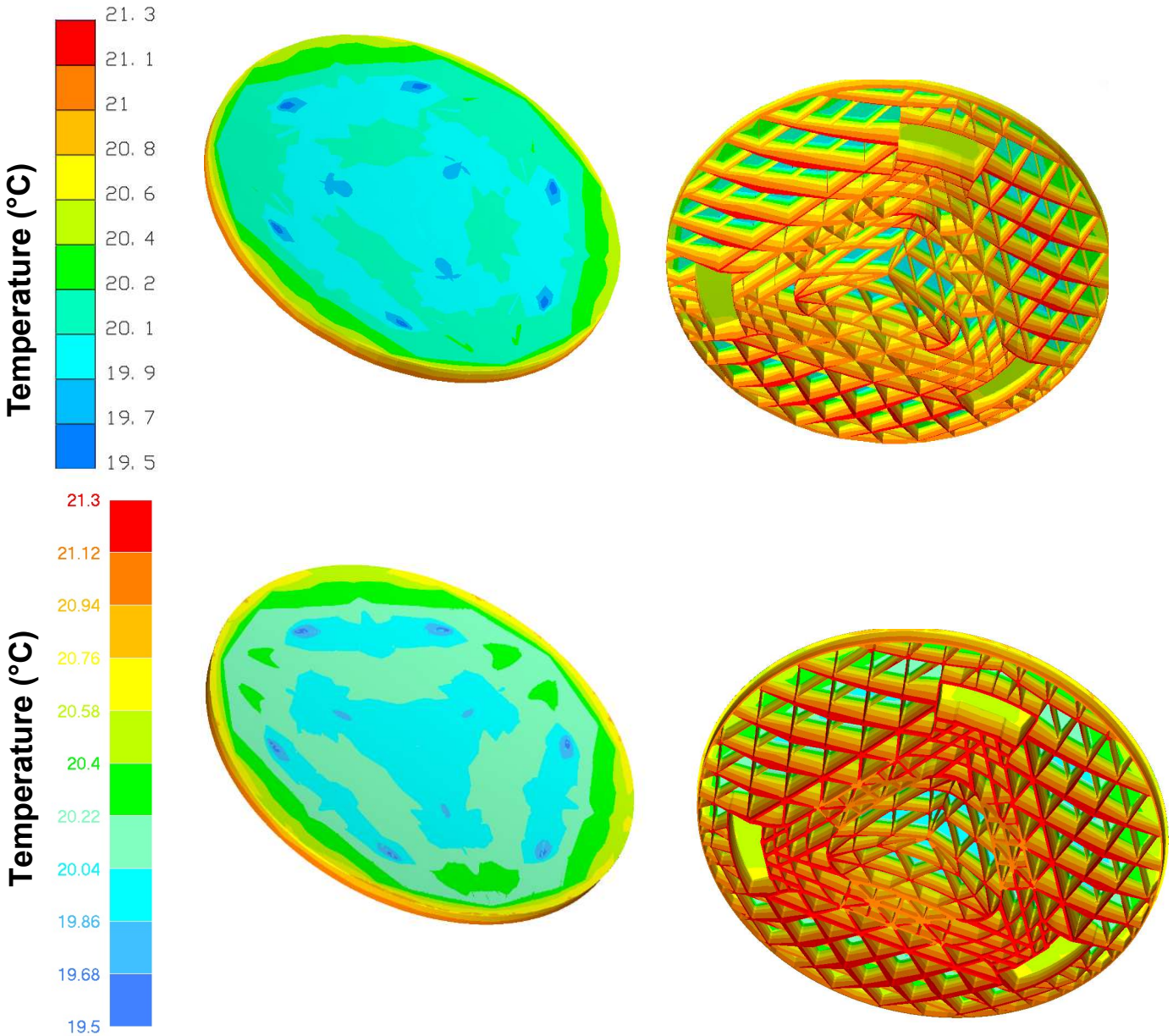

Figure 9: PM temperature mapping comparison: thermal model (top) and structural model (bottom)

2.3.3 Optical Performance

Following the temperature mapping of all necessary temperature sets onto the structural model, the CTE driven nodal displacements were calculated for the front (R1) surface of the PM. The static ground-to-orbit deformation was then calculated and rendered in **Figure 10**. This deformation map corresponds to the temperature map shown previously in **Figure 6**. As described earlier, a lower set-point is expected to reduce quasi-static spatial gradients, hence this static error is expected to be lower with a reduced set-point. **Table 2** contains a summary of the significant Zernike coefficients for the surface. It is apparent from **Table 2** that the majority of the optical error is focus (Z4). This is considered an on-orbit correctable term. The non-correctable residual WFE is ~4nm. This error could certainly be further improved by optimizing heater set-points.

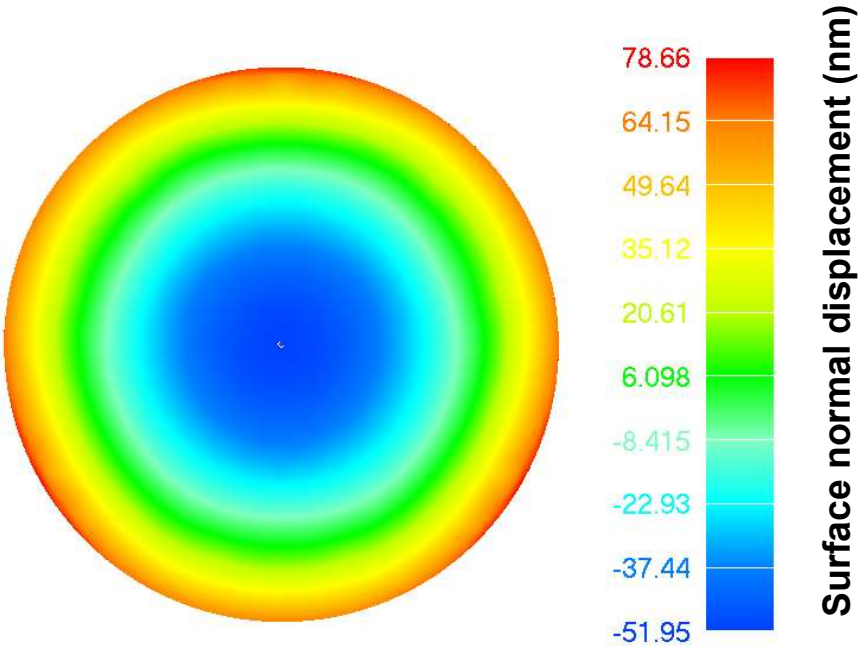

Figure 10: PM surface figure plot for thermally driven ground-to-orbit deformation

Table 2: Zernike decomposition for thermally-driven ground-to-orbit error

Contributor	Ground-to-Orbit RMS WFE (nm)
Focus	57.6
Astigmatism	0.4
Coma	0.2
Spherical	2.9
Residual	3.5
Combined Total	66.6

PM deformation results were also used to calculate the optical error associated with the long-term thermal instability (over the entire 56 hr orbital period). This result corresponds to the temperature map in **Figure 7**. **Table 3** contains a summary of significant Zernike contributors for this case. As with the previous results, the dominant optical error is focus (Z4). Because of the length of this evaluation period, it is likely not possible to remove this error using a focus correction. Although the total RMS WFE across this time period is beyond the target 10-minute budget value, it shows that the system stability is excellent over long periods of time and dramatic changes in telescope attitude. This further indicates that the thermal design would likely place few restrictions on the pointing and collecting operations. This performance could also be improved by further optimization of the thermal control system.

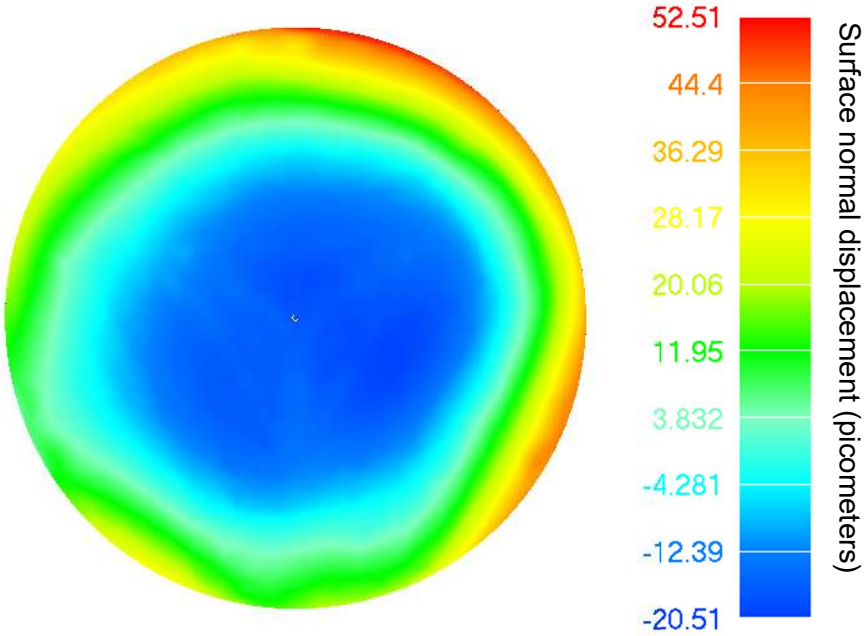

Figure 11: PM surface figure plot for worst-case long-term *stability*

Table 3: Zernike decomposition for worst-case long-term stability

Contributor	Long-term Stability RMS WFE (pm)
Focus	25.9
Astigmatism	4.2
Coma	7.4
Spherical	4.9
Residual	5.5
Combined Total	32.6

PM deformation results were also used to calculate the optical error associated with temperature changes across the 10-minute evaluation periods (at 6 orbital locations). These results correspond to the temperature

maps in **Figure 8**. As previous temperature results would indicate, the case at 11.5 hours was the worst of the 6. **Table 4** contains a summary of significant Zernike contributors for all cases, and again these errors could not be actively corrected during the observation period. The total observed RMS WFE associated with temperature changes over the 10-minute periods are well below 10pm. Table 4 also indicates the dramatic reduction in WFE that occurs when a pointing attitude is held constant. This type of analysis could be very useful in deriving operational constraints on slew rates and pointing attitude.

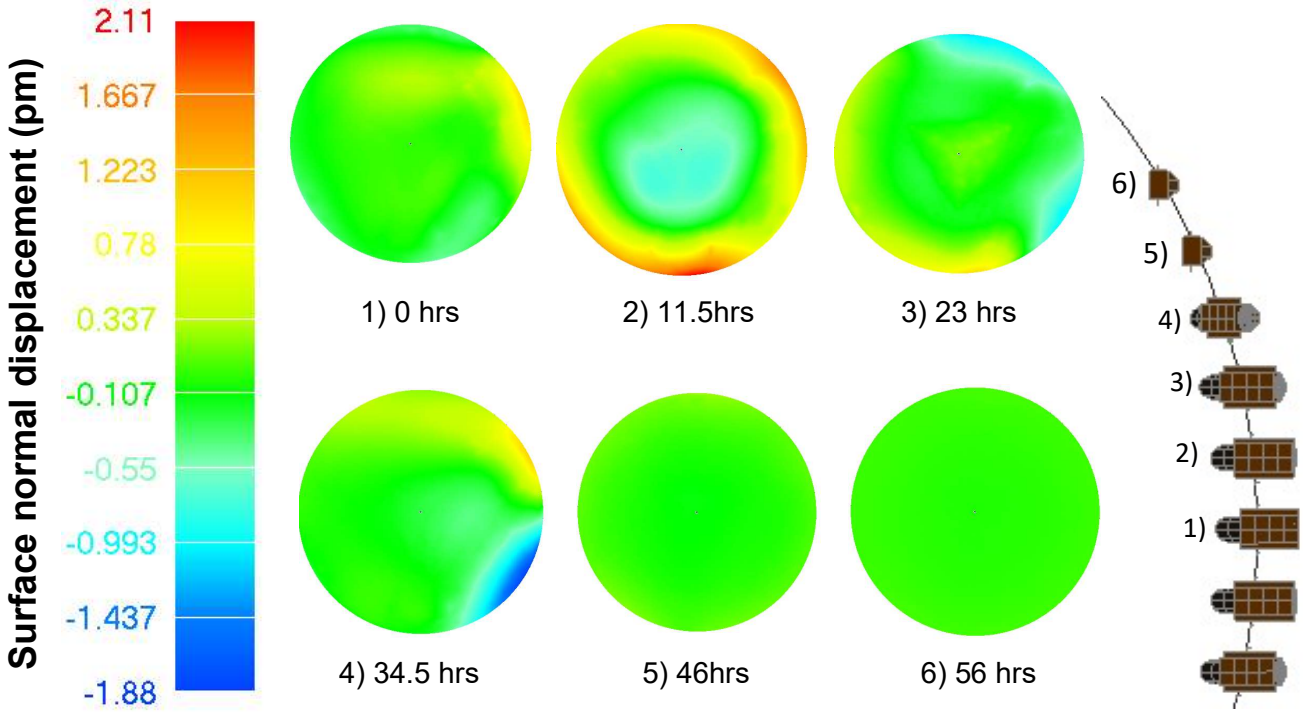

Figure 12: Primary mirror surface figure plots for the 10-minute temperature stability locations

Table 4: Zernike decomposition for worst-case 10-minute stability points

Contributor	10-min Stability RMS WFE (pm)					
	0 hrs	11.5 hrs	23 hrs	34.5 hrs	46 hrs	56 hrs
Focus	0.06	0.92	0.01	0.07	0.12	0.04
Astigmatism	0.19	0.29	0.02	0.49	0.03	0.01
Coma	0.21	0.28	0.37	0.17	0.01	0.003
Spherical	0.03	0.06	0.07	0.10	0.01	0.002
Residual	0.26	0.25	0.34	0.35	0.03	0.007
Combined Total	0.44	1.14	0.67	0.75	0.15	0.04

2.3.4 Power Consumption

The Collins thermal architecture is largely successful due to the design of the telescope insulation system. An added benefit to this approach is that the overall rate of heat loss is relatively low for a system of this size. Model estimates place the orbital average and peak power values in the following ranges:

- Orbital average: 500 - 600 W
- Peak Power: 1600 – 1800 W

To be clear, these power estimates consider only the power consumption of the heaters themselves (no other electronics, communication, etc.). The largest design feature that could impact this estimate is the forward barrel. If the insuation treatment or setpoint were varied dramatically, for some design purpose, this estimate could shift substantially. The Collins model does, however, show that maintaining excellent thermal stability does not imply high power consumption.

2.4 Future Test and Analysis

The proposed Collins thermal control architecture for the HabEx program has preliminarily demonstrated the following capabilities:

- Successful thermal control solution that is based on existing materials, technologies, and methods
- Acceptable ground-to-orbit primary mirror temperature distribution and optical distortion levels
- Primary mirror temperature stability through a representative slewing maneuver:
  0.0012°C (56hr period) 0.00003°C (over sliding 10-minute window)
- PM optical deformation through a representative slewing maneuver:
  32.6pm (56hr period) 1.14pm (over sliding 10-minute window)
- Low orbital average power consumption (500W - 600W)

The results of the present study are promising; however, there are a number of developmental tasks that could be pursued to further develop the control architecture. The following list summarizes additional objectives that are organized by both modeling / design efforts and prototype testing campaigns:

<u>Modeling / Design</u>

- Refinement of the applicable orbital cases and pointing CONOPS
- Development of system level thermal and structural models to allow a more complete estimation of performance
- Adaptation of the Collins thermal architecture to the metering support structure
- Further optimization of thermal architecture elements to improve key performance metrics
- Development of practical thermal operational constraints
- Sensitivity study of CTE inhomogeneity on PM performance
- Analysis of potential hygral impacts on composite structure elements
- Development of representative mirror segment structural/thermal models and adaptation of thermal control approach for a segmented architecture

- In particular, further definition of mirror mounts and assessment of metrology approach(es) to, e.g., characterize g-release and ensure consistency of mirror and mount design with primary mirror error budgets

Testing / Prototyping

- Characterization of long and short term stability and associated modeling methods of, e.g., composite materials at picometer levels (particularly thermal/hygral behavior) to ensuring adequacy of more complex built-up models for dimensional stability prediction:
  - Progressive test program beginning at laminate/coupon level for characterization of optical bench materials and identification of appropriate modeling methods for thermal, hygral, and dynamic behaviors at picometer levels
- Thermal Vacuum (TVAC) testing staged approach to identify achievable temperature stability:
  - Design and qualification of a TVAC configuration capable of accurately mimicking realistic solar loads and space environment stability
  - Verification of supporting technologies such as high accuracy temperature measurements and optimizing heater control algorithms for target time periods
  - Testing to assess temporal stability of a composite structure prototype with representative thermal control
  - Addition of an optical element to assess temporal stability of the combined system
  - Potential testing of a scale demonstration system

3. Task 2: Coatings

3.1 Coating Process candidate Overview

3.1.1 Coating Process Matrix

There are numerous trades to consider for the application of a highly reflecting far ultra violet (FUV) aluminum coating to a large mirror substrate. This study explores the pros and cons of potential coating processes ranging from those that are familiar and well characterized to those that are derived from emerging technologies. Given the atomic layer deposition (ALD) family of processes are the only ones to demonstrate the required FUV reflectivity while maintaining reasonable durability the focus will be on this set of processes.

3.1.2 Legacy FUV Coating Process

Legacy coating processes can be used as a baseline for comparison. Coatings produced via ebeam and thermal evaporation have existed for decades and have yielded solid spectral and durability performance for their missions. A legacy process such as the one used on the Hubble Space Telescope (HST) utilized an Aluminum reflector protected with an MgF_2 overcoat. This system provides a great deal of performance for its cost. Furthermore, the coating process utilized is extremely compatible with standard optical fabrication processes.

Table 5 Coating Process Matrix

Process	Spectral Performance	Coating Durability	Process Concerns
Baseline (Legacy)	Limited performance below 120nm FUV	Proven Long-Term Durability	Highest TRL
Evaporation & Sputtering Hybrid process	FUV performance - TBD (No expectation of FUV reflectivity below 120nm)	TBD	Layer thickness control
Evaporation & ALD Hybrid process	Demonstrated FUV reflectivity	Limited Durability	High temperatures required will require changes to optical fabrication order of operations or substrate properties
Evaporation & ALE (Atomic Layer Etching) + ALD Hybrid process	Demonstrated FUV reflectivity	Limited Durability	High temperatures required will require changes to optical fabrication order of operations or substrate properties
Evaporation & PEALD Hybrid process	TBD	Limited Durability	RF plasma may affect other components of flight optic Not clear how much lower process temp would be with PEALD

The process focuses on a vacuum chamber capable of reaching an ultra-high vacuum (UHV) environment reducing all potentially harmful background gasses to a minimum. These gasses include O_2 and water vapor that can rob the aluminum coating of its FUV reflectivity. The fact that this process is done cold not only contributes to the high reflectivity of the aluminum film, it also removes distortion and material property concerns associated with high temperatures. However, creating a durable and high performing FUV coating with this method is probably not feasible and therefore this process is not a strong candidate. High performing FUV coatings require extremely thin, pinhole-free coatings to deliver the combination of reflectivity and durability. Conventional processes simply do not offer this level of defect density and thickness control.

Figure 13 Collins 72" optical coating chamber can be configured for single rotation (1.5m capacity) or with (3) 28" dia planets. Similar chambers are available in our Danbury facility for coating mirrors up to 2.5-meters

3.1.3 Hybrid Processes

Given the reflectance of the aluminum layer will be optimized via thermal evaporation the final desired process will almost certainly end up as a hybrid process where the reflective Al layer is deposited via thermal evaporation and the thin protective layer is arrived at by some other process. Sputtering is one such process as is ALD or a plasma enhanced version it.

Although Sputtering is a well characterized process it is unclear if its benefits regarding durable, dense, low-defect films will be realized in a coating process supporting FUV reflectance. Fluorides are not known to behave well as targets for RF magnetron sputtering. They are typically plagued with cracking and other issues.

Since high FUV reflectance is determined to be the critical technical need the most promising process center around ALD. ALD can deliver extremely thin (< 20 angstroms) defect free continuous layers of protective overcoats such as AlF3. These overcoats show promise as a safe trade between FUV spectral performance and durability in hi-bay environments. However, there are drawbacks to arriving at such a process. Most notably ALD requires elevated temperatures to grow dense and durable films as well as to support the reaction between the precursor and the co-reactant gas. Additionally, ALD processes typically use toxic gasses requiring special equipment for handling.

One of the more favorable options is to use a plasma enhanced ALD process (PEALD). This option allows an RF plasma to excite the ALD film being deposited taking the place of the high process temperature. An investigation would need to be conducted to determine the extent that plasma enhancement can reduce process temperature.

3.2 Mirror Storage and Cleaning

Storage and cleaning of all these sensitive optics poses yet another threat to coating survival. Given the ultra-thin properties of the protective overcoats the coated optics will require a controlled environment (minimal humidity exposure) to maintain their performance over the course of AI&T which is expected to be measured in years.

Some potential protection solutions are gaseous nitrogen (GN2) or clean dry air (CDA) purge, and vacuum storage of optics and sub-assemblies. Often a simple protective cover will suffice for light-weighted mirrors, but this baseline solution is not expected to be enough to prevent these delicate coatings from degrading. The mentioned storage options naturally have pros and cons associated with them. GN2 storage is a familiar practice, but could run into complications for assemblies this complicated posing a personnel safety risk as well as a repeated delay for each metrology sequence during AI&T. This delay would be driven by the system coming to equilibrium with the local environment as it re-absorbs moisture. CDA and or Vacuum storage eliminates the asphyxiation safety risk, but not the wet/dry metrology complications. Vacuum storage also brings with it the added cost and maintenance of pumps and semi-ridged chambers.

One solution to consider early on in the mirror design stages is to allow for protective covers that only protect the coated optical surface of the individual optics. Although each mirror would require special design features to accommodate such a cover, these covers would only purge the areas that most need it providing a high degree of protection without the water absorption / desorption delays that might be associated with purging the entire subassembly or complete structure.

Table 6 Potential Protection Solutions

Process	Description	Pros	Cons
Purge (GN2)	Purge assembly or assemblies in nitrogen gas (GN2)	- High TRL - Low Cost - Simple structures - Scale-up	- Safety concerns (asphyxiation) - Requires a constant GN2 source and vent - Potential metrology issues in AI&T associated with moisture absorption / desorption
Vacuum	Store optics / assemblies in vacuum Dry scroll or even small turbos	- No personnel safety risk - Minimal contamination risk	- Cost - each assembly requires it's own pumping station (>5k per unit). - Requires a ridged structure (chamber) - Scale-up - Potential metrology issues in AI&T
Clean dry air (CDA)	Purge optics with CDA	- No personnel safety risk - High TRL - Low Cost - Simple structures - Scale-up	- Testing required to determine if coatings are robust enough to endure long durations in this environment
Exposed /covered (Baseline)	Leave optics exposed to ambient Hi-bay conditions (requires robust coating)	- Easiest storage method - Minimal schedule impact to AI&T	- Unlikely FUV coatings can withstand long term exposure to atmosphere (even lab air) without degrading

3.3 Vendor collaboration activities

A successful coating development scale-up program will require a collaborative effort with each team helping to meld their expertise into a successful deposition on a flight article. Collins has working relationships with a wide range of vendors with different specialties. The intent would be to pull on some of those vendors' strengths to scale up a durable, high performing FUV coating.

MLD Technologies (Eugene, Oregon) specializes in visible and NIR optical coatings. Although there heritage is based in ion beam sputtering they have recently delved into ALD processes specific to optical coatings. While they do not currently have fluoride ALD deposition capability in-house their optical background combined with their large 1- meter capacity ALD chamber should be considered and asset to the development effort.

ALD NanoSolutions (Broomfield, Colorado) lacks the optical background, but they do have experience in fluoride depositions which is not common. In addition to this they have strong ties to University of Colorado Boulder which specializes in both ALD depositions (George Research Group) and FUV measurements (LASP).

Finally CHA industries (Fremont, California) designed and developed a Mark 80 variant of their line of vacuum coating chambers. The Mark 80 is unique since it has (2) large processing chambers separated by a 2.3 meter gate valve to facilitate load-lock operation. While this chamber was initially designed for horizontal material processing, one could envision this chamber being used to coat mirrors with a hybrid PVD / ALD process. The lower spool piece unit would contain all the hardware required for PVD (thermal) depositions of aluminum metal. The upper spool piece would be used for ALD processing and the gate valve would be used to separate the two. Needless to say there are a lot of details to work out regarding pumping and thermal control, but the long throw distances for the thermal depositions would promote uniformity and the gate valve would enable ALD deposition to occur within the limited volume of the smaller chamber expediting pump & purge cycles of the ALD depositions.

3.4 Future Test and Analysis

For any coating development effort a design of experiments (DOE) would be conducted to determine the optimal coating process for a particular mission. Given the extreme needs of this particular coating a very detailed DOE would be required. The following is a proposed test protocol to support a down-select of the optimal durable FUV reflector coating process:

1) Produce multiple batches of coating samples focusing on ALD process variants:
    a. Critical process parameters to vary for DOE:
        i. Physical thickness of protective layer(s)
        ii. Protective layer materials (LiF & AlF_3 are leading candidates)
        iii. Process temperature (50 to 300 deg C)
        iv. Process pressure
        v. ALD Cycle time
        vi. Delay time between Al metal and protective layers
        vii. Power levels of PEALD processes
2) Measure BOL spectrals FUV – VIS – LWIR
3) Subject samples from each batch to typical optical coating durability tests:
    a. MIL-F-48616 – standard test
    b. Enhanced Humidity
    c. Salt Fog per ASTM B-117
    d. 10 day Humidity

    *Note severity of test can be adjusted to support relative characterization of test runs. FUV reflective samples should not be expected to be as robust as other coating samples.
4) Subject samples from each batch to typical contaminants and an array of potential cleaning methods:
    a. Contaminants:
        i. Particulate
        ii. Glove & finger prints
        iii. Water spots
        iv. IPA & Acetone overspray
    b. Cleaning Methods:
        i. Solvent Wipe
        ii. Ionized GN2
        iii. CO_2 Snow cleaning
        iv. Low tack protective films
5) Measure Post-Test spectrals FUV – VIS – LWIR

A durable FUV reflective coating creates numerous challenges for manufacturing and especially coating operations. There are multiple paths to consider and evaluate prior to committing to a particular manufacturing flow. Given the promise ALD coating depositions hold for both spectral and durability performance, these paths should be prioritized to raise their maturity level. Any investigation into these processes should include a task to evaluate methods for reducing process temperatures and therefore increasing compatibility with standard optical fabrication practices.

7.2 Harris Report

HARRIS®

Final Report

System-Level Segmented Telescope Design Study (SLSTDS) for NASA ROSES D-15

From:
HARRIS CORPORATION
Space and Intelligence Systems
Rochester, NY 14629
Karen Kelly
Contracts Manager
kkelly06@harris.com
585-269-5872

To:
Lockheed Martin Space
Contract No. **4103822451**
1111 Lockheed Martin Way
Sunnyvale, CA 94086-3504
Dr. Alison A. Nordt
alison.a.nordt@lmco.com

Approvers	Function /Title
Lynn Allen	Program Manager
Laura Abplanalp	Director, Civil & Commercial Imaging Business Area
Mike Anstett	Sr. Manager, Trade Compliance
Bryan Fromm	Sr. Manager, Security
Leslie Crossen	Director, Contracts

Table of Contents

List of Figures

List of Tables

Executive Summary

Harris is proud to partner with Lockheed Martin on the System-Level Segmented Telescope Design Study (SLSTDS) program for NASA ROSES D-15 Phase 1. This report satisfies the requirements for Lockheed Martin Contract Number 4103822451 by completing preliminary assessments and analyses that give confidence in the successful future development of solutions to meet the engineering challenges posed by the LUVOIR and HabEx Large Mission Concepts.

This report provides details in three major sections:

1. Primary Mirror (PM) and PM Segment Mirror Assembly (PMSA) design concepts and related trades
2. High-volume / rapid PM segment manufacturing and metrology approaches required to produce the ~120 mirror segments in a cost-effective and timely manner (~5 years)
3. Discussion of potential testbed and technology demonstrations intended to advance Technology Readiness Levels (TRL) for key areas in preparation for the Large Mission Concepts

The output and recommendations from this study are described in greater detail in each respective section. The results of this work provide the basis for further discussion and may be applied to the next phases for the SLSTDS project. Harris looks forward to working with Lockheed Martin on the SLSTDS Phase 2 and Phase 3 projects.

1.0 Introduction

Harris Corporation (Harris) is pleased to be a member of the Lockheed Martin Space (LM) System-Level Segmented Telescope Design Study (SLSTDS) team for the NASA ROSES D.15 Phase 1 study. This final report is in response to and fulfillment of the Lockheed Martin Contract Number 4103822451.
The key objectives of this study identified by LM are:

- Address system-level design challenges of large, Ultraviolet/Infrared (UV/IR) space telescopes to achieve picometer-level wavefront stability for coronography-based science.
- Identify and develop test bed opportunities to anchor picometer-class integrated models.
- Inform NASA technology development plans to support large telescope missions for the 2020 Decadal Survey.

The goal of the overall effort is to establish first-order engineering confidence in the feasibility of picometer stability for large space-based telescopes through analysis and identification of anchoring testbeds. NASA-sponsored Science and Technology Development Teams (STDTs) are developing the telescope concepts in preparation for the 2020 Astrophysics Decadal Survey. Industry support to the STDTs and NASA Headquarters supports the study teams through assessment of the current state of technology, as well as identification of technology development needs based on current understanding of requirements for the respective missions.

This report is Harris' response to the following tasks as outlined in the agreed-to Statement of Work (SOW), in the context of two of NASA's Large Mission Concepts: The Large Ultraviolet-Optical-Infrared (LUVOIR) Surveyor and the Habitable Exoplanet Imaging Mission (HabEx). For clarity, the ensuing discussion covers both LUVOIR or HabEx even though only one may be mentioned. The SOW tasks are:

1. Identify trade studies recommended to support technology development for future large space telescopes.
2. Develop concepts for testbeds that can address significant uncertainties (testbeds to be completed during years 2 and 3).
3. Primary Mirror Segment Manufacturing Process concepts
   a. Mirror manufacturing approach for large numbers of off-axis, lightweight mirror segments for large space-based telescopes like LUVOIR
   b. Use of novel processes including Harris approaches, robotics and automation

1.1 Background and Experience

Harris has considerable experience and success in the development, design and delivery of exquisite optical systems for both space-based and ground-based programs. This experience includes assured performance to meet challenging mission requirements. Highlights of our experience include:

- Successful delivery of over 130 missions in orbit with Harris components.
- More than 50 years of operational excellence meeting the most stringent optical requirements for the high-performance optical systems.

- Industry (both domestic and international) leadership in optical component, assembly and system design; deterministic processing; assembly and testing through vertical integration, driving solutions to meet technical, cost and schedule requirements.

Harris has been at the forefront of innovation and development related to large optical components, both in design and in optical processing for more than 50 years. Our capabilities to design, mount, process and test large optical components and systems to meet both civil and proprietary needs is world-class. A graphical timeline of Harris innovation is shown in **Figure 1**. Continuation of this demonstration of innovation and execution will be leveraged to benefit the NASA Large Mission Concepts moving forward.

Figure 1: Harris innovation of more than 50 years to advance lightweight mirror technology for both space- and ground-based optical systems through design and manufacturing processes to reduce timelines and cost while meeting demanding requirements.

2.0 PMSA related Design Trades

2.1 Summary of Technology Gap for PM Segments

LUVOIR will need affordable, ultra-precise mirror segments fabricated to Ultraviolet (UV) surface figure error (SFE) specifications. In addition, the mirror and structures demand picometer level stability, driving thoughtful and thorough specification and selection of materials, processes, and control systems. Certainly, Corning ULE® provides an excellent starting point to produce high-stiffness, closed back mirror segments. The LUVOIR-A system needs 120 – 1.2m class lightweight mirror segments for the 15m primary mirror (PM) aperture; this requires high production throughput and cost-effective processes to meet program budgets and timelines (say on the order of five years production duration).

2.1.1 Current State-of-the-Art (SOTA)

UV quality mirrors are routinely fabricated at small sizes, <0.5m, for the semiconductor industry. Large, lightweight mirror segments have been processed to 8nm RMS (Root Mean Square) surface quality, but a mirror segment meeting the UV requirement of <5nm RMS surface quality for both low and mid-spatial frequencies, has not been demonstrated. The key capabilities that must be demonstrated are:

- Ability to deterministically control low, mid, and high (micro-roughness (μR)) spatial frequency content of the mirror surface to achieve UV requirements.
- Ability to perform mirror metrology to a high enough precision (with sufficiently small uncertainties) to verify that UV requirements are met.
- Produce a lightweight, high-stiffness mirror design and calibrated opto-mechanical model to enable accurate predictions of on-orbit performance based on 1-G measurements.
- Perform the three tasks above in an affordable and timely manner

The key capabilities of an affordable, full solution to produce large, lightweight mirror segments that meet UV requirements must be demonstrated including the level and method in which actuators are used to achieve the required stability.

2.1.2 PM Trade Space

2.1.2.1 PM Baseline Description

LUVOIR-A has a f/1.45 PM with parent radius of curvature (ROC) of 43.5m. Over the nominal segment size of 1223mm flat-flat (1442mm point-point), the maximum sag across any mirror segment is relatively low, ranging between ~5.5mm to 6mm depending on location.

Harris fabricated similar segments for the Multiple Mirror System Demonstrator (MMSD) program, with ROC less than half that of the LUVOIR-A concept. The current SOTA described in Section 2.1.1 refers to the MMSD program in this paper are documented in a 2010 SPIE Mirror Technology Days presentation (paper 42, https://optics.msfc.nasa.gov/tech/tech_days_2010/) and, for U.S. persons, available through Dr. H. Philip Stahl of the NASA Marshall Space Flight Center.

2.1.2.2 MMSD Mirror Description and Process

Harris manufactured several segments for the MMSD program, a ground demonstration program led by NASA JPL. The mirrors were constructed of Corning ULE® glass and fabricated using the Harris proprietary Low Temperature Fusion (LTF) and Low Temperature Slumping (LTS) processes. When using the LTF/LTS manufacturing process, Harris polishes the mirror components, the front and back plates (considerably thicker than the finished dimensions), and the core solids as planos (i.e. flat surfaces). The core solids are then light-weighted using Abrasive Waterjet (AWJ) cutting and then fused to the plates via the LTF process. A CAD schematic of the MMSD mirror is shown in **Figure 2** and a photo of the MMSD PMSA is shown in **Figure 3**. After the mirror blanks were fused, the facesheets were thinned (the back plates to final thickness) and then the mirror blank was slumped over a mandrel that had the best fit sphere of the parabolic optical surface via the LTS process. The front faceplate was conventionally processed, with subsurface damage removed after final plate thinning, followed by polishing operations and finally with ion beam figuring (IBF) to achieve the requisite surface figure error requirements.

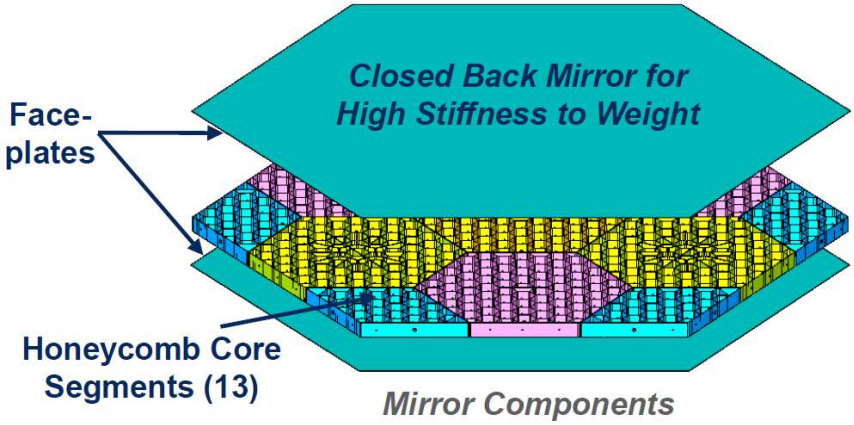

Figure 2: Schematic of the MMSD Mirror utilized a segmented core to mitigate risk of glass breakage during AWJ light weighting.

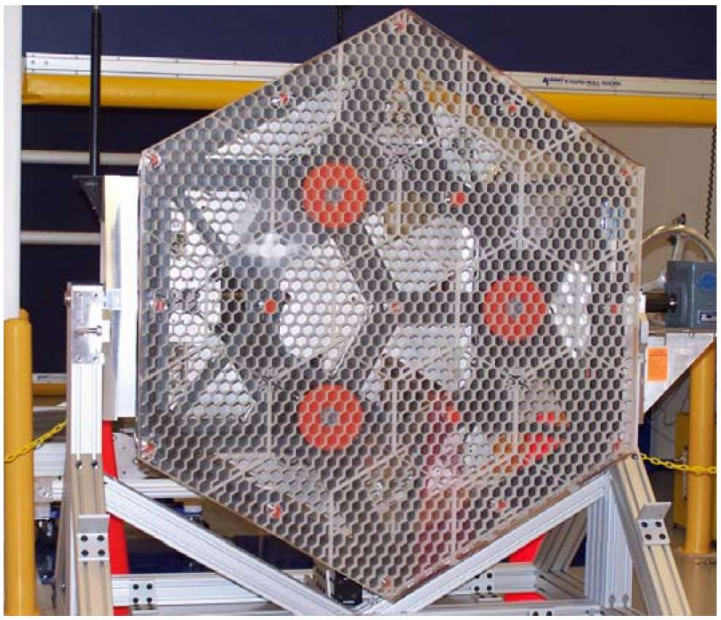

Figure 3: An MMSD PMSA shown in a ground support test stand.

2.1.2.3 Mirror Production Advancements

Following the completion of the MMSD program, Harris developed an advanced mirror blank manufacturing process known as Capture Range Replication (CRR). Using the CRR process, which is described in detail in Section 3.2, the mirror blank is fused with both facesheets at final thickness to the light-weighted mirror core structure, and then replicated over a precision mandrel via a process similar-to LTS described earlier. Mandrels may be used multiple times for duplicate mirror types, common on large segmented primary mirrors. The CRR process delivers a replicated optical surface that is within “capture range” (i.e. within a handful of microns of the desired SFE p-v) of deterministic mirror finishing processes, and then leverages the processes that use computer-controlled solution to converge rapidly to the final SFE requirement for each mirror. Deterministic processes include IBF and Magneto-rheological Finishing (MRF), both well-suited for ULE® mirrors.

Successful replication using CRR eliminates the costly and time-consuming conventional mirror off-axis aspheric surface generation and polishing processes, and therefore significantly reduces mirror production cycle time and cost. This process is well-suited for high-volume production of precision, light weight, ULE® mirrors. Feasibility and demonstration of the CRR® process has been completed on Harris IRAD projects at the sub-scale level, achieving excellent results, and is now in the implementation phase for larger mirrors on production programs.

2.1.2.4 PM Segment trades

Harris has incorporated CRR into mirror manufacturing flows in two different ways. With the first method, components are initially processed plano-plano, identical to the LTF process, with the facesheets at final thickness prior to LTF. The mirror blank is then “formed” in a single LTS cycle over the precision mandrel. With the second CRR method, mirror components (facesheets and core solids) are initially processed curved, and then a single LTF/CRR furnace cycle is used to form the ULE® mirror blank.

For LUVOIR, both manufacturing approaches have a slight impact on the mirror design details. Given the small sag (<6mm) for the PM segments, it is likely that when trading the two process approaches, the first method (process plano components, LTF and CRR cycle) may reduce the number of process steps, thereby reducing cost.

Since the MMSD segments were manufactured (2008 timeframe), there have been additional advancements in AWJ technology that have increased machine and process reliability and reduced process times. These have been accomplished by using higher water pressures that give higher cutting speed while yielding finer surface finishes. Given these advancements, an additional trade aspect of the LUVOIR PM segment design that will be considered is a segmented core versus a monolithic core. A monolithic core enables a lighter-weight PM and potentially enables other technologies (still in development) such as core pressurization during CRR to minimize quilting / mid-spatial SFE contributors and to generate mirror geometries to tighter tolerances. Additive manufacturing and constructed core technologies currently in development may also become part of the PM segment design trade space.

The large lift capacity of future launch vehicles may relieve constraints on mass enabling open-back mirrors made from Schott Zerodur® or other materials to be considered for LUVOIR. This is another trade for future consideration.

Other trades to be considered at the PM segment and assembly level, assuming a closed back Corning ULE® mirror are those typically performed during any mirror design or optimization. These include:

- Facesheet thicknesses
- Core geometry
- Mirror first mode (free-free and mounted) and mirror dynamic factors affecting telescope dynamic performance
- Mirror Mounting approach
  - Requires attention on LUVOIR due to the telescope WFE stability specification of 10 picometers over 10 minutes

2.1.3 PMSA Trades

2.1.3.1 Mechanical Architecture Trades

One trade for consideration at the PMSA level involves evaluating the amount of control authority over each PM segment. The baseline LUVOIR-A design includes “7 degree of freedom (DOF)” of control authority: 6 DOF in rigid body and 1 DOF for radius change. As mirror manufacturing and thermal control system technologies mature, it may be viable to have a PMSA with only the 6 DOF rigid body actuation.

On the other hand, there could be advantages to incorporating greater figure control authority over each segment and replacing the single radius actuator with a suite of 10 Figure Control Actuators (FCAs). This could allow low spatial frequency errors in the segment to be corrected to better than single digit nm rms SFE accuracy.

Stability, heat dissipation and the dynamics of the FCAs will require detailed assessment. Harris envisions that FCAs (including a radius control actuator) would be “set and forget” and hence heat dissipation in the FCAs would only be of concern during system initialization and calibration. If required, the FCAs could be used to correct PM SFE on a seasonal basis or an even longer time scale to correct for longer term instabilities from items such as composite dry-out and Invar growth. Operation of FCAs at higher frequency will require technology demonstrations and adequate WFSC feedback.

Due to the nature of the LUVOIR performance requirements, Harris envisions during normal operations that sensors will be used as feedback for closed loop control of PM segment phasing through use of the RBAs. The required RBA technology is described in Section 2.3. During coronographic observations needing 10 picometers of telescope WFE stability over 10-minute time periods, better performance may be achieved by powering down the RBAs, assuming that this can be done in a manner that maintains mirror segment phasing to required tolerances. This is another system-level trade that should be performed as the details of the LUVOIR architecture are developed.

PMSA reaction structure (RS) design has its own trade space that will be somewhat dependent on the PMSA actuation architecture discussed above and dependent on the Thermal Control System Considerations discussed in Section 2.2. Other design considerations to be traded are typical of precision structures in terms of composite material and fitting material selection, composite layup design, and fitting designs to accommodate all interfaces with the PM segment and the PM back plane.

2.2 Thermal Control System Considerations

2.2.1 PMSA Thermal Control System (TCS) Trades and Development

The LUVOIR PMSA has both a near steady-state or average thermoelastic shape which dominates the ground to orbit thermal shift, and a temporal thermoelastic shape driven by temperature changes in the environment surrounding the mirror and its support system. The sunshade temperature changes seasonally, long term with finish degradation, and with orbital maneuvers, and these small changes result in optical instability. Minimization of these perturbations is essential to the success of the exoplanet mission of LUVOIR.

2.2.2 System Thermal Design and Trades – Average and Ground-to-Orbit Shift

The PMSA, as with other space-based optical payloads, will cool towards deep space proportional to the emissivity of the mirror coating, and then draw heat from the support structure heaters at the uncoated surfaces of the mirror proportional to its emissivity, reaching a radiative equilibrium temperature. This heat flow sets up a natural gradient in the mirror, resulting in a global cooling of the mirror and a predominantly axial gradient, with the front surface colder. The magnitude of the gradient will be dependent on the mirror geometry and material properties; for glass mirrors this will typically be 2-7K in this size class.

However, the gradient field is somewhat more complex than axial due to local design features such as mounts and actuators, resulting in some radial and diametrical changes in addition to the axial term. The thermoelastic deformation of the mirror that results will be dependent on the gradients, the spatially dependent Coefficient of Thermal Expansion (CTE) of the mirror, and the strains induced through the mirror support system.

2.2.2.1 Thermal Trade 1 – Optimized Nominal Heater and Insulation Layout

Managing these gradient conditions is typically achieved with an active thermal system configured to a single average setpoint to hold the mirror at a nominal temperature. With a more capable variable setpoint heater control system, the temperature surrounding the mirror can be tailored using a circumferential and radial heater configuration to better offset some of the thermal conditions. Additionally, the CTE of ULE® front and back plates can be selected and coordinated, and since the gradient direction is deterministic, the bending of the mirror due to axial gradient can be minimized.

In summary,

- Optimize heater placement and setpoints (one set point or many)
- Desensitize thermoelastic deformations due to axial gradient with ULE® plate selection (determine the benefit and uncertainty of this option)
- Consider mirror edge and support system thermal management – heaters vs passive insulation vs no insulation

2.2.2.2 PMSA Thermal Stability

To address the temporal stability in the PMSA, several “tools” are available in our telescope control electronics including proportional integral derivative (PID) control, variable setpoint, and milli-Kelvin or better control with rigorous thermal and electrical design. For example, control sensors must be closely coupled to heaters, and PID control parameters must be carefully tuned during ground test to insure stability. Additionally, selecting a bandwidth for the heater

control system with respect to the thermal time constant of the optic can maximize control stability.

Figure 4 illustrates this latter point. Consider initially that the heater controls installed below a lightweight optic are updating at 1 Hz or faster, very little disturbance is noted in the mirror due to the radiative coupling. However, the PMSA temperature will tend to proportionately follow a slow-moving slew and resulting sunshade temperature change over 24 hours (~10^{-5} Hz). This latter scenario can be addressed with tailoring the radiative coupling to the shade via its thermal design (i.e. optimizing T^4 x emissivity). Perhaps even more promising, with on-board or ground processing "intelligence" of thermal telemetry, the small change in temperature of the mirror due to the slew can be measured, characterized, and even anticipated with the mirror heaters gradually tuned to optimum control settings (aka Predictive Therma Control, PTC) ahead of a maneuver.

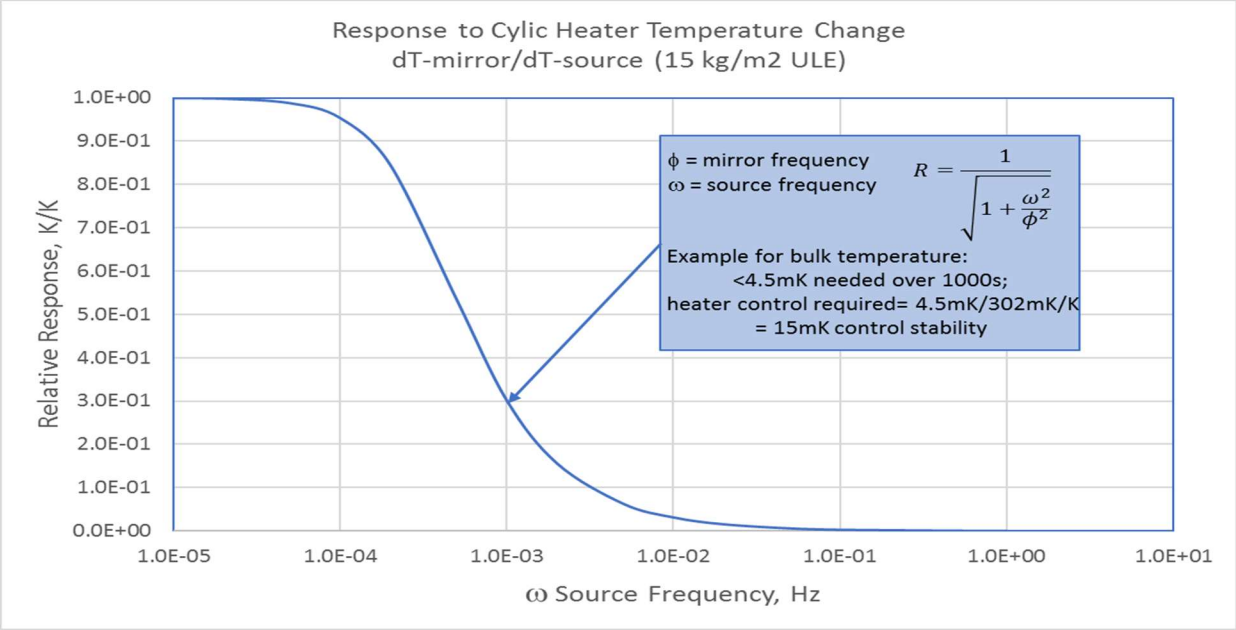

Figure 4: Mirror temperature response to cyclic heater temperature changes

2.2.2.3 Thermal Trade 2: Minimizing Response to Sunshade Temperature Drift

Both passive and active methods will be explored to maximize stability during a slew. First desensitization to shade changes through optimization of radiative coupling and shade temperature. This is a trade at the system-level that should engage the systems and shade teams. Second, explore predictive thermal control methods to enhance stabilization time and to minimize the total gradient change in the mirror.

2.3 Summary of Technology Gap for PM Actuation

LUVOIR needs ultra-precise and stable RBAs to accomplish UV primary mirror segment phasing and coronagraph science. It is assumed that to accomplish this a course alignment stage along with an in-series ultra-fine stage of sub-nanometer precision is required. Sub-nanometer stability is required during coronagraphic image collections. A high-level conceptual design of an RBA with flexure ends is shown in **Figure 5**.

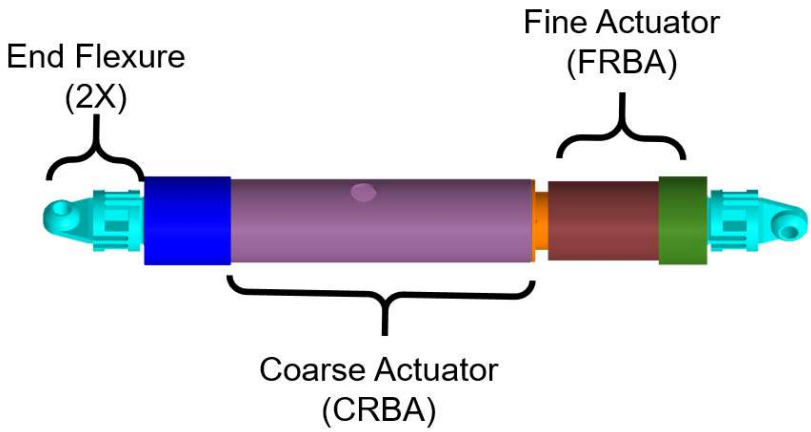

Figure 5: High level concept of an RBA with coarse and fine stages in series

2.3.1 Current State-of-the-Art

The overall LUVOIR precision and stability specifications are not well-defined or attained in any system-level actuator at this time. The coarse stage concept is reasonably straight forward, but when combined with the stability requirements becomes very difficult due to the metallics involved in the construction of the various strut and DC brushless motor components. The fine stage, comprised of a piezo stack and currently requires 18 to 20 bit voltage precision to obtain the required sub-nanometer precision, is pushing the SOTA for control electronics. When the coronographic imaging stability requirements are considered the current SOTA control electronics may not be adequate.

It should be noted that at the time of this report, Harris is developing a dual-stage RBA and will be subjected to testing to advance the TRL to 6. The specific design of this RBA does not meet the requirements of LUVOIR but serves as an excellent point-of-departure design when developing the actuators needed for LUVOIR.

2.3.2 Rigid Body Actuator (RBA) Trades

Trades in the mechanical and electrical design on the RBAs will be required as the existing RBA is modified and matured to meet the requirements of LUVOIR. On the mechanical side, trades on material selection and RBA axial- and end-flexure lateral stiffnesses will be traded. Trades on the control system design and the level of bit precision in the electronics need further study, assessments and development. This is discussed in some additional detail in Section 4.1.2.

3.0 Mirror Manufacturing and Metrology Approaches

3.1 Introduction

Future segmented space telescope mirrors need not be constrained by the cost precedent set by JWST. The Advanced Mirror System Demonstration (AMSD) development, which created prototype mirrors and production plans for beryllium and ULE® mirror segments, ultimately projected significant cost and schedule advantages for the production of ULE® substrates[1]. Just as beryllium was selected for JWST as the best technical performance solution for the cold environment, ULE® is a technical solution best suited for ultraviolet optical infrared (UVOIR) environments. Mirrors for a UVOIR 400μm diffraction-limited system need surface figures with at least 5x less errors than JWST and feature challenging requirements for surface micro-roughness (μR) as well. However, there is no requirement to operate at cryogenic temperatures. UVOIR challenges are not necessarily more difficult than cryogenic, but they are different. The fact that the LUVOIR mission nominally operates at 270K as opposed to room temperature complicates design, manufacturing and test of the PM segments and other mirror components. A summary of notional UVOIR requirements is in **Table 1**.

Table 1 Notional UVOIR requirements

Spatial Frequency Band	Spatial Freq Definitions	Spatial Periods (assuming 9m aperture)	Estimated Requirement (surface figure error)	Surface Error Drivers/ Limitations
Low	Full parent aperture- ~ 6 CPA	~9m-1.5m	<5nm rms	• Segment to segment alignment / radius matching
Mid	~6 cpa-60cpa	~1.5m- 0.15m	<5nm rms	• Corrected through deterministic finishing • Final surface figure **only limited by metrology cycle reproducibility**
High	>60 cpa	~0.15m-0.001m	<1.5nm rms	• Corrected through smoothing • Leverages calculated stiffness polishing tools to globally conform to the low order optical prescription while appearing "stiff" to mid-spatial frequency errors
Micro-roughness	High angle scatter	~1mm-0.001mm	<0.5nm rms	• Corrected through optimized polishing parameters • Slurry, polishing tool

Specifically, JWST beryllium mirror substrate development was challenged by factors including its' toxicity to humans during machining processes and challenges in polishability. In contrast, ULE® is non-toxic, has maximum compatibility with polishing and deterministic finishing processes, and may be thermally formed. It should be noted that other glass substrate materials have properties in-family with ULE® that could be attractive for UVOIR applications including, but not limited to Zerodur® and Cordierite. With the advent of replicated mirror production for ULE® mirrors, something not viable with glass ceramics such as Zerodur®, significant opportunities exist to enable acceptable programmatic cost and schedule for large UVOIR segmented space telescope primary mirrors.

[1] H. Philip Stahl, Lee D. Feinberg, Scott C. Texter, "JWST primary mirror material selection," Proc. SPIE 5487, Optical, Infrared, and Millimeter Space Telescopes, (12 October 2004); doi: 10.1117/12.549582

3.2 Background and Prior Art

The challenging requirements for UVOIR segments are fully addressed by deterministic finishing techniques which use metrology and computer-controlled material removal methods to achieve a mirror surface that meets SFE requirements. These processes are fully data-driven and parallelizable, which means that the most challenging requirements for UVOIR segments will not create a bottleneck that limits the rate of production of many segments. Fabricating a massive quantity of segments for a LUVOIR primary mirror in a reasonable timeframe can leverage existing industry strengths and capabilities.[2] Processes for both final mirror figuring and metrology are now being developed and implemented for the segmented primary mirrors for programs such the European-Extremely Large Telescope (E-ELT) and the Thirty Meter Telescope (TMT). Even though these are large ground-based telescopes, the methodologies will provide useful information and capabilities for LUVOIR PM segment production.

3.3 High Volume Mirror Manufacturing

For facilities that fabricate large optics, assembly line approaches are the exception, not the rule. Only a handful of completed primary mirrors have been comprised of a significant number of mirror segments (for example the Keck telescopes, the Hobby-Eberly Telescope (HET), the South African Large Telescope (SALT), the Gran Telescopio Canarias (GTC), and the James Webb Space Telescope (JWST)), and of these, only JWST is space qualified. Optical fabricators must bring to bear production economies of scale to enable LUVOIR or large in-space-assembled telescopes. These approaches are also applicable to HabEx. As discussed briefly in an earlier section, a key enabler to scaled production of many mirror segments is Capture Range Replication (CRR).[3] CRR is a process which eliminates the high costs associated with traditional mirror generating, grinding and polishing by enabling replication of multiple common mirror segments using a precision mandrel.

Figure 6 explains how abbreviating the steps to reach a finished optic reduces cost and schedule. The area under the curve in the righthand plot (representing replication) is significantly less than the area under the left-hand curve, indicating lower cost. The remaining cost of deterministic finishing becomes the new focus.

[2] Thomas Hobbs, Mary Edwards, and Andrew Fox "High volume ULE® segment production", Proc. SPIE 9912, Advances in Optical and Mechanical Technologies for Telescopes and Instrumentation II, 99123G (22 July 2016); doi: 10.1117/12.2235351; https://doi.org/10.1117/12.2235351

[3] James T. Mooney, Steven Desmitt, James Bolton, Stephen Oliver, "Advanced mirror construction: ULE replication," Proc. SPIE 10706, Advances in Optical and Mechanical Technologies for Telescopes and Instrumentation III, 1070608 (10 July 2018);

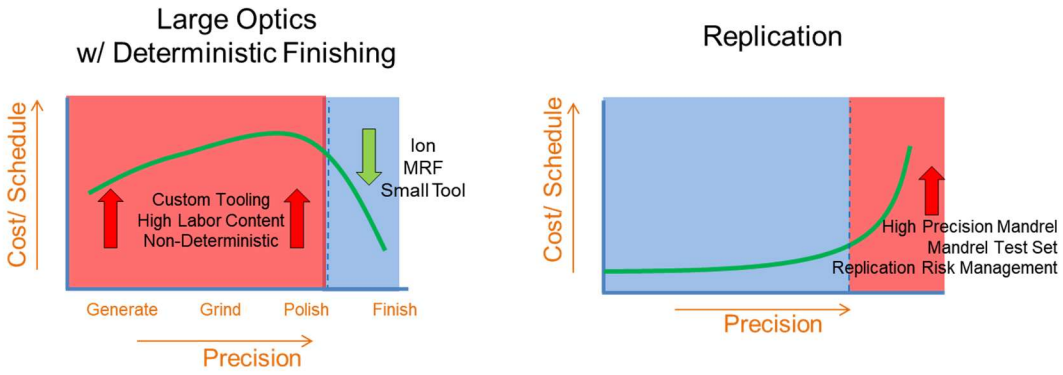

Figure 6: Advantage of Capture Range Replicated Optics

Instead of forming the mirror surface by generating the sag, grinding an asphere and polishing to required SFE, the lightweight mirror components enter a furnace with minimal pre-processing, and leave the furnace with the optical surface near the final optical prescription, or specifically, within "capture range" of final required SFE. Specifically, segments ultimately exit the furnace within capture range of deterministic finishing processes like ion beam figuring (IBF), MRF or computer-controlled small-tool processing (CCSTP). The process is scalable, repeatable, and can be used to produce many segments with same or similar optical prescriptions at a lower cost. CRR also mitigates challenges of radius-matching between many mirror segments.

The optimized implementation of CRR involves minimal pre-processing. Steps include wire-saw cutting of ULE® material into flat plates and cores, and lightweighting of the cores. Lightweight cores can be produced by component assembly methods (such as additive core construction) or by AWJ. Both methods are parallelizable and scalable. The mirror surfaces are then given a low-precision polish in preparation for Low Temperature Fusion (LTF) bonding. The components are LTF bonded and then sagged near the final shape. The process steps for the CRR process are outlined in **Figure 7**. **Figure 8** shows a summary of the traditional large optic processing steps which are eliminated by the CRR process.

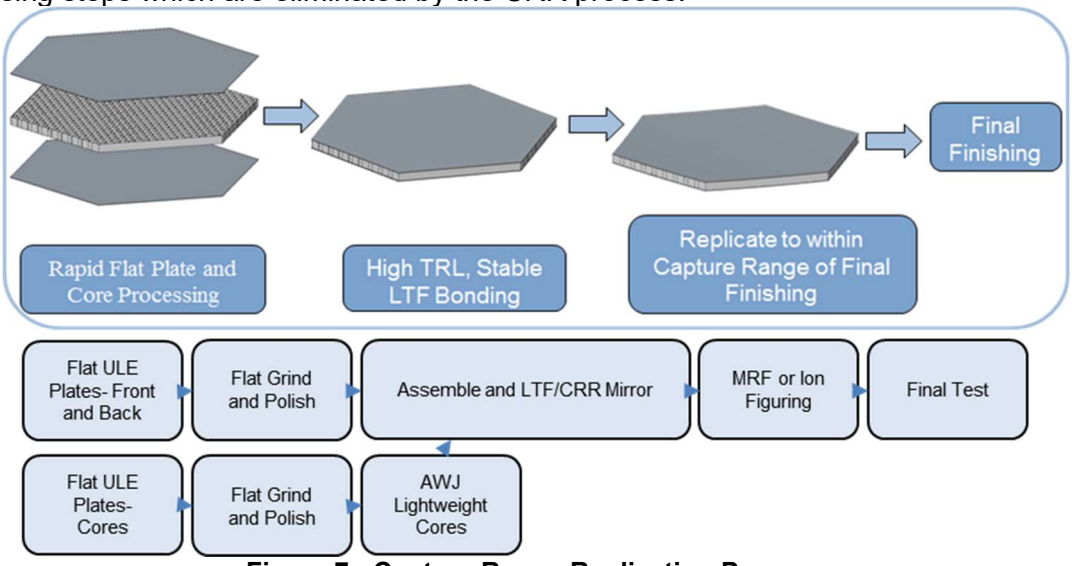

Figure 7: Capture Range Replication Process

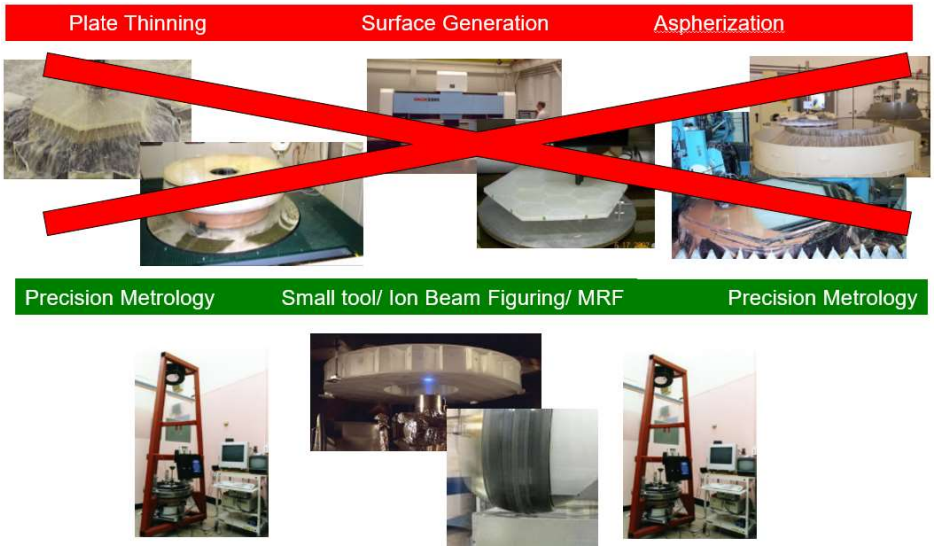

Figure 8: CRR Reduces mirror finishing cycle time for multi-unit production by omitting processes

While many traditional optic processing steps are eliminated, other steps and process equipment remain. There are opportunities to improve and optimize these remaining steps for multi-unit production. **Figure** essentially describes the approximate number of machines / equipment for each type needed to enable a certain throughput in UVOIR mirror substrate production, avoiding a given machine or process creating a bottleneck in the process. Note that **Figure** is built on assumptions about overall process definition for the throughput of each process. At production rates over 32 segments-per-year, some additional machines are included in this estimate for redundancy, as risk of downtime increases with more machines in use.

The scaling described in **Figure 9** applies to equipment / processes needed, with appropriate scaling to meet production demand. It is also assumed that all personnel have appropriate training and expertise and are available to support all phases at scale. Assumptions with respect to training and process expertise reflect a different learning curve. It is recommended that production process definition, training, and low rate of initial production (LRIP) are emphasized early in a large UVOIR program, to expedite the primary mirror fabrication. It is expected that PM segment fabrication will typically dominate the schedule critical path early in such programs. The outlined mirror assembly, integration and test processes are sufficiently parallelized as to not have any bottlenecks in the production cycle and meet expected schedule constraints.

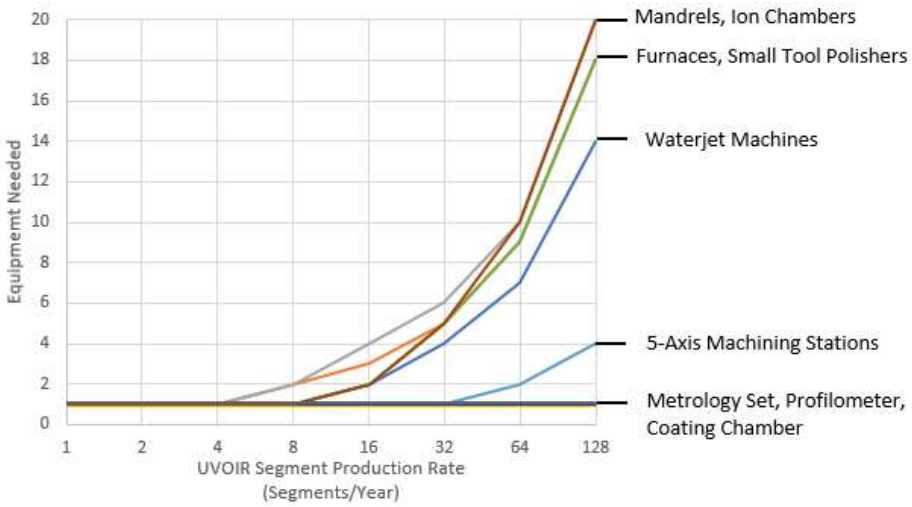

Figure 9: Scaling of Infrastructure and Heavy Equipment Needs

There are opportunities to enhance cost and schedule performance within the replicated mirror fabrication process. Specifically, flame polishing may represent a low-cost method to prepare plates and lightweight core surfaces for the replication process; this will reduce the burden on polishing and smoothing equipment shown in **Figure 9**. Also, additive core construction manufacturing may reduce the need for large waterjet machines highlighted in **Figure 9**, enable the use of fewer and smaller machines, and reduce the amount of material consumed. Additive manufacturing is an emerging technology that could further revolutionize the production of many precision mirror segments. The need for several IBF chambers may also be mitigated by forming in-situ metrology hardware, to rapidly iterate between measuring and deterministically figuring the mirror substrates via MRF or CCSTP, minimizing the need for IBF in final optical processing. This concept of in-situ metrology has been implemented on E-ELT and becomes essential when approaching high production rates. By identifying and developing approaches to improve each step of the mirror replication process, further cost and schedule gains can be realized. Note that segmented concepts for HabEx[4] can also take advantage of the efficiencies of producing multiple mirrors, but the required production rate would be much closer to the left-hand side of the plot in **Figure 9**. There would be no need for infrastructure investments.

There are also opportunities where mirror substrate fabrication and integration overlap. It is possible to perform final optical testing and IBF on a mounted mirror assembly. This enables looser tolerances in mount-induced strain, potentially reducing mirror segment assembly time. By relaxing mount-induced strain requirements for the integration process, quicker, more efficient mounting processes can be used, which will be especially essential for mirror systems with figure control actuators. Figure-actuated mirrors, which use many actuators (6-18) to actively or passively control the mirror surface, require numerous mechanical interfaces to the mirror. Integration and test of the mirrors will become a schedule driver, unless optimized processes and support equipment can be developed and tested in advance of mirror fabrication. By demonstrating how substrate fabrication strengths can reduce integration complexity and duration, the overall primary mirror fabrication schedule can be reduced.

[4] James T. Mooney, Matthew East, Bruce Rottner, Christopher Sullivan, David Wideman, David Redding, Kevin Schulz, "Mirror design study for a segmented HabEx system," Proc. SPIE 10698, Space Telescopes and Instrumentation 2018: Optical, Infrared, and Millimeter Wave, 106983I (24 July 2018);

3.4 Mirror Metrology

3.4.1 In-Process Metrology

In process metrology needs to be accurate to sub-micron levels. Given that the PM segments are fabricated from near-zero Coefficient of Thermal Expansion (CTE) glass or glass-ceramic materials, early in-process testing can be performed at ambient temperatures. There are new non-contact profilometers emerging that will be available for the testing of LUVOIR mirror segment sizes when LUVOIR is in production. In particular, a non-contact measurement technique called the “NANOMEFOS,” which stands for “Nanometer Accuracy Non-contact Measurement of Freeform Optical Surfaces,” originally developed by the Dutch organization TNO and commercialized by Dutch United Instruments, will be well-suited for in-process metrology.

Currently the NANOMEFOS technology can measure optics up to 1.0 m in diameter[5], but DUI has plans to scale the technology to a 2-meter platform. The initial NANOMEFOS platform developed by TNO can measure optics up to 0.5m in diameter with a claimed measurement uncertainty of <15 nm, a typical setup time of <1 hour, and a running time of <15 minutes (from TNO Technologies for Astronomy brochure). The technology promises to be ready and capable of meeting in-process metrology needs of the LUVOIR PM Segments.

3.4.2 Higher-Fidelity Metrology

The metrology approach shown in **Figure 10** (Burge, et al[6]) uses a full-aperture Fizeau test plate with a spherical convex reference surface on the test plate (TP). Computer-generated holograms (CGHs) are used to create the spherical reference wavefront and the aspheric wavefront of the unit under test (UUT). A concave reference optic (aka calibration sphere) is also required for in-situ calibration.

This technique is planned to be used for TMT primary mirror segment assembly testing and should be well-suited for testing the many LUVOIR PM segments and PMSAs at ambient or nominal operating temperature. It is likely that for system throughput efficiency, the higher fidelity metrology described will only be used at the operating temperature. A thorough assessment of metrology uncertainties with this testing approach are required to confirm compliance with LUVOIR requirements. None the less, this approach for testing many TMT PM segments is a worthy of attention for LUVOIR PM segment and PMSA optical testing and verification.

Evaluation of this approach in a horizontal test configuration to eliminate gravity-induced uncertainties will also be required. This may increase the complexity of this test concept considerably.

[5] (https://dutchopticscentre.com/measuring-freeform-optics-with-nanomefos/)

[6] James H. Burge, Chunyu Zhao, and Matt Dubin "Measurement of aspheric mirror segments using Fizeau interferometry with CGH correction", Proc. SPIE 7739, Modern Technologies in Space- and Ground-based Telescopes and Instrumentation, 773902 (19 July 2010)

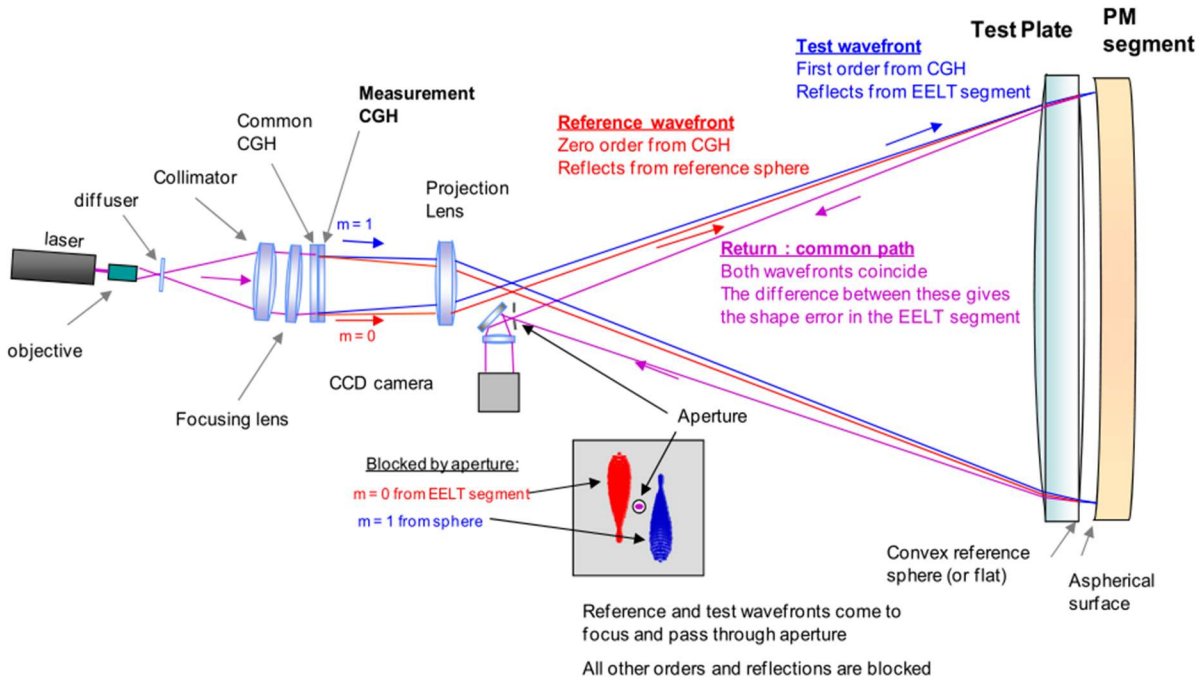

Figure 10: Schematic layout for the CGH Fizeau test. The test and reference wavefronts are split at the CGH (test wavefront uses +1 and reference wavefront uses 0 order of diffraction). They are recombined at the test plate so that they coincide for the imager.[6]

The referenced paper[6] states: “There are significant benefits in terms of cost and performance for Fizeau interferometry, which does not require accurate wavefront control. We propose to measure the off-axis segments using a Fizeau interferometer that has the following:

- Full aperture Fizeau test plate with spherical convex reference surface. Uses interference between reference and test wavefronts.
  - Reference wavefront created from reflection of convex surface of test plate
  - Test wavefront from reflection from mirror segment
- Uses computer generated holograms to control the absolute and relative wavefronts.
  - Common CGH, 60 mm diameter, corrects both reference and test wavefront.
  - Measurement CGH, 60 mm diameter, corrects only test wavefront (reference wavefront used at zero order). Both CGHs can be made as a single pattern on the same substrate.
- Convex spherical surface calibrated in situ using a spherical reference mirror
- Radius of curvature matching. The dominant error comes from the variation in the spacing between the test plate and the mirror segment. An uncertainty of 0.1 mm here causes only 1 nm RMS error in the surface power. (Important note: These values depend on the prescription and the CA of the UUT, so these values are not directly applicable to this program.)
- Excellent imaging. The imaging system requires no wavefront correction, so the images are undistorted and can be made at very high spatial resolution. Furthermore, the diffuser in the projection portion of the system greatly reduces the coherent or speckle noise that often affects interferometric measurements.”

3.4.3 Metrology Assumptions

3.4.3.1 Surface Figure Generation Assumptions

It is assumed that by the time LUVOIR segments begin production that capture range replication (CRR) will produce surfaces with <5 microns of low-order error and that deterministic finishing will be used to remove mid-order and high-order errors. The optical test method that is selected must be rapid to maintain the manufacturing process flow.

3.4.3.2 Un-mounted and Mounted PM Segment Testing Assumptions

The selected optical test method ideally will have the ability to test PM segments without and then with a support assembly. For unmounted segments, a multi-point support levitator (either with pneumatic force actuators or a statically determinant whiffle tree) could be used; this would require a test configuration with the gravity vector aligning with the normal to the segment vertex. This would be compatible with all segments, regardless of optical prescription.

3.4.4 Thermal Considerations

Final segment testing occurs at the nominal operating temperature of 270K. To minimize test cycle durations, it is assumed that the final PM and PMSA testing occurs in a thermally-controlled environment at ambient pressure (i.e. no vacuum). Testing in vacuum, if required, increases complexity significantly. Even testing at 270K at ambient pressures poses unique challenges given the cadence at which PM segments and PMSAs must be produced to meet a credible LUVOIR production schedule.

To minimize thermally-induced errors during testing, the entire chamber must be maintained at the test temperature, as thermal stability of the test plate (TP) is critical. A difference between the PMSA and TP temperatures will change the shape of the reference surface of the TP. Any thermal gradients induced in the TP must equilibrate prior to optical testing.

To simplify and increase the cadence of segment testing with different optical prescriptions (the off-axis aspheric form of PM segments changes with location, and it is likely there will be 6 common surface shapes relative to the parent PM), it is assumed that the wavefront projection / imaging optics - where the CGH is installed - must be accessible (i.e. the imaging optics maintained at ambient pressure and temperature conditions). Automation for removing / installing / placing CGHs is possible and should be studied. However, automation may introduce thermal sources due to motorized mechanisms in the chamber, increasing uncertainty in measurements.

If the imaging optics are maintained at ambient conditions, then a high-quality transmission window will be required to isolate the imaging optics from the test chamber environment. The homogeneity requirements on this plate will require careful calibration.

To minimize soak times when the PMSA is loaded into test, insulated “thermal carts” will be used to equilibrate the PM segment to the test temperature. It is envisioned that a single PM segment or assembly would be placed into a thermally-controlled cart, equilibrated to the test temperature, and then moved into the test chamber. Automation will be used for moving and placement of the PMSA in and out of the test chamber to minimize thermal affects. Multiple PM segments or assemblies would be stabilizing and ready for testing. This approach increases efficiency, shortens test cycles and reduces test uncertainty. Analysis of this process flow will determine the infrastructure and fixturing needed to ensure smooth and continuous operation. However, even with this approach, some “soak time” after the PM segment installation into the

test chamber will be required. It will be essential that the TP and PM segment under test are at thermal equilibrium before beginning optical test. Thermal telemetry would be applied to confirm thermal equilibrium is achieved prior to commencement of optical testing.

The test set calibration sphere requires a thermal cart as well. The calibration sphere is used in place of a PM segment or PMSA to calibrate the optical test set. There will be an initial calibration of the test set prior to first use and then follow-up calibrations at appropriate intervals based on a risk assessment and other factors. Test set calibrations may require a few days.

4.0 Potential Test-Bed and Technology Demonstrations

4.1.1 PM / PMSA Design and Manufacturing

A rigorous analysis, design, and development program under carefully controlled test conditions will be required to verify that primary mirror segments can be produced in an affordable manner that meet LUVOIR requirements.

The objectives are as follows:

1. Develop an overall error budget that provides the required optical performance and stability required for LUVOIR including the utilization of actuators.
2. Demonstrate analytically that this budget can be met with specific focus on the process, metrology and opto-mechanical model error budgets.
3. Develop rapid production mirror processing capability to meet UV requirements while reducing the overall cost of segments including near-scale demonstrations to validate design, metrology, and manufacturing approach and management of 1-g testing.
    a. Empirically demonstrate CRR replication accuracy to within 5 microns-rms of desired prescription
    b. Empirically demonstrate the accuracy of PM Segment and PMSA optical metrology uncertainties at 270K
4. Develop and execute a test program to verify performance and stability (quasi-static (thermal) and dynamic) of PMSAs that are sufficiently well correlated to analytical predictive models
    a. This could be done on a new test bed or be part of upgrades to existing test beds such as the Advanced Optics System Demonstrator (AOSD) testbed at Harris or the Segmented Mirror Demonstrator (SMD) testbed at Lockheed Martin
    b. The test program would incorporate appropriate metrology to advance the SOTA in predictive thermal control

The previously mentioned development program can be executed in 2-3 years to drive the primary mirror technology needed for LUVOIR requirements to a TRL of 5-6.

4.1.2 Rigid Body Actuators

A rigorous analysis, design, and development test program under carefully controlled test conditions will be needed to verify that a primary mirror segment RBA can be developed that meets all requirements.

The objectives are as follows:

1. Develop long and precision stroke actuator system capable of sub-nanometer precision (drives phasing capability)
2. Test actuator for effective picometer telescope WFE stability over 10 minutes (drives coronagraph performance)
3. Test actuator for sub-nanometer stability over days (drives overall phase stability of the telescope)

The development and demonstration of the RBA should occur in parallel with mirror development and be ready for incorporation into a segmented mirror testbed after approximately two years.

5.0 Summary and Path Forward

Harris is pleased to support the Lockheed Martin (LM) System-Level Segmented Telescope Design Study (SLSTDS) for the NASA ROSES D.15 Phase 1 project. All SOW tasks required by Lockheed have been addressed. The initial assessment completed in this study provides a reasonable level of confidence that development of solutions to address the significant engineering challenges posed by the LUVOIR and HabEx Large Mission Concepts are achievable. The derived requirements for the primary mirror segments and assemblies are driven by the 10 picometer WFE stability over 10-minute time-period system performance requirement.

The output and recommendations from this study are summarized below. These include trade study and testbed / technology demonstration recommendations, as well as PM mirror segment manufacturing approaches to meet high-volume, meter-class lightweight primary mirror segment production. All recommendations are intended to increase the confidence in solution development and to advance TRL levels in continuing phases of this study.

Recommended trade studies include:

- High-Level Trades: Thermal Control System Architecture
- PM Segment and PM Segment Assembly Trades:
  - Mirror Design Parameters – mass, stiffness, material, mounting
- Control Authority (# of FCAs)
- PMSA Thermal Design
- Rigid Body Actuator Mechanical Design
  - Stiffness and Stability
- PM segment design for manufacturing - trades for optimization of CRR, deterministic finishing process, constructed core and additive manufacturing technologies

  - Recommended testbed concepts / technology demonstrations include:
- PM Segment Manufacturing and Metrology
- Rigid Body Actuator Accuracy and Stability
- 2-3 PMSA System Demonstrator
  - Phasing
  - Latching
  - Dynamic and Thermal Stability
  - Correlation with predictive analytical models

Manufacturing and metrology concepts for production of large numbers of high-stability, lightweight, 1m class ULE® off-axis mirror segments over reasonable program duration (i.e. 5 years) to meet a LUVOIR-like large mission requirements were described. The use of advanced mirror manufacturing concepts such as CRR, coupled with deterministic optical finishing processes (IBF and / or MRF) indicate that high-precision mirrors may be produced at much higher rates than previously demonstrated. Advancements in metrology capabilities also support this. The emergence of new technologies and methods within the realm of automation, advanced mirror construction and additive manufacturing provide additional opportunities to increase production rates and lower cost while meeting requirement demands.

The results of this work provide the basis for further discussion. These may be applied to the next phases for the SLSTDS project. Harris looks forward to working with Lockheed Martin on the SLSTDS Phase 2 project.

6.0 Acronym List

Acronym	Definition
AMSD	Advanced Mirror System Demonstration
AOSD	Advanced Optics System Demonstrator
AWJ	abrasive waterjet cutting
CAD	Computer aided Design
CCSTP	computer-controlled small-tool processing
CGH	Computer-generated holograms
CRR	Capture Range Replication
CTE	Coefficient of Thermal Expansion
DOF	degree of freedom
EAR	Export Administration Regulations
E-ELT	European-Extremely Large Telescope
FCA	Figure Control Actuators
GTC	Gran Telescopio Canarias
HabEx	Habitable Exoplanet Imaging Mission
HET	Hobby-Eberly Telescope
IBF	ion beam figuring
IRAD	Independent Research and Development
ITAR	International Traffic in Arms Regulations
JPL	Jet Propulsion Laboratory
JWST	James Webb Space Telescope
LRIP	low rate of initial production
LTF	Low Temperature Fusion
LTS	Low Temperature Slumping
LUVOIR	Large Ultraviolet-Optical-Infrared
MMSD	Multiple Mirror System Demonstrator
MRF	Magneto-rheological Finishing
µR	micro-roughness
NANOMEFOS	non-contact measurement technique
NASA	National Aeronautical and Space Administration
PID	proportional integral derivative
PM	Primary Mirror
PMSA	PM Segment Mirror Assembly
PTC	Predictive Therma Control
RBA	Rigid Body Actuator
RMS	Root Mean Square
ROC	radius of curvature
ROSES	Research Opportunities in Space and Earth Sciences (US NASA)
RS	reaction structure
SALT	South African Large Telescope
SFE	surface figure error
SLSTDS	Segmented-Level Segmented Telescope Design Study
SMD	Segmented Mirror Demonstrator
SOTA	Current State-of-the-Art
SOW	Statement of Work
SPIE	International Society for Optical Engineering
STDT	Science and Technology Development Teams
TCS	Thermal Control System
TMT	Thirty Meter Telescope
TP	test plate
TRL	Technology Readiness Level
ULE	Ultra Low Expansion
UUT	unit under test
UV/IR	Ultraviolet/Infrared
UVOIR	Ultraviolet-Optical-Infrared
WFE	Wavefront Error

7.3 Coherent Report

Coherent SLSTD-03 Report

1.0 REFERENCE DOCUMENTS

1.1 Coherent Quotation COHR-33939-1
1.2 Coherent Task Statement ROSES RevisedJuly2018.docx
1.3 https://nvlpubs.nist.gov/nistpubs/Legacy/MONO/nbsmonograph29.pdf
1.4

2.0 Background

SLSTD is a study of segmented telescope concepts in support of future, very large aperture space based astronomy. Coherent has a relatively unique perspective on these segmented telescopes, in that Coherent built the factory and subsequently polished all the mirrors in the James Webb Space Telescope. In addition, Coherent has unique, world class surfacing technology for bare aluminum mirror finishing, and has built some of the largest visible quality aluminum mirrors.

The two missions being considered for large segmented telescopes are OST (Origin Space Telescope) and LUVOIR (Large UV/Optical/IR Survey telescope). OST is of particular interest to consider from Coherent's perspective, as materials under consideration are either bare beryllium, or bare aluminum with planned operation of OST at very cold (4K) temperatures.

3.0 Scope of Study

Topics/study tasks listed below (3.1 to 3.6) have been identified for Coherent to address in this phase 1 study. The OST project leads at NASA Goddard have recently (Dec 2018) baselined bare beryllium for the mirror material. Despite this, it is worth describing the advantages and issues in adopting an aluminum approach, as a comparison to the current baseline bare beryllium approach, and aluminum substrates will be considered in the study tasks.

By comparison, LUVOIR is not actively considering metal substrates, and is mainly trading various low CTE glasses, with a preference for ULE™. Coherent can offer valuable perspective in commissioning a large optics facility that could be capable of fabricating the large numbers of mirror segments needed for a mission such as LUVIOR. Other study partners with more experience in glass substrate design can address the material and substrate fab trades in various low CTE glasses.

With that context, study topics 3.1 to 3.6 are listed.

3.1 Assess feasibility of JWST sized aluminum mirror segments for use in OST segmented telescope.
3.2 Provide performance estimates.

3.3 Provide concepts for large-scale production based on JWST lessons learned.
3.4 Provide sample of 30cm class spherical mirror TBD f#, that could be used in a cryo test in the LM red chamber in 2020.
3.5 Identify significant uncertainties in aluminum segment technology
3.6 Develop concepts of testbeds that can address significant uncertainties (testbeds to be done during years 2 and 3)

3.1: Feasibility of JWST sized aluminum mirrors

Al6061-T6 is a common material used in aerospace, in applications ranging from aircraft structures to telescope optical benches and mirrors. The material is commonly utilized in infrared airborne and ground sensors. IR applications typically specify surface roughness at 50-100A rms. In contrast, visible wavelength sensors more commonly specify roughness at 20angstrom rms.

Because matching mirror materials to their optical bench material of construction offers such significant advantages for ease of manufacture and performance over temperature, Coherent developed a unique surfacing capability to yield glass like figure and finish in Al6061-T6 material. Figure 14 below shows some results from this process. The process can be adapted to utilize equipment employed in the polishing of bare beryllium mirrors, such as those used in JWST.

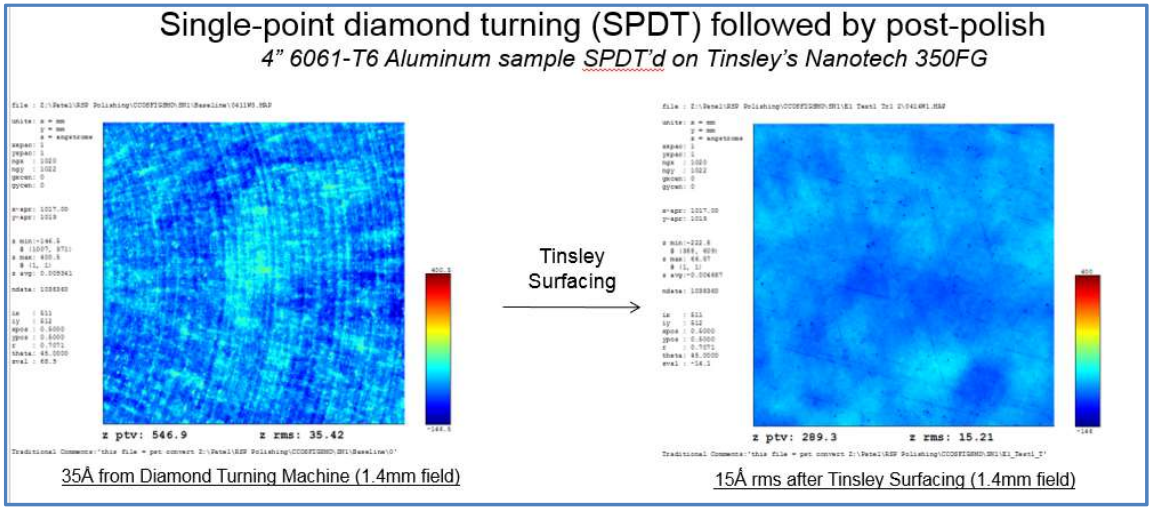

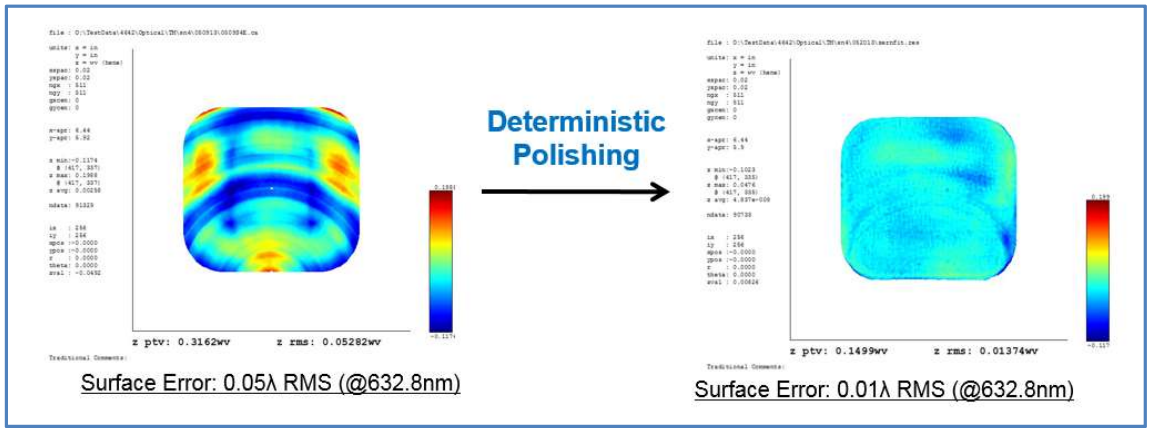

Figure 14: Al6061 Polishing Results from a 2012 SPIE Paper

This surfacing capability opens up the potential of using Al6061 as a substrate for space based telescopes with imaging capabilities in the visible and UV wavelengths.

The standard steps in manufacturing aluminum mirrors are substrate procurement, machining, polishing, and coating. A schematic of this flow is shown in Figure 15.

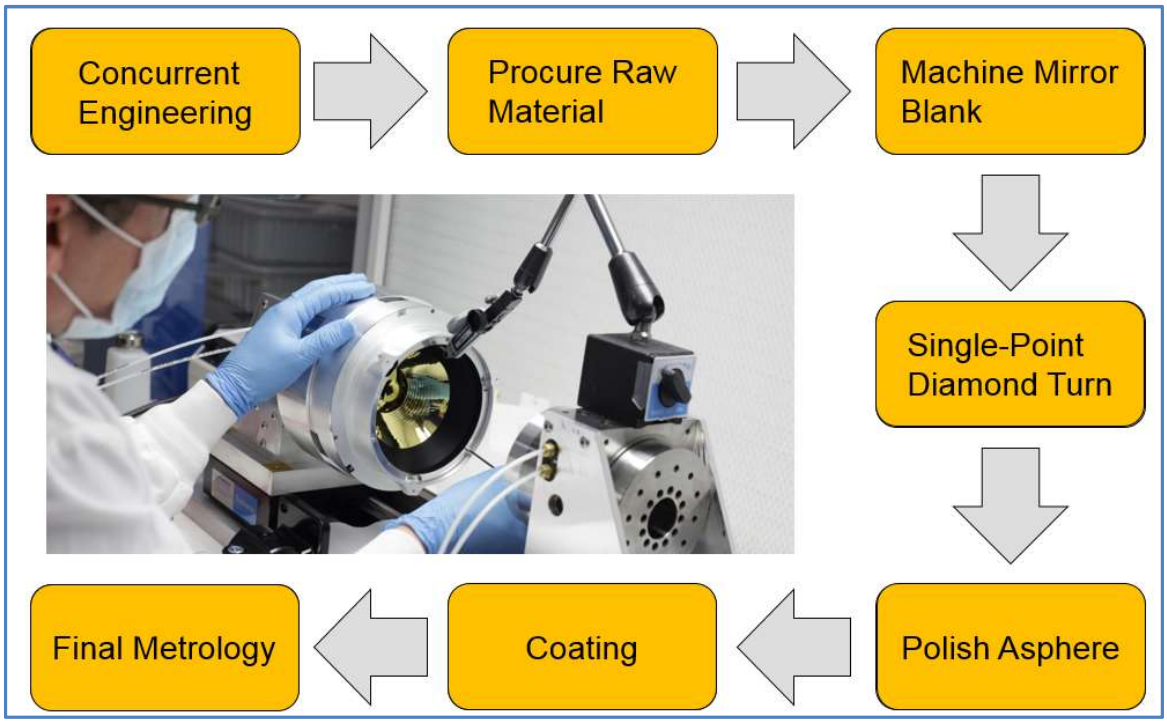

Figure 15: Al6061 Mirror Manufacturing Flow

As mentioned before, JWST type equipment can be adapted to surface aluminum mirrors. Coating works near identically, with the same equipment used to coat glass or beryllium able to coat bare aluminum.

Material procurement presents somewhat greater, but not insurmountable challenges. In order to achieve the Figure 14 polishing results, tighter specifications and processing controls on the Al6061 need to be levied, relative to the typical specifications offered by aluminum manufacturers. These specifications and processing controls are Coherent trade secrets. Coherent commonly employs these methodologies in fabrication of visible quality aluminum mirrors in the 10-400mm size range, and has built mirrors up to 650mm with these methods.

Three areas that would need attention to fabricate 1500mm scale optics include aluminum forging, heat treatment equipment, and diamond turning equipment. Forges of sufficient size are available in industry, but have not been used to yield optical substrates at 1500mm. Coherent is not familiar with heat treating equipment, but expects that such equipment is either available, or could be set up for a significant project like OST.

Starting CNC polish from a diamond turned surface is certainly more economic if there is an existing piece of equipment that can diamond turn the substrate, but aluminum mirrors can also be fabricated starting with a machined surface. There are currently no diamond turning centers of sufficient size to fabricate 1.5m mirrors in US industry, but machines of this scale have been set up in the past. An example is LODTM (Large Optics Diamond Turning Machine) which was in operation at Lawrence Livermore National Lab in the 1990's.

Substrate design is also important to consider. Aerial density is often a key driver for mirror material selection, and aluminum typically doesn't compare favorably to other candidate mirror materials for applications with critical mass or thermal stability needs. (Aluminum can be very attractive for cryogenic applications, where the optics and structure property matching is desirable.)

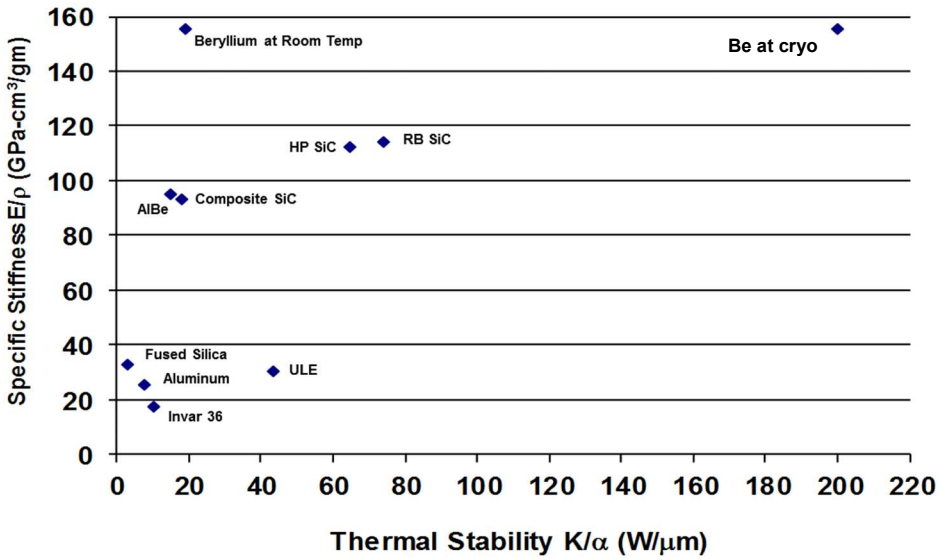

Figure 16: Specific Stiffness and Thermal Stability Parameters of Various Mirror Materials

Also, mirror design for aluminum will drive somewhat higher mass from print though considerations, relative to glass or beryllium. Figure 17 shows the parameters and print through from smoothing the beryllium JWST mirrors. The print through results from smoothing the mirror surface to improve mid frequency errors in the surface, and to improve microroughness. After smoothing, a fine figuring process is applied to the surface that removes the print through, with relatively little microroughness degradation. Face sheet thickness and spacing are governed by plate equations, with print through scaling with polishing pressure, with the inverse of Young's modulus, and with the cell size to the 4th power. Considering all else equal, beryllium can support designs with an 18-1 cell size to face sheet thickness. Glass can be designed at 14-1, and aluminum at 11-1.

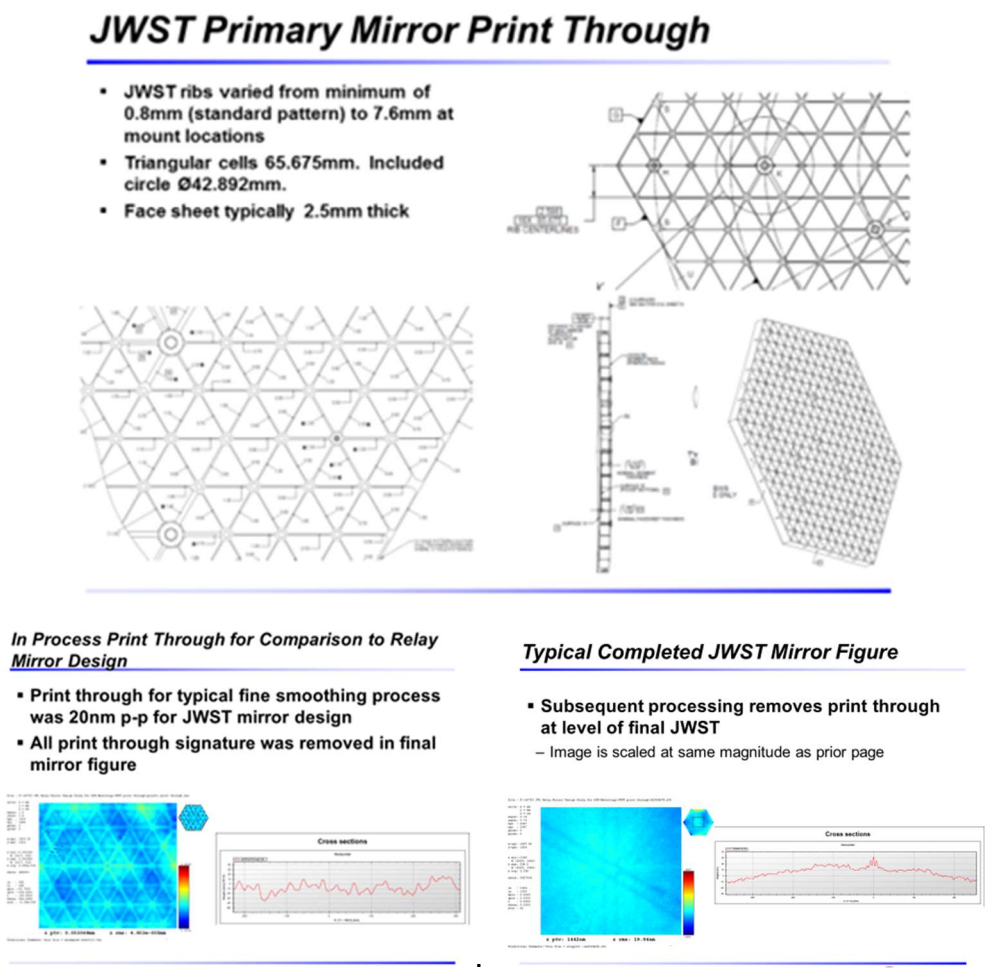

Figure 17: Print Through in JWST Mirror Manufacturing

In summary, technical feasibility of manufacturing JWST sized mirror segments in aluminum is not a significant issue, but the performance of such mirrors from a mass standpoint would likely be poorer than glass or beryllium.

3.2: Performance Estimates of Aluminum Mirrors

Aluminum mirrors can be assessed by both their optical and optomechanical properties. Aluminum mirrors can be surfaced to achieve visible wavelength figure and finish, as described in Figure 14.

From an optomechanical perspective, aluminum mirrors will have good/comparable stability at 4K compared to beryllium. NIST data shows aluminum CTE <.05ppm/C below 10K, while beryllium is <.01ppm/C.

At ambient temperature, aluminum CTE is approximately 25ppm/C, compared to 11.2ppm/C for beryllium. The JWST mirrors had to achieve temperature homogeneity of 0.002degC to keep thermal deformation errors small enough to polish the mirrors to a 10nm rms surface figure level. Aluminum mirrors of equivalent stiffness would need to be held to a proportionally tighter temperature homogeneity to deliver consistent test results. This requires the environmental control in the test environment to be better.

Aluminum mirrors will be much heavier at equivalent stiffness, relative to beryllium. The magnitude of the difference can be estimated with modeling, but the estimation of the difference is beyond the scope of this investigation.

In summary, equivalent performance aluminum mirrors will be much heavier, and somewhat more challenging to test, relative to beryllium, offset by likely significantly lower substrate price.

3.3 Provide concepts for large-scale production based on JWST lessons learned.

Starting in 2004, Coherent IOS (then SSG-Tinsley) began facilitization of a large optics test and polish facility in order to perform the surfacing and buyoff of the mirrors for JWST. The mirrors included the 18 primary mirror flight segments, spares for each flight segment type (3 types, A, B, and C), a secondary mirror and spare, a tertiary mirror and spare, and a small flat mirror. The secondaries, tertiaries, and flats were mostly run on existing, redeployed cnc polishing equipment. Eight new 1.6m class CNC polishers, and associated testing assets were configured into a facility of approximately 20k ft^2. These assets still exist at Coherent, servicing various commercial, aerospace, and scientific optics programs.

A similar amount of space, or repurposing of the existing facility, could be done to fabricate an array of aluminum or bare beryllium mirrors.

Some key lessons for such an endeavor, and key lessons learned from the JWST program, are listed below.

3.3.1 Metrology

3.3.1.1 JWST mirror fabrication took significant effort to bring up Shack Hartmann Wavefront sensing as a bridge technology to characterize surface form when optical test was inadequate to capture the full aperture, but cmm measurements would yield inadequate density of data. Modern cmm's, with scanning non contact optical probes make the need for a Shack Hartmann technology unnecessary. These cmms scan at high rates, and can gather adequate surface error data in sufficient time to support robust convergence.

3.3.1.2 Environmental control: Analog temperature control in metrology labs is relatively expensive and energy intensive, relative to "bang bang" type control systems that work over windows of temperature. The very tight temperature gradient requirements needed for testing metal mirrors at room temperature made temperature control a critical issue, and up front investment in very high performance temperature control, as well as consideration of heat sources in the metrology lab, would result in much faster and more robust test turn around.

3.3.1.3 Characterization of edges: Full aperture metrology for 1.5m substrates did an inadequate job of characterizing edges of the mirrors on JWST, and subaperture metrology needed to be developed to provide data to capture edges adequately enough to obtain sufficient convergence in mirror fabrication.

3.3.2 Fabrication

3.3.2.1 Etching: Etching of beryllium was a critical process applied before Tinsley received the beryllium mirrors. Experts in the etching process should be consulted to reproduce the etching process that was eventually arrived at for JWST, as it allowed lower overall cost and cycle time in mirror surfacing.

3.3.2.2 Edge control: The JWST primary mirrors had a tight freeboard requirement (Freeboard = distance from CA to edge of mirror). This requirement drove considerable process development on the EDU and first deliverable mirror segments, which consumed significant schedule. A future program should consider running subsize samples to validate these processes, so they are understood and baselined ahead of flight mirror fabrication.

3.4 Provide sample of 30cm class spherical mirror TBD f#, that could be used in a cryo test in the LM red chamber in 2020

Given that aluminum may not be strongly considered for OST, this effort may be tabled. There are some emerging efforts at NASA Goddard in support of Discovery missions that plan to characterize performance of aluminum down to 170K. This doesn't cover the OST temperature range, but should generate much better quality data that exists currently in literature for aluminum mirror substrates.

3.5 Identify significant uncertainties in aluminum segment technology

3.5.1 Design closure: Given the lower stiffness and corresponding higher mass to achieve necessary self weight deflection, and higher CTE, a significant risk is closure of aluminum mirror designs which meet program needs. Design studies should be performed to address this issue.

3.5.2 1.5m scale risks: In scaling up aluminum to 1.5m size, there are likely a series of subtle unknowns in the processing of the substrates. A pathfinder was run on JWST to address these issues, and to better inform a downselect between beryllium and low CTE glass on JWST. A similar pathfinder should be run if aluminum substrates remain a contender on OST.

3.6 Develop concepts of testbeds that can address significant uncertainties (testbeds to be done during years 2 and 3.

A full or subsize pathfinder at 1.5 or 1.0m should be considered as an OST technology demo if aluminum is carried in the program trade space. This pathfinder would be processed through the same processes used for smaller aluminum optics, and stability, polishability, and testability could be assessed and verified in Coherent's Richmond facility.

CHANGE HISTORY

Rev.	Date	Nature of Change
AA	25Mar19	First Draft

8 Study Conclusions and Recommendations

8.1 Analysis

The System Level Segmented Telescope Design (SLSTD) study described in this report supported directly the design and maturation of large space-based optical telescopes under consideration for the 2020 Decadal Survey. The key study findings were enumerated in the Executive Summary of this report. In addition to these, however, this study has laid a solid foundation for future trade studies and architecture analysis that will build further confidence in system performance and support technology maturation; many of these next steps were described in detail in Section 3.

While this study restricted modeling and performance prediction primarily to linear dynamic models and white Gaussian noise models, the extremely small allowable dynamic stability requirements suggest that an assessment be made of the contribution of neglected nonlinearities. This may be particularly important in the optical model, where contributions to WFE that are not merely linearly proportional to optical element motion may be significant. Further study of the impact of neglected nonlinearities is warranted.

During the course of this study, we arrived at some key recommendations or lessons learned:

1) *Segmented Primary Mirror Linear Optical Model development*: Development and validation of a linear optical model is a significant technical undertaking and requires a closely integrated team. This effort illustrated the importance of utilizing a single optical modeling environment that includes all optical elements that comprise a segmented optical system. Close coordination between structural, controls and optical engineers is essential during this process, and model quality test cases are critical to establish confidence in the model.
2) *Computational limitations for integrated modeling*: The integrated control-structure dynamic models developed for this study met a minimum threshold for providing quality performance metrics of dynamic stability, but even achieving this minimum threshold for the LUVOIR 15-meter baseline was almost beyond the capabilities of Commercial analysis software packages, and even then, significant model truncation was necessary. Computation of system performance over the broad spatial and temporal scales that are needed for performance assessment beyond this first-order analysis may require customized analysis software, or computational parallelization of the analysis.

8.2 Technology Roadmap

Over the course of this study and through numerous interactions with the mission STDTs, several technologies have been identified that require advancement to enable future missions. We focus here on technologies that are related to the work in this study by all team members. There are several technology areas that will require development that are acknowledged yet are outside the scope of this study. These are specifically related to the instruments and large deployable structures such as LUVOIR's sunshade.

8.2.1 Vibration Isolation and Precision Pointing System (VIPPS)

A system-level assessment of the Technology Readiness Level (TRL) of VIPPS involves assessing the technology readiness of the integrated VIPPS system, which is essentially comprised of three components: (a) non-contact interface sensors and actuators, and its associated mechanical packaging and integration; (b) drive electronics that support the interface

sensors and actuators, and that host real-time firmware and/or software; and (c) control algorithms themselves that map sensor measurements to actuator commands, and that are realized in the integrated system as real-time firmware and/or software.

To-date, VIPPS as an integrated system has achieved TRL 4; the laboratory system that has achieved this TRL level is illustrated in Figure 8.2.1-1. This laboratory system involved structural mass simulators of payload and spacecraft, separated by a non-contact interface with a full complement of 6 custom large-gap voice coil actuators and non-contact sensors. The non-contact sensors used in the laboratory prototype were non-flight traceable. Additionally, the control algorithms were realized on a “soft real-time” processor, in which control system sample rates were derived from an operating system master clock, but hard real-time software features necessary for a flight implementation were not implemented. Finally, the laboratory environment necessitates gravity offload of the bodies, which itself restricted the number of rigid-body degrees of freedom from that which would be present in the space environment.

Figure 8.2.1-1 illustrates what an ideal, full system-level TRL-6 demonstration would entail. First, a fully flight traceable drive electronics system would be implemented, including current drive modules and analog electronics modules for full, independent current control of the voice coil actuators, in a manner that would be implemented on the flight electronics subsystem. Second, the software and firmware would be developed and deployed in the same hard-real-time environment as the flight system. Third, full flight-traceable non-contact sensors and actuators would be employed, that are flight equivalents. Fourth, the gravity-free space environment would allow for testing of the overall pointing and control system in all 12 rigid-body degrees of freedom.

The technology maturation plan for VIPPS involves an integrated set of testbeds, modeling and simulation, and subscale flight demonstration that, taken together, effectively realizes the integration TRL 6 system shown on the right-hand side of Figure 8.2.1-1 for the full-scale LUVOIR system. This 5-step integrated plan is graphically illustrated in Figure 8.2.1-2.

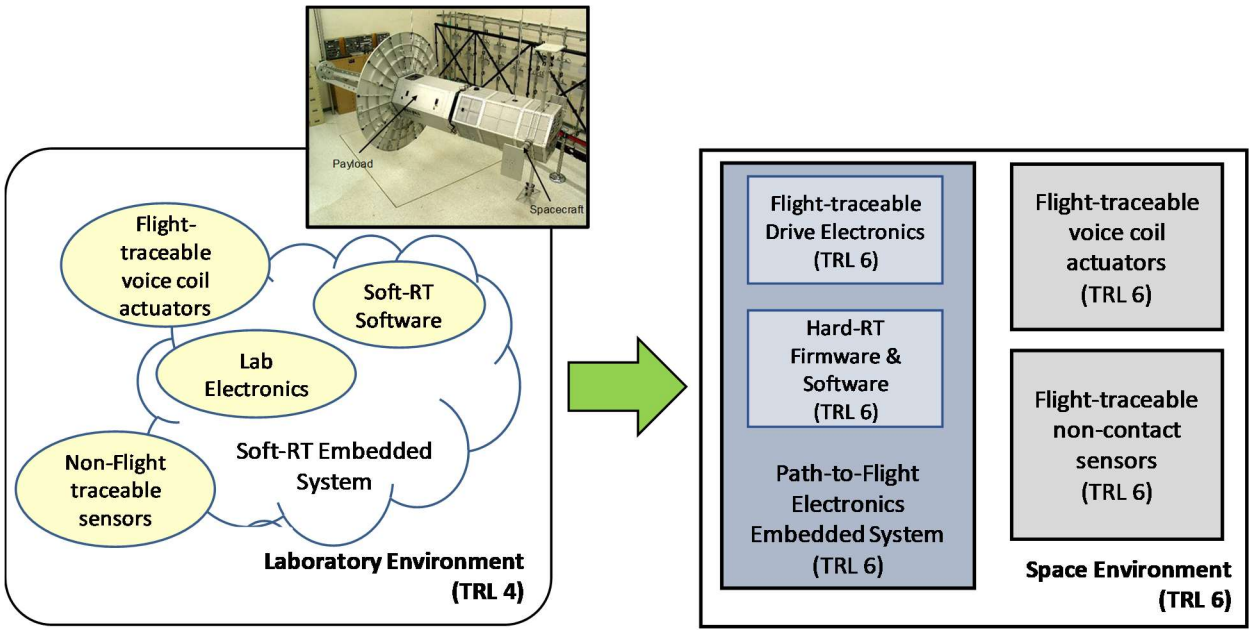

Figure 8.2.1-1: Current and planned VIPPS Technology Readiness Level

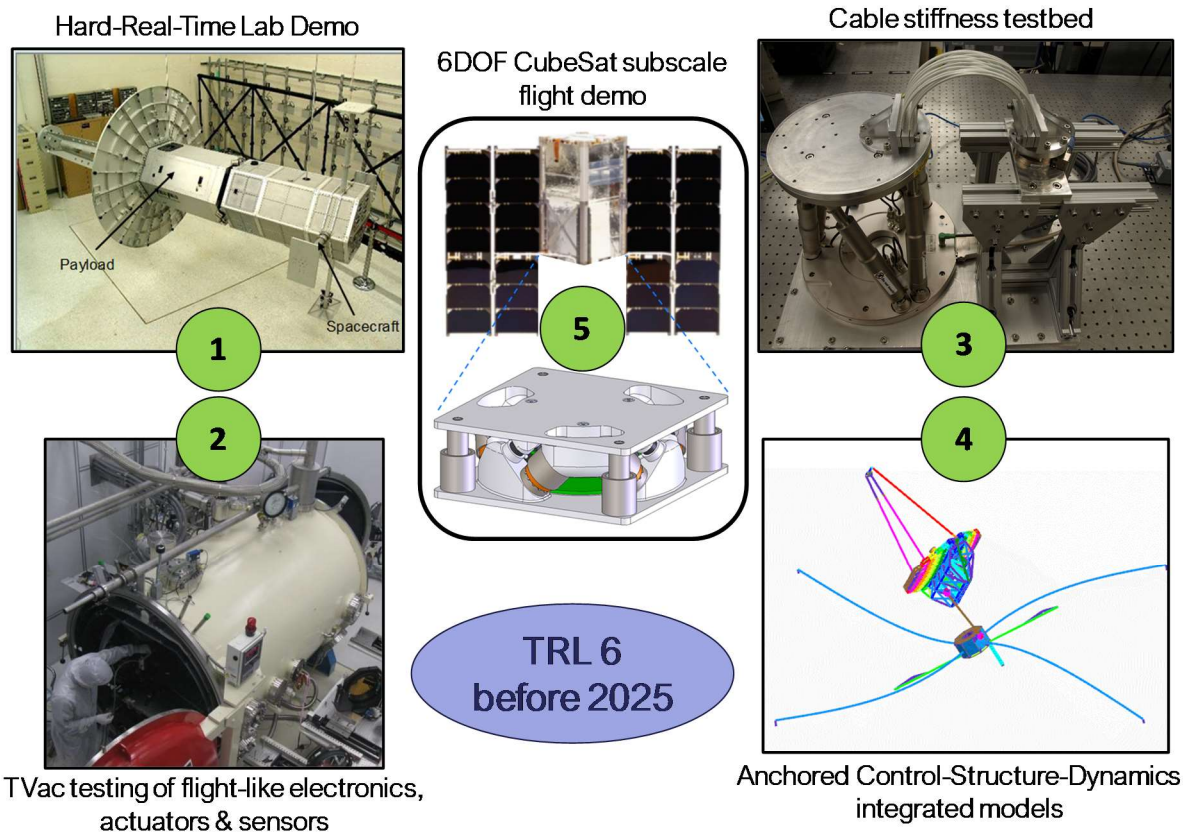

Figure 8.2.1-2: The five focus areas for VIPPS technology maturation

8.2.2 Picometer Metrology

The development of relative distance measurement systems with picometer capability is required for both ground verification of the stability characteristics of materials, components, and structures, and as part of the architecture of an on-orbit telescope alignment control system. Unlike previous programs such as Space Interferometry Mission these systems are not likely to be required to measure long motions of several mm with picometer accuracy but instead monitor very small motions. An estimate of the likely requirement for a single dimension of relative measurement would be a few picometers of measurement error at a range of several meters. This is required during a period of 10 minutes, over distance changes of 100 nanometers, in vacuum, at room temperature, with a system temperature stability in the tens of millikelvin range. In addition to measurement along a single dimension, measurement of 6DOF motion of a structure or subsystem will require multiple single dimension measurements forming an optical truss. Optical truss measurements of the motion of objects at picometer levels will be required for both ground verification and on orbit.

8.2.3 Dual-stage Primary Mirror Segment Rigid Body Actuators

Section 7.2 of this report outlined efforts by Harris to mature dual-stage segment Rigid Body Actuators (RBAs). In particular, it was discussed that Harris is currently developing a dual-stage RBA; that effort is focused on achieving TRL 6 of a dual-stage RBA that does not meet LUVOIR dynamic stability requirements but is an excellent point-of-departure for the LUVOIR point design.

More details of the RBA design trades are provided in section 2.3.2 of the Harris report (contained within section 7.2 of the overall table-of-contents structure of this report). The technical objectives of any TRL maturation plan will address the following design aspects:

1. Develop long and precision stroke actuator system capable of sub-nanometer precision;
2. Test actuator for effective picometer telescope WFE stability over the required stability window (~10 minutes for LUVOIR) for coronagraph performance;
3. Test actuator for sub-nanometer stability over days, as dictated by overall telescope long-duration phase stability.

9 References

[1] NASA Goddard Space Flight Center, "The Large UV Optical Infrared Surveyor (LUVOIR) Interim Report," National Aeronautics and Space Administration, 2018.

[2] Jet Propulsion Laboratory, "HabEx: Habitable Exoplanet Observatory Interim Report," National Aeronautics and Space Administration, 2018.

[3] P. A. Lightsey, J. S. Knight, L. D. Feinberg, M. R. Bolcar and S. B. Shaklan, "First-orderr error budgeting for LUVOIR mission," *Proc. SPIE,* vol. 10398, p. 103980C, 2017.

[4] P. A. Lightsey, J. S. Knight, M. R. Bolcar, L. D. Feinberg and W. L. Hayden, "Optical budgeting for LUVOIR," in *Proc. SPIE 10698*, Austin, 2018.

[5] LUVOIR, *LUVOIR System, OTE ans SI WFE Budgets,* LUVOIR Internal Program Memo, 2018.

[6] B. Nemati, H. P. Stahl, M. T. Stahl and G. Ruane, "HabEx Telescope WFE stability specification derived from coronagrpah starlight leakage," *Proc. SPIE,* vol. 10743, p. 107430G, 2018.

[7] H. P. Stahl, "Baseline 4-m telescope for the habitable-zone exoplanet observatory (DRAFT)," HabEx Design Team, 2019.

[8] B. Nemati, M. T. Stahl, H. P. Stahl and S. B. Shaklan, "The effects of space telescope primary mirror segment errors on coronagraph instrument performance," *Proc. SPIE,* vol. 10398, p. 103980G, 2017.

[9] L. Feinberg, M. Bolcar, S. Knight and D. Redding, "Ultra-stable segmented telescope sensing and control architecture," in *Proc. SPIE 10398, UV/Optical/IR Space Telescopes and Instrument: Innovative Technologies and Concepts VII*, San Diego, 2017.

[10] L. Leboulleaux, J.-F. Sauvage, L. Pueyo, T. Fusco, R. Soummer, J. Mazoyer, A. Sivaramakrishnan, M. N'Diaye and O. Fauvarque, "Pair-based Analytica Model for Segmented Telescopes Imaging from Space (PASTIS) for sentitivity analysis," *Journal of Astronomical Telescopes, Instruments ans Systems (JATIS),* vol. 4, no. 3, p. 035002, 2018.

[11] P. Janine-Potiron, P. Martinez and M. Carbillet, "Analytical decomposition of Zernike and hexagonal modes over a hexagonal segmented optical aperture," *OSA Continuum,* vol. 1, no. 2, 2018.

[12] L. Leboulleux, L. Pueyo, J.-F. Sauvage, T. Fusco and J. Mazoyer, "Sensitivity analysis for high-contrast imaging with segmented space telescopes," *Proc. SPIE,* vol. 10698, p. 106986H, 2018.

[13] P. Janin-Potiron, P. Martinez and M. Carbillet, "Analytical decomposition of Zernike and hexagonal modes over a hexagonal segmented optical aperture," *OSA Continuum,* vol. 1, no. 2, pp. 715-726, 2018.

[14] T. B. Andersen, "Multiple-temperature lens design optimization," *Proc. SPIE,* vol. 2000, pp. 2-6, 1993.

[15] P. Forney, "Integrated optical design," *Proc. SPIE,* vol. 4441, pp. 53-59, 2001.

[16] T. B. Andersen, "Efficient and robust recurrence relations for the Zernike circle polynomials and their derivatives in Cartesian coordinates," *Opt. Express,* vol. 26, no. 15, pp. 18878-18896, 2018.

[17] V. N. Mahajan and G.-m. Dai, "Orthonormal polynomials in wavefront analysis: analytical solution," *J. Opt. Soc. Am. A,* vol. 24, no. 9, pp. 2994-3016, 2007.

[18] K. Patterson, J. Shields, X. Wang, H. Tang and A. Azizi, "Control design for momentum-compensated fast steering mirror for WFIRST-AFTA coronagraph instrument," in *Proc. SPIE 9605, Techniques and Instrumentation for Detection of Exoplanets VII*, San Diego, 2015.

[19] N. Pedreiro, "Spacecraft architecture for Disturbance Free Payload," *J. Guidance Control and Dynamics,* vol. 26, no. 5, pp. 794-804, 2003.

[20] Schott, "TIE-43: Properties of Zerodur," Schott, 2019.

[21] S. T. Gulati and M. J. Edwards, "ULE-Zero expansion, low density and dimensionally stable material for lighweight optical systems," in *Proc. SPIE 10289*, 1997.

[22] Schott, "TIE-33: Bending strength of optical glass and Zerodur," Schott, 2015.

[23] P. Hartman, "ZERODUR: deterministic approach for strength design," in *SPIE Optical Engineering 51(12)*, 2012.

[24] P. Hartman, "Minimum lifetime of ZERODUR structures based on the breakage stress threshold model: a review," in *SPIE Optical Engineering 58(2)*, 2019.

[25] The Aerospace Corporation, "Dynamic fatique of ultra-low expansion glass for space mirrors (Reissue A, Report SD-TR-86-49)," The Aerospace Corporation, 1988.

[26] National Aeronautics and Space Administration, "Fracture toughness and crack growth of Zerodur (NASA TM 4185)," NASA, 1990.

[27] ASTM International, "Standard practice for reporting uniaxial strength data and estimating Weibull distribution parameters fo radvanced ceramics (ASTM C1239-13)," ASTM International, 2018.

[28] S. M. Weiderhorn, "Subcritical crack growth in ceramics," in *Fracture Mechanics of Ceramics*, Plenum Press, 1974.

[29] P. Hartman, G. Kleer and T. Rist, "ZERODUR: new stress corrosion data improve strength fatique prediction," in *Proc. SPIE 9573*, 2015.

[30] T. B. Andersen and Z. A. Granger, "Correction of wavefront aberrations in focal and afocal TMAs," *Proc. SPIE,* vol. 10745, p. 107450C, 2018.

[31] "OpticStudio is a trademark of Zemax LLC, www.zemax.com".

[32] K. Tajdaran, L. Dewell, E. Eason, R. Bell, K. Liu, et al, "Telescope line-of-sight slew control and agility with non-contact vibration isolation for the large ultraviolet/optical/infrared (LUVOIR) surveyor concept," in *SPIE*, San Diego , 2018.

[33] S. Macfarlane, E. Croft, "Jerk-Bounded Manipulator Trajectory Planning: Design for Real-Time Applications," in *IEEE Transactions on Robotics and Automation* , 2003.

[34] J. S. Knight, *Ultra-Stable Large Telescope Research and Analysis (ULTRA) Progress to Date,* SPIE, 2018.

[35] M. Meixner, L. Armus, C. Battersby, J. Bauer and E. Bergin, "Overview of the Origins Space Telescope: science drivers to observatory requirements," *Proc. SPIE,* vol. 10698, p. 106980N, 2018.